Design, Characterization and Functionalization of DNA Materials

Daniel Schiffels

München 2013

Design, Characterization and Functionalization of DNA Materials

Daniel Schiffels

Dissertation
an der Physik
der Ludwig–Maximilians–Universität
München

vorgelegt von
Daniel Schiffels
aus Freiburg im Breisgau

München, den 04. Oktober 2013

Erstgutachter: Prof. Dr. Liedl
Zweitgutachter: Prof. Dr. Fygenson
Tag der mündlichen Prüfung: 19. November 2013

Contents

List of Figures

List of Tables

Zusammenfassung

DNA wird seit einigen Jahren zur Herstellung von Strukturen mit Nanometer Präzision genutzt. Mittels der am häufigsten verwendeten Techniken, "Tile" und " DNA Origami", wurden verschiedenste DNA Objekte wie unter anderem DNA Kristalle, DNA Nanotubes, gebogene und verdrehte Zylinder und selbst komplexe 3D Strukturen hergestellt. Aufgrund der einzigartigen Kontrolle über die räumliche Anordnung von DNA Molekülen wird DNA Nanotechnologie heute in verschiedensten Forschungsgebieten wie struktureller Biologie, Nanomedizin, Einzel-Molekül Detektion oder Plasmon-Forschung verwendet.

In dieser Arbeit wird systematisch die Biege-Steifigkeit (Persistenz Länge) von DNA Nanotubes (HX-Tubes) als Funktion des Umfangs untersucht. Dazu wurden mikrometerweite thermische Nanotube Fluktuationen mittels Fluoreszenz Mikroskopie analysiert (A,B). Zusätzlich wurden intrinsische und thermische Nanotube Verdrehungen durch Anbindung von Gold-Nanopartikeln (AuNP) und Transmissions Elektronen Mikroskopie (TEM) sichtbar gemacht (C). Aus diesen Messungen ergibt sich, dass die Peristenz Länge sich proportional zum Flächenträgheitsmoment des Nanotube Querschnitts verhält, intrinsische Verdrehungen nur auftreten, wenn sie durch die DNA Sequenzen vorgegeben sind und dass thermische Verdrehungen über sehr viel kürzere Distanzen als die Persistenz Länge auftreten. Des weiteren wurde ein DNA Nanotube Elastizitäts-Modell hergeleitet, das Verformungen von doppelstängiger DNA sowie von Cross-Overn berücksichtigt und gezeigt, dass alle Messungen in guter Übereinstimmung mit dem Modell sind.

Um ein besseres Verständnis für den Zusammenhang zwischen Persistenz Länge und dem Aufbau von DNA Nanotubes auf der Ebene einzelner DNA Moleküle zu gewinnen wurden die thermischen Verbiegungen von verschiedenen sechs-Helix-Tubes mit unterschiedlichen DNA Architekturen untersucht. Die Ergebnisse zeigen, dass das Anordnen von mehreren Cross-Overn innerhalb einer Tube Querschnittsfläche sowie die Verringerung der Dichte von DNA Cross-Overn die Persistenz Länge verringert. Die Ergebnisse werden im Rahmen des zuvor hergeleiteten Elastizitäts Modell diskutiert.

Es wurden verschiedene Strategien zur Herstellung von gebogenen und verdrehten DNA Nanotubes entwickelt. Biegung und Drehung wurden durch gezielte Einfügung oder Auslassung von Basenpaaren, speziell programmierten Faltungswegen, oder spezielle Anordnung von komplementären DNA Sequenzen innerhalb der Nanotubes kontrolliert. Nanotube Konturen wurden mittels TEM, Rasterkraftmikroskopie (AFM), UV-Absorption, sowie stochastischer optischer Rekonstruktionsmikroskopie (STORM) charakterisiert. Die Messungen zeigen, dass gebogene Nanotubes meist geschlossene Ringe bilden und Nanotubes

mit Biegung und Drehung helix-förmig sind (D).

Es wird gezeigt, dass Anbindung des organischen Farbstoffs Cy3 an einen oder mehrere DNA Stränge der HX-Tubes ebenfalls zur Ausbildung von Helix-förmigen Nanotubes führt (E). Ganghöhe und Radius der Nanotubes mit Cy3 Anbindung wurden systematisch in Abhängigkeit der Cy3-Bindungsposition gemessen und das Ergebnis mit einem einfachen Cy3-DNA Bindungsmodell verglichen. Des weiteren wurden die optischen Eigenschaften von Cy3 Molekülen, gebunden an HX-Tubes mittels Fluoreszens-Polaristations-Mikroskopie (FPM) und Fluoreszenslebensdauer Messungen untersucht. Es wurde ein Zusammenhang zwischen Anisotropie (gemessen mittels FPM) und der Orientierung der Cy3 Dipol Achse hergeleitet. Die beobachtete Anisotropie entspricht in diesem Modell einem Winkel von ca. 60° zwischen Cy3-Dipol und DNA Achse.

Es wird gezeigt, dass die Ausbildung von fluoreszenten Silber Clustern, bestehend aus wenigen Atomen (Ag-DNA) innerhalb von einzelsträngigen "DNA hairpins" an der Oberfläche von DNA Nanotubes stattfinden kann (F). DNA Nanotubes mit Ag-DNA Clustern sind fluoreszent und konnten mittels Fluoreszenz Mikroskopie sichtbar gemacht werden. Als Nebenprodukt der Ag-DNA Synthese wurde Aggregation von DNA Nanotubes beobachtet.

Es wurden zwei neue Methoden zur Weiterentwicklung der DNA Origami Methode untersucht: 1) Kristallisierung von rechteckigen DNA Origami Strukturen zu 1D Ketten und 2D Gittern (G) und 2) Anbindung von "Tiles" an einer DNA origami "Schablone". Die Faltungs-Ausbeute beider Strategien wurde mittels Gel Elektrophorese, TEM und AFM charakterisiert.

Schließlich wird im letzten Kapitel eine Sammlung von Matlab Programmen vorgestellt, die benutzt wurden um DNA Nanotube Kontouren automatisch aus Bild Daten auszulesen, Persistenz Länge zu bestimmen, polarisierte Fluoreszenz Bilder auszuwerten und DNA Sequenzen zu generieren.

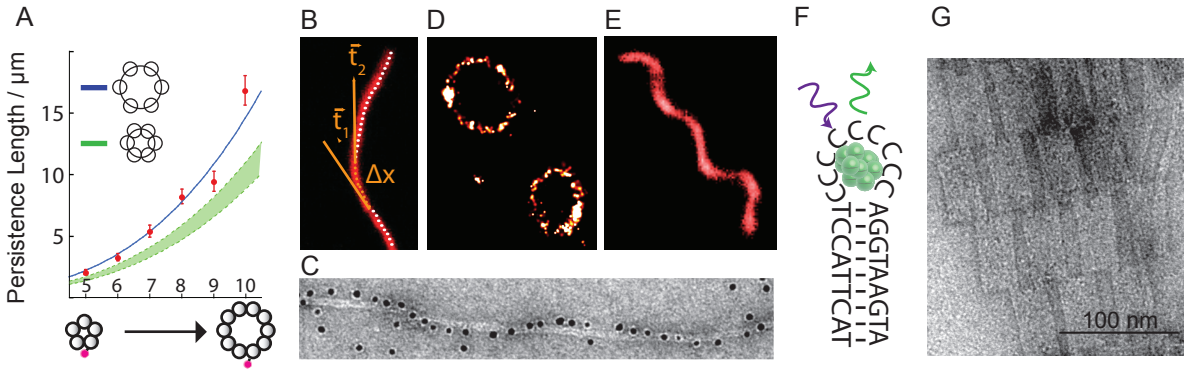

Abstract

In recent years it has been demonstrated, that the sequences of a set of DNA molecules can be specifically programmed to drive their self-assembly into a predesigned nanoscale shape with nanometer precision. The two main techniques, "tiled" assembly and "DNA origami" have been used for the construction of DNA crystals, DNA nanotubes as well as single- and multi-layer DNA objects including cuboids, curved and twisted bundles and even complex 3D geometries such as hollow containers. Because of this unique spatial control, today, DNA nanotechnology is actively used in a wide range of research areas such as structural biology, nanomedicine, single-molecule detection and plasmonics.

We systematically measure the bending stiffness (persistence length) of DNA nanotubes (HX-tubes) as function of their circumference by analyzing micron-scale thermal fluctuations using fluorescence video microscopy (A, B). We further characterize intrinsic and thermal HX-tube twist by direct visualization of gold nano particles (AuNP), bound to specific positions of the tubes by electron microscopy (TEM) (C). We find that persistence length scales with the tube's second moment of inertia, intrinsic twist tends not to be present except when forced by sequence design and thermal twist occurs on lengths much shorter than the persistence length. We show that these results can be understood in terms of a quantitative DNA nanotube elasticity model, which takes the deformations of the DNA duplexes, as well as the strand cross-overs between them into account.

To gain a better understanding of the interplay between the molecular architecture of DNA nanotubes and their micrometer-scale persistence length we study the thermal bending fluctuations of several six-helix-tubes with variations in the density and placement of strand cross-over and backbone nicks. We find that staggering cross-overs in one cross-sectional plane as well as decreasing the overall density of cross-overs significantly decreases persistence length and discuss these results in terms of the previously derived elasticity model.

We present several design strategies for DNA nanotubes with defined intrinsic torsion, intrinsic curvature and combination of both. Curvature and torsion were controlled by either targeted insertion and deletion of basepairs, specific programming of the folding pathway or specific placement of complementary sequence motifs within the DNA nanotube lattice. We characterize intrinsic tube deformations by TEM, atomic force microscopy (AFM), temperature controlled UV-absorbance and stochastic image reconstruction microscopy (STORM) and show that intrinsically curved tubes predominantly form closed rings (D) and tubes with a combination of curvature and torsion have a helical contour.

We show that the attachment of the organic dye Cy3 to one or several DNA oligonucleotides of HX-tubes can also cause tube deformations (E). We systematically study pitch and radius of the observed helical tube contour as function of Cy3 attachment position and propose a Cy3-DNA binding scheme that depends on the DNA microenvironment of the binding site. We further investigate the optical properties of Cy3 on HX-tubes by fluorescence polarization microscopy (FPM) and fluorescence lifetime measurements. We derive a relation between anisotropy and alignment of Cy3 dipoles. Our model suggests an angle of approximately 60° between Cy3 dipole and DNA axis.

We demonstrate that the self-assembly of fluorescent few-atom silver clusters (Ag-DNA) can be directed to hairpins on the surface of DNA nanotubes as a means of fluorescent labeling (F). We find that Ag-DNA on DNA nanotubes produces bright fluorescence, easily detectable by fluorescence microscopy. However Ag-DNA synthesis also promotes aggregation of DNA nanotubes.

We investigate two new methods for the construction of micrometer scale DNA assemblies based on the DNA origami technique: 1) Crystallization of rectangular DNA origami blocks into 1D and 2D lattices (G) and 2) Growth of DNA tiles on a ribbon shaped DNA origami template with sticky ends. The yield of both methods is estimated by gel electrophoresis, TEM and AFM.

Lastly, we describe a set of Matlab tools that were written and used for automated tube contour digitalization from image data, calculation of persistence length, analysis of FPM data and design of DNA sequences.

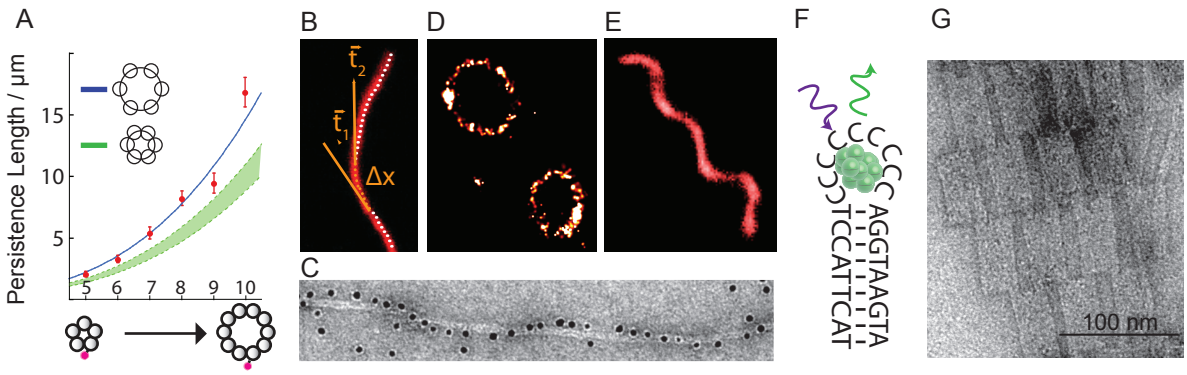

Chapter 1

Introduction

DNA molecules store genetic information in living organisms. Since the 1970s synthetic DNA of specifically "programmed" sequence has been used *in vitro* for the self-assembly of increasingly complex DNA objects [92]. This field, called DNA nanotechnology, relies on the well studied interaction of single stranded DNA molecules (ssDNA) *via* the specific hybridization of guanine with cytosine and thymine with adenine bases to program molecular recognition.

Two ssDNA molecules of complementary sequence can hybridize and form double-stranded B-form DNA (dsDNA) with the well known double helical geometry, formed by the DNA's phosphodiester backbones (figure 1.1 a). Each ssDNA molecule, also called DNA "strand", has two distinct ends, 5' ("five prime") and 3' ("three prime"). The 5' to 3' direction is marked by arrows. DNA hybridization only occurs between strands of opposite directions. dsDNA has a diameter of 2.1 nm, a length of 0.34 nm per base-pair and completes two helical turns per 21 base-pairs [106].

Complex nanoscale objects can be constructed by interlinking multiple dsDNA molecules in a predefined geometry. This can be achieved by strand cross-overs as well as "sticky ends", shown in figure 1.1 b. In this simplified illustration, used throughout all chapters, DNA strands are shown as straight lines, letters depict DNA bases and base-pair interactions are shown as black dashes. The 5' and 3' ends are marked by squares and arrows respectively. Strand cross-overs are junctions in which DNA strands from one DNA double helix ("duplex") cross-over to an adjacent DNA duplex. Sticky ends are single stranded DNA overhangs at the end of a dsDNA molecule. Two dsDNAs with sticky ends of complementary sequence can end-to-end join by hybridization.

The most commonly used technique for the assembly of nanoscale DNA objects is called "DNA origami" [76]. In DNA origami, a ssDNA of about 8000 bases, the "scaffold strand", is folded into a specific shape by programmed interactions of about 200 "staple strands". Staple strands are synthetic ssDNA with 40-60 bases in length. Their sequence is complementary to several sites of the scaffold strand and "staples" those sites together by formation of strand cross-overs. DNA origami self-assemble during thermal annealing of the sample, typically from 90°C to room temperature (figure 1.2 a, b). At 90°C all DNA components are single-stranded because hybridization is unstable. As the temperature is

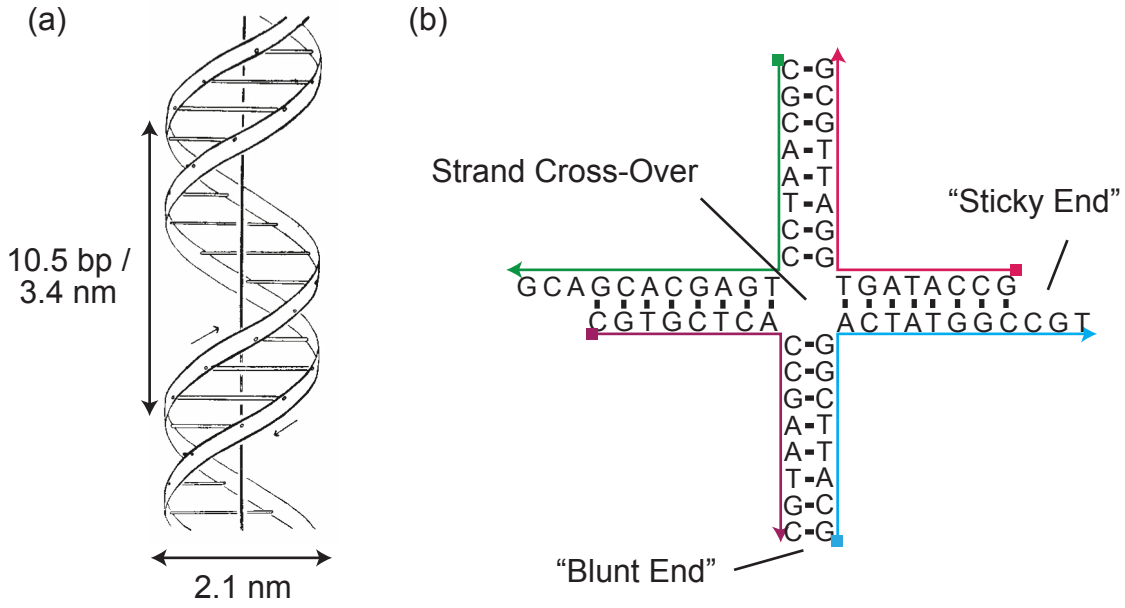

Figure 1.1: (a) Geometry of double stranded DNA (dsDNA) [2]. (b) DNA strand cross-over formed by four ssDNA molecules. Bases are identified by letters, base-pairing is indicated by dashes, 3' ends are illustrated as arrows.

lowered staple strands hybridize to their programmed target sites and fold the scaffold into a predefined shape.

DNA origami is excellent for the construction of objects with well defined dimensions and has been used to create a diverse set of 2D [76] and 3D shapes [21, 22, 41, 17, 48, 32, 36, 99, 96, 119, 8], from simple rectangles to nano flasks. The self-assembly process yields a fraction of scaffold strands which are "mis-folded" *i.e.* because some staple strands are missing or two scaffold strands are connected by shared staple strands. This fraction is typically between 10% and 90% depending on the complexity and size of the target geometry as well as buffer and annealing conditions. Depending on the assembly yield of well-folded structures, DNA origami are often purified after self-assembly to remove mis-folded structures.

A different technique, called "tiled assembly" requires only a small set of typically 1-10 synthetic ssDNA molecules for the construction of periodic, micrometer sized "tile lattices" [77, 61, 59]. A tile can be a rigid structural element, such as a double cross-over molecule, consisting of two dsDNA interlinked by two cross-overs [77], or a single ssDNA [116]. Tiles are designed to interact with each other by sticky ends. Tiles with an intrinsic curvature form DNA nanotubes. The size of the resulting lattices or DNA nanotubes is not defined by the tile design and can depend on the concentration of DNA, annealing time

[2]Figure 1.1 a was adapted by permission from Macmillan Publishers Ltd: Nature from Watson, J. D. & Crick, F. H. C. Molecular Structure of Nucleic Acids. Nature 171, 737738 (1953)., copyright 1953

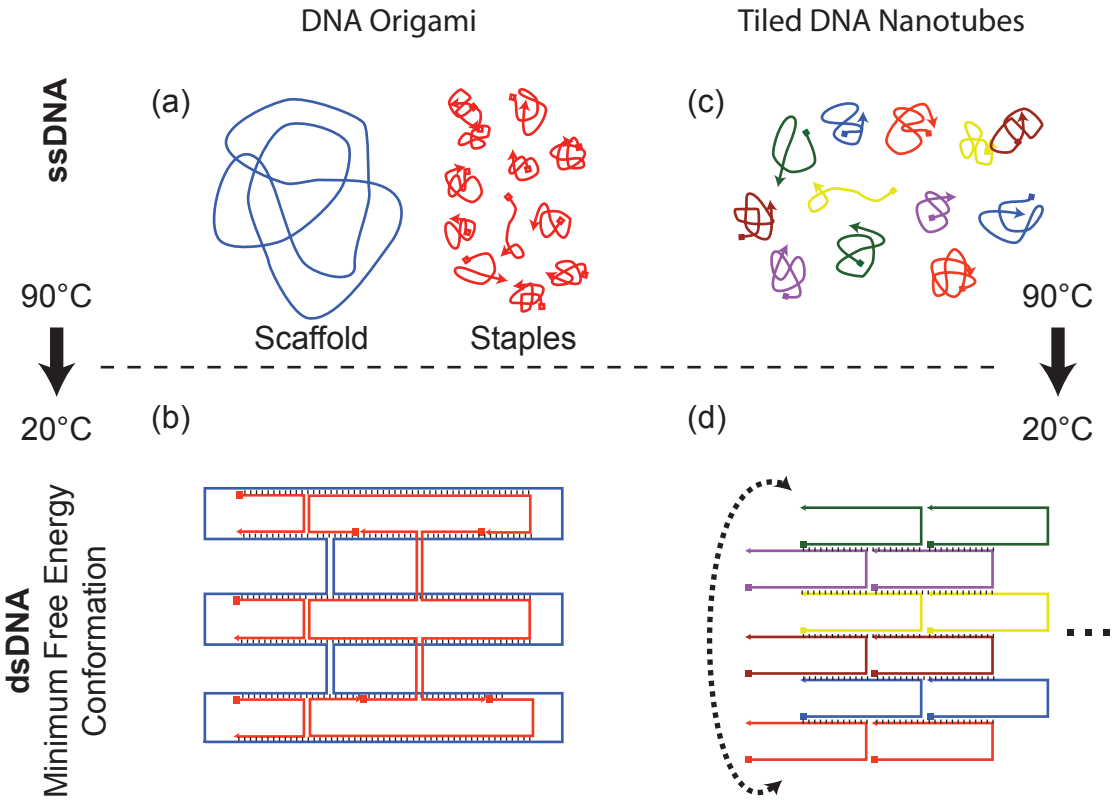

Figure 1.2: Illustration of DNA self-assembly techniques. In DNA origami a "scaffold" strand is mixed with "staple" strands (a). During thermal annealing "staple" strands fold the scaffold strand into a predesigned shape (b). In tiled assemblies a set of synthetic DNA strands which are programmed to interact with each other is thermally annealed (c). Tiles form a periodic lattice, which grows until free tiles are depleted from solution (d).

and salt concentrations. The assembly of single-stranded tiles [116] into a DNA nanotube is illustrated in figure 1.2 c, d.

Today DNA nanotechnology is actively used in a wide range of research fields such as structural biology [20, 120, 9], nanomedicine [19, 52] nanoelectronics [60], plasmonics [102, 46] and single-molecule detection [100, 26, 99, 8, 108, 24, 44]. DNA objects often function as templates to position other nanoscale elements such as gold nanoparticles (AuNP), organic dyes or quantum dots with nanometer precision.

Chapter 2

Nanoscale Structure and Microscale Stiffness of DNA Nanotubes

2.1 Introduction

[1] The ability to build structures of defined shapes and mechanical properties has always been a prerequisite for the development of new technologies. Modern research facilities, as well as the instruments used within those facilities, rely on fundamental knowledge of how building materials such as steel or concrete behave mechanically. On the nanometer scale, self-assembly has proven to be a viable method for building structures with reliability and precision. At first an exotic discipline, DNA-based self-assembly [93] in particular has developed into an enabling technique that is finding application in such disparate fields as structural biology [20, 120, 9], nanomedicine [19, 52] nanoelectronics [60], plasmonics [102, 46] and single-molecule detection [100, 26, 99, 8, 108]. With the ever-increasing requirements DNA structures must fulfill in order to perform their tasks comes the need to carefully study the mechanical properties of their main building motifs. Just as steel and concrete construction could reach its present capacity and reliability only with advanced knowledge of the mechanical properties of those materials, a detailed understanding of the mechanical behavior of building motifs in DNA nanotechnology will boost the development of complex nanoscale architectures.

In many studies that employ DNA as a building block, DNA double helices are arranged in parallel to form multi-helical bundles or sheets [20, 77, 61, 59, 66, 117, 105, 2, 107, 42, 76, 21, 17, 41, 48]. As a result, the persistence length of the DNA double helix is multiplied and micron-scale objects can be created. Parallel arrangements can be achieved by tile-assembly or by the scaffolded DNA origami approach. Previous work has shown that the stiffness of multi-helical bundles can be estimated by approximating the DNA double-helices as continuously connected cylinders of homogenous material with isotropic Young's

[1] Chapter 2 is reprinted (adapted) with permission from Daniel Schiffels, Tim Liedl, and Deborah K. Fygenson (2013) Nanoscale Structure and Microscale Stiffness of DNA Nanotubes. ACS Nano. Copyright (2013) American Chemical Society.

moduli [77, 66, 48, 105] but also that deviations from this picture can be observed [40, 105].

Given the very well studied material properties of double-stranded DNA [13, 12], the key parameter which determines bending stiffness of arrays of DNA helices is their second moment of inertia, J. We studied a set of DNA nanotubes of defined circumference (HX-tubes) [117] which allowed us to systematically vary J and measure the associated persistence length P. This approach confirmed that persistence length scales with the second moment of inertia and revealed structural features of DNA nanotubes such as the average helix spacing under solution conditions. The observed helix spacing is in good agreement with recent cryo-EM studies [5], which provided a pseudoatomic model of a DNA origami structure.

Being tiled structures, HX-tubes can form with the DNA duplexes either parallel to or twisting about the tube axis in discrete amounts (supertwist). Geometrically, J and, therefore, P depend on the amount of supertwist. The single helix resolution, required to directly visualize supertwist, cannot be achieved by conventional transmission electron microscopy (TEM) or atomic force microscopy (AFM). We therefore characterized the supertwist by placing gold nanoparticles (AuNP) on a specific DNA helix of the tubes and tracking their position relative to the tube axis using TEM. This approach revealed that (i) HX-tubes tend not to form with supertwist unless forced by sequence design; (ii) Thermally excited tube twist occurs on length scales much smaller than the persistence length; and (iii) The pitch of forced supertwist is much larger than geometrically expected.

To explain our observations, we propose an elastic cylinder model for DNA nanotubes. In the model, adjacent cylinders can shear with respect to each other at an elastic cost, associated with deforming the strand-crossovers between them. We calculate the Free Energy gained upon closing a duplex sheet into a tube and show that it is minimized at the observed, minimum supertwist allowed by HX-tube sequence design. The model also predicts untwisting of forced supertwist and captures the observed supertwist pitch. We show that the low twist persistence length can be explained by cylinder shearing.

2.2 Persistence Length of HX-Tubes

In 2008, Yin and co-workers pioneered the use of "half-crossover" (HX) tiles and designed a set of DNA nanotubes with a defined number of B-form double-helices in circumference, known as "n-helix tubes" or nHT [117]. To better understand HX-based structures and characterize the effective Young's modulus of dsDNA materials, we measured the stiffness of nHT with n ranging from 5 to 10.

We measured nHT stiffness in terms of *persistence length*, P, the length over which correlations in the orientation of a thermally fluctuating contour decay exponentially. To characterize their thermally fluctuating contours, we assembled nHT with one or more fluorescently labeled DNA strands, confined them to two dimensions between polymer-coated glass surfaces, and imaged using fluorescence videomicroscopy.

In a two-dimensional system, P is defined by:

$$\langle \hat{\mathbf{t}}(x) \cdot \hat{\mathbf{t}}(x + \Delta x) \rangle = e^{-\Delta x / 2P} \tag{2.1}$$

where $\langle \hat{\mathbf{t}}(x) \cdot \hat{\mathbf{t}}(x+\Delta x) \rangle$, called the tangent correlation, is the average inner product between two unit tangent vectors separated by a distance Δx along a contour (figure 2.1a). We used an automated tracing algorithm [110] to assign coordinates to a set of points along a contour, spaced every 4 pixels ($\sim 0.25\ \mu$m) between manually selected start and end points. We then used a home-made matlab script to calculate the tangent correlation as a function of Δx from the trace coordinates.

A deviation from exponential dependence was present at the smallest and largest Δx in every dataset (figure 2.1b). At large Δx, it takes more time for the tangents of a given nanotube to randomize. To avoid relying on the ∼100 conformations from a single (longest) tube, we set an upper bound, $\Delta x < \Delta x_{\max}$, by excluding tangent correlations for which there were less than 500 tangent pairs in the data set. At small Δx, tangents were excessively correlated due to the finite thickness of the sample volume ($\leq 2\ \mu$m), which accomodates small amplitude fluctuations perpendicular to the image plane. We therefore obtained the persistence length by fitting a modified version of equation 2.1

$$\langle \hat{\mathbf{t}}(x) \cdot \hat{\mathbf{t}}(x + \Delta x) \rangle = e^{-(\Delta x - x_0)/2P} \tag{2.2}$$

and restricting the data to $\Delta x > 2\ \mu$m.

We estimated the uncertainty in P using a bootstrap method: from the full set of contours ($167 < U < 844$) for a given nHT, a subset U_i was randomly chosen (with replacement) and its persistence length P_i obtained. As this process is repeated (typically 5000 times), the mean of P_i approaches the value of P obtained using the full contour set, and the standard deviation, σ_P, provides an estimate of the uncertainty in the measurement of P. The uncertainty was uniformly $\leq 10\%$ of P and not sensitive to the sample size (table 2.1).

Table 2.1: Persistence lengths of nHT and characteristics of the data sets from which they are derived.

	n (helices)	P (μm)	σ_P (μm)	x_o (μm)	$\Delta x_{\max}$ (μm)	N (tubes)	U (contours)
5HT	5	2.0	0.2	0.34	2.3	5	167
6HT	6	3.3	0.3	0.24	6.7	13	503
7HT	7	5.4	0.5	0.57	4.9	7	212
8HT	8	8.2	0.6	0.62	7.9	5	377
9HT	9	9.4	0.8	0.69	7.7	5	336
10HT	10	16.8	1.2	0.50	13.8	13	844
$6HT_2$	6	2.1	0.2	0.61	3.3	10	269
$6HT_{3Cy3}$	6	2.7	0.3	0.00	4.4	4	306

We find that P increases with n, as expected (table 2.1). To interpret $P(n)$ quantitatively in terms of nHT structure, we model each double-helix as an elastic cylinder of radius, r, and Young's modulus y, and each nanotube as an array of such cylinders uniformly spaced along the circumference of a circle with radius R.

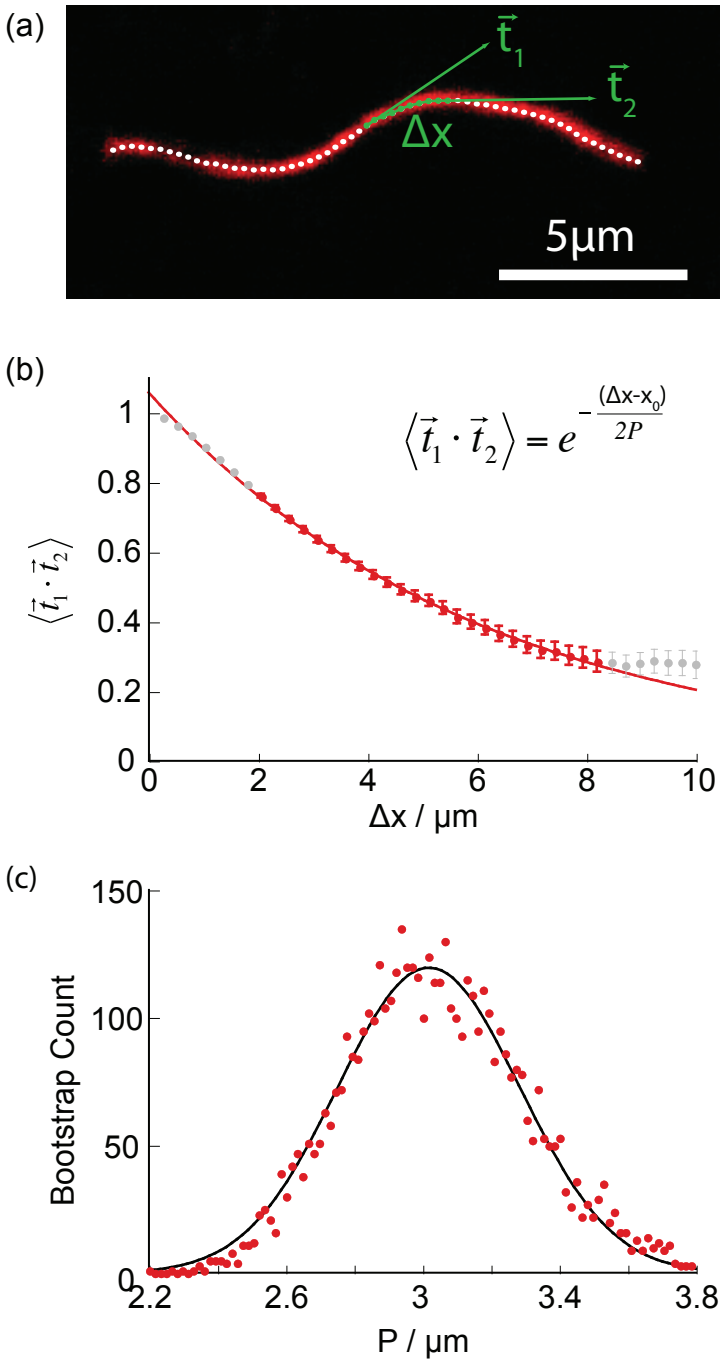

Figure 2.1: Calculation of persistence length from a set of contours: (a) Typical fluorescence image of a DNA nanotube with its trace superimposed, indicating two tangents t_1, t_2, and their separation distance Δx. (b) Tangent correlation function with a curve fit of 2.2. Data plotted in grey are outside the fit limits. (c) Persistence length distribution obtained by a bootstrap method and its least-squared-error fit to a gaussian profile.

The persistence length of a cylinder is

$$p = \frac{y}{k_B T}\, j \tag{2.3}$$

where $j = \pi r^4/4$ is the area moment of inertia and $k_B T$ is the thermal energy, the product of the temperature, T, and Boltzmann's constant, k_B. Similarly, the persistence length of a nanotube is

$$P = \frac{Y}{k_B T}\, J \tag{2.4}$$

where Y is the effective Young's modulus of dsDNA in the nanotube and J is its area moment of inertia. Given the spacing between neighboring helices, $s = 2R\sin(\pi/n)$ (for $n > 2$), J can be calculated from j using the parallel axis theorem. The result

$$P = np\left(\frac{Y}{y}\right)\left[1 + 2\left(\frac{R}{r}\right)^2\right] = np_{\text{eff}}\left[1 + \frac{(s/r)^2}{2\sin^2(\pi/n)}\right] \tag{2.5}$$

is independent of the angle at which the neutral axis bisects the nanotube (section 2.7.1). Here we define $p_{\text{eff}} = (Y/y)p$ to be the effective persistence length of a DNA double helix within the tube.

In previous work, it has been assumed that complete crossovers (in which two DNA strands exchange between neighboring helices) do not change the effective Young's modulus of dsDNA ($Y = y$) and that the double-helices are tighly packed ($s = 2r$) [77, 66, 48, 105]. With these assumptions, equation 2.5 reduces to

$$P = np\left[1 + \frac{2}{\sin^2(\pi/n)}\right]. \tag{2.6}$$

Fitting equation 2.6 to our data with p as a free parameter yields an estimate of $p = 65 \pm 2$ nm. However, measurements of the persistence length of dsDNA consistently find $p \leq 50$ nm near room temperature.[31] Under conditions like ours, with high Mg^{++} concentration and a high density of backbone nicks, values closer to 40 nm are reported.[28, 6] 2.2a plots 2.6 for 40 nm $< p <$ 50 nm (shaded region) alongside our measurements (red points), making it clear that, given realistic values for the persistence length of dsDNA, equation 2.6 underestimates nHT stiffness.

The most likely explanation is that the double-helices are not tightly packed ($s > 2r$). DNA duplexes have been observed bowing away from one another between complete cross-overs in DNA nanostructures[76, 117, 41, 5]. The reported distance between the centers of neighboring duplexes ranges from 2.6 nm, measured by cryo-EM[41, 5], to 3.0 nm, measured by AFM[76]. This separation is presumably due to electrostatic repulsion between phosphates along the DNA backbones of neighboring helices.

Fitting equation 2.5 to our data does not identify a unique set of values for s and p_{eff}. Taking the reported values of s as bounds yields a range of 32 nm $< p_{\text{eff}} <$ 45 nm. For $s = 2.8$ nm, in the middle of the reported range, $p_{\text{eff}} = 38 \pm 1$ nm and the resulting function is plotted as a solid line in figure 2.2a. Best fit functions for all other values of s

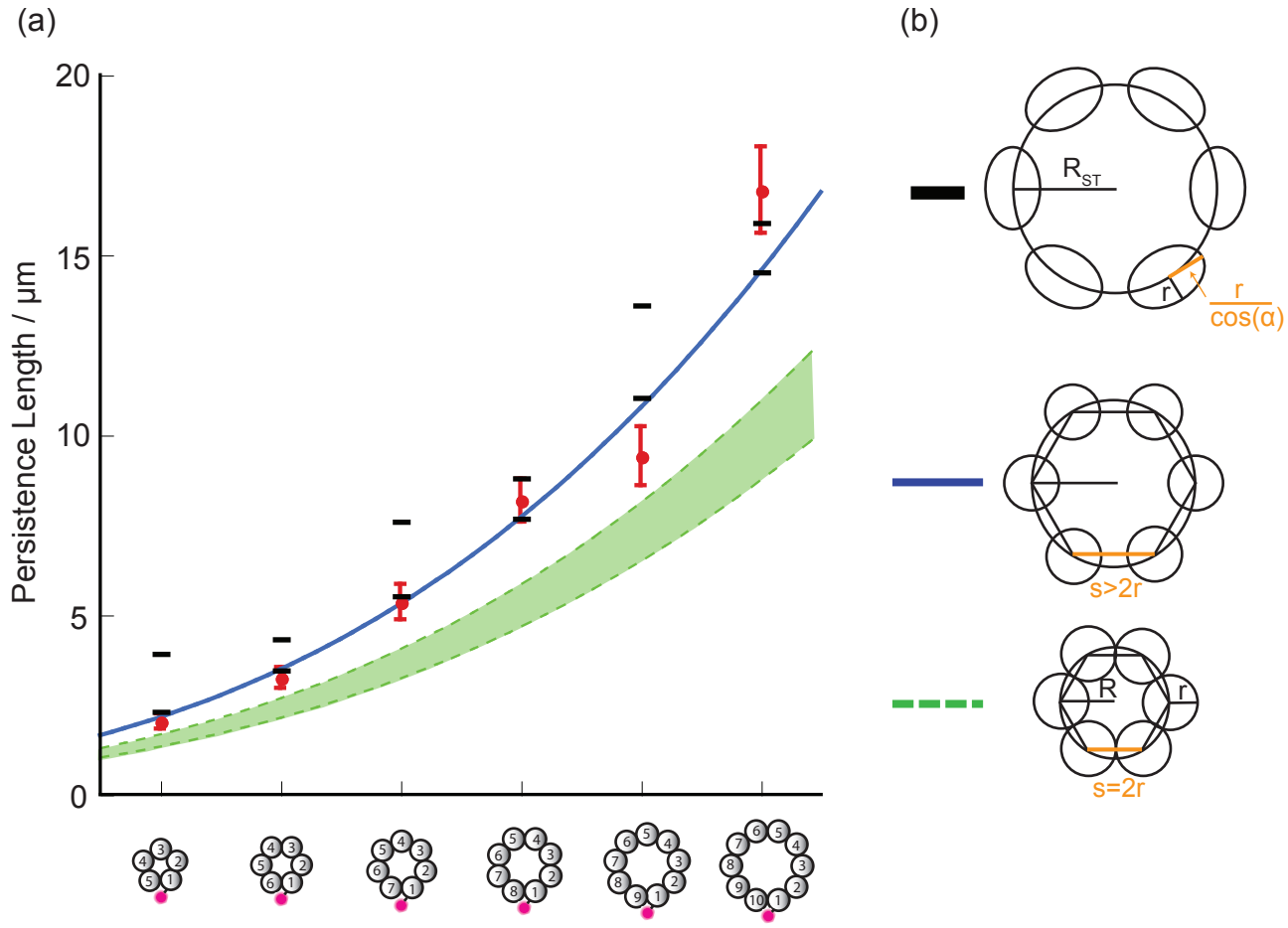

Figure 2.2: Persistence length of n-helix tubes. (a) Red dots and error bars: measured data. Dashed curves and shaded region: close-packed model ($s = 2.1$ nm) with 40 nm $< p <$ 50 nm. Solid curve: Weighted least-squared-error fit of equation 2.5 with $s = 2.8$ nm yields $p_{\text{eff}} = 38 \pm 1$ nm. Black bars: calculated persistence lengths for $s = 2.8$ nm, $p_{\text{eff}} = 38$ nm and supertwist (shown are ST_0, ST_2 for even-nHT, ST_1 and ST_3 for odd-nHT). (b) Illustration of the cross-section of a 6HT for close-packed tubes (bottom), swollen tubes (middle) and supertwisted swollen tubes (top).

look the same: they fit well to measurements of 5HT through 8HT, but they overestimate the stiffness of 9HT and underestimate the stiffness of 10HT.

Tangent correlation analysis on the contour sets of individual nHTs showed that tubes with the same number of helices may have significantly different persistence lengths (Tables B.1 and B.2). In the case of 9HT, four of the five individual contour sets yielded persistence lengths between 9.9 μm and 13.6 μm. The fifth nanotube was significantly more flexible (P=5.5±1.1 μm). Among individual 10HT, nine of the thirteen individual contour sets yielded persistence lengths consistent with 14.5 μm, the value predicted by the fit. The other four nanotubes were significantly stiffer, with an average persistence length of 22.2 μm.

2.3 Supertwist of HX-Tubes

Structural differences among nanotubes of the same circumference, which may underlie these deviations, could result from the repetitive nature of the tile DNA lattice. This lattice structure makes it possible for an open sheet of interwoven duplexes to close into a tube with any number of discrete offsets along the edge (figure 2.3). If ℓ_0 is the sequence repeat length (21 basepairs = 2 helical turns ≈ 7.14 nm), the allowed edge offsets q are given by

$$q_{\text{even}} = (2m)\frac{\ell_0}{2}; \qquad q_{\text{odd}} = (2m-1)\frac{\ell_0}{2} \tag{2.7}$$

for even and odd numbers of duplexes in the sheet, respectively, where m is an integer. Notice that even-nHT can form with no edge offset, but odd-nHT contain a seam, between the first and nth strands, along which the duplex sheet must shear in order for the bounding strands to hybridize. Whenever a sheet closes with finite edge offset, the duplexes follow a helical path about, rather than align parallel to, the axis of the nanotube (figure 2.3c). We refer to nanotubes with such helical double-helices as "supertwisted".

The integer value in parenthesis (equation 2.7) provides a convenient label by which to name the "supertwist state" of a nanotube according to the number of helical turns offset upon closure. Using this nomenclature, tubes with an even number of duplexes can only have even supertwist states (..., ST_{-2}, ST_0, ST_{+2}, ...), and tubes with an odd number of duplexes can only have odd supertwist states (..., ST_{-1}, ST_{+1}, ...).

To determine whether nHT in different supertwist states were present in our samples, we developed a method to directly measure the amount of supertwist in the DNA nanotubes. One of the DNA strands common to all nHT was replaced with an elongated version that had eight additional adenine bases at the 3′ end (section 2.6.3). The resulting nanotubes were similar in quality to the original, as viewed by fluorescence microscopy. We used these 8A handles as docking sites for gold nanoparticles (AuNP) that were coated with DNA strands of complimentary sequence (8T).

Figure 2.4 shows representative TEM images of AuNP-decorated nHT. The distribution of their spacing indicates that each AuNP typically binds two docking sites, consistent with geometrical constraints (section 2.6.3). The distribution of their position with respect to

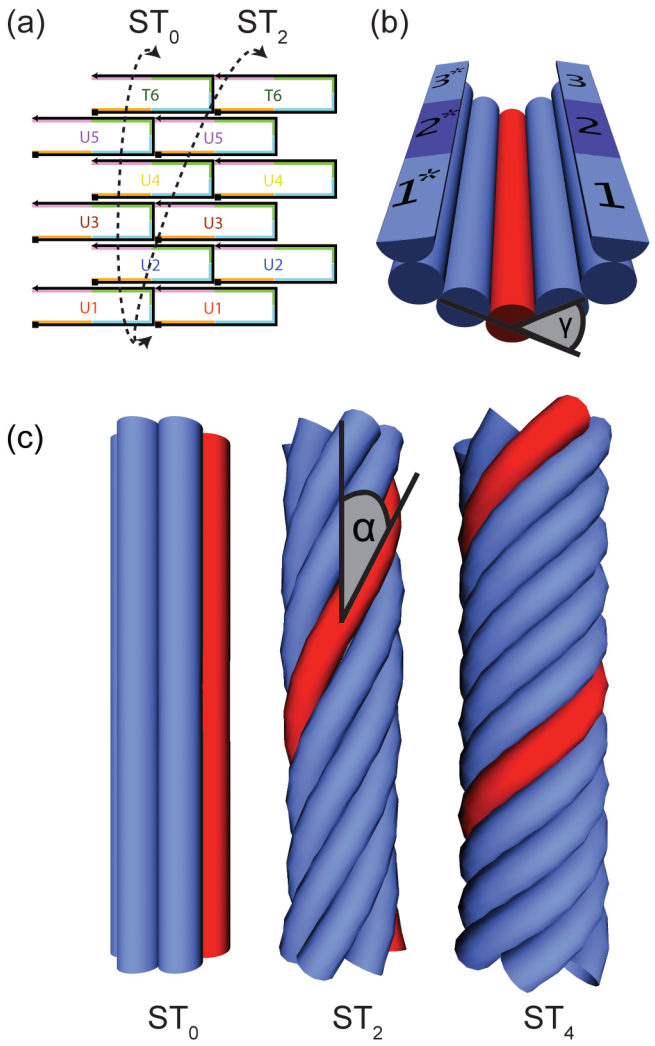

Figure 2.3: (a) Illustration of 6HT strand design adapted from [117]: each DNA strand forms a single cross-over between adjacent DNA duplexes and has four binding sites, indicated by colors. (b) Cylinder model of an open DNA sheet of 6 double-helices (cylinders) and (c) three different supertwist states of the closed DNA sheet. In (b) half cylinders represent ssDNA, numbers indicate domains of identical sequence (21 bases each). Hybridization of domains 1 and $1^\star$ yields ST_0, hybridization of 1 and $2^\star$ yields ST_2, hybridization of 1 and $3^\star$ yields ST_4. The angle α, between the duplex axis and the tube axis, characterizes the supertwist. The angle γ, supplementary to the angle between successive cross-overs along a given duplex, characterizes the torsional constraint imposed by the cross-overs. γ takes one of the two values $\gamma = \frac{3}{8}(\frac{4\pi}{21})$ and $\gamma = \frac{11}{8}(\frac{4\pi}{21})$ on alternate duplexes [117], as dictated by the number of basepairs between the cross-overs, the preferred pitch of the double helix and the angular span of the minor groove.

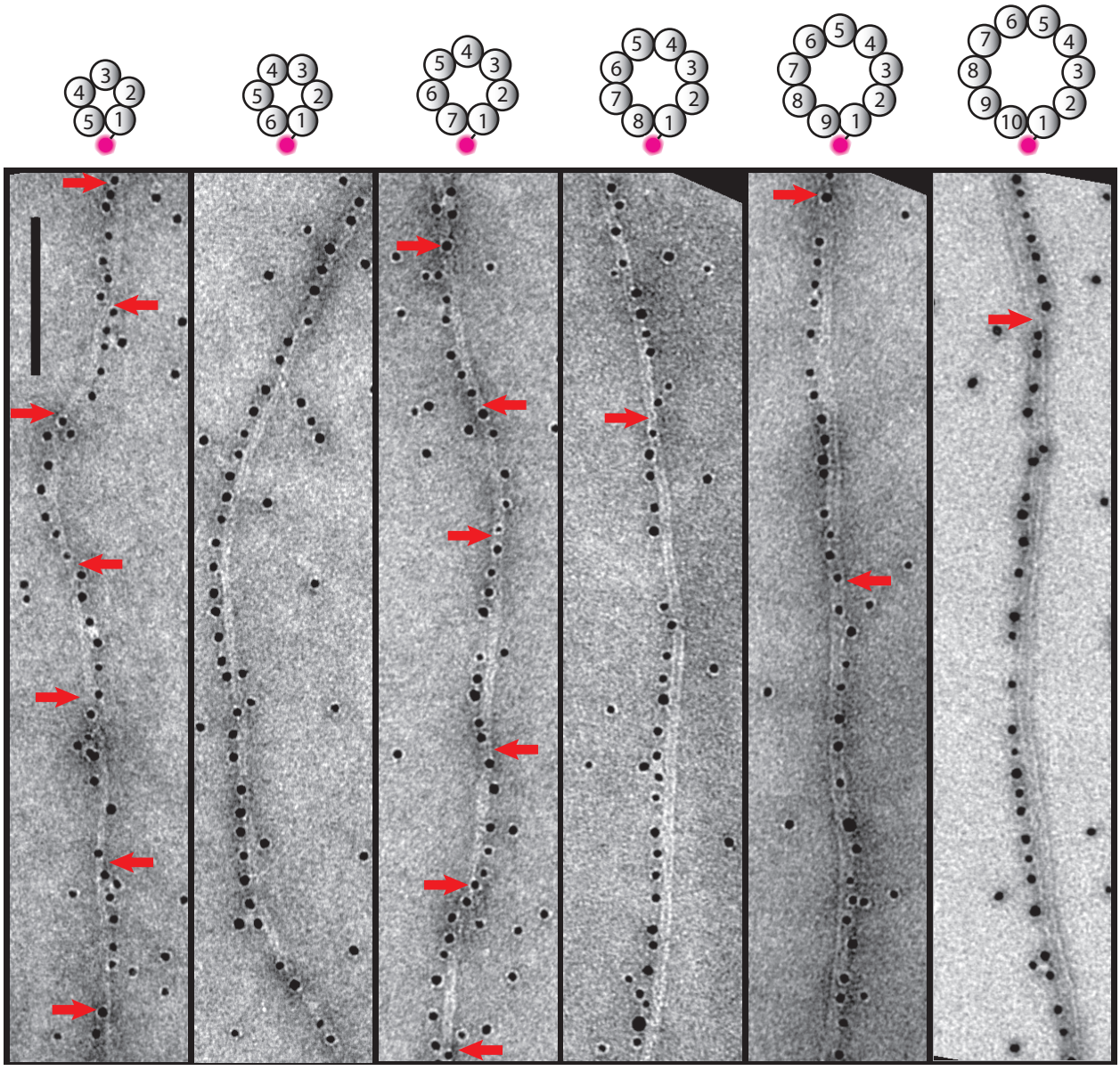

Figure 2.4: TEM of AuNP bound to DNA nanotubes. Red arrows indicate points where the attachment site of AuNPs crosses the tube axis. Scalebar: 100 nm.

the nanotube axis can be divided into two classes: On even-nHT, AuNPs lie mostly to one side of the nanotube, consistent with ST_0, in which the DNA duplexes, and hence the AuNP docking sites, are parallel to the nanotube axis. Rare instances in which the line of AuNPs crosses the tube axis may be attributed to thermally excited twist of the DNA nanotube as a whole. On odd-nHT, by contrast, the line of AuNPs periodically crosses from one side of the tube to the other. This is consistent with finite supertwist, which appears in TEM as the 2d projection of the 3d helical path of the decorated duplex. Among the ≈ 100 nHT surveyed, none had a AuNP alignment indicating supertwist higher than ST_0 for even-nHT and ST_1 for odd-nHT.

We measured the distance d over which AuNPs remained on one side of the nHT without crossing the tube axis. For odd-nHT, the average $\langle d \rangle$ can be compared to a half turn of the computed superhelical pitch for ST_1 geometry, d_{theory}. We find that on average $\langle d \rangle = 2.3 d_{\mathrm{theory}}$ (2.2). Hence the measured superhelical pitch is much larger than predicted by DNA sequence/geometry alone and tubes are untwisted with respect to the geometrically predicted supertwist. For even-nHT we note a mismatch of more than an order of magnitude between $\langle d \rangle$ and the tube twist persistence length, P_T, expected from calculation of the polar moment of inertia (equation 2.50 in section 2.7.3).

Table 2.2: Average and standard deviation of the distance d over which AuNPs remained on one side of the nHT without crossing the tube axis. N denotes the number of measurements of d that were taken from 2-4 different tubes per tube type. d_{theory} is the expected value of d based on sequence design and B-form DNA geometry.

Tube	$\langle d \rangle$/nm	σ_d/nm	N	d_{theory}/nm
5HT	81	19	23	32
6HT	246	247	17	∞
7HT	115	38	61	58
8HT	299	240	34	∞
9HT	229	94	31	94
10HT	372	173	8	∞

2.4 Elasticity Theory of HX-Tubes

To understand the observed untwisting of odd-nHT, the low twist persistence length of even-nHT and the absence of higher supertwist states, we consider the Free Energy, F, of nHT relative to an open sheet of dsDNA. Again modeling the nanotube as an array of elastic cylinders, we begin by calculating the energetic costs of bending or twisting a short length, $d\ell$, of a single cylinder [58]:

$$dG_{\mathrm{Bend}} = \frac{1}{2} B \frac{1}{r_{c,ST}^2} d\ell \tag{2.8}$$

$$dG_{\mathrm{Twist}} = \frac{1}{2}C\left(\frac{d\phi}{d\ell}\right)^2 d\ell \tag{2.9}$$

where B is the bending modulus (related to the bend persistence length by $p_{\mathrm{Bend}} = B/k_BT$), $r_{c,ST}$ is the bend radius of curvature, C is the twisting modulus ($p_{\mathrm{Twist}} = C/k_BT$), and ϕ is the angle through which the cylinder is twisted about its axis.

To the extent that the cylinders are torsionally constrained, the Free Energy calculation should also include a twist-bend energy term[58]

$$dG_{\mathrm{T-B}} = \frac{1}{2}D\frac{1}{r_c^2}\frac{d\phi}{dl} \tag{2.10}$$

This term's linear dependence on $d\phi/dl$ breaks the degeneracy between positive and negative supertwist, favoring one particular handedness of tube supertwist. However, to our knowledge, neither the magnitude nor even the sign of the twist-bend coupling constant D have been determined. Furthermore, the torsional constraint imposed by cross-overs between adjacent cylinders is weakened by the fact that the entire tube is free to twist about its axis, making it likely that $D_{\mathrm{eff}} \ll D$. We therefore do not include a twist-bend energy term in our calculations.

Closing a sheet into a tube costs deformation energy ΔG whether or not the tube has supertwist. This is because each cylinder must twist, first one way and then the other, to accommodate the difference between the natural curvature of the sheet (imposed by the spacing between crossovers) and the curvature required for closure into a tube. The natural curvature of the sheet is described by the angle γ, supplementary to the angle between successive cross-overs along a given duplex (2.3b). The sequence design is such that γ is either $\frac{11}{8}(\frac{4\pi}{21})$ or $\frac{3}{8}(\frac{4\pi}{21})$, depending on the duplex.[117] Assuming the closed sheet is circular in cross-section, each duplex must twist an amount $d\phi/d\ell$ that is the difference $\frac{2\pi}{n}\cos(\alpha) - \gamma$ divided by the distance between cross-overs, $\ell_0/2$ (section 2.7.2). Here, α is the angle, illustrated in Figure 3c, between cylinder axis and the tube axis

$$\tan\alpha = \frac{q}{\pi s}\sin(\frac{\pi}{n}). \tag{2.11}$$

In a supertwisted tube the cylinders are bent and further twisted. Their bend is characterized by a radius of curvature $r_{c,ST} = R_{\mathrm{ST}}/\sin^2\alpha$, making the bend energy associated with a supertwisted tube:

$$dG_{\mathrm{Bend}} = n\left[\frac{1}{2}B\left(\frac{\sin(\frac{\pi}{n})\sin(2\alpha)\sin\alpha}{s}\right)^2\right]d\ell \tag{2.12}$$

The cylinders' twist is also increased by an amount $2\pi/L_{\mathrm{ST}}$, where L_{ST} is the arc length of one helical turn of supertwist, such that the net twist of a cylinder becomes

$$\frac{d\phi}{d\ell} = \left(\frac{2\pi}{L_{\mathrm{ST}}}\right) \pm \frac{(\frac{2\pi}{n}\cos\alpha - \gamma)}{\ell_0/2}. \tag{2.13}$$

Here sign of the second term alternates between successive cross-overs along the cylinder. In even-nHT, half of the cylinders have one value of γ and half have the other. In odd-nHT there is one extra cylinder for which $\gamma = \frac{3}{8}(\frac{4\pi}{21})$ (section 5, Supp. Info.). Therefore, the mean twist energy associated with closing a sheet into a supertwisted tube is

$$dG_{Twist} = \frac{1}{2}C\left[n\left(\frac{\sin(\frac{\pi}{n})\sin(2\alpha)}{s}\right)^2\right. \tag{2.14}$$

$$\left.+\frac{n-\delta}{2}\left(\frac{\frac{2\pi}{n}\cos\alpha - \frac{4\pi}{21}(\frac{7}{8})}{\ell_0/2}\right)^2 + \frac{n+\delta}{2}\left(\frac{\frac{2\pi}{n}\cos\alpha - \frac{4\pi}{21}(\frac{3}{8})}{\ell_0/2}\right)^2\right] d\ell \tag{2.15}$$

where $\delta = 0$ for even-n and $\delta = 1$ for odd-n.

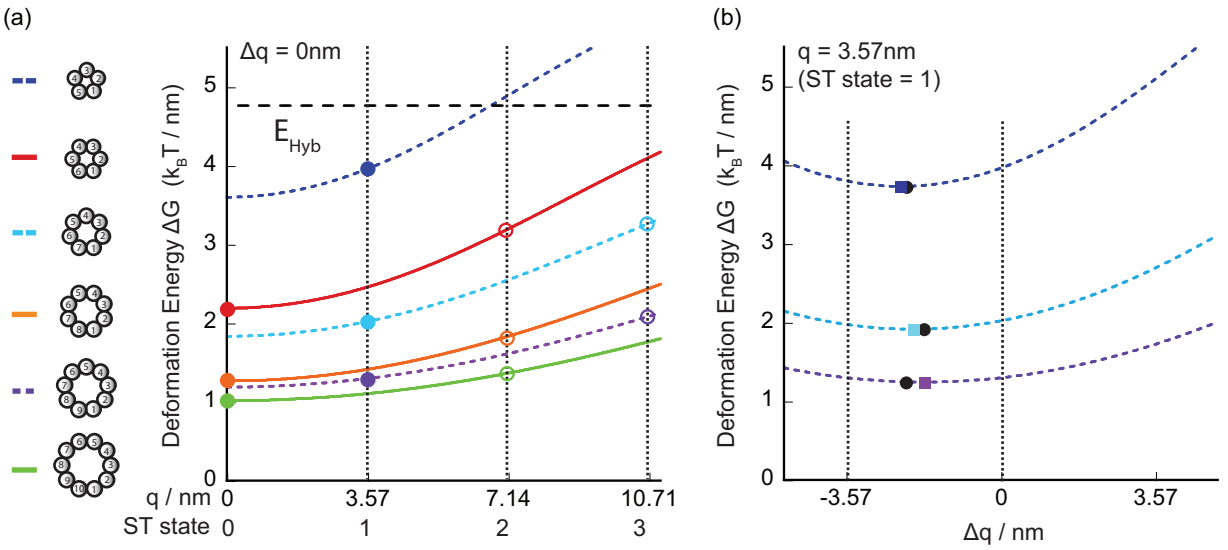

Figure 2.5: Plots of 2.17 using $s = 2.8$ nm, $B = 156$ pN·nm^2 (corresponding to $p_{\text{eff}} = 38$ nm) and $C = 107$ pN·nm^2. (a) Comparison of the hybridization energy gain, E_{hyb}, (horizontal dashed line) to the deformation energy cost of tube closure ΔG for nHT with $\Delta q = 0$nm as a function of q, the edge offset, or, equivalently, the supertwist state. Geometrically calculated ST states are indicated with circles, filled circles mark the lowest energy supertwist state. (b) Deformation energy of odd nHT with $q = 3.57$ nm (ST state = 1) as function of Δq with $k = 0.56$k$_B$T/nm^2. Minima are highlighted with colored squares, black circles show measured untwisting. Dashed lines at $\Delta q = -3.57$ nm and $\Delta q = 0$ nm indicate full untwisting and no untwisting respectively.

The deformation energy cost ΔG of closing a sheet of $5 \leq n \leq 10$ duplexes into a tube, (*i.e.*, the sum of equation 2.12 and equation 2.15) is plotted in figure 2.5a as a function

of edge offset q, using values of B and C corresponding to bend and twist persistence lengths (at room temperature) of 38 nm and 26 nm, respectively. [2] The cost decreases with increasing n, as expected, because the intrinsic curvature of the duplex sheet is closest to that of a 10HT. All curves have a minimum at $q = 0$ nm, predicting that the lowest accessible supertwist state is always the most favorable to form.

We propose that the observed untwisting of odd-nHT is due to shearing of adjacent cylinders with respect to each other. Structurally, shearing may occur by 1) rearrangement of the phosphate backbones in the cross-overs and 2) melting of basepairs flanking cross-overs. Thus the energetic cost of cylinder shearing, dG_{Shear}, may have a complicated and sequence specific dependence on the amount of shearing, Δq. For simplicity we assume a harmonic potential for dG_{Shear} with spring constant k:

$$dG_{Shear} = n\frac{k}{\ell_0}\left(\frac{\Delta q}{n}\right)^2 d\ell \tag{2.16}$$

The deformation energy is thus generalized to:

$$dG(n, s, q, \Delta q) = dG_{Bend}(n, s, (q + \Delta q)) + dG_{Twist}(n, s, (q + \Delta q)) + dG_{Shear}(n, \Delta q) \tag{2.17}$$

Setting $2\langle d\rangle$, obtained from our TEM data, equal to the supertwist pitch (Eq. S21), we find that the amount of shear, Δq, necessary to yield the observed supertwist is -2.2 nm, -1.8 nm and -2.2 nm for 5HT, 7HT and 9HT, respectively. If distributed evenly across all pairs of adjacent cylinders, the required shift ($\Delta q/n$ = -0.44 nm, -0.26 nm, -0.23 nm) is comparable to the full extent of the cross-over backbone between neighboring bases. By requiring equation 2.17 be minimized for odd-nHT with $q = 3.57$ nm at the measured values of Δq we obtained the cross-over spring constant $k = 0.6$ k_BT / nm^2, 0.7 k_BT / nm^2 and 0.3 k_BT / nm^2 for 5HT, 7HT and 9HT, respectively. Using $k = 0.56$ k_BT / nm^2 for all nHT yields the best fit of the minimum position of equation 2.17 to the measured Δq in a least-squares sense and captures all measurements to within 0.5nm (figure 2.5b).

The observation that $\langle d\rangle \ll P$ suggests that tube twist persistence length of even-nHT is much smaller than bend persistence length, in agreement with recent magnetic tweezers experiments on DNA origami tubes, which reported comparably low twisting rigidities [40]. This result is not consistent with a naïve twist persistence length, P_T, calculated using the polar moment of inertia of an HX-tube cross-section, which yields $P_T = 2P$ (section S6, Supp. Info). To resolve this discrepancy we propose that the cross-overs between helices are compliant, and thus individual cylinders are able to slide relative to one another to accommodate twist. The energetic cost of this twist mode is given by equation 2.17 and we can approximate an associated twist persistence length P_{TS} (section 2.7.3):

$$P_{TS} \leq \frac{1}{k_BT}\left(nC + \frac{k}{\ell_0}\frac{\pi^2 s^4}{2n\sin^4(\pi/n)}\right) \tag{2.18}$$

[2] The choice of C, slightly below the range of reported values for (un-nicked) dsDNA[11] was based on comparison of the deformation energy to the energy gained from hybridization upon tube closure, $\Delta E_{\mathrm{hyb}} = 4.8\, k_BT$/nm, as estimated using the DINAMELT webserver[57] with T=49°C (the tube folding temperature [117]). $\Delta G - \Delta E_{\mathrm{hyb}}$ must be negative for a sheet to close into a tube. Given that 5HT are stable, and even 4HT have been reported to form[117], we conclude that $C_{\mathrm{eff}} \leq 107pN \cdot nm^2$.

The value of $k = 0.56 k_B T/nm^2$ derived from odd-nHT data yields upper bounds for P_{TS} of 220 nm, 347 nm and 521 nm for 6HT, 8HT and 10HT respectively, which easily allow for the observed tube twist.

Given k, equation 2.17 can be used to predict the relative abundance of supertwist states. However, a quantitative prediction depends on the shape and size of the duplex sheet that closes into a tube, which to our knowledge has not been studied for HX-tiles. We therefore limit our discussion to two cases: symmetric sheets of $n \times n$ tiles and minimal sheets ($2 \times n$ tiles). To obtain the deformation energy of a sheet, equation 2.17 must be multiplied by the sheet length $T\ell_0$, where T is the number of tiles. For even nHT, neglecting supertwist states above ST_2, the probability of $ST_{\pm 2}$ is given by:

$$Q_2 = \frac{2e^{(-T\ell_0 \cdot dG_{ST2})}}{e^{(-T\ell_0 \cdot dG_{ST0})} + 2e^{(-T\ell_0 \cdot dG_{ST2})}} \tag{2.19}$$

where dG_{ST2} and dG_{ST0} are the deformation energies of ST_2 and ST_0 segments respectively, obtained by minimizing equation 2.17 with respect to Δq. For $n \times n$ sheets, Q_2 is negligibly small for all nHT. For $2 \times n$ sheets, $Q_2 \leq 12\%$.

Given this probability and the finite size of our TEM data set, we considered if outliers in the persistence length measurements of individual tubes (tables S1, S2, Supp. Info.) may be due to a small fraction of tubes forming with higher supertwist states. We calculated the persistence length of a supertwisted tube by approximating the cross-section of each component cylinder in the plane perpendicular to the tube axis as an ellipse with its long axis tangential to the tube (figure 2.2b). The angle α determines the length of that long axis, $r/\cos\alpha$, and the consequent increase in nanotube radius, $R_{ST} = R/\cos\alpha$, both of which factor into the area moment of inertia J (section 4, Supp. Info.) and increase the expected persistence length to

$$P(\alpha) = \frac{n p_{\text{eff}}}{2}\left[\frac{1}{\cos(\alpha)^3} + \frac{1}{\cos(\alpha)} + \frac{(s/r)^2}{\sin^2(\pi/n)\cos(\alpha)^3}\right]. \tag{2.20}$$

which simplifies to 2.5 when $\alpha = 0$. Black bars in 2.2a mark persistence lengths calculated using 2.20 for the two lowest supertwist states for each tube type (with $s = 2.8$ nm and $p_{\text{eff}} = 38$ nm). Equation 2.20 predicts a persistence length increase of $\leq 25\%$ for ST_2 with respect to ST_0 tubes, too small to capture the range of observed outliers, one of which (10HT) is significantly more stiff, and several of which are significantly less stiff than predicted by the fit.

2.5 Conclusions

We studied the interplay between mechanical and structuralral properties of DNA nanotubes. Taking advantage of the modular design afforded by HX-tiles, we systematically varied the number of DNA duplexes in a tube and used fluorescence microscopy to visualize their free-floating contours and electron microscopy to reveal supertwist of their duplex lattice.

Our measurements provide a direct reference point for the properties of more complex DNA structures. They also show that not only the shape but also the mechanical properties of DNA nanostructures can be rationally designed: the persistence length of a DNA nanotube scales accurately with its second moment of inertia when nanoscale features of the tube architecture, such as the effective stiffness of a duplex and the size of the gaps between duplexes, are considered.

Direct visualization revealed that out of the multitude of possible structures (*i.e.*, supertwist states) allowed by the tiled nature of HX-tubes, the lowest supertwist state is strongly favored. Supertwist in odd-nHT, forced by sequence design is relaxed by rearrangement of the underlying DNA lattice. Twist in even-nHT, excited by thermal energy, appears on length scales much shorter than the bend persistence length would suggest.

We derived expressions for the elastic potential energy associated with bending and twisting cross-linked duplexes into a circular array and deformation of this array. In accordance to our data, this model predicts high twist flexibility, supertwist relaxation and a low abundance of higher supertwist states.

2.6 Methods

2.6.1 Nanotube Preparation

Samples of nanotubes ranging from five (5HT) through ten (10HT) helices in circumference were prepared by annealing the requisite strands at 1 μM concentration (per strand) in TAE buffer with 12 mM $MgCl_2$. The anneal was performed by submerging a 200 μL PCR tube, containing between 20 and 200 μL of strand solution, in 2L of water at 90°C. The beaker of water was placed in a covered styrofoam box, and left to cool gradually to room temperature over 48 hours. A hundred times dilution (10 nM concentration per oligo) was imaged using a fluorescence microscope (Olympus IX70) equipped with a CCD camera (Hamamatsu ORCA II) and a 100x, 1.4NA oil immersion objective (Olympus PlanApo 100x, 1.4NA).

2.6.2 2D - Confinement of DNA Nanotubes

2.6 shows typical fluorescence microscopy images of $6HT_{\{1,4,5\}}$, labeled with Cy3 dyes on three of the 6 helices. In samples prepared on glass slides (Gold Seal, Cat. No. 3010) and coverslips (Corning No.1, 22mm sq, Cat. No. 2865-22), DNA nanotubes strongly adhere to the glass surface due to the excess of magnesium ions in the buffer. When a drop of sample solution is put between slide and coverslip, the tubes align, most likely due to flow during adhesion (2.6a). Tangent correlation data obtained from samples prepared in this manner do not exhibit exponential decay and fitting to Eq. 2 severely overestimates the persistence length. Flow can be avoided by imaging a drop of sample on a coverslip without a slide. However, in this case the tubes display sharp bends (2.6b). Imaging during the adhesion process revealed that sharp bends occur as tubes immobilize in < 200

ms. Nanotube contours in such open samples are an intermediate of the projection of the tubes' 3D shape prior to adhesion and an equilibrated 2D conformation. This state is also undesirable for persistence length measurements. 2.6c shows a time series of a tube freely diffusing in 2D between PVP coated surfaces prepared as described in the main text.

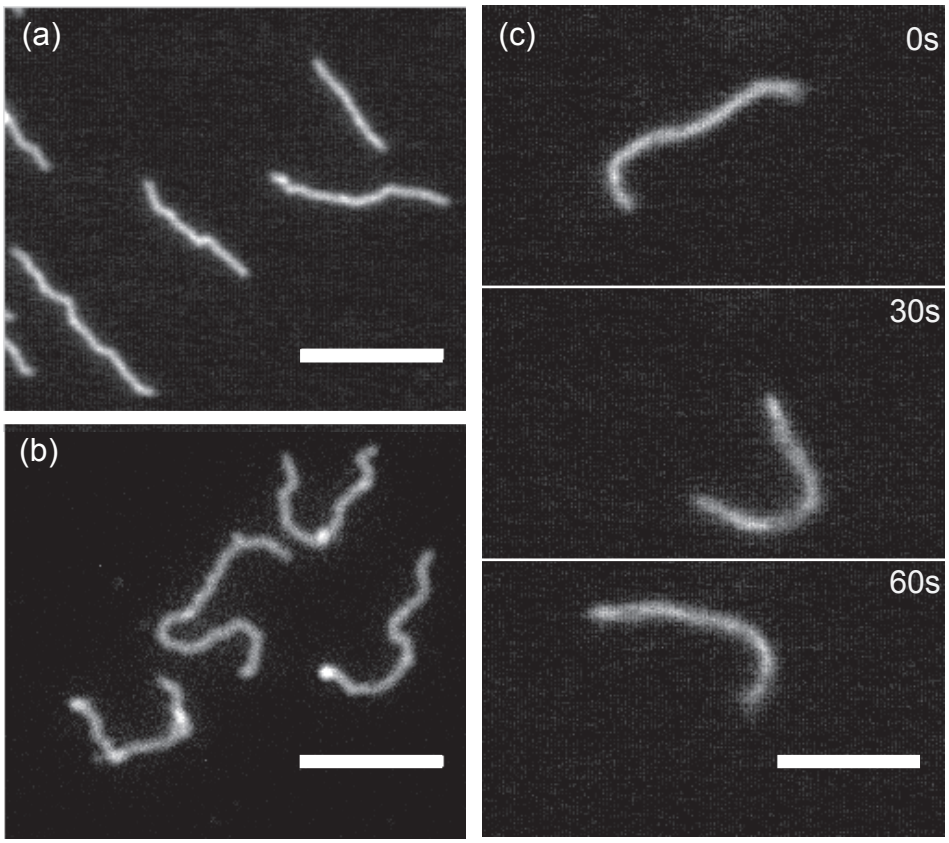

Figure 2.6: 6HT confined to 2D by adhesion to glass (a), (b) and in a thin (∼2 μm) PVP coated channel (c).

To avoid any flow-alignment effects (section 1, supp. info.) and obtain truly equilibrated conformations of DNA nanotubes in 2D, we coated the glass slide and coverslip with poly-(vinylpyrrolidone) (PVP) [98]. PVP coated slides and coverslips were gently pressed together in a home built press and sealed with epoxy. This confined the DNA nanotubes to diffusion in a channel of less than 2 μm in height and thus kept them in the focal plane (Figure S1c). Using this method we were able to capture multiple conformations of individual tubes (typically 20-300) using a shutter with a delay time of 2 s - 30 s to ensure that consecutive conformations are substantially different and independent of each other. A complete data set consisted of 4-13 such movies for any given tube type.

In rare instances we observed tubes that were trapped in regions where the PVP coatings of coverslip and slide contact each other. Such tubes do not display free 2D diffusion.

Instead they reptate through the polymer network. This behavior is easily spotted by looking at the sum of all images in a movie. Reptating tubes appear as scraggy lines, whereas freely diffusing tubes display round and smooth intensity profiles in the image sum. Only freely diffusing tubes were chosen for analysis.

The speed of tube contour deformation depended on the height of the PVP channel and could vary from tube to tube within one channel. Analysis of correlated contours can lead to wrong persistence length estimates: a time series with finite frame number of an initially straight tube most likely yields a greater apparent persistence length than a time series of the same tube starting with a curved contour if the tube doesn't deform sufficiently over the duration of the time series. To avoid this effect we obtained a seperate tangent correlation function TCF(Δx,t) of every contour in a time series and computed the autocorrelation function with respect to t for $\Delta x_{min} < \Delta x < \Delta x_{max}$ in intervals of 1μm. If the autocorrelation function exceeded the confidence bounds a fraction of frames was removed and the process repeated until TCF(Δx,t) was uncorrelated.

2.6.3 AuNP Preparation

AuNP with 5nm diameter, OD1 stabilized in citrate buffer were ordered from Sigma-Aldrich (741949). 5.16mL of 5M NaCl was added to 10mL of AuNP. The solution was centrifuged for 30min at 2200rcf. The clear supernatant was removed, 1mL of 1.5mM BSPP (Aldrich 479497-1G) and 2mL methanol was added. The solution was centrifuged again for 30min at 1600rcf. The supernatant was removed and 200μL of BSPP was added. The concentration of AuNP was measured as 7.82μM using a Nanodrop (ND-1000 Spectrophotometer).

The 8T strand was ordered with a -thiol modification at the 5'end. It was mixed with TCEP (Sigma 75259-1G) at final concentrations of 225μM and 10mM respectively and incubated for 30min at roomtemperature. 20μL of this solution was mixed with 7.67μ L of AuNP solution. 8μL of 100mM citrate buffer (pH3) and 4.3μL H_2O was added. After 3 minutes 10μL 500mM HEPES (pH 7.6) was added.

To remove unbound DNA oligos 450μL of 1x TAE buffer was added and the solution was run through a spin filter (Amicon 100kDa MWCO) at 10,000rcf for 10min. Solution that passed the filter was removed, 450μL of fresh 1xTAE was added to the filter and the centrifugation step was repeated. In total this centrifugation step was carried out eight times with one filter replacement after the fourth step. The concentration of DNA coated AuNP after removing the excess DNA was measured by Nanodrop to be 1.81μM.

4μL of DNA nanotubes at a concentration of 100nM per oligo (in 1x TAE with 12mM $MgCl_2$) was mixed with 1.1μL of coated AuNP to yield a ratio of about 1:5. The samples were incubated at roomtemperature for 2h. 2μL were placed on a TEM grid (Plano GmbH S162-3). After 2min the solution was removed and the sample was stained by addition and immediate removal of a drop of 7μL of 1% uranyl formate (UF) followed by a second UF drop, incubated on the sample for 5s.

Subsequent handle sequences that are used as anchor points for AuNP are separated by a DNA double helix of length 21bp (h_0 = 7.14nm). Assuming a chickenwire shape of the

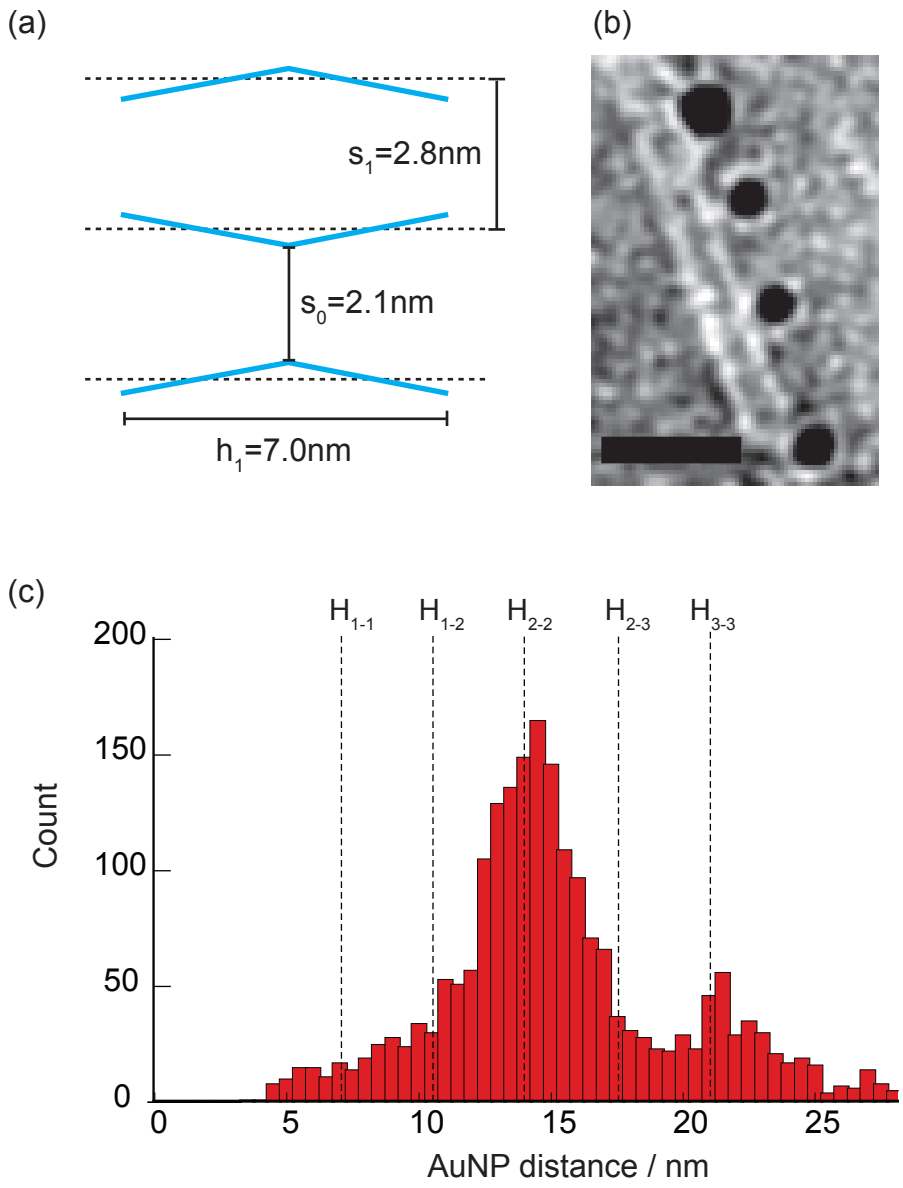

Figure 2.7: Distribution of AuNP on DNA nanotubes: (a) Geometry of arrays of DNA helices in chickenwire conformation. (b) TEM image of AuNPs attached to a 8HT. Scale bar: 20nm (c) Histogram of measured distances between pairs of AuNPs, N=2191

DNA lattice to accomodate an average helix spacing of $s_1 = 2.8$nm the distance of anchor points along the tube is reduced to $h_1 < h_0$ as illustrated in 2.7a. h_1 can be obtained geometrically:

$$h_1 = 2\sqrt{\left(\frac{h_0}{2}\right)^2 - (s_1 - s_0)^2} \tag{2.21}$$

which yields $h_1 = 7.00$nm. The diameter of AuNPs of 4nm $< d <$ 7nm (Sigma-Aldrich #741949) and the length of the anchor sequence (8T-thiol) of L=2.72nm allow a number of different binding modes. We denote a binding mode by H_x where x specifies the number of handles connecting tube and coated AuNP. Distances between a pair of AuNPs are labeled with two subscripts H_{xy} specifiying the binding modes of both. Note that H_1 and H_3 bound AuNPs are centered at a handle location while H_2 binding places AuNP inbetween two handles. Thus H_{xy} must be multiples of $h_1/2$. Given the geometric constrains AuNPs may bind to as many as 3 handles.

The distribution of relative distances of AuNP measured by TEM is plotted in 2.7c. The histogram was obtained using data from all tube types (5HT-10HT). The location of the main peak at $15nm$ is in good agreement with H_{22}. Distances larger than H_{33} are most likely due to unoccupied handles. 2.7b shows a TEM image in which connections between AuNPs and the DNA nanotube appear visible.

2.7 Model Derivations

2.7.1 Persistence Length Model Derivation

We describe the DNA double helix as an elastic cylinder with radius $r = 1.05$nm and effective persistence length $p_{\text{eff}} = 38$nm. The persistence length of an array of cylinders is proportional to the second moment of inertia of the array cross section J:

$$P = \frac{YJ}{kT} \tag{2.22}$$

We denote the cross-section of a cylinder in a plane normal to the tube axis with a. In the cross-sectional view the cylinder centers are placed on the vertices of a polygon with n edges (2.8).

For a regular polygon the radius R of a circle going through the polygon vertices is related to the length of the polygon edges s:

$$R = \frac{s}{2\sin(\frac{\pi}{n})} \tag{2.23}$$

The second moment of inertia of any cross-section with its center of mass at a distance d from the bend axis is given by:

$$j = \int_A x^2 dA + ad^2 \tag{2.24}$$

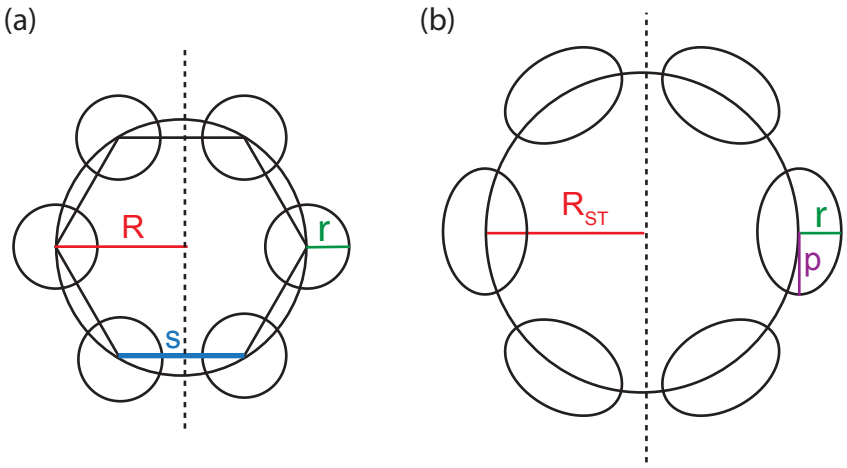

Figure 2.8: DNA nanotube cross-section. (a) Cylinders are parallel to the tube axis. (b) Cylinders are supertwisted about the tube axis.

where the integral is evaluated over the area of the cross-section and x is the distance of an area element to an axis parallel to the bend axis through the center of mass of the cross-section (parallel axis theorem). We write the second moment of inertia of the tube cross-section as the sum over of the second moment of inertia of the cylinder cross-sections:

$$J = \sum_{i=1}^{n} \left(\int_A x^2 dA + a d_i^2 \right) \tag{2.25}$$

with

$$d_i = R \sin(\frac{2\pi}{n} i + \delta) \tag{2.26}$$

where δ is an arbitrary chosen phase which represents the rotational orientation of the tube cross-section with respect to the bend axis. Evaluating the sum yields:

$$J = n \int_A x^2 dA + na\frac{R^2}{2} \tag{2.27}$$

independent of the δ, where we used Lagrange's trigonometric identity to replace the sum.

Parallel cylinders

If the cylinder axis is parallel to the tube axis (no supertwist) the area of each cylinder cross-section is circular with radius r and cross-section $a = \pi r^2$ (2.8a). The second moment of inertia of a cylinder cross-section is given by:

$$\int_A x^2 dA = \frac{\pi}{4} r^4 \tag{2.28}$$

and the second moment of inertia of a tube with n cylinders with spacing s is given by 2.27:

$$J = n\frac{\pi}{4}r^4\left(1 + \frac{s^2/r^2}{2\sin(\pi/n)^2}\right) \tag{2.29}$$

Supertwisted Cylinders

When a sheet of cylinders is folded into a tube with an "edge offse" q this geometrically defines a helical curve for each cylinder with angle α between cylinder and tube axis (2.9):

$$\tan(\alpha) = \frac{q}{2\pi R} = \frac{q\sin(\frac{\pi}{n})}{\pi s} \tag{2.30}$$

and radius:

$$R_{ST} = \frac{R}{\cos(\alpha)} = \frac{s}{2\sin(\frac{\pi}{n})\cos(\alpha)} \tag{2.31}$$

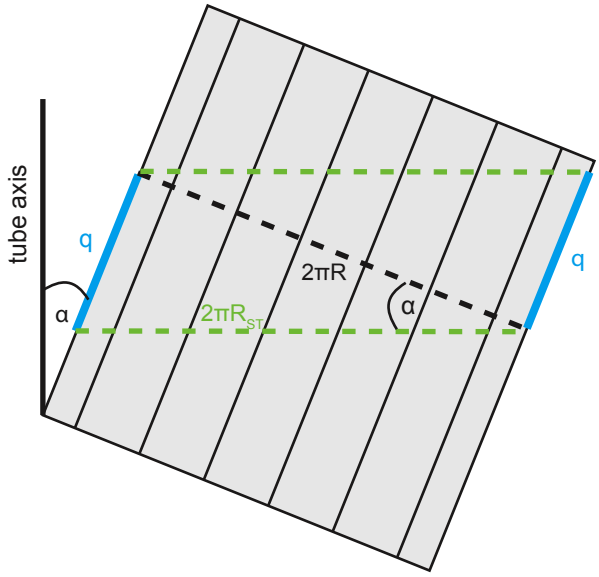

Figure 2.9: Paper sheet model for supertwist geometry

The tube radius and the cross-section of a cylinder normal to the tube axis is increased as compared to the parallel cylinder case. For the tube structures discussed in this paper $0^o < \alpha < 36^o$ (with the maximum for 5HT with ST_3). Thus we approximate the cylinder cross-section as an ellipse with area $a_{ST} = \pi r^2/\cos(\alpha)$ and its long axis $b = r/\cos(\alpha)$ tangential to the circumference of the tube (2.8b). The second moment of inertia of an ellipse which has an angle Δ between its long axis and the bend axis and a distance d between its center of mass and the bend axis is:

$$j_{ST}(\Delta) = \frac{\pi}{8}(rb^3 + br^3) + \frac{\pi}{8}(rb^3 - br^3)\cos(2\Delta) + a_{ST}d^2 \tag{2.32}$$

The second moment of inertia of the entire tube is given by the sum:

$$J_{ST} = \sum_{i=1}^{n} \left(\frac{\pi}{8}(rb^3 + br^3) + \frac{\pi}{8}(rb^3 - br^3)\cos(2\Delta_i) + a_{ST} d_i^2 \right) \tag{2.33}$$

with

$$d_i = R_{ST} \sin(\frac{2\pi}{n} i + \delta) \tag{2.34}$$

and

$$\Delta_i = \frac{2\pi}{n} i \tag{2.35}$$

This sum can again be simplified and yields:

$$J_{ST} = n \left(\frac{\pi}{8}(rb^3 + br^3) \right) + n \frac{R_{ST}^2}{2} a_{ST} \tag{2.36}$$

$$= n \frac{\pi}{8} r^4 \left(\frac{1}{\cos(\alpha)^3} + \frac{1}{\cos(\alpha)} + \frac{(s/r)^2}{(\sin(\frac{\pi}{n}))^2 (\cos(\alpha))^3} \right) \tag{2.37}$$

2.7.2 Deformation Energy Model Derivation

We model a DNA nanotube as an array of elastic cylinders. We define that a straight and untwisted cylinder has zero deformation energy $G = 0$. Bending has an energetic cost of:

$$dG_{Bend} = \frac{1}{2} B \frac{1}{r_c^2} d\ell \tag{2.38}$$

where B is the bending modulus connected to the bend persistence length of dsDNA by: $p_{Bend} = B/k_b T$ and r_c is the radius of curvature and $d\ell$ is a short cylinder segment. Twisting has an energetic cost of:

$$dG_{Twist} = \frac{1}{2} C \left(\frac{d\phi}{d\ell} \right)^2 d\ell \tag{2.39}$$

where C is the twisting modulus connected to the twist persistence length of dsDNA by: $p_{Twist} = C/k_b T$. ϕ is the angle of rotation about the cylinder axis and $\mathrm{d}\phi/d\ell$ is its derivation along the cylinder axis.

The trajectory of the cylinders (r_c and ϕ) can be determined geometrically. As a model one can think of a sheet of paper which is folded into a tube, as illustrated in 2.9. When the paper edges are offset by a distance q, they follow a helical path about the tube axis which is identical to the path of a cylinder in a DNA nanotube. Tube radius R_{ST}, cylinder pitch P_{ST}, arc length L_{ST} and radius of curvature of the cylinder r_c are given by:

$$R_{ST} = \frac{s}{2\sin(\frac{\pi}{n})\cos(\alpha)} \tag{2.40}$$

$$P_{ST} = \frac{\pi s}{\sin(\frac{\pi}{n})\sin(\alpha)} \tag{2.41}$$

$$L_{ST} = \frac{2\pi s}{\sin(\frac{\pi}{n})\sin(2\alpha)} \tag{2.42}$$

$$r_c = \frac{s}{2\sin(\frac{\pi}{n})\cos(\alpha)\sin(\alpha)^2} \tag{2.43}$$

where $\tan(\alpha) = q\sin(\pi/n)/(\pi s)$. It will later also be useful to consider a helical path normal to the cylinder axis with identical radius but inverse slope which has arc length:

$$L_N = \frac{\pi s}{\sin(\frac{\pi}{n})\cos(\alpha)^2} \tag{2.44}$$

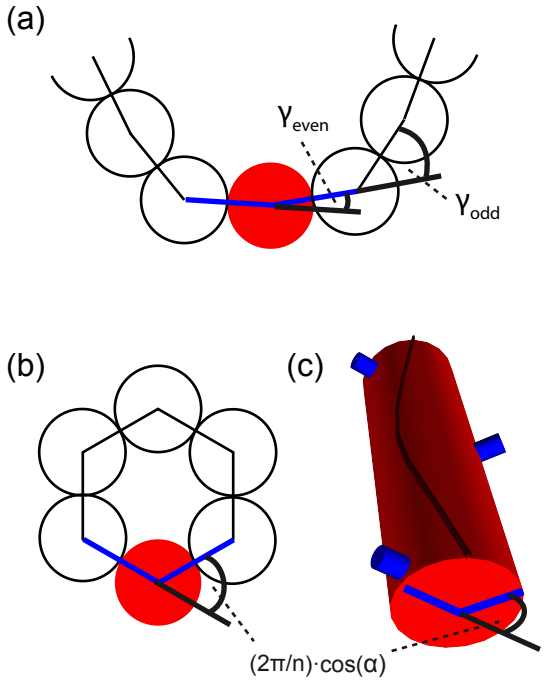

Figure 2.10: (a) Cross section of a sheet of 6 cylinders with equilibrium cross-sectional angles γ. (b) Cross-section of a tube of 6 cylinders (without supertwist). (c) Illustration of cylinder twist ϕ. An initially straight line on the cylinder surface acquires a zig-zag shape when the cross-sections containing subsequent cross-overs are rotated with respect to each other.

In order to calculate $d\phi/d\ell$ we need to consider that a cylinder must twist by $\Delta\phi = 2\pi$ over the length of one full supertwist turn, L_{ST}. In addition it must locally twist with a periodicity of $\ell_0 = 7.14$ nm because its twist coordinate ϕ is fixed every $\ell_0/2$ by pins to the adjacent cylinders (2.10). The magnitude of this local twist oscillation is given by the angular difference $(2\pi/n)\cos(\alpha) - \gamma$. Taking the mean of cylinder sections where the local

induced twist adds to and is substracted from the constant supertwist induced twist we obtain:

$$\left(\frac{d\phi}{d\ell}\right)^2 = \left(\frac{2\pi}{L_{ST}}\right)^2 + \left(\frac{(\frac{2\pi}{n}\cos(\alpha) - \gamma)}{l_0/2}\right)^2 \tag{2.45}$$

where γ has different values for even and odd cylinder numbers: $\gamma_{even} = \frac{3}{8}(\frac{4\pi}{21})$ and $\gamma_{odd} = \frac{7}{8}(\frac{4\pi}{21})$, as determined by the HX-tube cross-over placement.

Thus the bend energy of a cylinder in a supertwisted tube is given by:

$$dG_{Bend} = \frac{1}{2}B\left(\frac{2\sin(\frac{\pi}{n})\cos(\alpha)\sin(\alpha)^2}{s}\right)^2 d\ell \tag{2.46}$$

and the twist energy is:

$$dG_{Twist} = \frac{1}{2}C\left(\left(\frac{\sin(\frac{\pi}{n})\sin(2\alpha)}{s}\right)^2 + \left(\frac{\frac{2\pi}{n}\cos(\alpha) - \gamma}{l_0/2}\right)^2\right) d\ell \tag{2.47}$$

The total deformation energy of a tube segment of length $d\ell$ as given in the main text is:

$$\sum_{i=1}^{n}(dG_{Bend} + dG_{Twist,i}) \tag{2.48}$$

Note that $dG_{Twist,i}$ is different for even and odd cylinder numbers.

Free Energy

The deformation energy difference of closing a sheet of n cylinders and an integer number of tiles ν in length into a tube with ST_i or ST_j is given by:

$$\Delta G(n,i,j) = \left[\frac{dG(n,\alpha_i)}{d\ell} - \frac{dG(n,\alpha_j)}{d\ell}\right](\nu - \frac{1}{2})\ell_0 \tag{2.49}$$

Under the assumption that DNA sheets grow in a symmetric fashion (with equal numbers of each component strand), the hybridization energy upon tube closure is always largest for the smallest accessible supertwist state and thus $|\Delta F| > |\Delta G|$. $|\Delta G|$ is smallest for the difference between ST_0 and ST_2 of a 10HT. Since a sheet needs to be at least two tiles long to close with ST_2 we obtain: $|\Delta F(10, ST_0, ST_2)| > 9.6k_BT$ and $e^{-|\Delta F(10,ST_0,ST_2)|/k_BT}$ is negligibly small.

2.7.3 Twist Persistence Length Model Derivation

Twist persistence length, P_T, of an elastic object can be calculated in a manner similar to bend persistence length (2.7.1):

$$P_T = \frac{YJ_{pol}}{k_BT} \tag{2.50}$$

where J_{pol} is the polar moment of inertia, which is equal to the sum of axial moments of inertia. In the case of a HX-tube with a symmetric cross-section $J_{pol} = 2J$. We propose

that the observed tube twist of 180° over distances $\langle d\rangle \ll P_T$ arises from a tube twist mode that is enabled by shearing of adjacent DNA duplexes (treated as elastic cylinders) with respect to each other. In this section we derive a persistence length P_{TS}, associated with this twist-shear mode and show that $P_{TS} \approx \langle d\rangle$.

To begin, note that tube twist $d\Phi/d\ell$ is related to the angle α (defined in figure 3 and Eq. 11 of the main text) by:

$$\frac{d\Phi}{d\ell} = \frac{2\sin(\pi/n)\sin(\alpha)}{s} \tag{2.51}$$

and α is related to edge offset $q + \Delta q$ by:

$$\tan(\alpha) = \frac{q+\Delta q}{\pi s}\sin(\pi/n) \tag{2.52}$$

where q, is the edge offset, programmed by sequence, and Δq is edge offset generated by cylinder shearing. For tubes with ST_0, $q = 0$ and the deformation energy for twisting a tube by $d\Phi/d\ell$ due to Δq is:

$$dG_{TS} = dG_{Bend}(n,s,\Delta q) + dG_{Twist}(n,s,\Delta q) - dG_{Twist}(n,s,0) + dG_{Shear}(n,s,\Delta q) \tag{2.53}$$

Using equations (13), (15) and (17), 2.53 can be rewritten as:

$$\begin{aligned} dG_{TS} \;=\; & n\frac{1}{2}B\left(\frac{\sin(\pi/n)\sin(2\alpha)\sin(\alpha)}{s}\right)^2 d\ell + n\frac{1}{2}C\left(\frac{\sin(\pi/n)\sin(2\alpha)}{s}\right)^2 d\ell \\ & + \frac{(n-\delta)C}{4}\left(\frac{\frac{2\pi}{n}\cos(\alpha) - \frac{4\pi}{21}\frac{11}{8}}{\ell_0/2}\right)^2 d\ell + \frac{(n+\delta)C}{4}\left(\frac{\frac{2\pi}{n}\cos(\alpha) - \frac{4\pi}{21}\frac{3}{8}}{\ell_0/2}\right)^2 d\ell \\ & - \frac{(n-\delta)C}{4}\left(\frac{\frac{2\pi}{n} - \frac{4\pi}{21}\frac{11}{8}}{\ell_0/2}\right)^2 d\ell - \frac{(n+\delta)C}{4}\left(\frac{\frac{2\pi}{n} - \frac{4\pi}{21}\frac{3}{8}}{\ell_0/2}\right)^2 d\ell \\ & + \frac{nk}{\ell_0}\left(\frac{\pi s\tan(\alpha)}{\sin(\pi/n)n}\right)^2 d\ell \end{aligned} \tag{2.54}$$

For HX-tubes with $5 \le n \le 10$, the contribution of lines two and three of 2.54 accounts for the relaxation of cross-over induced cylinder twist due to decreasing tube wall curvature normal to the cylinders with increasing α. This contribution is thus negative and we can set an upper limit on dG_{TS}:

$$\begin{aligned} dG_{TS} \;\le\; & n\frac{1}{2}B\left(\frac{\sin(\pi/n)\sin(2\alpha)\sin(\alpha)}{s}\right)^2 d\ell + n\frac{1}{2}C\left(\frac{\sin(\pi/n)\sin(2\alpha)}{s}\right)^2 d\ell \\ & + \frac{nk}{\ell_0}\left(\frac{\pi s\tan(\alpha)}{\sin(\pi/n)n}\right)^2 d\ell \end{aligned} \tag{2.55}$$

Using 2.51:

$$dG_{TS} \;\le\; n\frac{1}{8}B\sin(2\alpha)\left(\frac{d\Phi}{d\ell}\right)^2 d\ell \tag{2.56}$$

$$+n\frac{1}{2}C(\cos(\alpha))^2\left(\frac{d\Phi}{d\ell}\right)^2 d\ell$$
$$+\frac{k}{4\ell_0}\frac{\pi^2 s^4}{n\left(\sin(\pi/n)\right)^4}\frac{1}{(\cos(\alpha))^2}\left(\frac{d\Phi}{d\ell}\right)^2 d\ell \tag{2.57}$$

and approximating for small angles: $\sin(2\alpha) \approx 0$ and $(\cos(\alpha))^2 \approx 1$ we find:

$$dG_{TS} \leq \frac{1}{2}\left(nC + k\frac{\pi^2}{2\ell_0 n}\left(\frac{s}{\sin(\pi/n)}\right)^4\right)\left(\frac{d\Phi}{d\ell}\right)^2 d\ell \tag{2.58}$$

2.11 is a plot of 2.53 and the approximated upper bound 2.58 for even nHT. The twist persistence length associated with 2.58 using values of C=107pNnm^2 and k=0.8k$_B$T/nm^2 are 264nm, 391nm, 551nm for 6HT, 8HT and 10HT respectively.

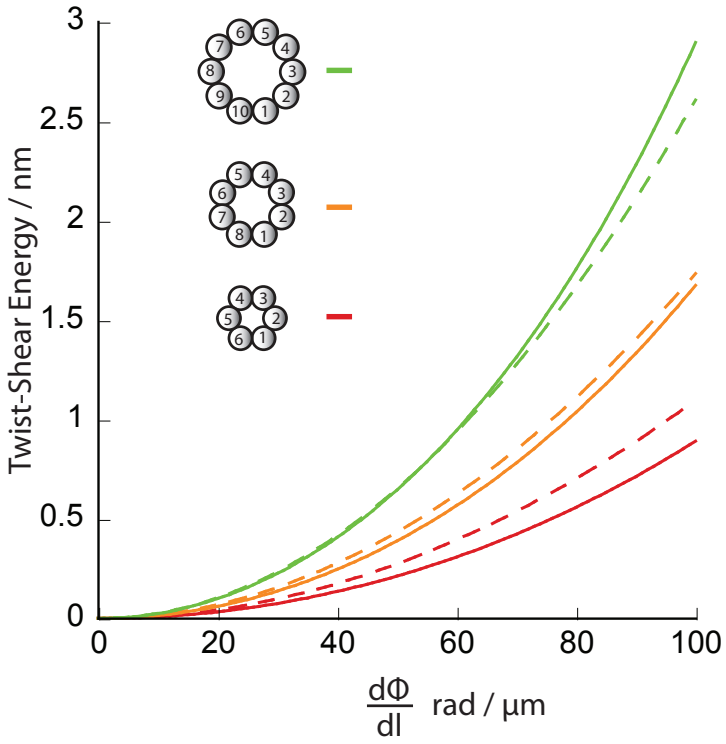

Figure 2.11: Twist-shear energy of even nHT. Dashed lines are approximated upper limits from 2.58, solid lines are the exact function 2.54

Chapter 3

Six-Helix-Tube Design Variations

We present a design of DNA nanotubes, made from six DNA helices, which we will refer to as 6HB ("six helix bundles") to avoid confusion with nanotubes discussed in the previous chapter (6HT). [1]

We compare the persistence length of 6HB motifs, which form 1D DNA nanotubes with zero (6HB), two (6HB+2) and three (6HB+3) DNA helices, externally attached to the outside of the nanotube. We find that the persistence length is smaller than expected, based on the model derived for HX-tube persistence length in the previous chapter. We compare two versions of 6HB+2 with alternate positioning of nicks in the DNA backbone and find that tubes in which several nicks are located in one cross-sectional plane ($6HB_P$+2) are significantly less stiff than tubes in which backbone nicks are staggered (6HB+2).

To further study how nanoscale tube architecture (*i.e.* positioning of strand cross-overs and backbone nicks) affects micrometer scale tube stiffness we designed a modified version of 6HT, $6HT_2$, which has perfect staggering (as 6HT) but only half the density backbone nicks. We find that the persistence length of $6HT_2$ is significantly lower than that of 6HT. We discuss different mechanical models to explain the observed dependence of persistence length on molecular DNA nanotube structure.

[1] Portions of Chapter 2 is reprinted (adapted) with permission from Wang, T., Schiffels, D., Martinez Cuesta, S., Kuchnir Fygenson, D. & Seeman, N. C. Design and Characterization of 1D Nanotubes and 2D Periodic Arrays Self-Assembled from DNA Multi-Helix Bundles. Journal of the American Chemical Society 134, 1606-1616 (2012). Copyright (2013) American Chemical Society. Contributions to the paper were as follows: Fluorescence microscopy experiments were preformed by T.W and S.M.C. and supervised by D.K.F. Fluorescence Microscopy analysis was preformed by D.S. and supervised by D.K.F. Persistence length calculations were preformed by T.W., D.S. and S.M.C. and supervised by D.K.F. and N.S. Experimental design and manuscript was done with input from all authors.

3.1 Tubes with External DNA Duplexes (6HB)

3.1.1 6HB Design

6HB is a designed cyclic arrangement of six DNA duplexes (Figure 3.1A). Two adjacent duplexes are held together through two crossovers to form a planar DAE double crossover [27] molecule with 21 nucleotide pairs between crossovers [59]. Thus, there are six DAE components in each 6HB. The dihedral angle of two adjacent DAE planes is 120°, which is achieved by designing seven base pairs (two-thirds of a 10.5-fold double helical turn) between the crossovers of two adjacent DAE components.

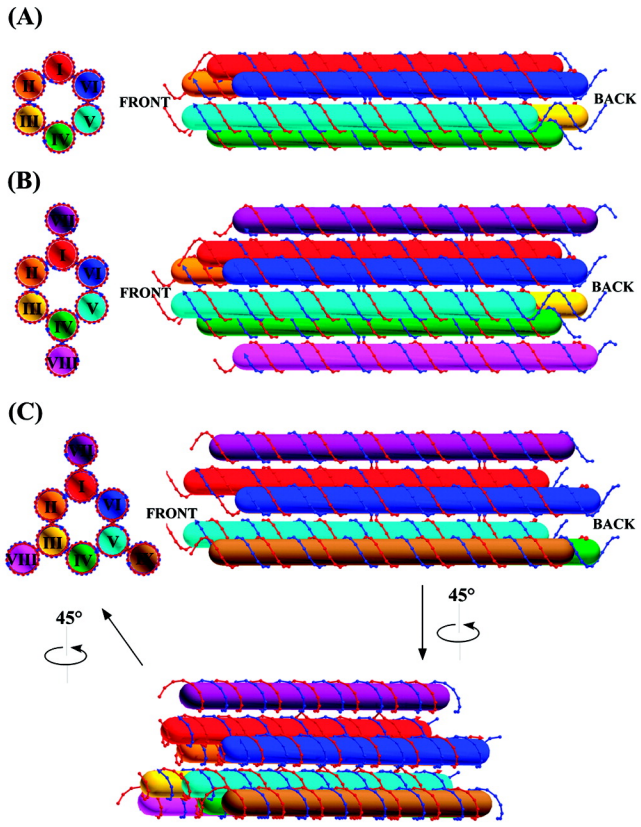

Figure 3.1: Schematic drawings of the helix bundle motifs: (A) 6HB, (B) 6HB+2, and (C) 6HB+3. Cross-sectional views of DNA motifs, in which the duplexes are indicated by Roman numerals, are shown on the left in each panel, and side views are shown on the right in each panel. Cylinders in different colors represent different DNA duplex domains in each motif. Back and Front are indicated as the ends to be used for sticky-ended cohesion. 6HB+3 rotates 45° from the side view as indicated to generate the view shown in the bottom of (C); the relationship of this rotated view to the cross-sectional image is also indicated. Duplexes overlap in side views; for example, duplex II is farther from the viewer than duplex VI. Thus, duplex II is invisible to the viewer in the side view of (C).

Ideally, six duplexes form a hexagonal arrangement with a hollow channel (diameter ≈2 nm) in the middle of the 6HB motif. In addition to the direct formation of the 6HB molecule from a group of DNA single strands, we recently reported the formation of 6HB molecules from the lateral cohesion of a pair of bent three-helix molecules (BTX), thus potentially facilitating the capture of a nanorod [45, 104, 15]. Adding two and three extra DNA double helices, respectively, to the 6HB motif results in motifs that we term 6HB+2 (Figure 3.1B) and 6HB+3 (Figure 3.1C). Two extra duplexes are attached to opposite duplexes in the 6HB motif to form the 6HB+2; three extra helices attached in a trigonal arrangement to the 6HB motif to form the 6HB+3 motif (Figure 3.1). The extra duplexes in the latter two motifs are meant to add rigidity to the 6HB motif. Ideally the four helices in the vertical plane of the 6HB+2 motif (Figure 3.1B) are coplanar, and the three extra helices in the 6HB+3 motif (Figure 3.1C) are organized with 3-fold symmetry about the hollow channel. Thus, in principle, the individual 6HB, 6HB+2, and 6HB+3 motifs have 6-fold, 2-fold, and 3-fold symmetry axes, respectively, if the sequences and crossover positions are not taken into account (Figure 3.1). DNA sequences and folding schemes are listed in appendix C.

3.1.2 6HB Persistence Length Measurement

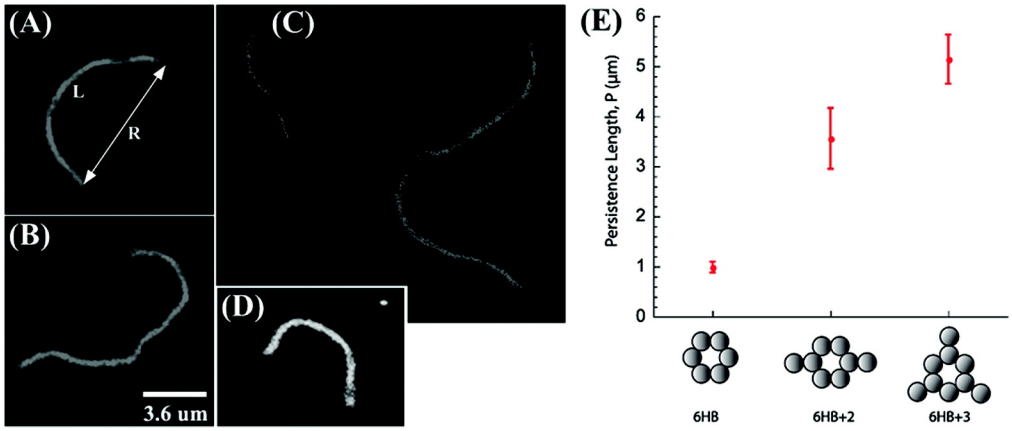

Figure 3.2: Fluorescence micrographs of nanotubes: (A,B) 6HB+2, (C) 6HB+3, and (D) 6HB. (E) The measured persistence lengths and associated uncertainties for the three different types of nanotubes are shown. Persistence length was measured by extracting the end-to-end distance, R, and contour length, L, from fluorescence images of several different nanotubes ($N > 4$) in many distinct conformations ($\langle U \rangle = 23$), and fitting the data to the 2D Kratky-Porod model.

Figure 3.2 shows fluorescence images of all three types of nanotubes. Several DNA single strands are labeled with fluorescein (FAM). Snapshots and movies were taken as the nanotubes diffused freely while confined to the focal plane of a microscope by two

polymer-coated pieces of glass. Fluorescence images confirm that multi-helix bundles self-assemble to yield unbranched linear DNA nanotubes. Nanotube stiffness was measured by extracting the end-to-end distance, R, and contour length, L, from fluorescence images of several different nanotubes (N > 4) in many distinct conformations ($\langle U \rangle = 23$) and fitting the data to the 2D Kratky-Porod model [67, 18]:

$$\langle R^2 \rangle = 4PL \left[1 - 2P \left(1 - e^{\frac{-L}{2P}} \right) / L \right] \tag{3.1}$$

The only free parameter in this fit, P, is the persistence length - the length scale over which the orientation of the nanotube is randomized due to thermal fluctuations - a standard measure of polymer stiffness. We measured persistence lengths of 1.0 ± 0.1, 3.6 ± 0.6, and 5.0 ± 0.5 μm for 6HB, 6HB+2, and 6HB+3, respectively (Figure 3.2E), where the uncertainty represents one standard deviation in the parameter values derived from a bootstrap analysis (see sections 2.2 and 9.5). Extracting R and L of dynamic nanotubes from fluorescence micrographs (rather than AFM data) ensured that our measurement was not affected by adhesion events and allowed us to exclude data from nanotubes with folding errors, which are visible as permanent kinks or hyper-flexible hinges. As expected, the motifs with extra duplexes (6HB+2, 6HB+3) are more rigid than the 6HB motif.

3.1.3 6HB Persistence Length Model

As in chapter 2, we compare these persistence lengths to a simple model in which the 6HB nanotube is represented by a ring of rigidly linked rods (DNA helices). Because the spacing, s, between adjacent DNA helices in this tube type has not been measured we set $s = 2 \times r = 2.0$ nm. In this model, the ratio of the tube persistence length to the helix persistence length is the same as the ratio of their second moments of inertia (J) [77, 67]:

$$P_{tube}/p_{helix} = J/j = N \left(1 + 2(R/r)^2 \right) \tag{3.2}$$

where r is the radius of a DNA duplex, R is the radius of the nanotube measured from the center of the nanotube to the center of the DNA duplex, and N is the number of helices in the nanotube circumference. The second moment of inertia of external helices is calculated using the parallel axis theorem (figure 3.2 and equation 2.24).

Setting $p_{helix} = 50$ nm, the value typically used for double stranded DNA [31, 28, 6], the estimated persistence lengths for 6HB, 6HB+2, and 6HB+3 are 2.7, 6.0, and 7.7 μm, respectively. Thus, equation 3.2 *over*-estimates the measured persistence length of all three 6HB variations. Note that in contrast, using the same parameters, equation 3.2 *under*-estimates the measured persistence length of HX-tubes, described in chapter 2. In particular the persistence length of 6HB and 6HT is significantly different, even though both are made from six interlinked DNA double helices.

3.1.4 6HB Cross-Over Placement

We propose that this low stiffness of the 6HB design might be due, in part, to the phasing of nicks in the DNA backbone. The sticky-ended cohesion that mediates the self-assembly

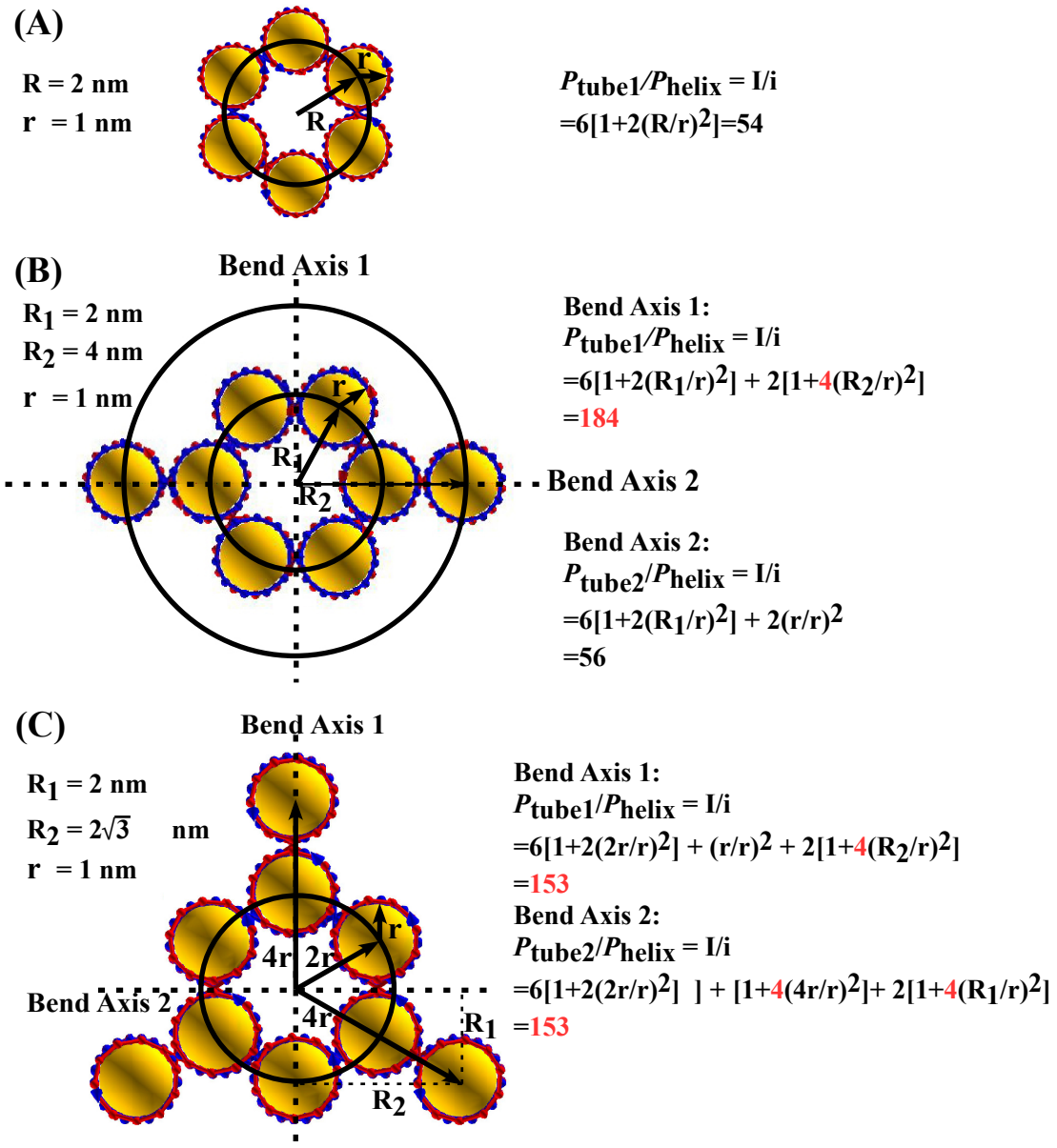

Figure 3.3: Estimation of the persistence lengths of nanotubes: (A) 6HB, (B) 6HB+2, and (C) 6HB+3. In the cases of 6HB+2 and 6HB+3, assuming two perpendicular bend axes, as indicated by the dotted lines, any bending of nanotubes can be treated as a combination of bends about those two axes. Thus, the overall persistence length was estimated to be the average of the persistence lengths calculated for each of the bend axes. For 6HB+2, estimates were calculated using r = 1 nm, R_1 = 2 nm, and R_2 = 4 nm. For 6HB+3, estimates were calculated using r = 1 nm, R_1 = 2 nm, and $R_2 \approx 3.5$ nm.

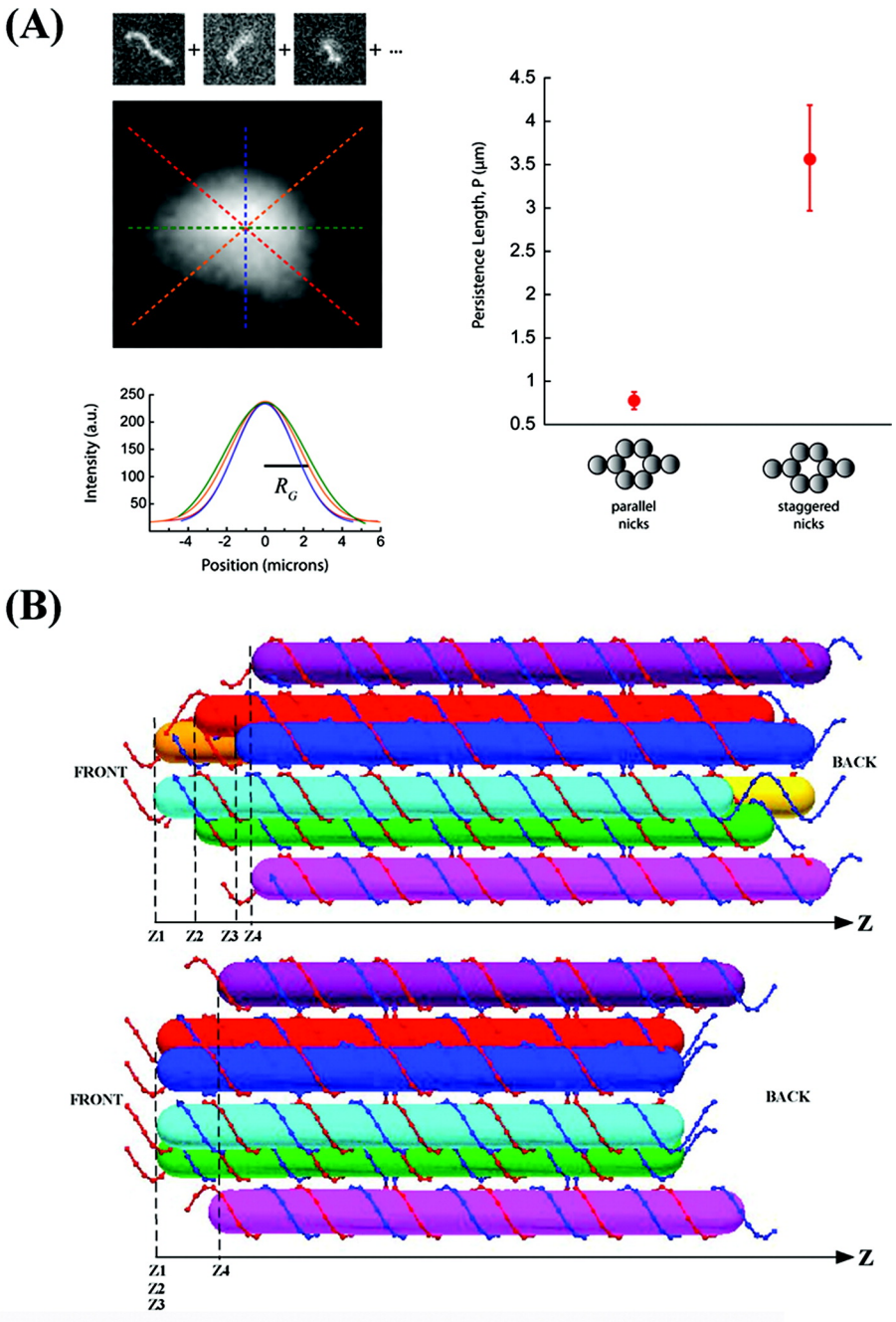

Figure 3.4: 6HB+2 made of molecules with parallel sticky ends are significantly less stiff than those made of molecules with staggered sticky ends. (A) Measurement of persistence length of 6HB$_P$+2 (parallel nicks) *via* the radius of gyration and persistence length of both 6HB+2 variations. (B) Positions of sticky ends in both 6HB+2 versions. In the staggered version (top panel) sticky ends are placed at four different Z-positions, in the parallel version Z1=Z2=Z3.

of our nanotube motifs necessitates a pair of nicks in the phosphodiester backbones of each of the DNA duplexes (one on each strand). These nicks may be weak points, where thermal forces can bend the DNA duplex most easily.

Consistent with this idea, two alternate versions of 6HB+2, with different sticky end placement yielded different persistence lengths. The designs of the two versions are shown in figure 3.4 B: 6HB+2, described above has backbone nicks at (staggered) Z-positions Z1, Z2, Z3 and Z4 (figure 3.4 B top). In the second version ($6HB_P$+2) three of the backbone nick positions are aligned such that Z1 = Z2 = Z3 (figure 3.4 B bottom).

The persistence length of $6HB_P$+2 was so small, that tubes could not be confined to 2D sufficiently to extract their contours. Thus we estimated persistence length using a different method, illustrated in figure 3.4A. Images of independent conformations of $6HB_P$+2 diffusing in 3D were aligned about their center of fluorescence and superimposed. The composite image was used to estimate the radius of gyration by averaging the width of Gaussian fits to line profiles through the center. The standard deviation, σ, of the fits was taken as a measure of the nanotube's radius of gyration (RG). The contour length (L) was measured from the most extended conformation observed. These parameters were related to the persistence length (P) of the nanotube using the following two equations:

$$RG = u^{\nu} P/(6)^{1/2} \tag{3.3}$$

$$L = uP \tag{3.4}$$

where $\nu = 0.6$ for a 3D self-avoiding random walk. The average persistence length of the $6HB_P$+2 nanotube design estimated in this manner was 0.78 ± 0.1 μm, based on analysis of two different nanotubes using 400 independent images of each. The persistence length differences between 6HB+2 and $6HB_P$+2 as well as between 6HB and 6HT clearly show that positioning of backbone nicks and strand cross-overs can significantly affect DNA nanotube persistence length.

3.2 HX-Tubes with decreased Cross-Over Density

To further study the relation between molecular tube architecture (placement of cross-overs and backbone nicks) and persistence length we designed a modified version of 6HT described in chapter 2, "$6HT_2$". All sequences for $6HT_2$' are listed in appendix C. Both of those six-helix-tube versions have perfect staggering of strand cross-overs and backbone nicks, but their overall density is different by a factor of two (figure 3.5.

$6HT_2$ was based on the HX-tube scheme [117]. The length of each motif was increased to 21 bases (figure 3.5). Thus, each of the six strands had a total length of 84 bases and the density of strand cross-overs and backbone nicks was reduced by a factor of two with respect to the original (6HT). $6HT_2$ formed unbranched, micrometer long tubes as confirmed by fluorescence microscopy.

The persistence length of $6HT_2$ was measured as described in section 2.2. The result, $P = (2.1 \pm 0.2)$ μm, was significantly smaller than $P = (3.3 \pm 0.3)$ μm of 6HT. This again

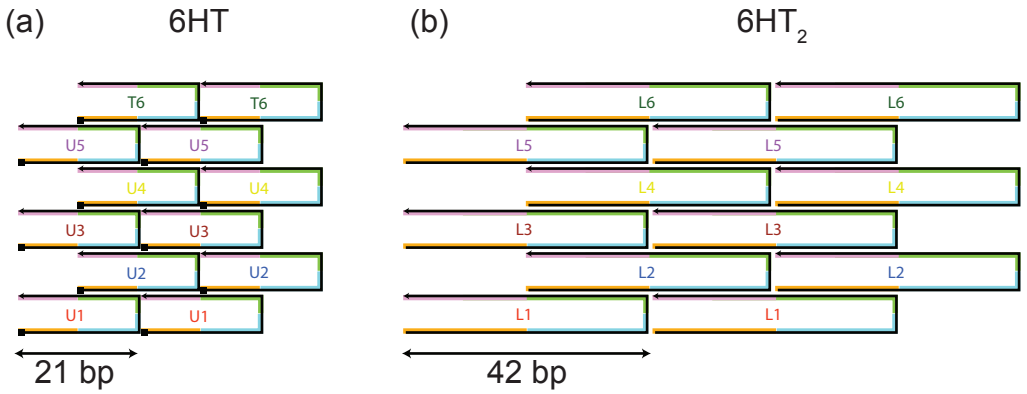

Figure 3.5: Strand design of 6HT (a) and $6HT_2$ (b). The distance between pairs of strand cross-overs and backbone nicks along the DNA axis is 21 base pairs in 6HT and 42 bp in $6HT_2$.

shows that DNA nanotube persistence length depends on the molecular tube architecture. In the following we discuss three models how tube ultrastructure may be related to persistence length.

3.2.1 Twist-Bend Coupling of DNA Molecules

To understand the decreased persistence length of $6HT_2$ in terms of the molecular DNA structure we first considered the different effect of twist-bend coupling on 6HT and $6HT_2$. As the distance between successive strand cross-overs is increased from $\ell_0/2$ in 6HT to ℓ_0 in $6HT_2$, the helix over- and under-twist, $\mathrm{d}\phi/\mathrm{d}\ell$, is reduced by a factor of two (section 2.7.2). Thus the DNA duplexes are closer to their natural twist in $6HT_2$.

Since the twist-bend energy, dG_{T-B} (equation 2.10), depends linearly on $(d\phi/d\ell)$ and the sign of $(d\phi/d\ell)$ alternates along each cylinder, one could argue that the cylinder's stiffness should also alternate: over-twisted sections should have a different stiffness than under-twisted sections. However, because each tube cross-section contains equal numbers of stiffened and weakened cylinders, the effect on tube persistence length is likely to be small.

3.2.2 Cross-Section Deformations

We also considered whether the persistence length difference between 6HT and $6HT_2$ might be caused by increased flexibility in cross-sectional shape. That is, rather than being confined to a circular cross-section (figure 3.6 a), DNA duplexes may be free to re-orient with respect to the bend axis upon tube bending, as illustrated in figure 3.6 b,c. The energies for the deformations, illustrated in figure 3.6 as a function of the deformation

angle γ_D and the spacing between successive cross-overs ℓ_x are given by:

$$dG(\gamma_D) = 2C\left(\frac{\gamma_D}{\ell_x}\right)^2 d\ell \tag{3.5}$$

for the geometry illustrated in figure 3.6b, and

$$dG_{(c)}(\gamma_D) = \frac{3}{2}C\left(\frac{\gamma_D}{\ell_x}\right)^2 d\ell \tag{3.6}$$

for the geometry illustrated in figure 3.6c. C is the twist modulus of the DNA duplex.

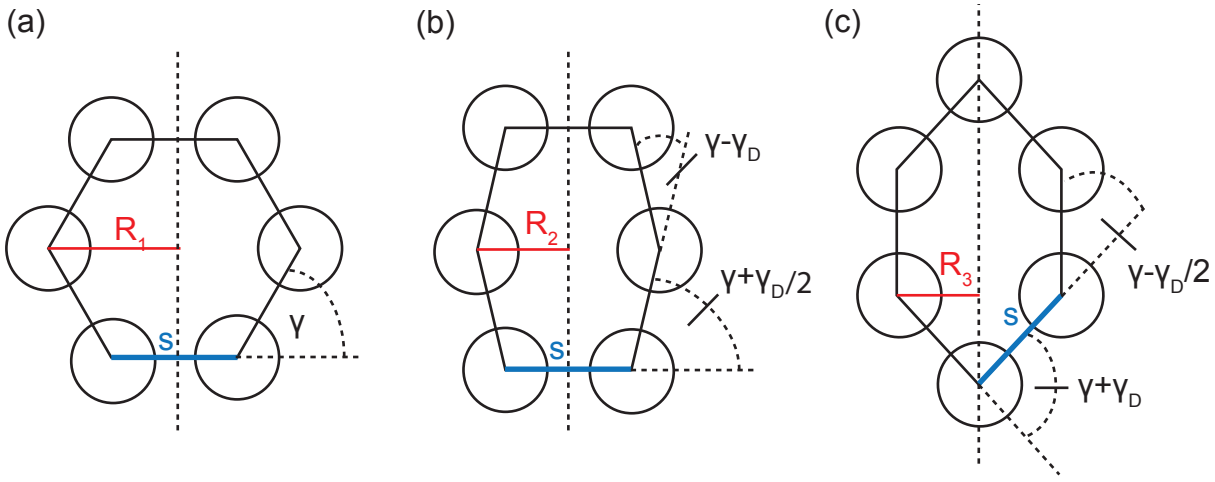

Figure 3.6: Illustration of a cross-section deformation of a 6HT. Circles represent cross-section of DNA duplexes with spacing s, aligned on a polygon grid. (b) and (c) show cross-section deformations obtained from (a) by addition / subtraction of the angle γ_D at indicated positions.

Since $\ell_x = \ell_0/2$ for 6HT and $\ell_x = \ell_0$ for $6HT_2$, for a given γ_D, dG of $6HT_2$ is smaller than dG of 6HT by a factor of four. Thus the $6HT_2$ cross-section is deformed more easily. To answer the question whether it is energetically favorable to deform tube cross-section while bending we considered the sum of tube bend- and cross-section deformation energy for the geometry illustrated in figure 3.6 c:

$$dG(r_c, \gamma_D) = \left[\frac{1}{2}B\left(6 + 16\left((s/r)^2\sin(\gamma - \gamma_D/2)^2\right)\left(\frac{1}{r_c}\right)^2\right]d\ell + \left[\frac{3}{2}C\left(\frac{\gamma_D}{l_x}\right)^2\right]d\ell \tag{3.7}$$

The first term was derived using the parallel axis theorem (eq. 2.24) with $R_3 = s\sin(\gamma - \gamma_D/2)$. For all radii of curvature, resolvable by light microscopy (approximately r_c >350 nm) equation 3.7 is minimum for $\gamma_D = 0°$ for both 6HT and $6HT_2$. The minimum of equation 3.7 only shifts towards $\gamma_D > 0°$ for much sharper bends ($r_c < 160$ nm for $6HT_2$). Thus it is unlikely that cross-section deformations facilitate bending on the observed scale.

3.2.3 Tube Bending by Stretching of DNA Cross-Overs

Here, we model the DNA nanotube as a bundle of n elastic cylinders. If sliding between cylinders (shearing) is not allowed, upon bending the outer cylinders of a tube need to be stretched and the inner cylinders compressed. The associated bend energy is given by:

$$dG_B = \frac{1}{2}B\left[n\left(1+\frac{(s/r)^2}{2\sin^2(\pi/n)}\right)\right]\frac{1}{r_c^2}d\ell \tag{3.8}$$

where the rectangular parenthetical term is the ratio of the tube's moment of inertia to that of a single cylinder, derived in section 2.7.1. If cylinders are able to shear bending can occur at an energetic cost equal to the bend energy of the individual cylinders plus the energy required for the shear. Instead of being stretched / compressed, the length of all cylinders remains the same. The path length difference between inner and outer cylinders leads to shearing between them. Following the derivation in section 2.7.3, in which stretching of a strand cross-over between adjacent cylinders over a distance Δq is possible at an energetic cost of $k\Delta q^2$, the shear energy of a tube segment of length dℓ is given by:

$$dG_{Shear}(\ell) = \sum_{i=1}^{n}\frac{k}{\ell_0}\left(\Delta q_i(\ell)\right)^2 d\ell \tag{3.9}$$

where ℓ is the position of the tube segment along a tube of length L with $-L/2 < \ell < L/2$ and $\Delta q_i(\ell)$ is the shear between cylinders i and $i+1$ at position ℓ. Assuming that the shape of the bent tube is a circular arc and that the path length difference between outermost and innermost cylinder is distributed evenly over the cylinders in-between, the required shear per cylinder pair is geometrically given by:

$$\Delta q_i(\ell) = \frac{4R}{nr_c}\ell \tag{3.10}$$

where R is the tube radius. Thus a tube of length L has a shear energy of:

$$G_{Shear} = n\int_{-L/2}^{L/2}\frac{k}{\ell_0}\left(\frac{4R}{nr_c}\ell\right)^2 d\ell \tag{3.11}$$

Solving the integral and substituting for R yields:

$$G_{Shear} = \frac{1}{2}\left(\frac{2ks^2}{3\ell_0\sin^2(\pi/n)n}L^2\right)\frac{1}{r_c^2}L \tag{3.12}$$

This derivation was made for an untwisted tube where shear accumulates over the entire tube length L.

For a tube which has twist $d\Phi/d\ell$ in addition to curvature, equation 3.10 becomes a function with dependence on $d\Phi/d\ell$ as well as r_c, because cylinders on the inner and outer side (towards and away from the bend axis) exchange their positions. For simplicity we

make the assumption that G_{Shear} of a twisted tube in which 180° rotations occur over the average distance $\langle d \rangle$ is equal to the sum of G_{Shear} of the constituent elements of length $\langle d \rangle$:

$$G_{Shear} \approx \frac{L}{\langle d \rangle} \left[\frac{1}{2} \left(\frac{2ks^2}{3\ell_0 \sin^2(\pi/n)n} \langle d^2 \rangle \right) \frac{1}{r_c^2} \langle d \rangle \right] \tag{3.13}$$

Further approximating that the shear energy is distributed evenly along the tube, the energy for bending a tube segment of length $d\ell$ via cylinder shearing, dG_{SB}, becomes:

$$dG_{SB} \approx \frac{1}{2} \left(nB + \frac{2ks^2}{3\ell_0 \sin^2(\pi/n)n} \langle d^2 \rangle \right) \frac{1}{r_c^2} d\ell \tag{3.14}$$

Because equation 3.14 is independent of L we can now associate a bend persistence length to this shear-bend mode, P_{SB}, by dividing the term in parenthesis by $k_B T$.

For 6HT, $\langle d \rangle^2$ was directly measured by TEM, and k derived, as described in section 2.3. Equation 3.14 then yields $P_{SB} = 32.5\mu$m, much larger than the measured persistence length (3.3 μm), which shows that this bend mode is not favored in 6HT.

In order to estimate P_{SB} for 6HT$_2$ without a direct measurement of $\langle d^2 \rangle$ we speculate that the ratio $\langle d^2 \rangle_{6HT} / \langle d^2 \rangle_{6HT_2}$ is equal to the square of the ratio of their twist persistence lengths $(P_{TS,6HT} / P_{TS,6HT_2})^2$ as predicted by equation 2.58. Then $\langle d^2 \rangle_{6HT_2} = 8.55 \times 10^4 nm^2$ and equation 3.14 yields $P_{SB} = 14.7\mu$m. Thus, bending of 6HT$_2$ *via* the stretching of crossovers still has a higher energetic cost than tube bending by stretching / compression of the DNA molecules themselves.

We propose that the observed tube deformations may be due to a combination of the two bending modes. The predicted difference between P_{SB} in 6HT and 6HT$_2$ follows the observed trend (6HT$_2$ is less stiff than 6HT).

3.3 Conclusions

We have demonstrated design schemes for six-helix-bundles with zero, two and three external helices and shown that they form micrometer long DNA nanotubes. We compared the persistence lengths of two versions of 6HB+2 with alternate crossover placement and found that it was significantly smaller when several crossovers where aligned in one cross-sectional tube plane. Further 6HB has a smaller persistence length than 6HT. Thus persistence length is not a simple function of the number of DNA helices in DNA nanotubes but also depends on the molecular architecture *i.e.* the placement of strand crossovers and backbone nicks.

We further compared persistence length of 6HT and 6HT$_2$, which both have perfect staggering of crossovers and nicks but at a density, different by a factor of two. We found that 6HT$_2$ had significantly lower persistence length and discuss three mechanisms how crossovers may contribute to tube bending deformations.

3.4 6HB Methods

3.4.1 Preparation of 6HB, 6HB+2 and 6HB+3

The strands of each tile were mixed stoichiometrically as estimated by OD260 and dissolved to 0.05-0.1 μM in either 1× TAE/ Mg^{2+} buffer (40 mM Tris-HCl, 20 mM acetic acid, 2 mM EDTA, 12.5 mM magnesium acetate, pH 8.0) or in 1× HEPES-Na buffer (10 mM HEPES-Na, 11 mM magnesium chloride, 1 mM EDTA, pH 7.8). The solutions were annealed from 90 C to room temperature over 48 h in a 2L water bath insulated in a Styrofoam box.

3.4.2 Preparation of Oxygen Scavenging System

For live fluorescence microscopy it is essential to scavenge oxygen so as to limit photo damage. The most convenient method for doing this is using a glucose oxidase/glucose/catalase mixture (OS mix). The component enzymes are stored as 100× stocks at ?80 °C and used for ≈2 h after mixing. It is important to keep the OS mix in a sealed tube on ice. The principle by which the mix scavenges oxygen is as follows: catalase: $H_2O + O_2 \rightarrow H_2O_2$ glucose oxidase: D-glucose + $H_2O_2 \rightarrow$ D-glucono-1,4-lactone. A 10× OS mix (0.35 mg/mL catalase, 2 mg/mL glucose oxidase, 45 mg/mL glucose, 5% β-mercaptoethanol) is prepared on ice and stored in a sealed tube on ice. For optimal results, a fresh 10× stock is prepared after ≈2h.

3.4.3 Preparation of Samples for Fluorescence Microscopy

Annealed DNA samples were stored at room temperature. Before microscope imaging, fresh OS mix was added to the DNA sample. Three μL of the DNA sample in 1× OS mix (0.035 mg/mL catalase, 0.2 mg/mL glucose oxidase, 4.5 mg/mL glucose, 0.5% β-mercaptoethanol) was then deposited onto a slide, covered with a coverslip, and sealed with epoxy or paraffin. The distance between the surfaces of the slide and the coverslip was ≈10 μm. When nanotube length (L ¿3 μm) and stiffness (p $\geq$ 1 μm) allowed, PVP-coated slides and coverslips were used to constrain nanotubes to diffuse in 2D. The thickness of the sample solution between the PVP coatings was 2 - 3 μm.

3.4.4 Fluorescence Microscopy

Samples were imaged on an inverted microscope (IX 70, Olympus) with a 100×/1.40 NA oil immersion objective. Blue light was filtered from a mercury arc lamp through an interference filter (475 nm) for excitation. The emitted fluorescence passed through a dichroic mirror (505 DRLP) and a green interference filter (525 nm). Raw images were captured and stored to a Mac mini via a cooled RETIGA EXi fast 1394 CCD camera (QImaging Corp.) using the corresponding software Qcapture (QImaging Corp.). Images were processed in ImageJ (NIH Image in Java: http://rsb.info.nih.gov/ij/).

3.4.5 Persistence Length Measurement

Persistence length, P, was measured in two different ways. In most cases it was possible to confine the nanotubes to 2D (see Preparation of Samples, above). The persistence length was then determined by extracting the end-to-end distance, R, and contour length, L, from fluorescence images of several different nanotubes (N > 4) in many distinct conformations ($\langle U \rangle$ =23) and fitting the data to the 2D Kratky-Porod model:

$$\langle R^2 \rangle = 4PL \left(1 - 2P \left(e^{-L/2P}\right)/L\right) \tag{3.15}$$

Each point on the $\langle R^2 \rangle$ versus L plot was derived from a set of U conformations observed for a single DNA nanotube. A complete data set for a given tube type consisted of N such points. Uncertainty in the persistence length thus determined was estimated using a bootstrap method: From every set of U confomations of a given nanotube, k conformations were selected at random with replacement (thus a particular conformation might be picked twice or not at all). The average end-to-end distance of the selected conformations, $\langle R^2 \rangle(k)$, was computed. This value typically differed only slightly from the end-to-end distance, $\langle R^2 \rangle(n)$, of the "original" set. A least-squares fit of the Kratky-Porod model to a plot of $\langle R^2 \rangle(k)$ versus L was performed and, accordingly, resulted in a slightly different estimate of the persistence length. For each type of nanotube, this process was repeated 1000 times using randomly selected sets of the same size as the original (that is, $k = U$). The resulting persistence length estimates were normally distributed about the one derived from the original data set and their standard deviation was taken as the uncertainty (67% confidence interval) in the measurement.

It was not possible to confine the 6HB+2 (parallel) nanotube (in which six out of eight sticky ends were at the same Z position along the helical axis) to 2D, so a different approach to estimating persistence lengths was taken. Movies containing several hundreds of frames were taken as a freely diffusing nanotube was manually tracked in the focal plane of a microscope. All independent images of a given nanotube were aligned according to their centers of mass and added together to generate a single composite image of the nanotube. The intensity profile along a straight line through the center of mass of the composite image fit well to a normalized Gaussian distribution, the standard deviation, σ, of which was taken as a measure of the nanotubes radius of gyration (RG). The contour length (L) was measured from the most extended conformation observed. These parameters were related to the persistence length (P) of the nanotube using the following two equations: RG = $n^{\nu}P/(6)^{1/2}$ and $L = nP$, where $\nu = 0.6$ for a 3D self-avoiding random walk. The average persistence length of the 6HB+2 nanotube design estimated in this manner was 0.78 ± 0.1 μm, based on analysis of two different nanotubes using 400 independent images of each.

Chapter 4

Curved and Twisted DNA Nanotubes

Curved and twisted filaments such as bacterial flagella [37] and FtsZ filaments [54] constitute an important class in biological systems with interesting mechanical properties. It has been suggested that such filaments can be described theoretically by a helical worm like chain (HWLC) model [53, 113]. However direct experimental verification of this model is difficult because model parameters such as filament stiffness or equilibrium curvature are not easily varied in biological filaments.

DNA nanotubes may serve as ideal model filaments of HWLC theory because of the ability to program curvature and twist. This programming has been achieved by targeted deletion and insertion of base pairs in DNA origami structures [17, 32] and tiled DNA nano rings [115]. In addition, straight and untwisted DNA nanotubes have been decorated with curved and twisted (helical) patterns of gold nano particles to demonstrate the fascinating optical properties of chiral nano structures [46].

Here, we describe methods for the construction of twisted, (un-curved) DNA nanotubes, which do not rely on generating torsion within individual DNA helices by introducing over- or under- twist. Instead twist is generated by folding a sheet of DNA helices into a tube with a defined edge offset (sections 4.1.1, 4.1.2). Tube formation and tube twist are studied by temperature-controlled UV absorbance experiments, fluorescence microscopy and atomic force microscopy (AFM).

Next we demonstrate the construction of curved (un-twisted) DNA nanotubes, which form rings with narrow size distribution (section 4.2.1). This is achieved by applying the principle of targeted deletion and insertion of base pairs. We show that the same method yields writhe-shaped nanotubes when the twist is non-zero and characterize their curvature and twist (section 4.2.2). We further show that changes in salt conditions can also induce writhe shape in (unwrithed) DNA nanotubes and discuss the underlying reasons.

Finally we given an outlook on how DNA nano-rings may serve as a template to construct lipid-DNA assemblies and show that DNA rings are stable under vesicle preparation conditions (extrusion), can be densely decorated with cholesterol “anchors” and be imaged by Stochastic Optical Reconstruction Microscopy (STORM) under solution conditions.

4.1 Intrinsically Supertwisted DNA Nanotubes

In chapter 2 we showed that based on their sequence design, HX-tubes can form with different amounts of supertwist. However, direct visualization of AuNP decorated tubes by TEM revealed that only the lowest accessible supertwist state was populated. Consistently calculation of the folding energy showed that higher supertwist states are energetically less favorable and thus much less likely to form.

In this section we present two designs to force a specific supertwist state by 1) reprogramming the assembly pathway (section 4.1.1) and 2) increasing the number of single stranded tiles per sequence repeat unit (section 4.1.2). We term both versions HX-ST tubes, where HX refers to the type of strand cross-overs in the tubes ("half-cross-overs") and ST denotes that they form with specific super twist.

4.1.1 HX-ST Tubes: Assembly Pathway Design

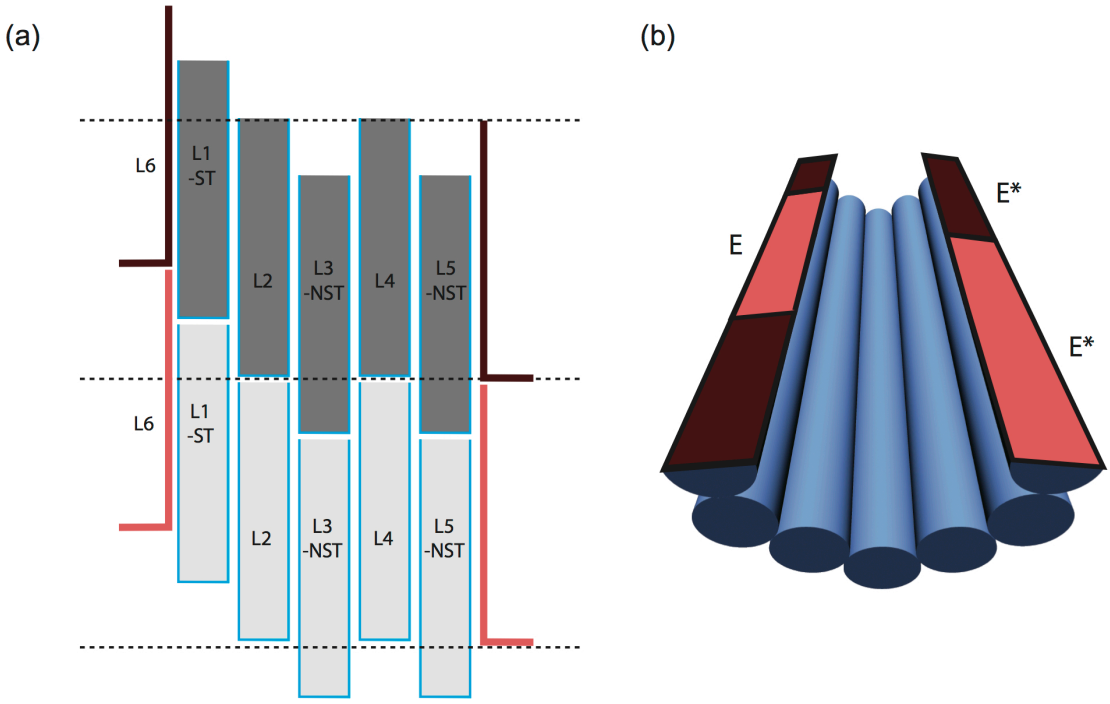

Figure 4.1: Strand design of 6HT-ST$_2$. (a) Shadings highlight units of 6 strands. (b) 3D model. Color coding of the sheet edges show the relative placement of complementary motifs.

We describe the design and characterization of HX-ST tubes. We will refer to these tubes as nHT-ST$_m$, where n specifies the number of helices in circumference and m the units of supertwist, as defined in chapter 2. Both n and m are modular and can be varied

independently. We propose a strategy to implement defined supertwist by designing a two-step folding process with step 1) DNA strands assemble into rings of defined supertwist, stable at high temperatures and step 2) ring association into tubes at lower temperatures.

Each strand in the HX-ST design has a length of 84 bases, which can be divided into four motifs. To separate tube formation into two steps, occurring at distinct folding temperatures, each strand has two 31 base long motifs and two 11 base long motifs. The strand design and 3D cylinder model of 6HT-ST$_2$ are illustrated in figure 4.1. The formation of a supertwist state can be controlled by the use of distinct versions of strands L1, L3 and L5. The two versions of each strand are called "NST", in which the long motifs are placed at 5' and 3' ends of the strand and "ST", in which long and short motifs alternate. DNA sequences are listed in appendix table C.4.

Because of this motif partitioning, "NST" strands align cross-overs of neighboring strands while "ST" strands introduce an offset of two helical turns. Thus the total edge offset of a sheet of DNA helices, before closing into a tube is given by 2 helical turns times the number of "ST" strands. Figure 4.1 illustrates the case of 6HT-ST$_2$, made by one "ST" strand (L1-ST) and two "NST" strands (L3-NST and L5-NST).

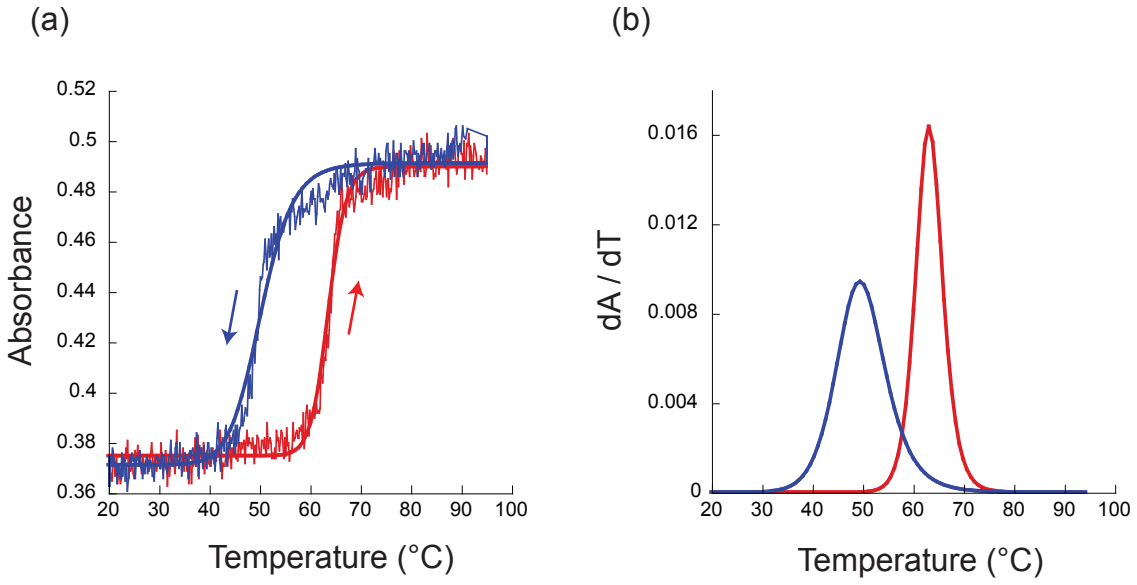

Figure 4.2: (a) UV absorbance at 260nm as function of temperature for 6HT at a heating / cooling rate of 1°C per minute. Melting is shown in red, annealing in blue. Solid lines are sigmoidal curve fits to the data. (b) Melting and folding rates given as the derivative of the fitted absorbance with respect to temperature. Their maxima are at 63.7°C (melting) and 50.3°C (annealing). The single, sharp transition in both processes is characteristic for one-step assembly.

Note that duplex sheets (open ribbons, containing several copies of each strand) with two "ST" strands would have an offset of four helical turns, which is equal to the sequence

repeat length and would allow tube formation without supertwist. Thus supertwist states higher than 6HT-ST$_2$ can only successfully form if sheet formation is not part of the assembly pathway. Instead the assembly process must be divided into two steps *i.e.* in figure 4.1a, sets of 6 strands (indicated by different shadings) must first form rings and subsequently end-to-end join with each other.

To verify the existence of two steps in the folding process of HX-ST tubes we monitored DNA UV absorbance during thermal melting and annealing. This technique relies on a change in extinction coefficient between double-stranded and single-stranded DNA and has been used to study various DNA hybridization reactions [117, 97].

First, as a reference, we measured UV-absorbance of 6HT. The result is shown in figure 4.2. The absorbance of melting and annealing data are fit with a sigmoidal curve, which yields 6HT melting and assembly temperatures of 63.7°C and 50.3°C respectively. The presence of hysteresis shows that the process is not at equilibrium, *i. e.* at slower heating and cooling rate, melting and annealing temperatures should approach each other. The data clearly shows only a single transition, characteristic of a one-step assembly.

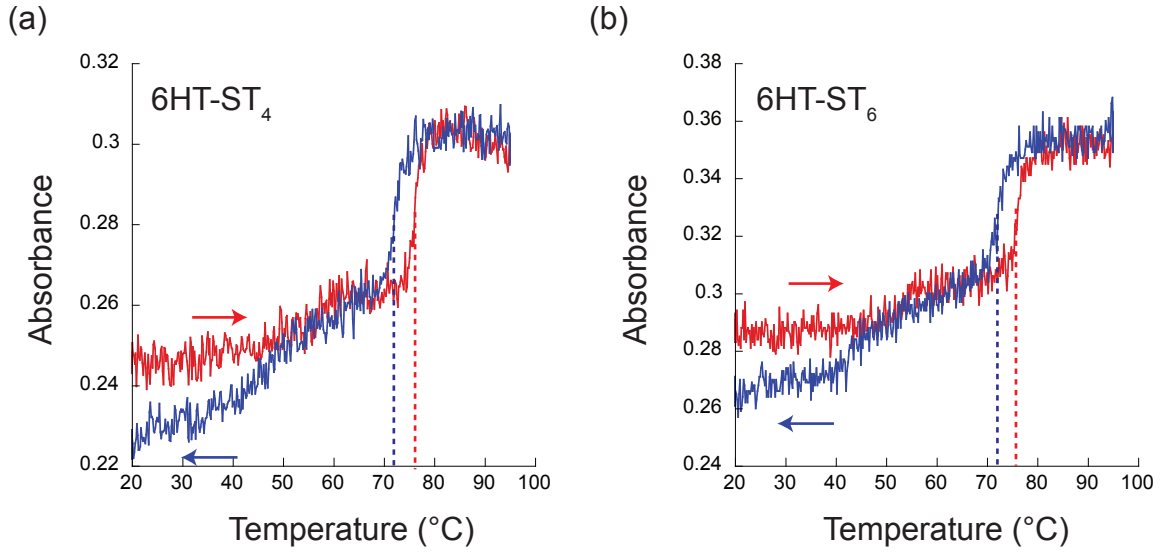

Figure 4.3: UV absorbance at 260nm as function of temperature for 6HT-ST$_4$ (a) and 6HT-ST$_6$ (b) at a heating / cooling rate of 1°C per minute. The absorbance has one sharp transition between 70°C and 80°C and a gradual change between 40°C and 60°C, as expected for a two-step process.

In contrast, absorbance measurements on 6HT-ST$_m$ showed two steps during melting and annealing: one sharp transition between 70°C and 80°C and a smaller, broader transition between 50°C and 70°C (figure 4.3 and appendix E). This is consistent with the expected assembly pathway because: 1) The absorbance change at the high temperature step is approximately three times larger than at the lower step. This reflects the ratio

of motif lengths that hybridize during ring formation (31 bp) at high temperature and ring joining (11 bp) at low temperature. 2) The observed high temperature transition is consistent with the predicted motif hybridization temperatures using the DINAMELT web server [57]. The low transition temperature overlaps with that observed for 6HT (figure 4.2). Thus, we conclude that HX-ST tubes did form in a two-step process as designed.

Figure 4.3 shows that the absorbance at 20°C before and after completion of the temperature cycle were different. This was not the case for 6HT-ST_0 and 6HT-ST_2 (appendix E). The absorbance difference indicates that, at the fast cooling rate [1] of the experiment, a fraction of the rings may form alternate structures with different absorbance, such as large aggregates.

To look for such structures and confirm tube formation we imaged 6HT-ST_m by fluorescence microscopy. Representative images are shown in figure 4.4. All four samples clearly contain tubes. The contour length of 6HT-ST_0 ranged up to 10 μm. The average contour length decreased with increasing supertwist. This result may reflect slower growth rates of tubes with the energetically less favorable, higher supertwist states. Besides individual tubes, some samples contained dense tube aggregates with diameters up to 20 μm. It is possible that the ratio of aggregated to individual tubes was dependent on the programmed supertwist state, however a quantitative measurement was not attempted because the number of tubes per aggregate is hard to estimate.

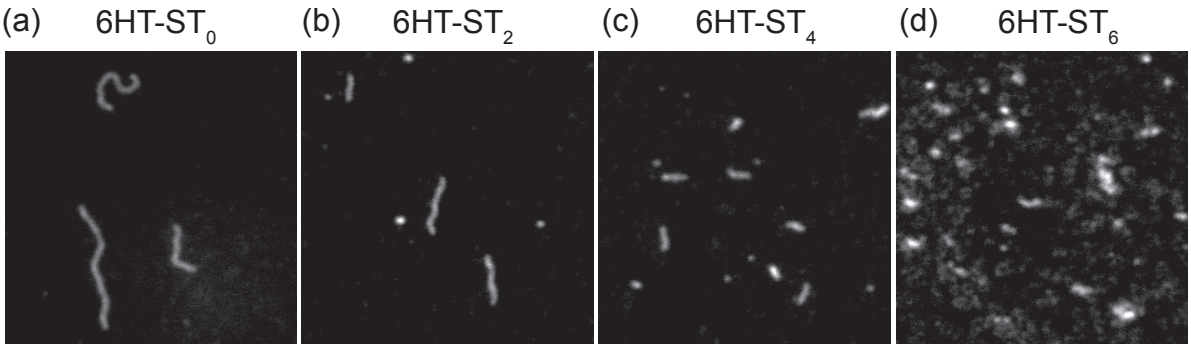

Figure 4.4: Fluorescence microscopy images of Cy3 labeled 6HT-ST_m. (a) - (d) are tubes with programmed supertwist ranging from ST_0 to ST_6 respectively. Image size: 15μm × 15μm

We asked if the defined supertwist had an effect on tube persistence length. Persistence length was measured by confining nanotubes to two-dimensional diffusion and measuring their thermal fluctuations as described in chapter 2. The result is shown in table 4.1. The persistence length of all measured 6HT-ST_m was significantly lower than that of regular 6HT or $6HT_2$. No clear trend between persistence length and supertwist could be observed.

[1] Tubes were prepared by thermal annealing in a 2L water beaker at 90°C, left to cool to room temperature in a styrofoam box over approximately 2 days. The heating and cooling rate during absorbance experiments was 1°C per minute

Table 4.1: Persistence Length of 6HT-ST_m and characteristics of the data sets from which they are derived. σ_P was obtained using 1000 bootstrap iterations. The lower fit limit, Δx_{min} was set to 1 μm.

	P (μm)	σ_P (μm)	x_0 (μm)	Δx_{max} (μm)	N	U
6HT-ST_0	1.2	0.14	0.35	4.9	4	420
6HT-ST_2	1.6	0.27	0.16	2.8	1	113
6HT-ST_4	1.2	0.21	0.35	1.8	1	99
6HT	3.3	0.3	0.24	6.7	13	503
$6HT_2$	2.1	0.2	0.61	3.3	10	269

We argued in section 3.2.3, that the persistence length of $6HT_2$ is smaller than that of 6HT because less thightly coupled DNA duplexes are able to shear with respect to each other more easily. We also outlined how supertwist may further decrease persistence length if shearing is possible. The persistence length measurements, shown in table 4.1 follow the predicted trend in part. However our model does not explain deviation between 6HT-ST_0 and $6HT_2$ and why 6HT-ST_2 has a higher persistence length than 6HT-ST_0 and 6HT-ST_4.

In future experiments these questions could be addressed by 1) Decorating HX-ST tubes with gold nano particles, as described in chapter 2 to directly visualize the amount of twist in the tile lattice. 2) Improving the assembly yield of long individual tubes to allow more accurate persistence length measurements.

Because the original HX-tube design forms long tubes with low defect density we reasoned that a HX-ST tube design more similar to the original HX-tube was a promising approach to address the latter point. Such a design is described in the next section.

4.1.2 HX-ST Tubes: Multi Tile Design

In chapter 2 we showed that supertwist is energetically unfavorable and thus HX-tubes tend to self-assemble with their lowest available supertwist state (ST_0 for even-nHT and ST_1 for odd-nHT). Here we describe a modified versions of HX-tubes in which specific supertwist states were made unavailable. This was achieved by replacing each strand of the original HX-tube design by 4 strands to increase the sequence repeat length of the tube (figure 4.5 a). For instance strand "U1" of the original design was replaced with "U1-R1", "U1-R2", "U1-R3" and "U1-R4".

Available supertwist states were programmed by different sets of "T-strands", which hybridize the edges of duplex sheets with a specific amount of "edge offset". The first 21 bases of the four T-strands are identical in each set. The last 21 bases are varied from set to set to control the relative placement of complementary sequences on sheet edges as illustrated in figure 4.5 b. The two integers following "R" in the "T-strand" naming scheme

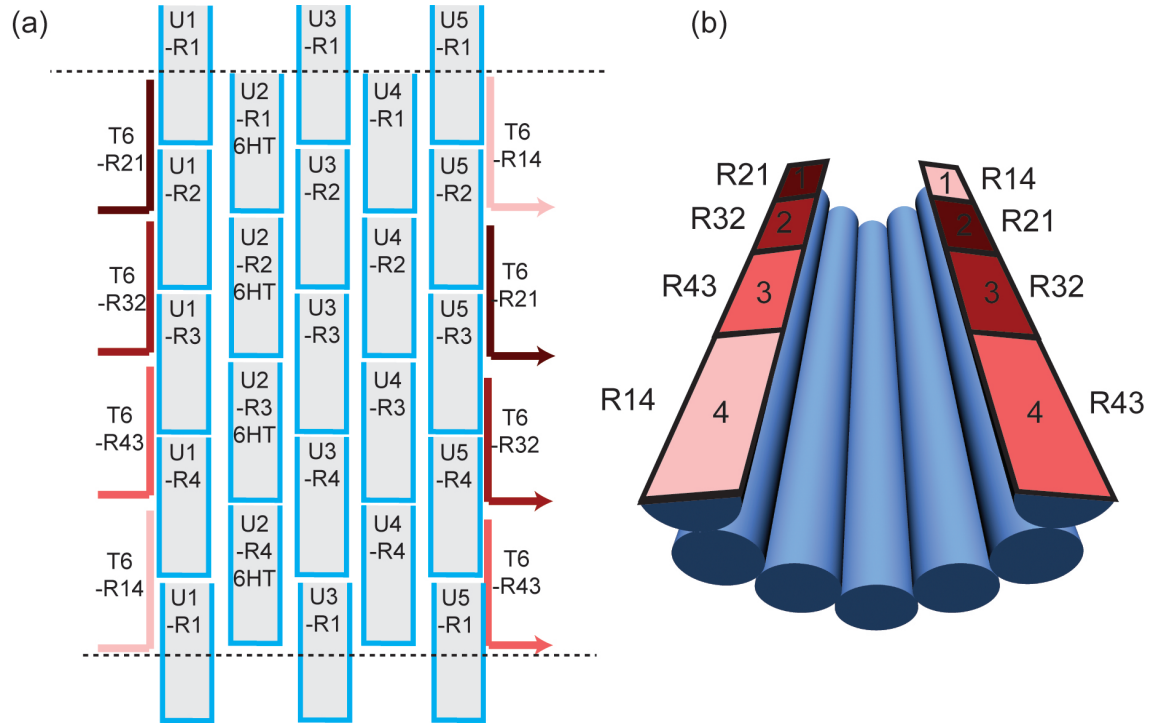

Figure 4.5: Design of 6HT-ST$_m$ tubes by using 4×6 DNA strands. Strand design (a) and 3D cylinder model (b) of 6HT-ST$_2$. Motifs on the right sheet edge in (b) can be shifted by using different "T6-strands" sets.

specify the row positions of 5' and 3' ends of the strand in the sheet. Four "T-strands" sets were designed to force supertwist states -2, 0, +2, +4. All DNA sequences were designed using a home-made script, described in chapter 9.

Because the repeat length of the DNA sequence is increased , the number of possibilities to close a sheet of duplexes into a tube is reduced with respect to the original HX-tube design: the closest alternate folding states of nHT-ST$_m$ are nHT-ST$_{m\pm8}$ while even- and odd- nHT can form with any even or odd supertwist state respectively. For instance alternate folding states for 6HT-ST$_2$ are 6HT-ST$_{10}$ and 6HT-ST$_{-6}$, both energetically extremely unfavorable.

Fluorescence microscopy images of nHT-ST$_m$, prepared under standard HX-tube folding conditions, did not contain resolvable tubes, only large fluorescent aggregates and resolution limited spots. When thermally annealed at a much slower rate (1 °C / 4 h, see methods section 4.6.2) the samples did predominantly contain micrometer length tubes. Typical fluorescence microscopy and AFM images are shown in figure 4.6.

6HT-ST$_m$, prepared under these conditions appeared significantly more stiff than 6HT. To test whether this was caused by tube formation with multiples of the designed circumference (*i. e.* 12HT or 18HT), we took higher resolution AFM images of sections, where tubes broke open and formed sheets on the mica surface (figure 4.7 a). As a reference we measured the width of 6HT sheets, which yielded 16.5 ± 1.5 nm (N=11), in good agreement

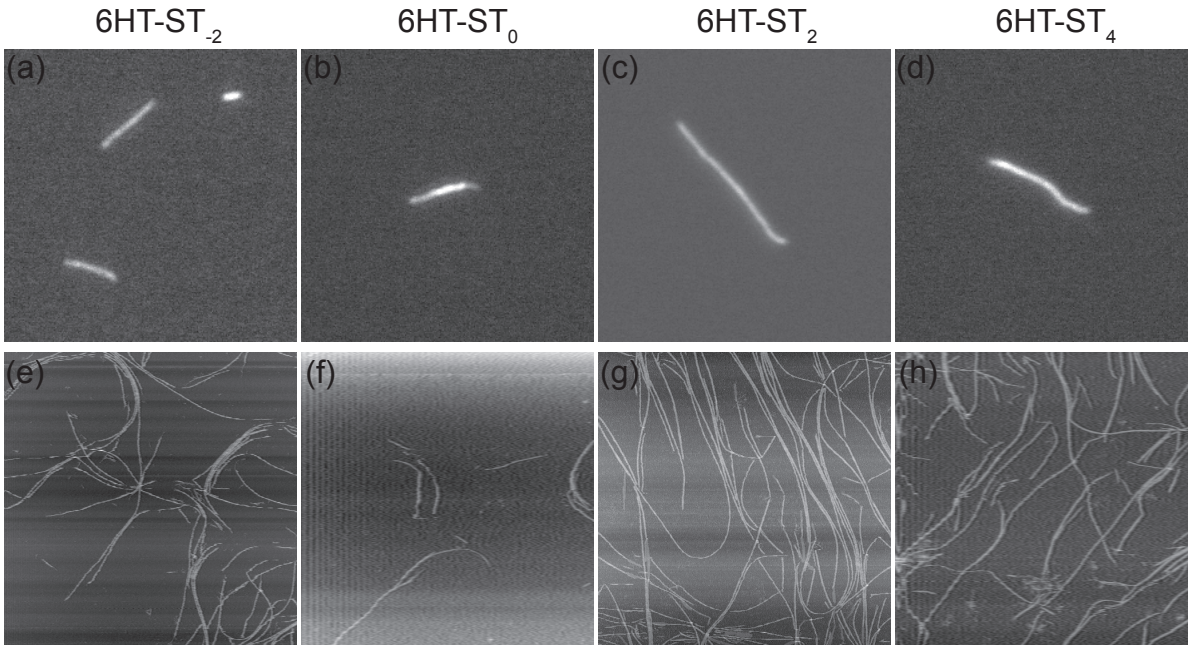

Figure 4.6: Fluorescence microscopy (a) - (d) and AFM (e) - (h) images of 6HT-ST$_m$. The programmed supertwist m ranges from ST$_{-2}$ (first column) to ST$_4$ (last column). Image size (a) - (d): 15 μm $\times$ 15 μm, (e) - (h): 5 μm $\times$ 5 μm

with measurements by Yin *et. al.* who demonstrated that the sheet width of HX-lattice assemblies, imaged by AFM is about 3 nm per DNA duplex [117]. We used this value to estimate the tube width of 6HT-ST$_m$, imaged by AFM under the same conditions. The results are listed in table 4.1. The measured width of 6HT-ST$_m$ clearly suggests formation with double to triple the designed circumference of six DNA duplexes (table 4.2).

Because opening events were rare and absolute size measurements by AFM can depend on parameters such as the shape of the tip, we used relative fluorescence intensity to further study tube diameter. 6HT-ST$_m$ was mixed with 6HT, both prepared with a subset of Cy3 labeled strands [2] and the sample was imaged by fluorescence microscopy (figure 4.7 b). Both tube types were easily distinguished by their intensity and the shape of their contour (6HT-ST$_m$ were more stiff than 6HT). The intensity of 6HT-ST$_m$, I_1, was compared to the intensity of 6HT, I_2, which have the known labeling density of 3 Cy3 molecules per 7.1 nm tube length. The circumference of 6HT-ST$_m$, n_{eff}, is then related to the ratio I_1/I_2 by:

$$\frac{I_1}{I_2} = \frac{r_1}{r_2} \times \frac{n_{\text{eff}}}{6} \tag{4.1}$$

where r_1 and r_2 are the fraction of Cy3 labeled strands (3 / 6 for 6HT and 2 / 24 for 6HT-ST$_m$). Intensity measurements were obtained by fitting gaussians to the intensities of line profiles, of neighboring tubes, as shown in figure 4.7 b.

[2] 2 out of 24 strands of 6HT-ST$_m$ and 3 out of 6 strands of 6HT had a Cy3 attachment

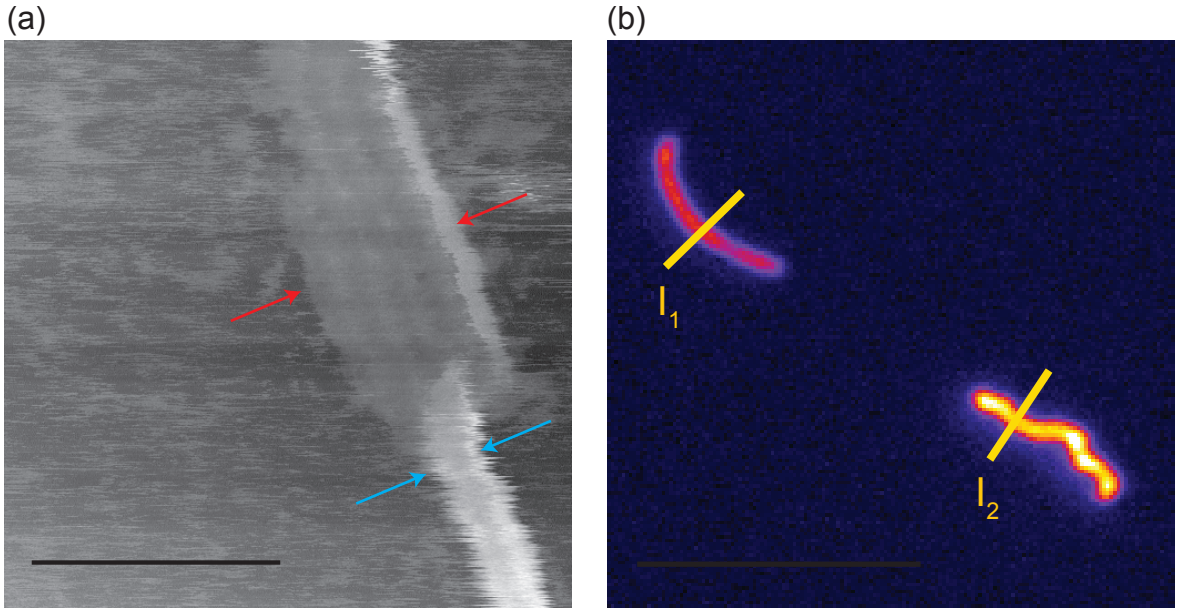

Figure 4.7: (a) AFM image of a 6HT-ST$_4$, which has an open sheet section (top) and a closed tube section (bottom). Open width (red arrows): 63 nm, closed width (blue arrows): 18 nm. (b) Fluorescence image of 6HT-ST$_4$, next to 6HT, recognizable by their high flexibility. The intensities I_1 and I_2 were measured by taking the height of gaussian fits to intensity line profiles at marked locations. Scale bars: 100 nm (a), 5 μm (b).

As a control, we measured I_1/I_2 of 6HT with only one Cy3 labeled strand, mixed with 6HT with 3 Cy3 labeled strands. The result, 0.36 $\pm$ 0.03 (N = 12) was in good agreement with the expected value of 0.33 (using r_1=1/6 and r_2=3/6). Tube circumference measurements of 6HT-ST$_m$ based on this method are listed in table 4.2. The results show good agreement with the AFM based method. Non of the methods yielded a circumference estimate for 6HT-ST$_0$ because tubes often varied in intensity along their lengths (figure 4.6 b) or contained branches (figure 4.6 f).

In addition to 6HT-ST$_m$ we designed four sets of 7HT-ST$_m$ with m = -3, -1, +1 and +3. Fluorescence microscopy of 7HT-ST$_m$ showed that all four samples contained micrometer long, unbranched tubes with significantly less bends than 7HT, suggesting multi-circumference. A quantitative width measurement on 7HT-ST$_{-1}$ suggested formation with double circumference (14 DNA duplexes, see table 4.2).

To explain, why HX-ST tubes formed tubes with multiples of the designed circumference we considered the deformation energy model derived in chapter 2. During thermal annealing there must be a temperature at which single strands can form a stable initial sheet. The addition of free strands to that sheet must be slightly favorable for the sheet to grow. Both HX- and HX-ST tubes can potentially close into a tube once the sheet reaches the width of n strands. The presented measurements suggest, that 6HT and 7HT form tubes at this point, while 6HT-ST$_m$ and 7HT-ST$_m$ sheets further grow in size until they

Table 4.2: Average, D, standard deviation, σ and number, N, of circumference measurements by AFM- and fluorescence microscopy on 6HT-ST$_m$

Tube	D_{AFM}	σ_{AFM}	N_{AFM}	D_F	σ_F	N_F
6HT	**5.4**	0.5	11	**6.5**	0.5	12
6HT-ST$_{-2}$	**10.8**	0.4	2			
6HT-ST$_{\pm 0}$						
6HT-ST$_{+2}$	**14.5**	5.8	9	**(34.2)**	(4.0)	(5)
6HT-ST$_{+4}$	**21.0**	-	1	**19.8**	2.5	9
7HT-ST$_{-1}$	**13.4**	2.9	11			

reach integer multiples of their designed width.

We considered if the inability of HX-ST sheets to close at width n was caused by 1) higher deformation energy, ΔG / nm, and lower gain in hybridization energy for tubes with forced supertwist or 2) a difference in the growth rates between HX- and HX-ST sheets resulting in different sheet sizes and geometries as explained below.

Following the logic of point 1, 6HT-ST$_0$ and 7HT-ST$_{\pm 1}$ should form with single circumference, since those DNA sheets have identical deformation energy, ΔG / nm, as 6HT and 7HT respectively. [3] Since 7HT-ST$_{\pm 1}$ did not form with single circumference, the difference in deformation energy between HX- and HX-ST tubes alone cannot explain the observed tube circumference of HX-ST tubes.

Thus we considered, if the difference in strand numbers between the two designs may cause a difference in the sheet growth kinetics which may in turn affect tube circumference. To understand why the sheet growth may be different for nHT and nHT-ST$_m$ designs we consider a simple model, illustrated in figure 4.8: DNA strands, and possible strand binding positions are represented by colored squares. Red illustrates occupied positions in the DNA sheet, blue and green represent unoccupied sheet positions. Each of the 3 $\times$ 3 sheets has six binding positions, which cause growth in the direction parallel to the DNA axis and six, which cause growth perpendicular to that axis.

Since all strands are present at equal concentrations during the self-assembly process, the chance of any strand coming in contact with the sheet are equal. We make the assumption that a strand, which contacts the sheet binds if its specific binding position is available and diffuses away otherwise. In this simple model the growth rate of the illustrated DNA sheets for a particular direction are proportional to the number of distinct binding positions in that direction divided by the total number of DNA strands.

For the sheet geometries in figure 4.8 this model yields different growth kinetics for HX- and HX-ST sheets: the former grows faster in direction parallel to the DNA axis than perpendicular to it. This is because the sheet edges in direction parallel to the DNA axis have more distinct open binding positions, than the edges in the perpendicular direction. HX-ST sheets grow at the same rate in all directions because all edges have three distinct

[3] This is based on direct supertwist measurement of 6HT and 7HT, described in chapter 2, which revealed that those tubes form with ST$_0$ and ST$_{\pm 1}$ respectively.

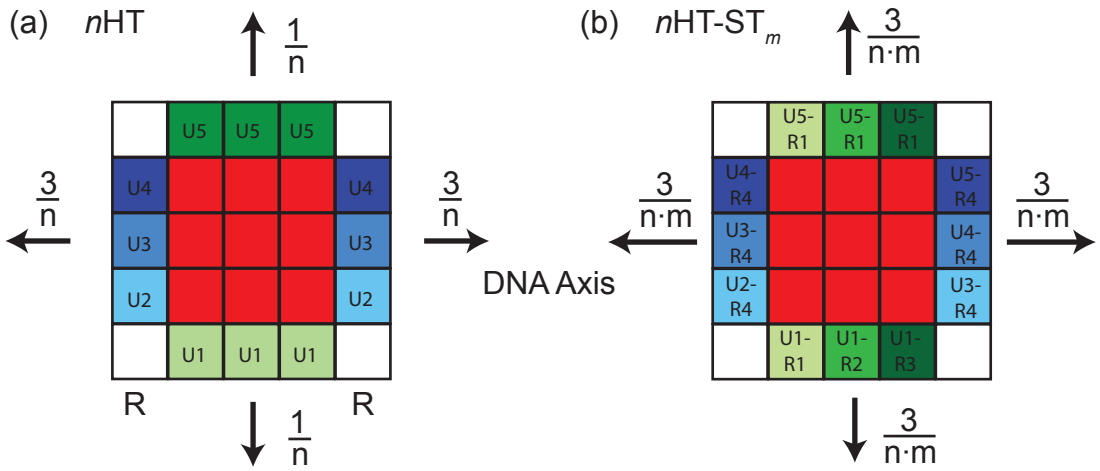

Figure 4.8: Growth rate models of nHT (a) and nHT-ST$_m$ (b) sheets. DNA strands of the sheet are illustrated as red squares. Distinct strand binding positions, causing growth perpendicular and parallel to the DNA axis are colored with distinct shades of green and blue respectively. Growth rates are calculated as the number of distinct binding positions divided by the total number of DNA strands.

binding positions. Based on this model it can be expected, that the geometric aspect ratio of HX- and HX-ST sheets evolves differently during the annealing process.

We propose that only DNA sheets within a specific range of geometric aspect ratios are able to close into a tube when reaching the designed width. In particular, the tube closure condition may be a minimum sheet length (parallel to the DNA axis) to allow a stable hybridization of sheet edges. Because HX-tubes preferentially grow in direction parallel to the DNA axis, this condition may be met for this tube type, but not for HX-ST tubes.

To better understand the formation of multi-cricumference tubes, we visualized their supertwist by AFM. Tubes with M - fold circumference can close with supertwist state $M \times m$. However, since in many cases $M \times m$ is larger than the sequence repeat length (eight helical turns) $M \times m$ is not always the smallest available supertwist state. The smallest supertwist state can be obtained by determining the minimum of $M \times m + x \times 8$, where x is an integer. For instance, 7HT-ST$_{-1}$ formed with $M = 2$ may have ST$_{-2}$ or ST$_{+6}$.

Because tube opening was rare, we were only able to obtain supertwist information about one sample, 7HT-ST$_{-1}$, in which several tubes opened over micrometer-long sections and displayed periodic features, as shown in figure 4.9a. High resolution images of sections where the DNA sheet twisted (figure 4.9) showed left-handed chirality, consistent with the chirality of the lowest accessible supertwist state (ST$_{-2}$).

In summary, the HX-tube design scheme based on increasing the number of strands yielded tubes with multiples of the defined circumference instead. AFM and relative fluorescence intensity measurements suggested that the designed circumference exceeded the

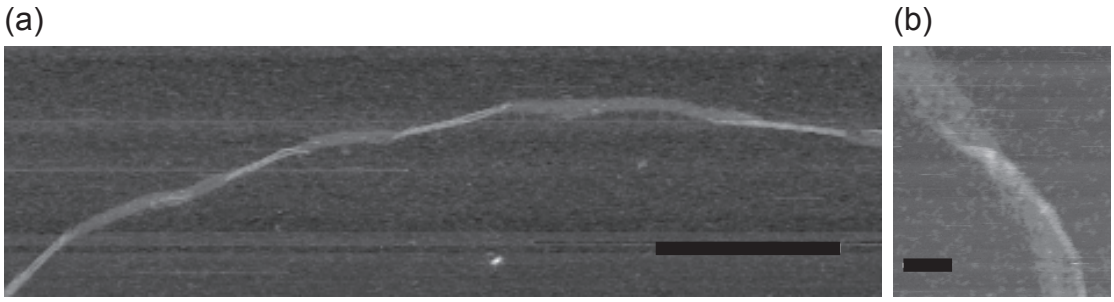

Figure 4.9: AFM images of 7HT-ST$_{-1}$. Width measurements of open sheets suggests double circumference. The supertwist appears left-handed. Scale Bars: 500 nm (a), 50 nm (b)

intended value by a factor of two to three. We hypothesized that this may be caused by differences in the growth rates between our design and the "original" HX-tube design, which yields single circumference tubes. In future experiments this HX-ST tube design may serve as an interesting model system to learn more about the self-assembly process of DNA-lattices with a finite number of states, each with a specific lattice deformation energy.

4.2 Insertion and Deletion of Basepairs

The cross-overs in DNA nano structures are typically placed in a way to allow each DNA helix to adopt equilibrium B-form DNA geometry. DNA helices which are unable to adopt this equilibrium geometry cause stress within the structure. Applying stress to specific points by targeted deletion and addition of base pairs has proven to be a successful method for the construction of curved and twisted DNA nano structures [17, 32, 115].

The basic principle of this method is illustrated in figure 4.10 for a DNA nanotube with six helices in circumference. Each DNA double helix (represented by cylinders) is divided into segments of repeating sequence. Grey cylinder sections represent 21 base pair long DNA double helices with equilibrium net twist. The red and blue cylinders' segments have a length of 22 and 20 base pairs respectively. Base pair addition (deletion) to a segment increases (decreases) the length and overall twist of the segment because base stacking favors a rotation of 34 degrees and a length increase of 0.34 nm per base pair.

Confined within the DNA nanotube lattice and cross-linked to adjacent DNA duplexes, the torque and force exerted by a modified (elongated or shortened) DNA duplex causes a curvature κ_0 and torsion τ_0 on the tube. Curvature and torsion depend on bending and twisting moduli of the DNA nanotube. In the following model we will assume that base pair addition and deletion result in the same magnitude of curvature and torsion but with opposite sign and that the effects of several modifications can be superimposed. Then, κ and τ can be expressed in a local, orthonormal coordinate system in which the z-axis is

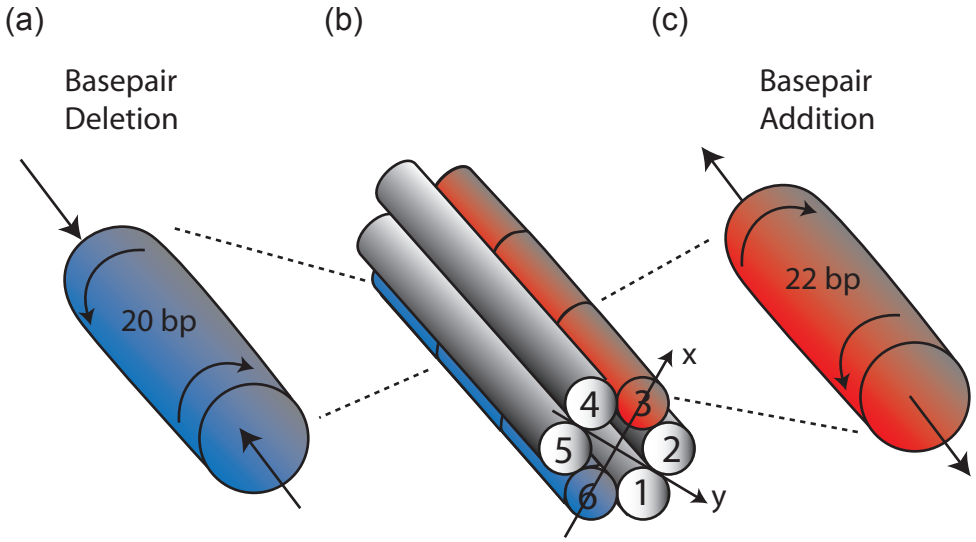

Figure 4.10: Programmed curvature and torsion of DNA nanotubes. Blue, grey and red cylinders represent DNA duplexes with 20, 21 and 22 base pairs per two helical turns respectively. Base pair deletion causes segment contraction and left-handed torsion (a). Base pair insertion causes segment elongation and right-handed torsion (c).

parallel to the tube axis and the x-axis intersects the n-th DNA duplex of the tube (figure 4.10 b):

$$\tau = \sum_{i}^{n} \tau_i \tag{4.2}$$

$$\kappa_x = \sum_{i}^{n} \cos(2\pi i/n)\kappa_i \tag{4.3}$$

$$\kappa_y = \sum_{i}^{n} \sin(2\pi i/n)\kappa_i \tag{4.4}$$

where κ_i and τ_i take on the values $-\kappa_0$, $-\tau_0$ if cylinder i has a base pair deletion, 0 if cylinder i is at equilibrium and κ_0, τ_0 if cylinder i has a base pair insertion. The total curvature κ can then be calculated by:

$$\kappa = \sqrt{\kappa_x^2 + \kappa_y^2} \tag{4.5}$$

A tube with constant curvature and torsion follows a helical path with Radius R and helical pitch λ:

$$R = \frac{1}{\kappa\left(1 + \left(\frac{\tau}{\kappa}\right)^2\right)} \tag{4.6}$$

$$\lambda = \frac{2\pi\tau}{(\kappa^2+\tau^2)} \tag{4.7}$$

Solved for curvature and torsion eqs. 4.6 and 4.7 can be rewritten as:

$$\kappa = \frac{R}{R^2+(\lambda/2\pi)^2} \tag{4.8}$$

$$\tau = \frac{\lambda/2\pi}{R^2+(\lambda/2\pi)^2} \tag{4.9}$$

4.2.1 Ring-Shaped DNA Nanotubes

Equation 4.2 predicts that a tube with one base pair insertion and one base pair deletion on diametrically opposite helices has equilibrium twist zero and thus must adopt a ring shape. Experimentally the formation of rings by base pair deletion and insertion has been demonstrated for a different type of tiled nanotube by Yang and coworkers [115]. Here, the formation of rings was investigated by modifying a 6HT as illustrated in figure 4.10. DNA helices were modified by replacing strands U2, U3, U5 and T6 with U2+1, U3+1, U5-1 and T6-1 (sequences given in appendix C).

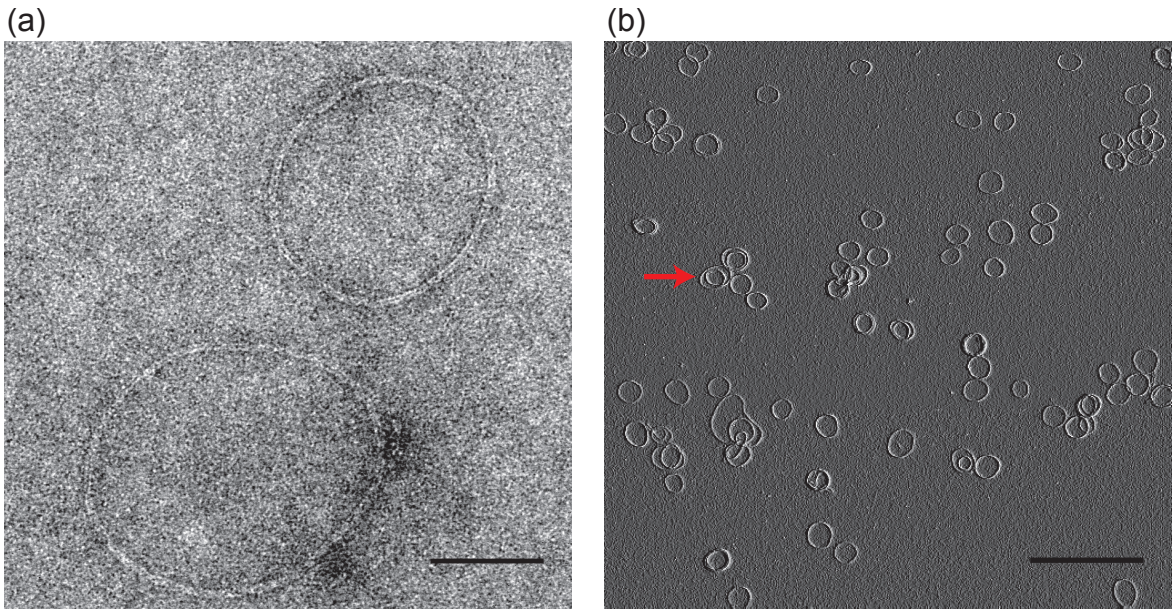

Figure 4.11: TEM (a) and AFM phase (b) images of ring-shaped DNA nanotubes. The arrows in (b) points to a tube, which did not close into a single ring. Scale Bars: 100 nm (a), 1000 nm (b)

All strands were annealed, using the same protocol as for unmodified HX-tubes and imaged using TEM and AFM. Representative images are shown in figure 4.11. Mean and

standard deviation of the ring circumference of 612 ± 83 nm was determined from N=106 measurements from AFM mages. Ring radius and curvature are related by equation 4.8. The measured radius corresponds to κ=10.1 ± 1.8 μm^{-1}. From equations 4.4 to 4.5 one finds that κ_0=κ/2=5.1 μm^{-1}.

This value may be an overestimate because the ends of curved tubes may come in contact and close into rings, before the tube is long enough to form a ring with equilibrium curvature. Besides rings, a fraction of the tubes formed alternate shapes. An example is marked by a red arrow in figure 4.11b.

4.2.2 Writhe-Shaped DNA Nanotubes

According to equations 4.2 to 4.5, the modification of only one DNA duplex results in DNA nanotubes with helical equilibrium contour. We will refer to helical DNA nanotubes as "writhed" to avoid confusion with the helical shape of double stranded DNA. When DNA nanotubes were prepared with strands U2+1 and U3+1 instead of U2 and U3, and imaged by TEM (figure 4.12), their contour clearly showed periodic features, consistent with a 2D confined writhe shape.

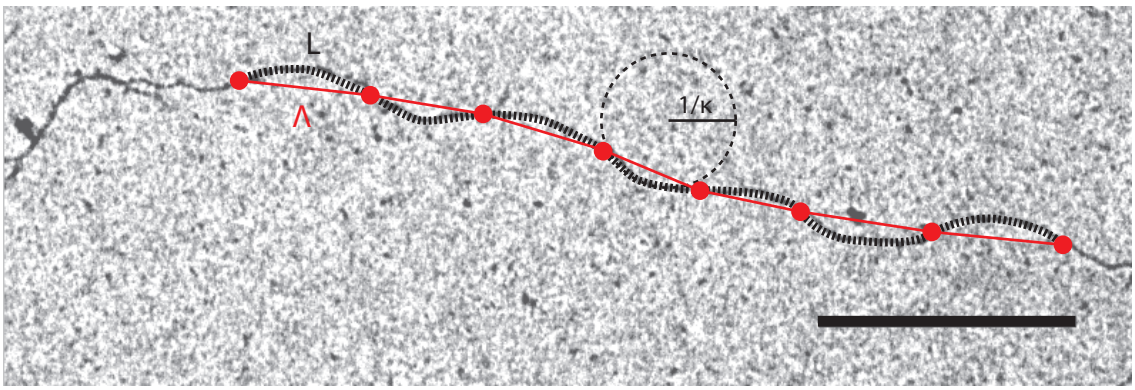

Figure 4.12: TEM image of writhe-shaped DNA nanotube (6HT). Red dots mark curvature inversion points ("twist kinks"), Λ and L are the (direct) distance between them and contour length between them respectively. Scale Bar: 500 nm

Extracting information about the 3D shape of a 2D confined helical filament is not trivial. The conformation of "squeezed" helical filaments, also called "squeelices" has been studied theoretically and by simulations [62]. We adopt the definition of "twist kinks" of a squeelix, which are points where the curvature changes its sign (marked by red dots in figure 4.12. Nam *et. al.* showed that the curvature κ of the squeelix is similar to that of the 3D helix prior to 2D confinement at points between two twist kinks. Direct curvature measurement by manual fitting of a circular arc at these points from figure 4.12 yields $\kappa = \kappa_0 = 5.4 \pm 0.2 \mu\text{m}^{-1}$, in good agreement with the value obtained from ring-shaped DNA nanotubes.

4.3 Ion Exchange Method

[4] When (unwrithed) HX-tubes, prepared in 1×TAE buffer with 12mM $MgCl_2$ were diluted into 40mM NH_4OAc their contour adopted a writhe shape under certain conditions. Images of 10HT in 40mM NH_4^+ with 40μM Mg^{++} and 80 μM Mg^{++} are shown in figure 4.13 (a) and (b) respectively. In this predominantly monovalent ion solution, tubes were stable over several days and did not adhere to the glass surface of the coverslip, enabling time-resolved fluorescence microscopy without the use of PVP coating.

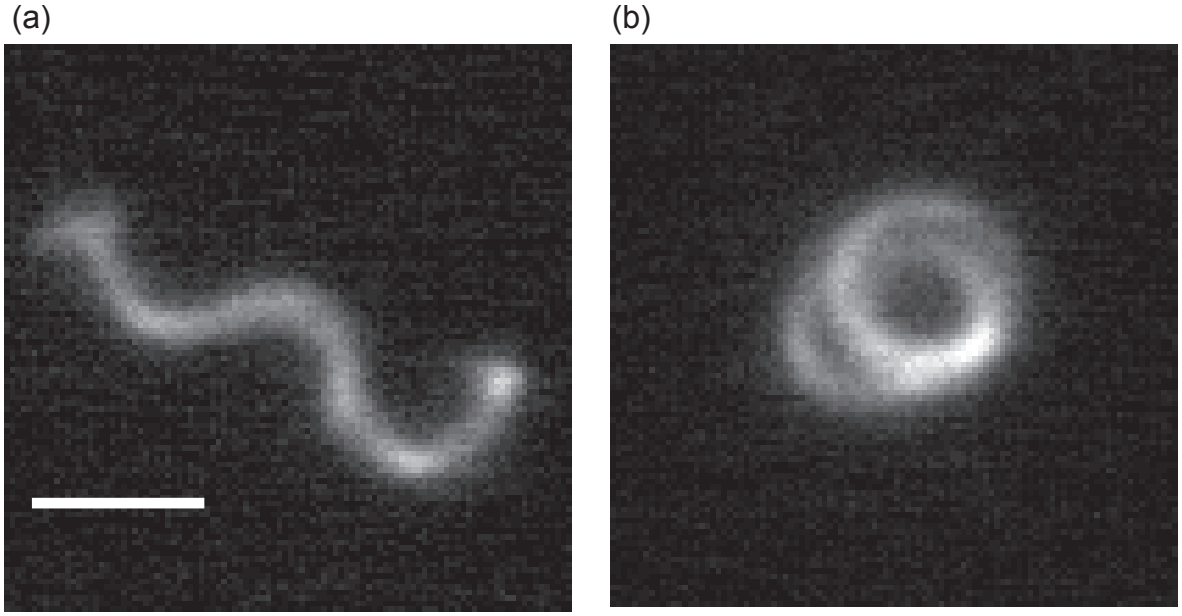

Figure 4.13: Fluorescence images of 10HT, labeled with Cy3 on strands U1, U4, U5 in 40mM NH_4^+ with (a) 40μM Mg^{++} and (b) 80 μM Mg^{++}. Scale Bar: 2 μm

Odd- nHT preserved their smooth contour while even-nHT (except 6HT) were resolvably writhed. We propose the observed writhe was induced by a change in the equilibrium helical repeat length of DNA upon ion exchange. The tube lattice may release this twist by adopting a writhe shape. Since odd-nHT did not display writhe it is possible that the handedness of the twist induced by ion exchange is opposite to the existing supertwist and the two thus counteract.

The influence of Cy3 molecules on curvature and torsion will be discussed in the following chapter. In principle, the observed writhe shape may also be caused by a change in Cy3 binding affinity upon ion exchange, however time resolved fluorescence anisotropy studies showed no dependence on salt concentration [81], suggesting that the binding affinity does not depend on ion concentration.

[4]Section 4.3 is reprinted (adapted) with permission from Daniel Schiffels, Tim Liedl, and Deborah K. Fygenson (2013) Nanoscale Structure and Microscale Stiffness of DNA Nanotubes. ACS Nano. Copyright (2013) American Chemical Society.

4.4 DNA Ring - Lipid Assemblies

Lipid coated DNA structures are a promising delivery system for gene therapy and drug delivery. It has been demonstrated that DNA and lipid molecules can self-assemble into cationic liposome-DNA (CL-DNA) complexes [74] and mono-nucleic acid lipid particles (mono-NALPs) [78]. Using tiled- or DNA origami structures in a delivery system will be of advantage because previous work has shown that DNA tetrahedral cages are not degraded by certain types of endonucleases and are stable over hours in mammalian cells [43, 103]. Zhao *et. al.* demonstrated that the cancer drug anthracycline doxorubicin (Dox) encampsulated in twisted DNA origami tubes had increased cytotoxicity and decreased intracellular elimination rate in breast cancer cells compared to free Dox [118]. CpG sequences embedded in DNA structures can be uptaken in cells and cause enhanced immunostimulation responses with respect to un-assembled CpG sequences. [85]. Many more examples can be found in a recent review on DNA nano carriers [14].

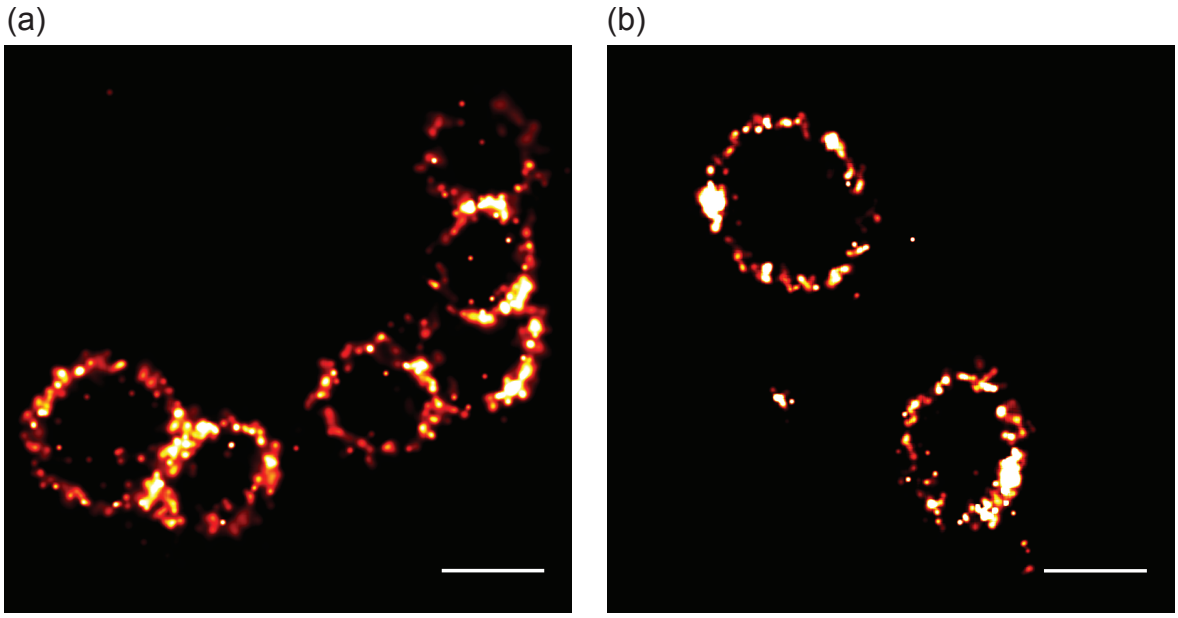

Figure 4.14: STORM images of DNA nano-rings, labeled with one Alexa 647 dye per ≈ 7 nm. STORM images were reconstructed from single molecule positions of blinking dye molecules, recorded over several thousand frames. Scale bars: 200 nm

We present steps towards the construction of a tiled DNA nano ring structure with programmable interaction to lipid vesicles. We use DNA nano-rings, described in section 4.2.1 as a starting point because their size is on the same order as that of lipid vesicles. Because lipid vesicles are unstable under dry conditions, one of the most suitable imaging techniques to characterize lipid-DNA assemblies is Stochastic Optical Reconstruction Microscopy (STORM) which can be used under solution conditions. STORM has been shown to have a resolution on the order of 10 nm [79, 33] and allows the use of different

labeling colors for the different components of the assembly. To test if DNA nano-rings were resolvable by STORM one of the DNA strands, "U1", was labeled with an Alexa 647 dye. Images of nano-rings, mixed with oxygen scavenging system (OSS) are shown in figure 4.14. The ring shape was clearly resolvable and the size of the rings in figure 4.14 (average 733 nm) is in good agreement with measurements in section 4.2.1.

Next, we tested if DNA rings were stable under conditions used for lipid vesicle preparation. Therefore the sample was forced 21 times through a single membrane with pore size 200nm (see methods section 4.6.4). We characterized the samples by measuring the ring size by AFM. Average and standard deviation of ring circumference before and after extrusion were 612 ± 83 nm (N=106) and 601 ± 94 nm (N=117) respectively. In addition, the circular equilibrium ring shape was maintained after extrusion. Thus, DNA rings took no detectable damage from extrusion.

Instead of relying on electrostatic interaction between the components of the assembly we propose to promote lipid-DNA interaction at specific sites on the DNA nanostructure by positioning hydrophobic cholesterol molecules on the surface of the DNA objects. We prepared modified ring versions which had cholesterol molecules at the inner perimeter of the ring by replacing strands "U5-1" or "T6-1" or both with, "U5-1-Chol" or "T6-1-Chol" which had identical sequences and a cholesterol modification at their 3' end. Modification of one strand places one cholesterol molecule every 7 nm at the inner perimeter of the ring. Using both modified strands doubles the cholesterol density (one per 3.5 nm).

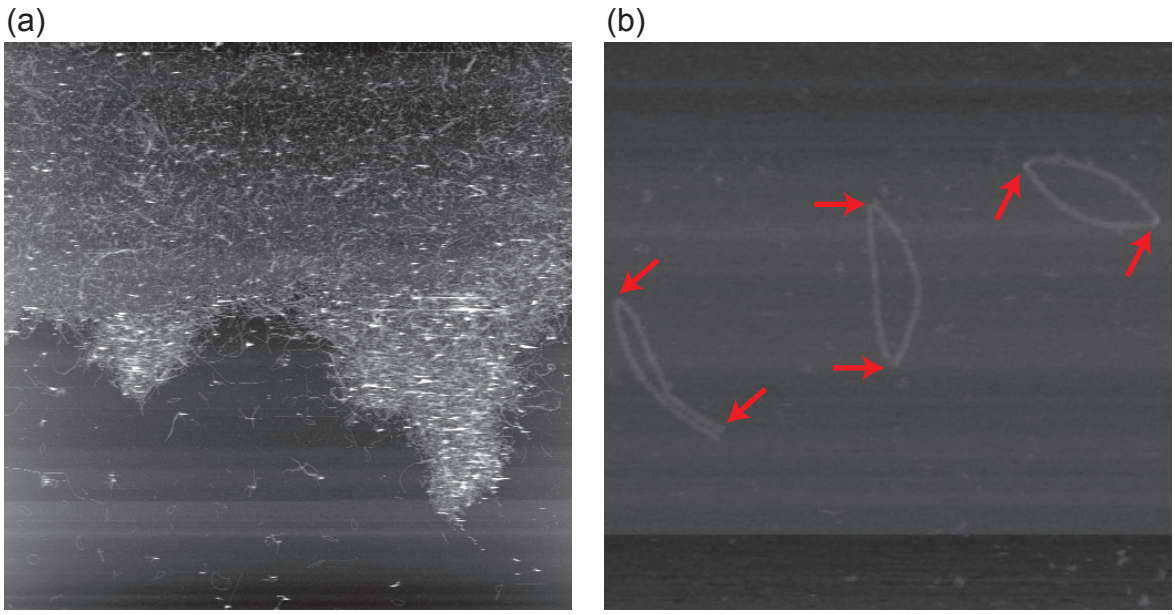

Figure 4.15: AFM Images of DNA Rings folded with "U5-1-Chol", which places one cholesterol molecule per 7 nm at the inner ring perimeter. Arrows in (b) highlight kinks in DNA rings. Scale: 10 μm × 10 μm (a), 1 μm × 1 μm (b)

AFM images of samples prepared with only "U5-1-Chol" are shown in figure 4.15.

The ring shape of samples prepared with "T6-1-Chol" appeared similar. Figure 4.15a shows a dense aggregate with micrometer dimensions. Possibly ring-ring interaction in such aggregates is mediated by cholesterol molecules. Zoom-ins on individual rings (figure 4.15b) revealed that their shape often contained kinks. Contact of two opposing ring sides may be energetically more favorable than a circular shape because it may allow several hydrophobic cholesterol molecules on opposite sites of the ring to interact with each other. Individual rings prepared with both cholesterol modified strands appeared kinked as well.

In summary our experiments show that DNA nano-rings are easily visualizable under solution conditions by STORM and don't take damage from lipid vesicle preparation methods. Our proposed lipid binding strategy *via* cholesterol molecules deforms the ring shape and promotes a certain degree of aggregation in the absence of lipid molecules but leaves the DNA rings itself intact. Future experiments are necessary to proof the ability of cholesterol patterns on DNA rings to tune their interaction with lipid vesicles.

4.5 Conclusion

We have presented several methods for the construction of DNA nanotubes with intrinsic twist, intrinsic curvature and both. Intrinsically twisted tubes were designed by incorporating DNA motifs with distinct melting temperatures in every DNA strand and thereby programming the tube assembly pathway. We showed that tube length decreased with the amount of forced intrinsic twist. A second design of intrinsically twisted tubes yielded tubes with multiples of the intended circumference instead.

Next we applied the principle of targeted insertion and deletion of base pairs to HX-tubes and demonstrated the construction of ring-shaped and writhed DNA nanotubes. We characterized their curvature and torsion by AFM and TEM. We demonstrate that HX-tubes can also adopt writhe shape upon changes of ion concentrations.

Finally we presented the construction of ring-shaped DNA nanotubes with cholesterol "anchors", imaged by STORM and gave an outlook on using this structure for lipid-DNA assemblies.

4.6 Methods

4.6.1 Temperature Controlled UV-Absorbance

6HT at a concentration of 100nM per strand (equivalent to 12.6μM concentration of base pairs) was placed in a cuvette (Starna Cells Inc., 100 μL, 10mm, Quartz Fluorometer Cell, catalog number: 16.100F-Q-10/Z8.5) and covered with 100μL of mineral oil to prevent evaporation. The sample was heated from 20°C to 95°C at a rate of 1°C per minute, left at 95°C for 5 minutes and cooled back to 20°C with -1°C per minute. The sample was illuminated using a high power Xenon light source (Mikropack, Order Number: HPX-2000) and absorbance was measured using a cooled array detector (Ocean Optics, QE65000).

4.6.2 Preparation of HX-ST Tubes with Multi-Tile Design

All DNA sequences were purchased with standard desalting from IDTDNA (sequence list given in appendix C). Strands were mixed at a concentration of 400 nM per strand in 50 μL of 1× TAE with 12 mM $MgCl_2$. Samples were thermally annealed from 80°C to 60°C at a rate of 1°C / min, from 60°C to 40°C at a rate of 1°C / 4 hours and from 40°C to 20°C at a rate of 1°C / min.

4.6.3 STORM

DNA rings were thermally annealed using strands U1-Alexa, U2+1, U3+1, U4, U5-1, T6-1. Sequences are listed in appendix C.3 and C.2. 10μL of annealed DNA rings at a concentration of 140nM per DNA strand were mixed with 2μL of oxygen scavenging system (OSS). OSS contained catalase (0.035 mg/mL), glucose oxidase (0.2 mg/mL), glucose (4.5 mg/mL) and 5% β-mercaptoethanol. 1 μL of sample was placed on a glass slide, covered with a coverslip (#1.5, Fisherbrand) and sealed with epoxy glue. Samples were imaged using a Nikon N-STORM system with an Apo TIRF 100X 1.49 Oil objective, EM-CCD Camera iXon DU897 (Andor), Ti-E TIRF with Perfect Focus System and a 647nm (100mW) Laser (AOTF modulated).

4.6.4 Extrusion of DNA Rings

200 μL solution of annealed DNA rings at a concentration of 100 nM per strand was placed in a syringe of a Avanti Mini-Extruder (Avanti # 610023) with a polycarbonate membrane (0.2μm, 19mm diameter, Avanti #610006). The solution was pressed through the filter 21 times at room temperature.

Chapter 5

DNA Nanotube - Dye Interaction

Many dye molecules are known to interact with DNA. Well known examples include Cy3 and Cy5 dyes, which have been shown to stack on double stranded DNA, similar to an additional base pair when terminally attached [64, 81, 34, 35]. YoYo and ToTo intercalate double stranded DNA [47, 83, 29].

DNA - dye binding can have two effects: 1) it changes the photophysical properties of the fluorophor 2) it deforms the geometry of the DNA molecule. The former plays a crucial role in binding studies *via* measurement of fluorescence lifetime, anisotropy, quantum yield or FRET. The latter is an important factor in the design of DNA nano structures. In this chapter we present approaches to study the interaction of DNA molecules, embedded in stiff DNA nanotubes, with Cy3 molecules.

Because of the micron-scale length and bending stiffness of DNA nanotubes, small bends and twists create large displacements, which can be visualized directly. We show that Cy3 molecules cause HX-tubes to adopt a writhe shape and measure curvature and torsion of these corkscrew-like shapes using electron microscopy (TEM) and fluorescence video microscopy. We find that even though DNA nanotube deformation depends on the attachment position of Cy3 molecules, the fluorescence lifetime of Cy3 does not (sections 5.1, 5.2).

We further study the fluorescence properties of Cy3 bound to DNA nanotubes by fluorescence polarization microscopy (FPM) [4, 39, 38], section 5.3, which is a powerful technique to study the orientation of fluorophor dipoles with respect to a reference structure. Because of the small persistence length of DNA, below the optical resolution limit it has not been possible before to study DNA bound dyes by FPM. We derive relations between dipole angles and FPM intensities and show that our data is consistent with an angle of approximately 60° between the DNA and dipole axis.

The last section contains defocused imaging data of individual Cy3 molecules on HX-tubes. Defocused imaging has been used to determine the 3D angles of randomly distributed Cy5 molecules [72]. We outline how this technique can be extended to determine the angles of individual dipoles with respect to the DNA axis.

5.1 DNA Nanotube Deformation

[1] In the experiments described in chapter 2, nanotubes were labeled on only one of the n strands. This strand, called "U1", was the same in every HX-tube. It had a Cy3 molecule attached to the last of two unpaired T-bases at its 5' end. The remaining 42 bases of its sequence were fully embedded in the tube. A Cy3 molecule thus attached is geometrically constrained to interact within a spherical volume of radius $<$ 1nm that intersects two DNA duplexes and a single stranded cross-over between them.

To test the effect of different numbers and positions of Cy3 molecules we prepared 6HT with Cy3 dyes on all possible subsets of strands 1, 4 and 5. We denote strands with Cy3 attached in subscript. Tubes with four of the seven labeling schemes ($6HT_{\{4\}}$, $6HT_{\{1,4\}}$, $6HT_{\{1,5\}}$ and $6HT_{\{4,5\}}$) had a permanent writhe shape, when imaged using time resolved fluorescence microscopy (FM). Two example images are shown in figure 5.1.

The pitch of the writhe, λ, was measured as illustrated in figure 5.1 b and was the same for all tubes with a specific set of labels but ranged from $\lambda = 0.7$ μm to $\lambda = 2.0$ μm for different labeling positions. Although no writhe was evident in $6HT_{\{1\}}$, $6HT_{\{5\}}$, or $6HT_{\{1,4,5\}}$, the persistence length of $6HT_{\{1,4,5\}}$, 2.7$\pm$0.3 μm, was significantly less than that of $6HT_{\{1\}}$ (3.3$\pm$0.3 μm). It is possible that this reduction in apparent stiffness is an artifact of a permanent writhe with a pitch several times the typical length of the nanotubes surveyed.

In order to understand the origin of the writhe shape we consider that the interaction of Cy3 with the complex architecture of the DNA nanotube can result in a combination of stretch and twist deformation of the DNA within the volume accessible to the Cy3 molecule. DNA stretch and twist deformations are common for other fluorophores [29] and can be expected for Cy3 based on the finding that it can stack like an additional basepair when attached near the blunt end of a DNA duplex [64, 34]. If Cy3 interacts with proximal DNA duplexes so as to stretch them, the entire tube will bend to accommodate the deformation. Similarly, if Cy3 exposed DNA duplexes are twisted, the entire tube will twist to accommodate. The consequence of such persistent bending and twisting is a helical tube axis.

Since $6HT_{\{4\}}$ is writhed but $6HT_{\{1\}}$ and $6HT_{\{5\}}$ are not, the magnitude of Cy3 induced deformation must depend on the local Cy3 environment (*i.e.*, basepair sequence or cross-over induced twist). Consistent with this, a strong dependence of Cy3 on its microenvironment has been observed in fluorescence lifetime, anisotropy and quantum yield studies [81].

We further analyzed the writhe shape of 6HT by TEM (figure 5.2), which revealed that two samples ($6HT_{\{45\}}$ and $6HT_{\{145\}}$) contained circularized tubes with diameters on the order of $\approx$ 100 nm, not visible by fluorescence microscopy. Circularization on this length scale suggests large equilibrium curvature. The shape of 2D confined tubes in TEM images was analyzed quantitatively by measuring the average of distance and curvature

[1] Parts of section 5.1 are reprinted (adapted) with permission from Daniel Schiffels, Tim Liedl, and Deborah K. Fygenson (2013) Nanoscale Structure and Microscale Stiffness of DNA Nanotubes. ACS Nano. Copyright (2013) American Chemical Society.

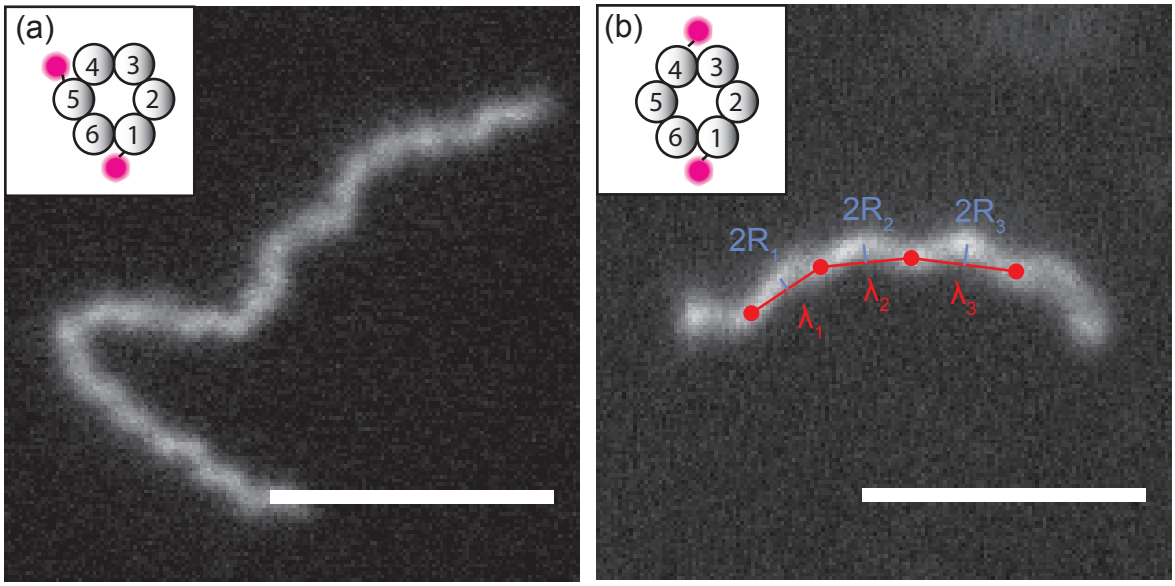

Figure 5.1: Snapshot of a $6HT_{\{1,5\}}$ (a) and $6HT_{\{1,4\}}$ (b) diffusing in a PVP channel. Pitch (λ) and radius (R) measurements are illustrated in (b) and yielded mean and standard deviation of $\lambda = (0.8 \pm 0.1)$ (a) μm and $\lambda = (1.7 \pm 0.3)$ μm (b). Scale bars: 5 μm.

between curvature inversion points, as described in section 4.2.2. Representative images of TEM and fluorescence microscopy of all labeling schemes can be found in appendix F. The measured characteristics are summarized in table 5.1.

Both measurement types show similar trends: $6HT_{\{1\}}$ and $6HT_{\{145\}}$ did not appear writhed. The writhe pitch λ, observed by FM, and the distance between curvature inversion points Λ, observed by TEM was largest for $6HT_{\{14\}}$. Because of the limited resolution, a reliable radius measurement from fluorescence images was only possible for $6HT_{\{14\}}$. In this case, we may calculate tube curvature and torsion using eq. 4.8 and 4.9 which yields $\kappa = 1.4$ μm^{-1} and $\tau = 3.1$ μm^{-1}. The curvature estimate by direct measurement from TEM images was $\kappa = 3.0 \pm 1.0$ μm^{-1}, significantly larger. Two possible reasons for the deviation of the two measurements are deformations of the 3D shape of the DNA nanotube by the narrow PVP channel in fluorescence measurements or deformations of the "squeelix" shape by surface interaction during nanotube adhesion on TEM grids.

As a possible mechanism how Cy3 attachment generates tube curvature and torsion we propose a simple model in which 1) Cy3 molecules can be in two states: unbound, without effect on DNA geometry or bound which causes a specific DNA deformation. 2) The binding probability depends only on the labeling position (the microenvironment of the dye). We then calculate the nanotubes' overall curvature and torsion, as a function of the labeling positions by applying a similar approach as in chapter 4. Each DNA helix consists of identical segments of 21 base pairs (figure 4.10). Each segment of a labeled DNA helix

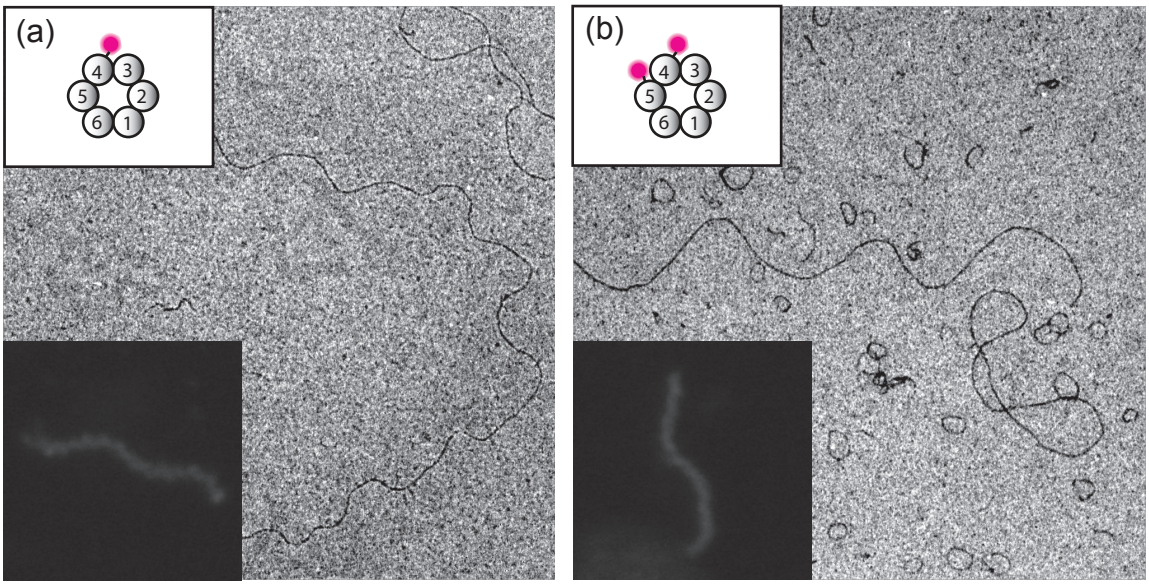

Figure 5.2: TEM images (size 4.8μm x 4.8μm) and fluorescence images (size 10μm x 10μm) of 6HT, labeled with Cy3 at positions indicated in inlets.

contains one Cy3 molecule. To each Cy3 binding position on helix i, we assign a binding probability k_i. Similar to the dependence of tube curvature and torsion on targeted base pair insertion or deletion (eqs. 4.2 to 4.4), we can now calculate τ and κ, averaged over many segments by:

$$\tau = \sum_i k_i \tau_{cy3} \tag{5.1}$$

$$\kappa = \sqrt{\left(\sum_i k_i \cos(2\pi i/n)\kappa_{cy3}\right)^2 + \left(\sum_i k_i \sin(2\pi i/n)\kappa_{cy3}\right)^2} \tag{5.2}$$

where $0 \leq k_i \leq 1$ and τ_{cy3} and κ_{cy3} are curvature and torsion of Cy3 deformed tube segments.

We compare eq. 5.2 to the TEM based curvature measurements listed in table 5.1. Since the curvature observed for $6HT_{\{4\}}$ and $6HT_{\{5\}}$ is of comparable magnitude as that, observed for tubes with an inserted base pair (section 4.2.2), the helix elongation by Cy3 is likely be on the length scale of a base pair or possibly even larger, if the binding rates k_4 or k_5 are less than one. However, the different radius of the squeelices in TEM images suggests that Cy3 induces a different torsion than inserted base pairs. Because $6HT_{\{14\}}$ and $6HT_{\{15\}}$ have smaller curvature than $6HT_{\{4\}}$ and $6HT_{\{5\}}$ it appears that the Cy3 molecules at position 1 do have some interaction with the DNA nanotube as well, which counteracts Cy3 binding at position 4 and 5. Consistent with our model, the curvature of $6HT_{\{45\}}$, where both binding sites are adjacent to each is largest.

Table 5.1: Writhe characteristics of 6HT of different Cy3 labeling schemes. λ (F), R (F) and N(F) are pitch and radius, determined from N(F) fluorescence microscopy measurements. Λ (TEM) and L (TEM) are average distance and contour length between curvature inversion points in 2D confined squeelices, obtained from TEM images. κ(TEM) is obtained from direct curvature measurements at curvature inversion points

	$6HT_{\{4\}}$	$6HT_{\{5\}}$	$6HT_{\{14\}}$	$6HT_{\{15\}}$	$6HT_{\{45\}}$
λ (F) / nm	675 ± 51		1724 ± 251	775 ± 88	785 ± 112
R (F) / nm			113 ± 45		
N (F)	13		44	13	5
Λ (TEM) / nm	332 ± 100	331 ± 100	430 ± 162	293 ± 93	302 ± 76
L (TEM) / nm	410 ± 126	384 ± 123	467 ± 213	328 ± 117	366 ± 97
κ / μm^{-1}	6.3 ± 2.0	6.4 ± 2.3	3.0 ± 1.0	4.8 ± 1.5	7.6 ± 3.2
N (TEM)	61	7	22	64	21

5.2 Fluorescence Lifetime

In the previous section we found that DNA deformation by Cy3 depends on the attachment position of Cy3. This prompted us to ask whether the photo physical properties of Cy3, in particular its fluorescence lifetime, correlates with DNA nanotube deformation. The fluorescence decay τ_L of Cy3 has been shown to be mono-exponential with $\tau_L = 0.18$ ns in the absence of DNA, and bi-exponential with $\tau_{L,1}$ =0.18 ns and $\tau_{L,2}$ =2.0 ns when attached to the 5' end of single stranded DNA [81]. The fraction, k_i, of bound Cy3 molecules at binding position i may thus determine the relative weight of fluorescence decays with $\tau_{L,1}$ and $\tau_{L,2}$. To look for such a correlation, we measured the fluorescence lifetime of $6HT_{\{1\}}$, $6HT_{\{4\}}$ and $6HT_{\{5\}}$.

The result is shown in figure 5.3. The fluorescence decay is mono-exponential in all cases. The mean and standard deviation of the lifetime measurements is τ_L = 2.3 ns ± 0.1 ns. Thus we find no correlation between fluorescence lifetime and DNA nanotube deformations.

The absence of the fast fluorescence decay component, characteristic of free Cy3 shows that the fluorescence mechanism of all Cy3 molecules is affected by the presence of the DNA nanotube. The mono-exponential decay shows that either all Cy3-DNA complexes have the same fluorescence lifetimes or that there is only one binding mode. Thus the above assumption of a bimodal binding behavior to explain the observed DNA nanotube deformation by Cy3 attachment is not supported in fluorescence lifetime measurements.

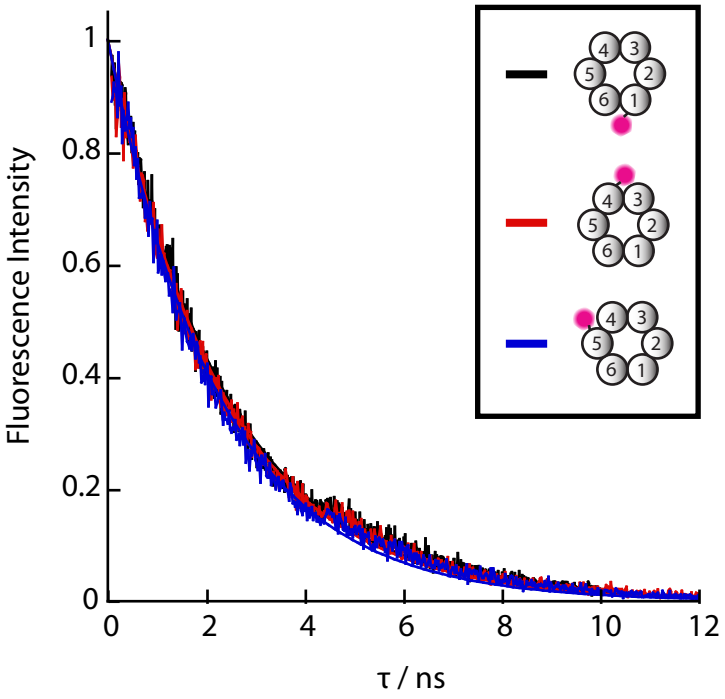

Figure 5.3: Time resolved fluorescence decay of $6HT_{\{1\}}$ (black), $6HT_{\{4\}}$ (red) and $6HT_{\{5\}}$ (blue). Mean and standard deviation of fluorescence lifetimes are τ_L =2.3 ns ± 0.1 ns.

5.3 Fluorescence Polarization Microscopy

We used fluorescence polarization microscopy (FPM) to further study the optical properties of Cy3 molecules, bound to HX-tubes. While a fluorescence microscopy (FM) image is a two dimensional intensity map $I(x, y)$, which contains information about the distribution of dye molecules in a sample, FPM data consists of two intensity maps $I_x(x, y)$ and $I_y(x, y)$, which are obtained by collecting light of perpendicular polarizations. In addition to spatial distribution, FPM can yield information about the rotational distribution of dye molecules. This is because fluorescing fluorophors behave like radiating dipoles [94].

As illustrated in figure 5.4 a, when a sample is illuminated with unpolarized light along the optical (z-) axis, dipoles in the xy-plane have the highest probability of excitation, whereas dipoles aligned with the z-axis the lowest. A dipole that has been excited emits light, predominantly polarized parallel to its dipole axis. Thus the polarization components of the emission light, which are measured independently, depend on the distribution of dipole orientations in the sample. The goal of FPM is to measure the intensities through x- and y- emission polarizers, I_x and I_y, at each point of the image and determine the orientation of fluorophor dipoles, from which these intensities originate.

In this experiment we measure the angle between the axis of a DNA nanotube and the axis of dipoles of Cy3 molecules, attached to the nanotube, α. This angle, α, is defined in

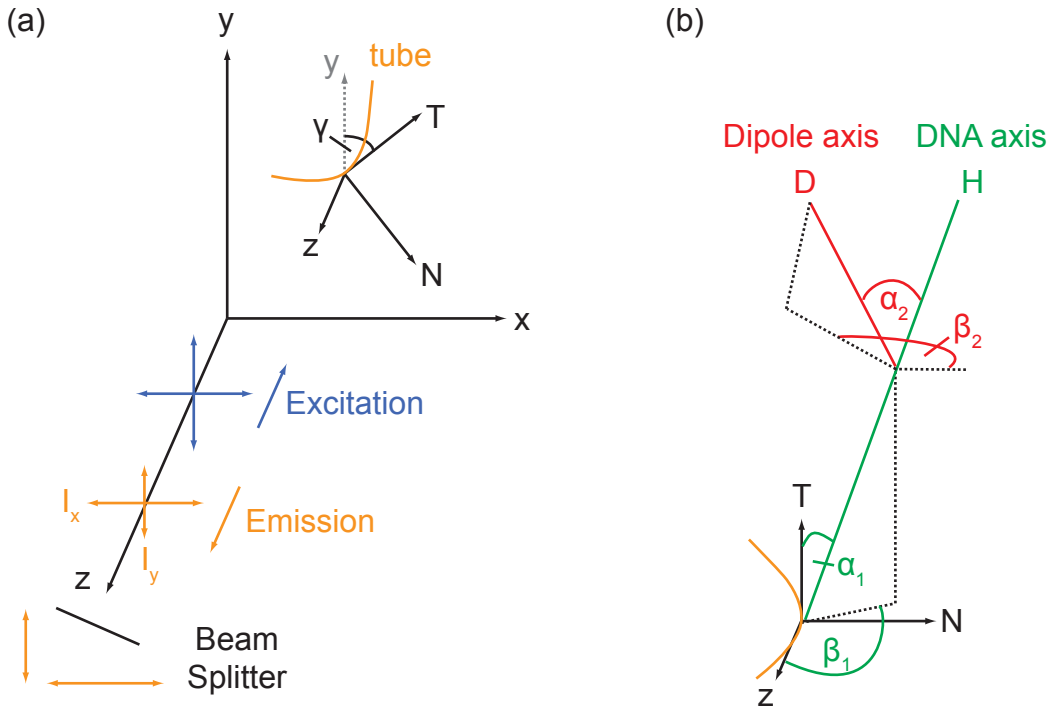

Figure 5.4: FPM setup. (a) lab fixed system (x,y,z) and tube-fixed system (T,N,z) are rotated by the angle γ about the z-axis with respect to each other. (b) Definition of angles between the axis of DNA nanotube (T), DNA (H) and dipole (D).

a tube-fixed coordinate system (T,N,z), rotated with respect to (x,y,z) about the z axis, such that the T-axis is everywhere parallel to the tube axis (figure 5.4a. α is related to the physically and biologically interesting angles α_2 and β_2, which are the polar and azimuthal angles of the dipole axis, bound to double stranded DNA, as well as α_1 and β_1, which describe the orientation of the DNA helices with respect to the nanotube axis (figure 5.4 b):

$$\alpha = \alpha_1 + \alpha_2 cos(\beta_2) \tag{5.3}$$
$$\beta = \beta_1 + \beta_2 sin(\alpha_2) \tag{5.4}$$

A beam splitter in the emission light path creates a spatial offset between the intensity maps I_x and I_y and thus each DNA nanotube creates two images in the camera. The emission intensities I_x and I_y are measured independently as shown in figure 5.5. In figure 5.5 a, it can clearly be seen that I_x and I_y depend on the orientation of a tube segment (γ). Since anisotropy experiments with randomly oriented dipoles and unpolarized excitation

light yield $I_x = I_y$, this shows that the dipole axis of Cy3 molecules is strongly ordered on DNA nanotubes.

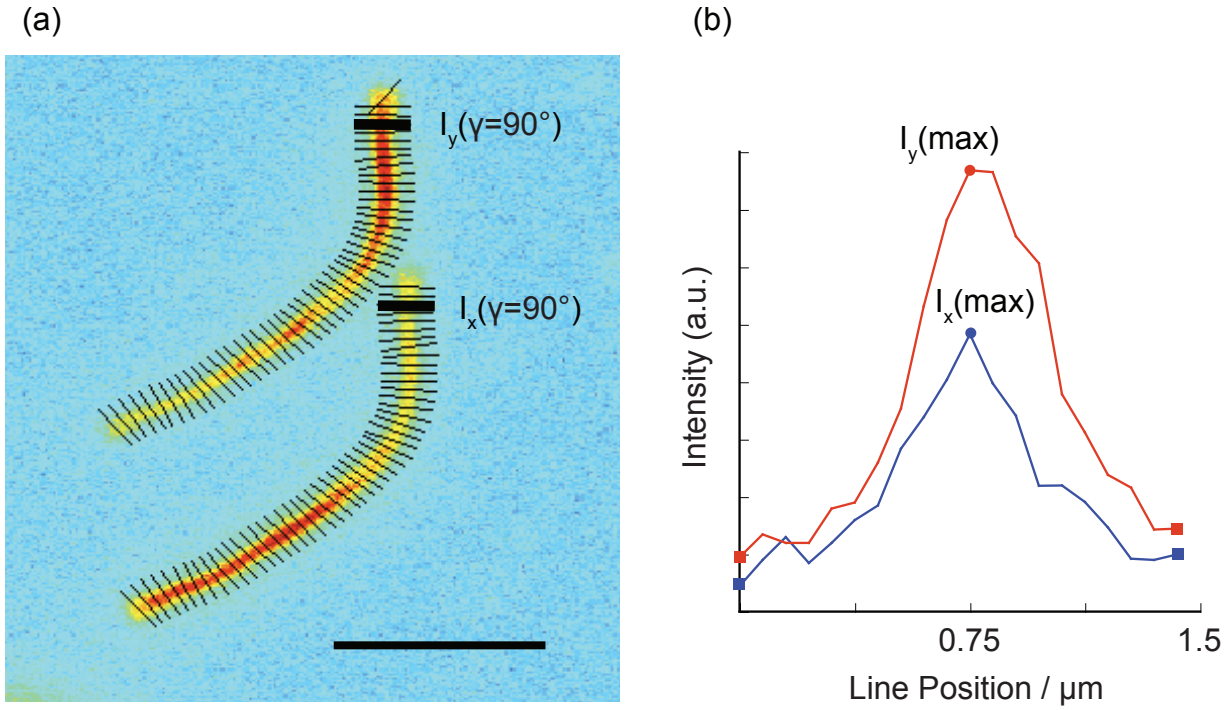

Figure 5.5: (a) FPM image of a Cy3 labeled DNA nanoutbe, over imposed with lines, used to obtain intensity line profiles. Scale bar: 5μm. (b) Intensity line profiles of highlighted tube segments in (a). Maximum and edge intensities are highlighted with a circle and squares respectively.

For quantitative analysis, the tube contour with intensity I_x was traced, as described in chapter 9 and divided into 4 pixel (≈ 0.256 μm) long segments. The same trace was super-imposed to the tube contour with intensity I_y by translating the trace by a beam-splitter defined distance. The intensity of each trace segment was obtained by taking the maximum pixel value minus the average of the edge pixel values of a 4 pixel wide line profile, perpendicular to the tube axis (figure 5.4 b). The orientation of each trace segment (γ) was saved, along with I_x and I_y. Based on their length, each trace segment contains 36 repeat units of the DNA nanotube and thus 36 Cy3 molecules per strand with Cy3 attachment.

We will now derive the relationship between DNA nanotube - dipole axis angle, α, and the intensities I_x, I_y. Therefore we express the directions of the dipole $\vec{D}$, as well as unit vectors $\vec{x}$, $\vec{y}$ and $\vec{z}$ in the (T,N,z) system:

$$\vec{D} = \begin{pmatrix} \cos(\alpha) \\ \sin(\alpha)\sin(\beta) \\ \sin(\alpha)\cos(\beta) \end{pmatrix}, \ \vec{x} = \begin{pmatrix} \sin(\gamma) \\ \cos(\gamma) \\ 0 \end{pmatrix}, \ \vec{y} = \begin{pmatrix} \cos(\gamma) \\ -\sin(\gamma) \\ 0 \end{pmatrix}, \ \vec{z} = \begin{pmatrix} 0 \\ 0 \\ 1 \end{pmatrix}$$

The components of $\vec{D}$ In the (x,y,z) system are given by:

$$\begin{aligned} D_x &= \vec{D} \cdot \vec{x} = \cos(\alpha)\sin(\gamma) + \sin(\alpha)\sin(\beta)\cos(\gamma) && (5.5) \\ D_y &= \vec{D} \cdot \vec{y} = \cos(\alpha)\cos(\gamma) - \sin(\alpha)\sin(\beta)\sin(\gamma) && (5.6) \\ D_z &= \vec{D} \cdot \vec{z} = \sin(\alpha)\cos(\beta) && (5.7) \end{aligned}$$

To understand how dipole orientation affects the measured polarization intensities, we first solve a simplified problem in which changes of polarization intensities due to transmission through optical components of high numerical aperture are ignored. With this simplification, the excitation probability of a dipole, P_{ex} illuminated with unpolarized light, propagating along the z-axis is proportional to the square of the angle between dipole and x-y plane:

$$\begin{aligned} P_{ex} &\sim D_x^2 + D_y^2 && (5.8) \\ &= (\sin(\alpha)\sin(\beta))^2 + (\cos(\alpha))^2 && (5.9) \end{aligned}$$

Because of the emission characteristics of a dipole, the intensity observed through a polarizer is proportional to the square of the projection of the dipole axis onto the polarizer transmission axis:

$$P_{em,i} \sim D_i^2 \tag{5.10}$$

where i can be x or y for respective polarizer orientations. The intensities F_x and F_y [2] of a tube segment, can than be obtained by:

$$\begin{aligned} F_x(\alpha,\gamma) &\sim \int_0^{2\pi} P_{ex} P_{em,x} d\beta && (5.11) \\ &= 2\pi\cos^4(\alpha)\sin^2(\gamma) + \frac{3}{4}\pi\sin^4(\alpha)\cos^2(\gamma) + \pi\sin^2(\alpha)\cos^2(\alpha) && (5.12) \\ F_y(\alpha,\gamma) &\sim \int_0^{2\pi} P_{ex} P_{em,y} d\beta && (5.13) \\ &= 2\pi\cos^4(\alpha)\cos^2(\gamma) + \frac{3}{4}\pi\sin^4(\alpha)\sin^2(\gamma) + \pi\sin^2(\alpha)\cos^2(\alpha) && (5.14) \\ F_z(\alpha,\gamma) &= \int_0^{2\pi} P_{ex} P_{em,z} d\beta && (5.15) \\ &= \frac{1}{4}\pi\sin^4(\alpha) + 2\pi\sin^2(\alpha)\cos^2(\alpha) && (5.16) \end{aligned}$$

[2] We denote the measured intensities F_x and F_y in a setup without high numerical aperture elements and I_x and I_y in a setup with high numerical aperture elements to avoid confusion.

where it was assumed that the angle α is the same for all dipoles. We may integrate over β, because each trace segment contains 36 (for single labeled) or 108 (for triple labeled) Cy3 molecules based on their length. Because of the low twist persistence length of HX-tubes and intrinsic super twist, the azimuthal angle β is randomized over distances smaller than the trace segment.

To account for optics with high numerical aperture in our setup, we must consider a mixing of the polarization components. Upon passing through high-NA optics, the excitation light gains a z- component, because it is focused on the sample at an angle with the optical axis between 0° and σ. The angle σ is related to the numerical aperture (NA) of the objective by:

$$NA = n \sin(\sigma) \tag{5.17}$$

Thus, even dipoles oriented perfectly normal to the x-y plane can be excited.

Light, emitted from an excited dipole, with polarization components D_i has x and y polarization components I_x and I_y after passing through the optics [4]:

$$I_x \sim K_a D_z^2 + K_b D_y^2 + K_c D_x^2 \tag{5.18}$$
$$I_y \sim K_a D_z^2 + K_c D_y^2 + K_b D_x^2 \tag{5.19}$$

where the weighting factors K_a, K_b and K_c are given by:

$$K_a = (1/3)(2 - 3\cos\sigma + \cos^3\sigma) \tag{5.20}$$
$$K_b = (1/12)(1 - 3\cos\sigma + 3\cos^2\sigma - \cos^3\sigma) \tag{5.21}$$
$$K_c = (1/4)(5 - 3\cos\sigma - \cos^2\sigma + \cos^3\sigma). \tag{5.22}$$

In what follows we only consider the correction to the emission polarizations, as in previous works with FPM [4, 39, 38].

The (high NA corrected) intensity difference between y- and x- polarized light of a tube segment, normalized by its total intensity can then be calculated as:

$$r = \frac{(K_a F_z^2 + K_c F_y^2 + K_b F_x^2) - (K_a F_z^2 + K_b F_y^2 + K_c F_x^2)}{(K_a F_z^2 + K_c F_y^2 + K_b F_x^2) + (K_a F_z^2 + K_b F_y^2 + K_c F_x^2)} \tag{5.23}$$

Eq. 5.23 is plotted as a function of γ and α in figure 5.6. We will refer to r as the anisotropy of a trace segment. The anisotropy has a maximum, when tube axis and dipole axis are aligned with the y-axis ($\gamma = 0°$, $\alpha = 0°$). Another smaller maximum appears for alignment of tube axis with the x-axis and dipoles with the y-axis ($\gamma = 90°$, $\alpha = 90°$).

We used the relation between dipole orientation and anisotropy given by eq.5.23 to study the alignment of Cy3 dipoles to 9HT, attached at three different DNA strands. [3] 9HT were chosen because of their high stiffness, which allows accurate determination of tangents to the DNA nanotube contour. The measured anisotropy, r, of $9HT_{\{1\}}$ and $9HT_{\{4\}}$ is plotted in figure 5.7 a as function of γ. Comparison to figure 5.6 shows that,

[3] Cy3 attachment positions were at strands 1, 4 and 5. HX-tubes, with Cy3 attachment at strand x are denoted as $9HT_{\{x\}}$

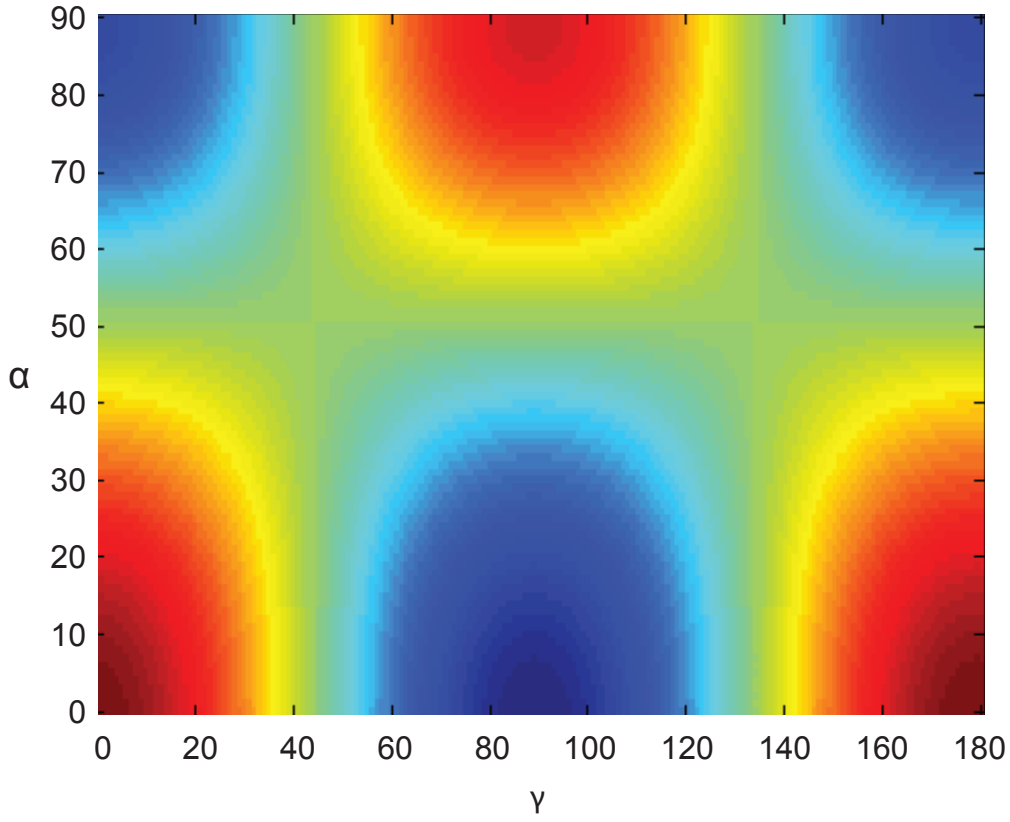

Figure 5.6: Plot of the tube segment anisotropy r (eq. 5.23) as function of γ and α. r-values range from -1 (dark blue) to +1 (dark red).

because the data peaks at $\gamma = 90°$, Cy3 molecules must have an alignment of $\alpha > 55°$. A curve fit of eq. 5.23 yields $\alpha = 64°$ and $\alpha = 62°$ respectively. $9HT_{\{5\}}$ (not shown for clarity) anisotropy was best fit with $\alpha = 64°$. Thus, like the fluorescence lifetime data, the anisotropy does not indicate a dependence of DNA-Cy3 interaction on the attachment position on the DNA nanotube.

To further test the hypothesis of microenvironment dependent Cy3-DNA interaction, we prepared a modified version of 9HT, in which the DNA architecture around one binding site (on strand 1) was severely altered. In this version, called 9HT-NST, two motifs of strand T9 were interchanged. This places the Cy3 molecules, attached to strand 1 in proximity to two strand cross-overs and a fully disrupted DNA helix, as shown in figure 5.7 b. The modified strand set formed micrometer length DNA nanotubes. FPM data of $9HT\text{-}NST_{\{4\}}$ / $9HT\text{-}NST_{\{5\}}$ yielded similar Cy3 angles α as $9HT_{\{4\}}$ / $9HT_{\{5\}}$. However the anisotropy of $9HT\text{-}NST_{\{1\}}$ was narrowly distributed around zero with almost no detectable dependence on γ, characteristic for randomly oriented dipole axis. Thus Cy3 alignment at the modified binding site was significantly different.

We further measured the peak anisotropy of $9HT_{\{145\}}$, which was slightly smaller than for single labeled tubes, yielding a best fit for $\alpha = 60°$. The small difference to single

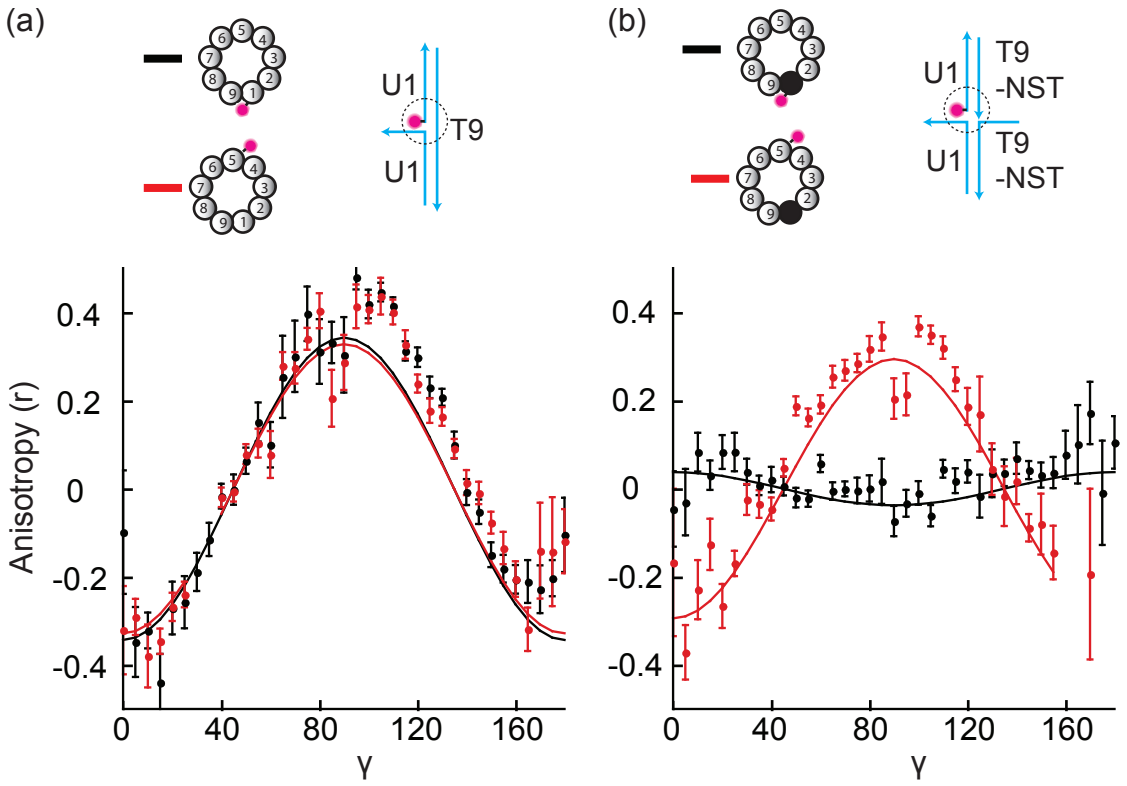

Figure 5.7: FPM data of 9HT (a) and 9HT-NST (b) with Cy3 at different labeling positions. Strand sketches illustrate the Cy3 microenvironment attached to strand 1.

labeled tubes may arise from deformations of the DNA nanotube itself, caused by the high labeling density. Next, we investigated if tube circumference affected anisotropy, using triple labeled tubes ($n\text{HT}_{\{145\}}$) to obtain a good signal to noise ratio. Fits of eq. 5.23 to the anisotropy of $n\text{HT}_{\{145\}}$ showed that α increased with increasing tube diameter from 57° ($6\text{HT}_{\{145\}}$) to 61° ($10\text{HT}_{\{145\}}$).

Besides interacting with DNA, we considered that Cy3 orientation might be affected by the presence of a substrate (coverslip). To test this hypothesis we compared the previously described anisotropy data of $9\text{HT}_{\{145\}}$ to data, obtained from $9\text{HT}_{\{145\}}$, freely diffusing in a PVP coated chamber. Two individual tubes, imaged over more than 100 frames yielded $\alpha = 62.1°$ and $\alpha = 61.6°$, close to the value observed on glass. Thus we conclude that either the glass coverslip does not interact with the Cy3 molecules on DNA nanotubes or that any such interaction does not alter the Cy3 dipole orientation with respect to the tube axis.

5.4 Defocused Imaging

DNA nanotube deformations (section 5.1), fluorescence lifetime (section 5.2) and anisotropy measurements (section 5.3) contain bulk information, averaged over many dye-DNA interactions. However characteristics such as the distribution of dipole binding angles α and β can only be obtained by single molecule measurements. One approach to measure α and β of individual dipoles is defocused imaging. It has been shown that the diffraction pattern of single, defocused Cy5 molecules can be mapped to the 3D orientation of their dipole axis [72].

We explored the applicability of this technique to dye molecules, bound to DNA nanotubes. To enable imaging of individual diffraction patterns of size $\approx 2\mu$m, 10HT were prepared with a ratio of 1:50 of Cy3-labeled to unlabeled strands "U1", dissolved in PVA solution and spin coated onto a coverslip (see methods section 5.7.2). Figure 5.8 a shows an image of the resulting nanotubes, decorated with individually resolvable Cy3 molecules. Because of the high bending stiffness of 10HT, the contour of the nanotubes can be estimated by drawing a segmented line through the observed points.

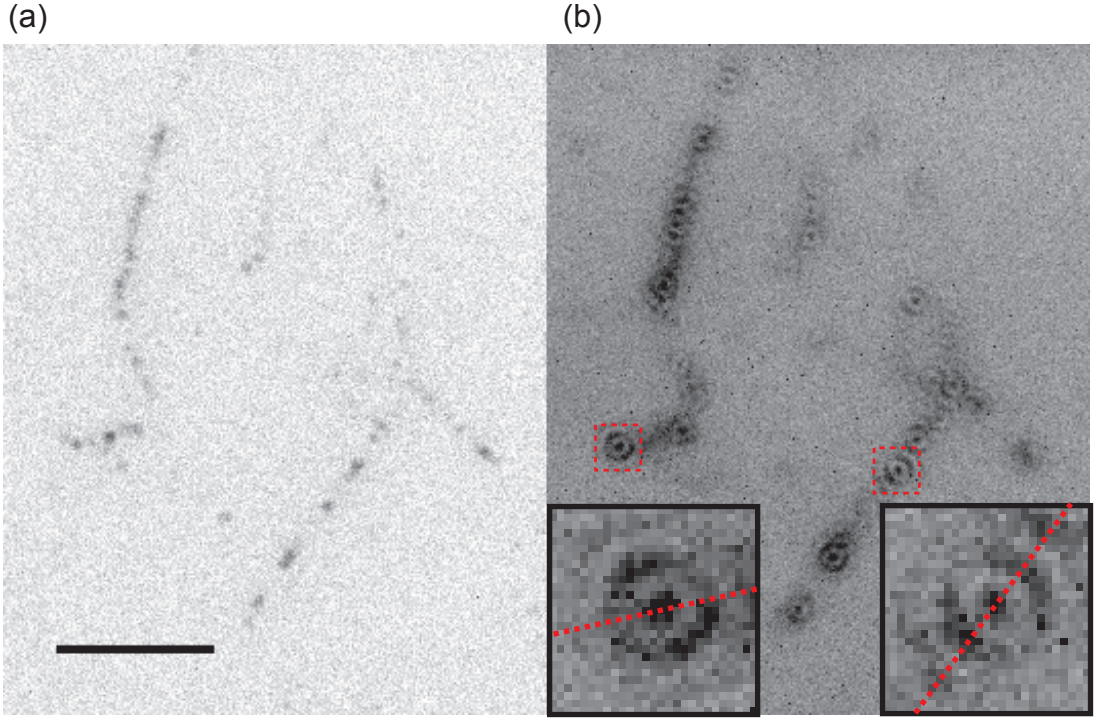

Figure 5.8: Inverted fluorescence microscopy images of 10HT folded with a 1:50 ratio of Cy3 labeled to unlabeled U1 strands. (a) focused fluorescence image. (b) defocused fluorescence image. Inlets shows magnification of highlighted areas. Dashed lines show the axis of the DNA nanotube. Scale bar: 5 μm

The distance between sample and objective was lowered by $\approx 1\mu$m and a second image

with 30 s exposure time was obtained (figure 5.8 b). In this defocused image each individual emitter created a diffraction pattern in the camera image. Comparison of the two magnified dipole diffraction patterns shows that the intensity distribution is not identical for all dipoles: the peak intensity of the first maximum intersect the tube axis in the right image and the normal to the tube axis in the left image.

Note that different diffraction pattern shapes with respect to the nanotube axis are expected even if all Cy3 dipoles are aligned at fixed angles, α, with respect to the DNA. This is because the nanotube itself has torsional stiffness of less than 1 μm (chapter 2) and thus adjacent diffraction patterns originate from dipoles with different azimuthal angles, β. A quantitative mapping of the diffraction pattern to α and β in future experiments will require calibration of the defocus distance as well as a measurement of the thickness of the PVA layer.

5.5 Outlook: Determination of Helicity

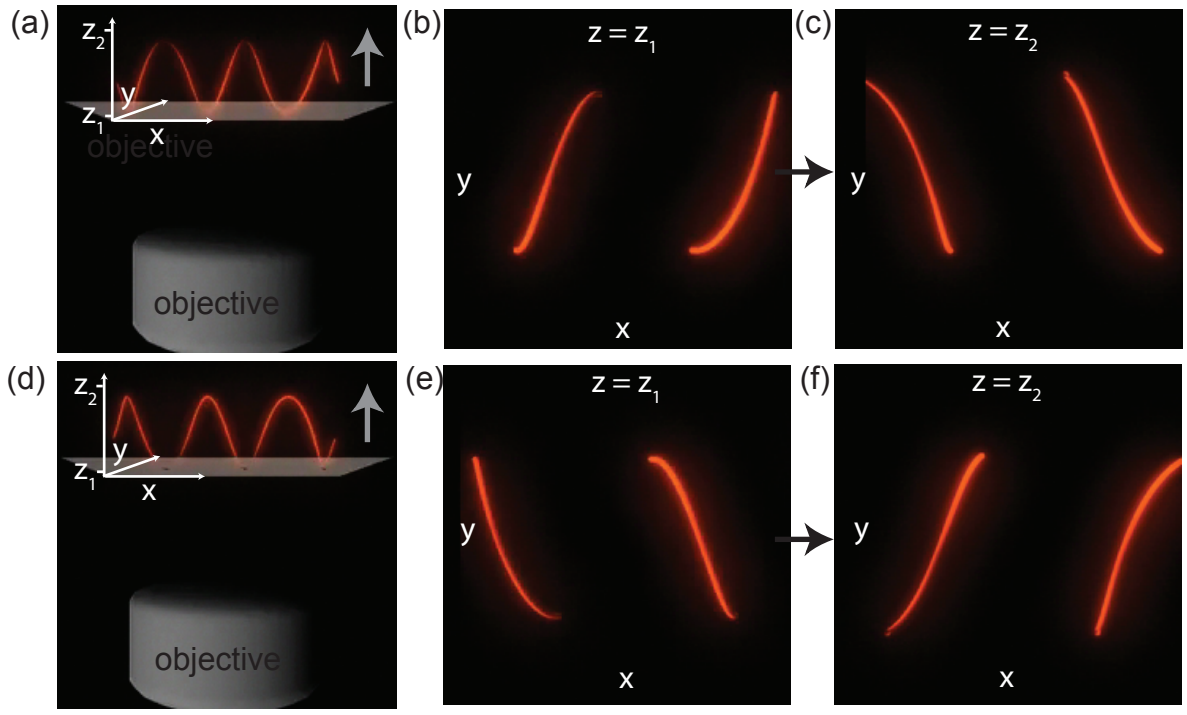

Figure 5.9: Scheme for determination of handedness from "tomographic" image slices of right-handed (a) - (c) and (d) - (f) left-handed polymers. Movement of the objective towards the sample yields distinct sets of images, depending on the helicity of the object.

To better understand HX-tube deformations caused by Cy3 attachment (section 5.1) or ion exchange (section 4.3) we propose to measure the handedness of the writhed contours

by fluorescence microscopy in future experiments. The information about handedness is lost in microscopy images, which only yield a 2D projection of the 3D shape of an object.

We propose to obtain "tomographic" slices at different "z-heights" as illustrated in figure 5.9. The method relies on using a high numerical aperture objective with narrow focal width. The focal plane is first set to $z = z_1$ and then slowly moved through the sample volume to $z = z_2$. Left- and right- handed contours yield distinct sets of images during this process as illustrated in figure 5.9 b,c and e,f.

5.6 Conclusion

We have presented different approaches to study DNA nanotube - dye interaction 1) by measuring DNA nanotube deformation (section 5.1) and 2) by measuring the photo physical properties of DNA bound dyes (sections 5.2 to 5.4).

We found that attachment of Cy3 molecules caused DNA nanotubes to adopt a writhe shape with pitch and radius dependent on the attachment position and proposed a simple model for Cy3-DNA interaction. In contrast to nanotube deformation, fluorescence lifetime and anisotropy of Cy3 did not have a significant dependence on the labeling position on HX-tubes.

The anisotropy of Cy3 on HX-tubes, measured by FPM was consistent with an angle of $\alpha = 60° \pm 4°$ between dipole and tube axis in all measurements. When the tube lattice was disturbed in proximity of a Cy3 attachment position by alignment of two backbone nicks and strand-cross-overs, the anisotropy was close to zero, characteristic for randomly oriented dipoles.

Our measurements established that the use of stiff DNA nanotubes makes fluorescence polarization microscopy (FPM) a viable technique to study DNA-dye interactions. The setup and theory established in this chapter can easily be applied to a wide variety of fluorophors, both intercalating and covalently attached to DNA. Defocused imaging is a promising complement to FPM studies by providing the full distribution of dipole angles.

5.7 Methods

5.7.1 Fluorescence Polarization Microscopy

The fluorescence polarization microscopy (FPM) setup was identical to the fluorescence microscopy setup, described in chapter 2, except for a Sénarmont prism, placed in front of the camera.

5.7.2 PVA Spin Coating

1 μL of DNA nanotubes (1.4μM per strand) were mixed with 99 μL of 1× TAE buffer with 12mM Magnesium Acetate and 5mg / mL Polyvinyl alcohol (PVA). This mixture was spin-cast onto a bare glass coverslip at 1700 rpm for 1 min to create a PVA film.

5.7.3 Fluorescence Lifetime Measurements

Luminescence life-time measurements were performed using Time-Correlated Single Photon Counting (TCSPC) [7]. Approximately 200 femtosecond (fs) excitation pulses with wavelength 360 nm were generated by doubling the fundamental frequency of the femtosecond pulses from a Ti:Sapphire laser (Coherent Mira 900) using a commercial optical harmonic generator (Inrad). The laser repetition rate was reduced to 2 MHz by a home-made acousto-optical pulse picker in order to avoid saturation of the chromophore. The TCSPC system was equipped with an ultrafast microchannel plate photomultiplier tube detector (Hamamatsu R3809U-51) and electronics board (Becker & Hickl SPC-630) and had an instrument response time of about 60-65 picoseconds. The triggering signal for the TCSPC board was generated by sending a small fraction of the laser beam onto a fast (400 MHz bandwidth) Si photodiode (Thorlabs Inc.). The fluorescence signal was dispersed in an Acton Research SPC-500 monochromator after passing through a pump blocking, long wavelength-pass, autofluorescence-free, interference filter (Omega Filters, ALP series). The monochromator is equipped with a CCD camera (Roper Scientific PIXIS-400) which monitored of the time-averaged fluorescence spectrum. Luminescence transients were not deconvolved with the instrument response function since their characteristic time-constants were much longer than the width of the system response to the excitation pulse.

Chapter 6

Few-Atom Fluorescent Silver Cluster Assembly on DNA Nanotubes

6.1 Introduction

DNA oligomers have been shown to stabilize few-atom silver clusters (Ag-DNAs) [73, 30, 87] with remarkable fluorescent properties [65, 63]. The assembly process of Ag-DNAs is illustrated in figure 6.1a. A DNA hairpin, or single stranded DNA, is mixed with silver ions and reduced by $NaBH_4$, resulting in few-atom clusters, stabilized by the single stranded DNA bases. A given sequence can host different species of Ag-clusters and only a subset of the stabilized Ag-DNAs has fluorescent properties. Typical cluster sizes range from 10 - 20 atoms [88].

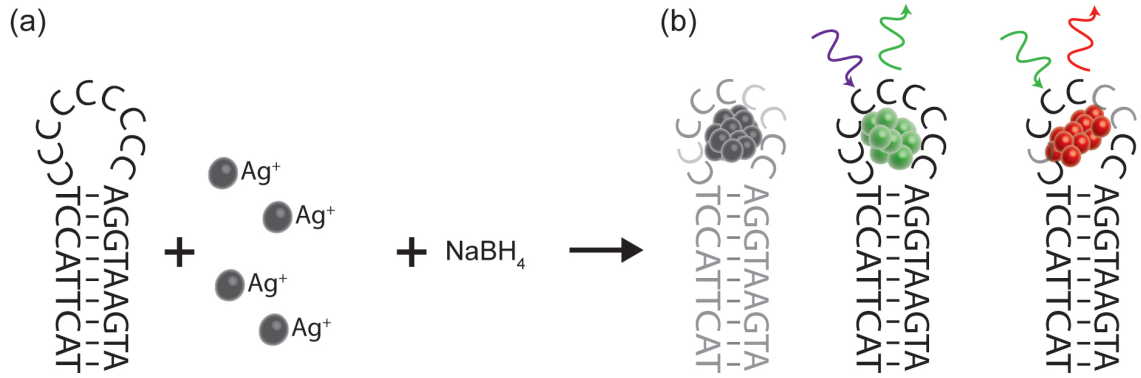

Figure 6.1: Illustration of Ag-DNA cluster assembly. (a) DNA hairpin with 9 base-pair stem and 9 single-stranded cytosine bases is mixed with silver ions and reduced with $NaBOH_4$. (b) The resulting solution contains several Ag-DNA species with no (grey), red or green fluorescent properties.

It has been shown that some fraction of the Ag atoms in Ag-DNAs are in an ionic state while the remaining atoms are neutral. It has been proposed that the neutral Ag atoms

nucleate in a linear framework along the DNA template and the length of the resulting free electron system governs the optical properties [86].

Unlike other metal ions silver preferentially binds to the DNA bases rather than the DNA backbone [10] making the formation of Ag-clusters specific to the DNA host: cluster size, charge and fluorescent properties depend on the DNA sequence [87, 88]. The control over fluorescent properties across the entire visible spectrum by DNA sequence, combined with the ability to naturally incorporate Ag-DNAs into structural DNA assemblies such as DNA origami makes them highly promising for the construction of complex, nanoscale optical breadboards.

In this chapter we use a DNA hairpin ("9C hairpin"), which has previously been shown to host two fluorescent species with 11 and 13 Ag atoms, exhibiting fluorescence in the green and red respectively [69]. We demonstrate that fluorescent silver clusters can be directly synthesized on DNA nanotubes with "9C hairpin" extrusions and that Ag-DNAs on DNA nanotubes exhibit nearly the same fluorescent properties as Ag-DNAs free in solution. [1] We further outline experiments towards the assembly of previously synthesized and purified Ag-DNAs on DNA nanostructures to further improve the control and yield over positioning of fluorescent clusters.

6.2 Results and Discussion

To template the formation of Ag-DNA with a high surface density we used a modified version of DNA nanotube, based on "DX-tiles" [77]. Figure 6.2 shows a schematic of the tube design, adapted from ref [77]. Each tube consists of a cylindrical lattice of identical tiles comprised of five different DNA strands, numbered 1 to 5. Each tile consists of a pair of parallel double helices joined at two points where one strand from each helix crosses over to the adjacent helix. Single-stranded overhangs of five unpaired bases at each corner of the tile direct tile-tile interactions. Extensive characterization by atomic force and fluorescence microscopy has shown that such double-crossover or DX tiles assemble into hollow tubes roughly 10 nm in diameter [77], with exponential length distributions yielding many tubes 10 μm or longer [25].

As originally designed, the nanotube lattice is completely double-stranded, save for unpaired overhangs at the tube ends. Fluorescent Ag clusters, on the other hand, preferentially form on single-stranded DNA [30]. We therefore used a modified version of strand no. 1 (see table C.1) to incorporate a DNA hairpin into the nanotube lattice, as previously described [77]. The modification we used orients hairpins radially outward from the tube surface. We changed the sequence in the single-stranded loop region from four adenines to nine cytosines, because earlier work indicates that poly dC are better than poly dA at

[1] Partes of chapter 6 are reprinted (adapted) with permission from ONeill, P. R., Young, K., Schiffels, D., & Fygenson, D. K. Few-Atom Fluorescent Silver Clusters Assemble at Programmed Sites on DNA Nanotubes. Nano letters 12, 5464-5469 (2012) [68]. Copyright (2013) American Chemical Society. Fluorescence microscopy experiments were preformed by P.O., K.Y. and D.S. and supervised by D.K.F. Experimental design and manuscript was done by P.O., D.S. and supervised by D.K.F.

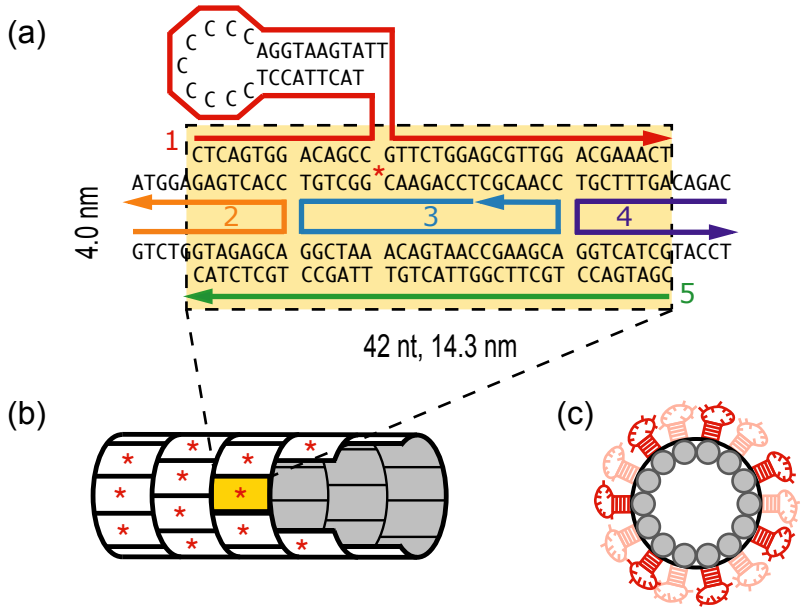

Figure 6.2: Schematic of DNA nanotube with hairpin protrusions. (a) Tile, arrows point to the 3' end. The hairpin region of strand no. 1 was omitted to create bare tubes. (b) tube, tiles, with hairpins represented by red asterisks. (c) axial view showing outward orientation of the hairpins.

templating the formation of fluorescent silver clusters.[30, 69]

DNA tubes were assembled with or without hairpins, referred to herein as hairpin tubes and bare tubes, respectively. Strands no. 2-5 were identical for both types of tubes. Hairpin tubes used the modified version of strand no. 1 described above, and bare tubes used the original version of strand no. 1 without the hairpin. The preparation of DNA nanotubes and Ag-clusters is described in section 6.4.

To examine the effect of Ag^+ on DNA tubes, prior to reduction of the silver to form fluorescent clusters, hairpin tubes and bare tubes were imaged before and after the addition of $AgNO_3$ (figure 6.3). The 3' end of strand no. 3 in these tubes was covalently attached to a fluorescein derivative (FAM) by the manufacturer (IDT DNA). Initially well-dispersed hairpin tubes aggregated into large tangles in the presence of Ag^+. Bare tubes, on the other hand, remained well-dispersed. Ag^+ ions can mediate non-Watson-Crick base pairing [95] and are reported to link cytosine homopolymers through cytosine-Ag^+-cytosine interactions. Since the hairpin tubes present a high linear density of polycytosine loops, it is likely that C-Ag^+-C bridges between hairpins on different tubes mediate the observed tangling. Ag^+ ions can bind DNA bases in double- stranded DNA too [95]. We therefore expect that Ag^+ ions also bind to the bare DNA tubes. However, because all the bases in the bare tubes are already paired in double helices, there are no sites for Ag-mediated interactions between different tubes.

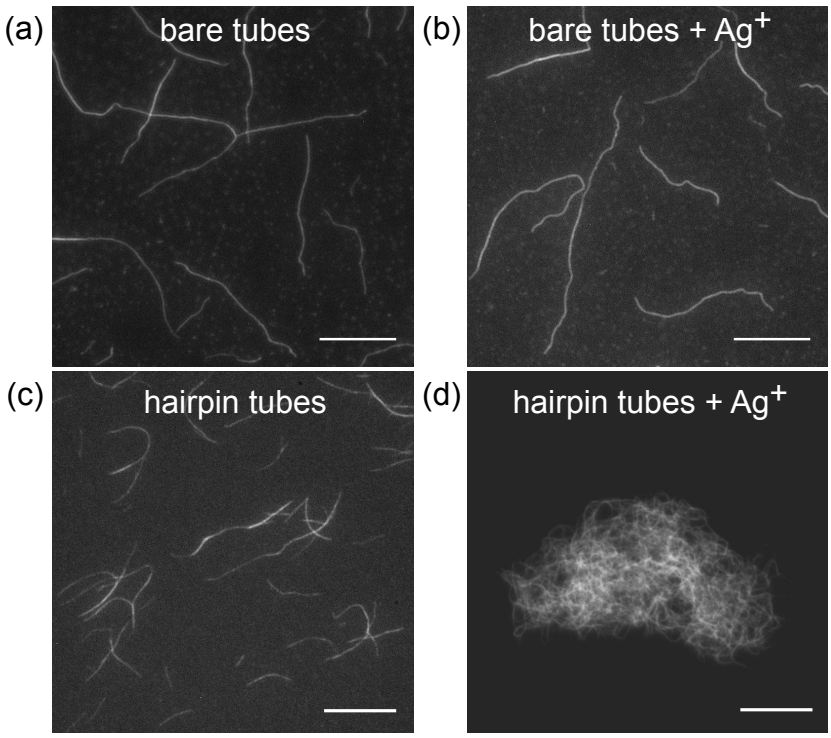

Figure 6.3: Fluorescent images of dye-labeled DNA tubes before and after addition of Ag^+ ions. Bare tubes (top images) remain well- dispersed on Ag^+ addition, while Ag^+ mediated interactions between hairpins causes tangling of the hairpin tubes. Scale bars: 10 μm.

Figure 6.4 shows the formation of red and green emitters on hairpin tubes after reduction of the Ag^+ ions with $NaBH_4$. These tubes were not dye-labeled, so Ag clusters provided the only fluorescence. Shortly after reduction (30 min), only red emitters were visible, but at longer times (1 h to 1 week), both emitters were present. While the majority of tubes, initially tangled by the addition of Ag^+, remained tangled (Figure 6.4a,b), some individual tubes were found and were also labeled with red and green emitters (Figure 6.4c,d), illustrating that hairpin protrusions from individual tubes are sufficient to stabilize the fluorescent clusters.

For the specific hairpin sequence studied here, hairpin tubes and free hairpins (in solutions without tubes) supported nearly identical Ag cluster fluorescence spectra [68]: a green species with peak excitation/ emission wavelengths at 460/545 nm and a red species with peak excitation/emission at 560/620 nm. The latter emission was slightly blue-shifted compared to fluorescent species that form on free hairpins (620 vs 628 nm), but the three other peak wavelengths were the same to within the resolution of our measurement ($\pm$2 nm).

Additional experiments were performed to differentiate between Ag cluster formation directly on the nanotubes and the possibility that nonspecific adsorption of free hairpin-stabilized Ag clusters accounted for the nanotube fluorescence (Figure 6.5). Ag clusters

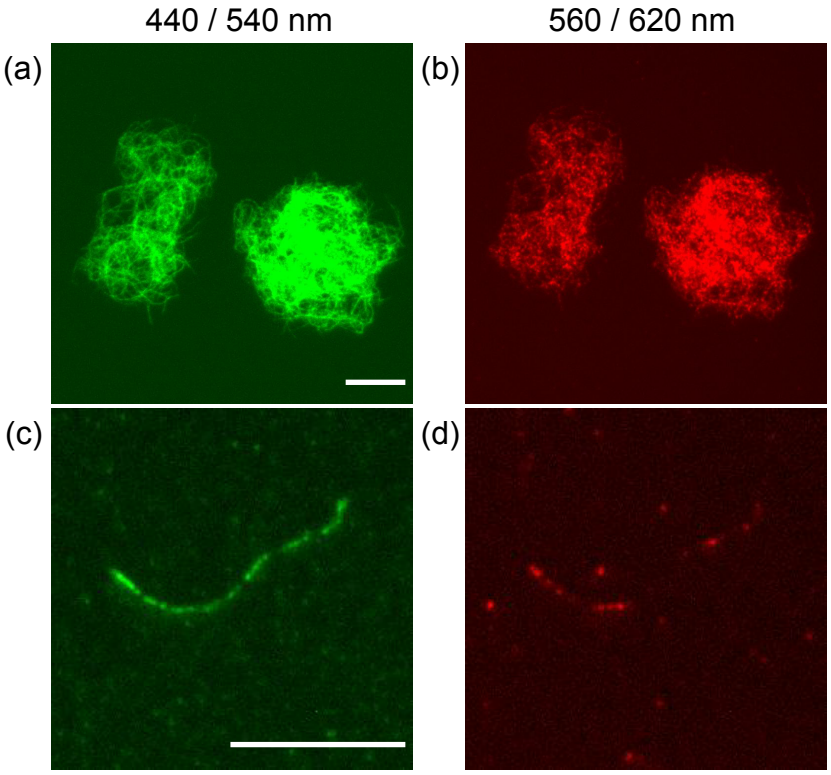

Figure 6.4: Fluorescent Ag clusters on DNA tubes with hairpin appendages. Unlike the tubes in Figure 6.3, these tubes are not labeled with a fluorescent dye, so all fluorescence is attributable to Ag clusters. Both large nanotube tangles (a,b) and individual nanotubes (c,d) were decorated with red and green emitters. (a,b): 17 h after Ag reduction. (c,d): 1 week after reduction. Prior to imaging, the nanotubes were spin-cast in PVA. Scale bars: 10 μm.

were synthesized in a solution of free hairpins, mixed with a solution of untreated hairpin tubes 1 day after Ag reduction, and imaged 1 day after mixing. Some weak green fluorescence was observed along the tubes, but the signal was small compared to the fluorescence observed when Ag was added and reduced directly in the solution of hairpin tubes. Dialysis of the free hairpin- stabilized Ag clusters to remove free $AgNO_3$ and $NaBH_4$ prior to mixing with the untreated hairpin tubes did not substantially reduce the bulk fluorescence of the solution, but no fluorescence was observed along the tubes after mixing.

These results indicate that Ag cluster fluorescence that forms along nanotubes following Ag reduction in solutions of hairpin tubes results primarily from the formation of clusters directly on the nanotubes at the programmed hairpin sites. The ability of hairpin protrusions to template the same Ag cluster fluorophores as free hairpins is consistent with the expectation, based on the high predicted melting temperature of the 9 base pair hairpin stem (57.5 °C), that free hairpins and hairpin protrusions should be similar in their

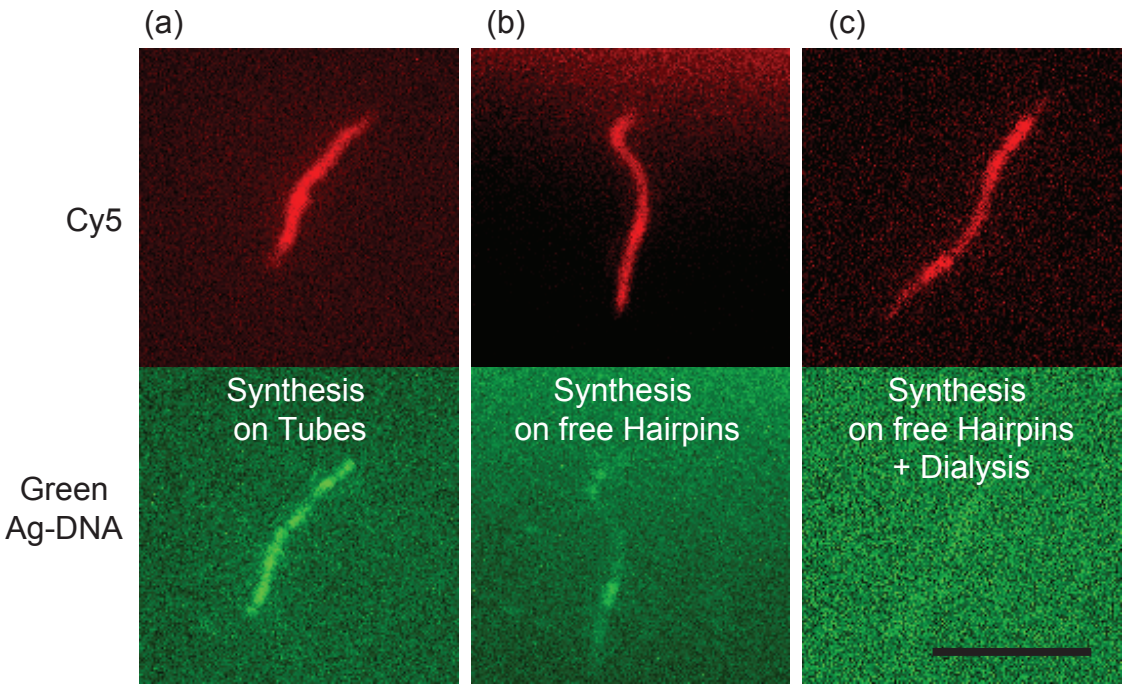

Figure 6.5: Ag cluster fluorescence along hairpin tubes results primarily from direct Ag cluster assembly on the tubes rather than non-specific adsorption of free hairpin- stabilized Ag clusters. (a) Ag clusters synthesized directly on hairpin tubes. (b) Ag clusters synthesized in a solution of free hairpins, mixed with hairpin tubes 1 day after Ag reduction, and imaged 1 day after mixing. (c) Same as (b) but with 6 h dialysis of Ag cluster solution to remove free $AgNO_3$ and $NaBH_4$ prior to mixing with the tubes. Scale bar: 5 μm.

conformational flexibility and in their ability to template fluorescent Ag cluster growth.

It is evident from the discontinuous fluorescence intensity along individual DNA nanotubes in figure 6.4 that not all hairpins template the formation of fluorescent Ag clusters. O'Neill *et. al* estimated an upper bound for the yield of the red fluorescent species of 45% using single molecule photo bleaching experiments [68].

Regarding the constructing of optical breadboards with Ag-DNAs, described in the introduction, this moderate yield of individual Ag-DNAs may pose a challenge because the yield of mulit-component assemblies depends on the product of the individual component's yields. Thus, as an alternative to one step synthesis of multiple Ag-clusters directly on a DNA template we asked if a DNA template could be decorated with previously purified Ag-DNAs. [2] As a template, we used a modified version of 10HT (described in chapter 2) in which strand "U6" was replaced with "U6-H". The modified strand had 18 additional DNA bases at its 3' end which provided a binding site for oligomers of complementary

[2]The following experiment (figure 6.6) was done in collaboration with Stacy Copp, Danielle E. Schultz, and Elisabeth Gwinn with the following contributions: fluorescence microscopy experiments done be S.C., supervised by E.G., Ag-DNA purification by D.E.S., strand design by D.E.S., S.C., D.S.

sequence (sequences listed in appendix C).

This complementary sequence was appended to a Ag-DNA, "Rockstar" which has previously been shown to have excellent fluorescence properties for imaging purposes and can easily be purified using high-performance-liquid-chromatogrophy (HPLC) [86]. To avoid altering the properties of the fluorescent Ag-DNA species the appended sequence predominantly contained A and T bases, which are known to have the smallest probability of templating Ag-cluster formation [87]. The fluorescence spectra under UV-excitiation of original and modified "Rockstar" were unchanged with peak excitation and emission at 600nm and 670nm respectively

Fluorescence microscopy of 10HT, annealed with U6-H and a fluorescein labeled strand, "U1-FAM" confirmed the formation of micrometer long tubes under Ag-DNA friendly buffer conditions (40mM NH_4OAc, 12mM MgOAc). Tubes were mixed with HPLC purified, fluorescent "Rockstar" at a ratio of fluorescent Ag-DNA to U6-H of 6 :1. After approximately 30 min at room temperature the sample was imaged. Fluorescence that originated from fluorescein and Ag-DNA was collected separately through different filter sets. Images of the same area, taken through both filter sets as well as an overlay are shown in figure 6.6.

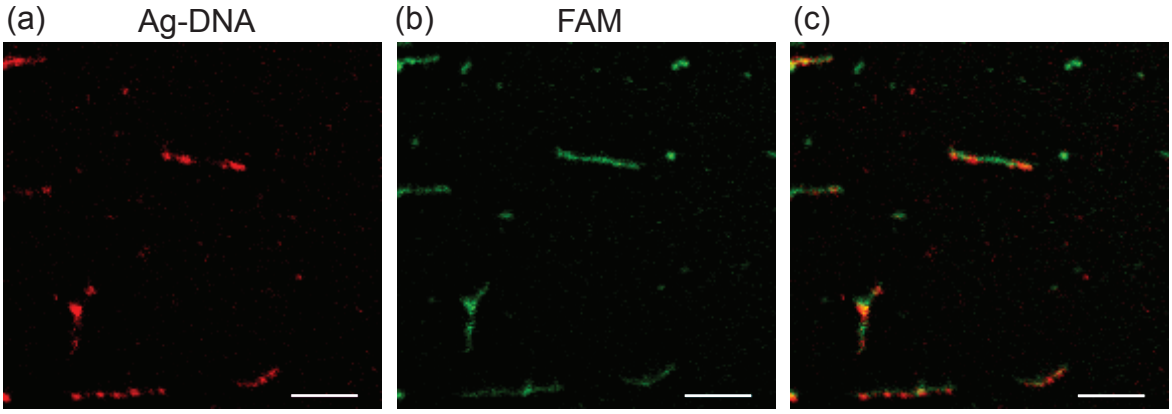

Figure 6.6: Fluorescence images of 10HT, containing FAM labels and "handle" sequences mixed with HPLC purified, fluorescent "Rockstar" Ag-DNA with complementary "handle" sequences. (a) imaged using a filter set for Ag-DNA: intensity along tubes is not homogeneous. (b) imaged using a filter set for FAM. (c) overlay of both images shows that Ag-DNA and FAM fluorescence originates from the same tubes. Scale bars: 5 μm.

The co-localized fluorescence of both channels clearly shows, that Ag-DNA stably hybridized to 10HT. However, as in the experiments described before the fluorescence intensity along the tube contours emitted by Ag-DNA was not homogeneous. Instead, Ag-DNA fluorescence originated from distinct, sometimes resolution limited spots along the tube contour. Tube regions between such spots were not distinguishable from the background. Given the expected yield of fluorescent clusters after HPLC purification, close to 100%,

this result indicates that either"Rockstar" handle sequences did not efficiently hybridize to the complimentary tube handle or that this hybridization and associated change in microenvironment destabilized the Ag-DNA or promoted a structural change leading to loss of fluorescence. The stability of "Rockstar" upon changes of the DNA environment as well as the presence of other Ag-DNA in nanometer proximity has recently been demonstrated by FRET [89]. A decrease in hybridization efficiency on the other hand may be caused by Ag binding to the "Rockstar" handle sequence during Ag-DNA synthesis. The presence of such dark silver products may hinder DNA hybridization.

6.3 Conclusions

We demonstrated two methods to decorate DNA nanotubes with few-atom fluorescent silver clusters. First, by reducing silver ions in a solution containing DX-tubes with hairpin protrusions. As a control, we showed that bare tubes without hairpins did not stabilize the formation of fluorescent Ag-DNA, which is consistent with previous observations that, while Ag^+ ions can bind to DNA bases in both single and double-stranded DNA, only single-stranded DNA offers the flexibility and accessibility of the bases required for fluorescent Ag cluster formation [30]. Our results show that this preferential formation on single-stranded DNA allows fluorescent cluster assembly to be confined on a DNA nanostructure to sites that present single-stranded regions, like DNA hairpins.

In the second method we mixed HPLC-purifed Ag-DNA with a "handle" sequence with 10HT with single stranded protrusions of complementary sequence. We demonstrated by multi-color fluorescence microscopy that Ag-DNA did hybridize to 10HT but did not continuously label the tube contour. Our experiments have demonstrated a proof of principle that tiled DNA nanostructures can host a large number of fluorescent Ag-DNA. Promising future directions to improve the control over Ag-DNA assemblies on DNA nanostructures include sequence optimization to find fluorescent Ag-DNA species with higher yield and Ag-synthesis under conditions which prohibit tangling of DNA structures (*i.e.* embedded in a gel).

6.4 Methods

6.4.1 Preparation of DNA Nanotubes

DX-Tubes

The five DNA strands comprising the tile were mixed at 1.8 μM (each strand, sequences are listed in appendix C.1) in 40 mM ammonium acetate/10 mM magnesium acetate. The Tris-based buffer most commonly used for DNA self-assembly was avoided because AgDNA syntheses performed in Tris-acetate resulted in significantly less fluorescence compared to those in ammonium acetate, reflecting either reduced chemical- or quantum-yields for the

AgDNAs. The mixtures were submerged in a 90 °C water bath and left to cool to room temperature over 2 days inside a Styrofoam box.

10HT with Handle Sequences

Out of the ten DNA strands required for 10HT, listed in appendix C.2, "U1" was replaced by U1-FAM and "U6" was replaced by "U6-H" (table C.3). All strands were mixed at a concentration of 1.4μM in 40 mM ammonium acetate/10 mM magnesium acetate and thermally annealed over 2 days in a water bath from 90°C to room temperature.

6.4.2 Preparation of Ag-clusters on DX-Tubes

Ag cluster synthesis was performed in solutions of hairpin tubes and bare tubes following the most common approach for AgDNA synthesis [73] whereby $AgNO_3$ is added to the DNA solution, followed by reduction of Ag^+ to Ag with $NaBH_4$. Ag^+ ions bind to DNA bases (not the phosphate backbone) [3], and reduction of bound Ag^+ ions by BH_4^- catalyzes the formation of Ag clusters. The DNA guides the formation of Ag-atom clusters in a sequence-dependent manner, limits their growth, and stabilizes against aggregation. A portion of 50 μL of DNA tube solution (with or without hairpins) was mixed with 2.8 μL of 192 μM $AgNO_3$. After 30 min at 4 °C, the mixture was reduced with 2.8 μL of 1 mM $NaBH_4$ and stored at 4 °C. Final concentrations were 1.6 μM DNA tiles, 35.6 μM ammonium acetate, 8.9 μM magnesium acetate, 9.7 μM $AgNO_3$, and 50.4 μM $NaBH_4$. Both $AgNO_3$ and $NaBH_4$ were prepared fresh in water just minutes prior to use. For imaging, 10 μL of the Ag/ DNA tubes solution was mixed with 90 μL of a solution containing 5 mg/mL polyvinylalcohol (PVA, average molecular weight 16 kD), 40 mM ammonium acetate, and 10 mM magnesium acetate. This mixture was spin-cast onto a bare glass coverslip at 1700 rpm for 1 min to create a thin PVA film. The samples were imaged on an inverted fluorescence microscope (Olympus IX70) equipped with a CCD camera (DVC 1310), a 100×, 1.4 NA oil immersion objective (Olympus PlanApo, 100×, 1.4NA), and the following filter sets (from Omega Optical, except as noted): Green emitter - EX: 475AF40, DC: 505DRLP, EM: 510ALP. Red emitter - EX: 535RDF45, DC: 560DRLP, EM: HQ620/75 (Chroma Technologies).

6.4.3 Preparation of HPLC purified Ag-clusters on 10HT

15 μM of "Rockstar" sequence with appended "handle" sequence (appendix C.3) was mixed with 188 μM $AgNO_3$ and reduced by adding $NaBH_4$ to a final concentration of 94 μM. After 24 h the solution was purified using high-performance-liquid-chromatographie following the protocol of Schultz *et. al.* [88]. Briefly, the solution was pre-concentrated roughly 3×. Samples were injected in 200 μL volumes into a 50 mm × 4.6 mm Kinetex C18 core-shell column with 2.6 μm particle size and 100 Å pore size (Phenomenex). Samples were run at room temperature with a flow rate of 1 mL/min using a Waters 2695 Separations Module with auto-injector and a Waters 2487 Dual Wavelength absorbance detector (10 μL volume), set to monitor 600 nm. The mobile phase consisted of 35 mM triethylammonium

acetate (TEAA) in water (solvent A) and 35 mM TEAA in methanol (solvent B). A linear methanol gradient from 16 to 30% B allowed for the elution of modified Rockstar at 26% B, at which time fluorescent material was collected. Fluorescent aliquots were then combined and concentrated into 50 mM NH_4OAc using 10 kDa MWCO centrifugal filters (Millipore).

Chapter 7

DNA Origami Crystallization

One of the main goals driving the development of DNA nanotechnology has been the crystallization of DNA molecules into programmable, periodic lattices. This goal has been achieved using DNA "tiles" as the crystals' unit cell. DNA tiles typically comprise two DNA helices, connected by strand cross-overs and exhibit "sticky ends" to bind to other tiles in a specific geometry. Several tile types have been designed, and individual tiles [80] as well as their assemblies into DNA nanotubes [77, 61, 59, 50, 66, 45, 117, 112, 105] and continuous lattices [59, 105] have been studied experimentally. The interaction between tiles has also been described theoretically [16].

Besides the formation of structural elements like DNA nanotubes, controlled 2D DNA self-assemblies may become useful "breadboards" to position functional elements such as optically active, plasmonic or electrically conducting objects or to guide crystallization of target molecules, attached to the DNA. The latter is of particular interest for target molecules, such as membrane proteins, which can not easily be crystallized by themselves. The design of DNA structures, which bind to membrane proteins and subsequently assemble into a regular lattice may be a viable method for enabling X-ray scattering techniques for protein structure determination [91].

Since DNA tiles have a typical size of only ≈ 100 basepairs and thus provide limited docking sites for the controlled alignment of guest molecules, the crystallization of DNA origami objects, which are larger and can host more complex binding sites, is a promising path towards DNA-guided assemblies. Even though there has been much progress towards this goal [75, 51] the factors determining successful crystallization remain poorly understood.

This chapter contains a study of the crystallization of rectangular DNA origami blocks into 1D chains and 2D lattices. We examine which factors are important in the design of a DNA origami monomer and compare different crystallization conditions. High resolution imaging using TEM and AFM of 2D lattices, assembled in solution, reveals that the substrate onto which the sample is deposited has a significant effect on the lattice shape. We approach the topic of membrane protein crystallization by measuring the diffusion constants of individual dye labeled DNA origami structures with "sticky ends" on supported lipid bilayer (SLB) and give an outlook on how the intensity distribution of resolution lim-

ited spots may be used to monitor 2D lattice growth. Finally we demonstrate that DNA origami lattices can be metallized by ion deposition and are thus promising to template the self-assembly of nanoscale electronic devices.

7.1 DNA Origami Monomers

This section describes the design and construction of two DNA origami structures, serving as monomers for crystallization. Both structures, called Mono$A$ and Mono$B$ have cuboid shape, as illustrated in figure 7.1 and were designed using caDNAno [23]. Mono$A$ is based on a hexagonal lattice [21] using a circular, 7560 bases long plasmid (p7560) as the scaffold strand. Mono$B$ is based on a square lattice [41] using a 8064 bases long plasmid (p8064) and was adapted from Stein *et. al* [99].

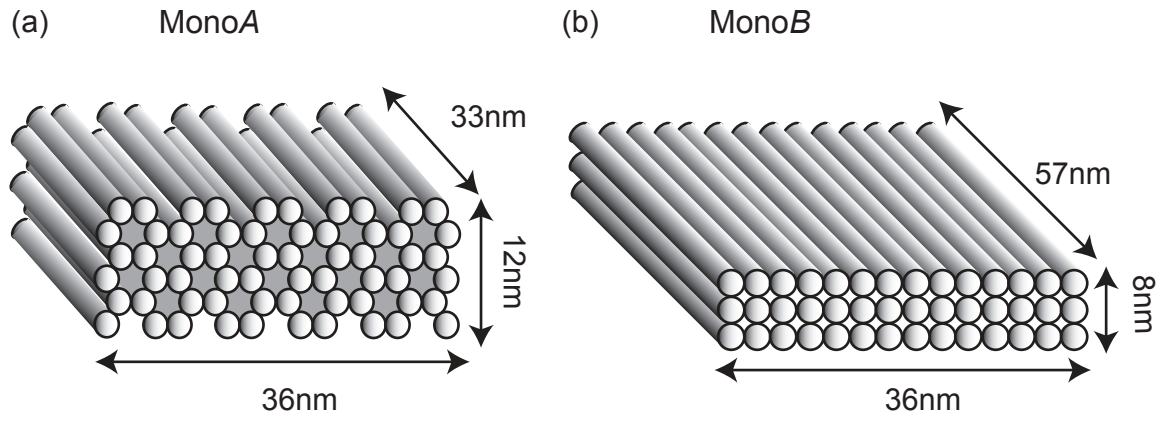

Figure 7.1: Geometry of Mono$A$ (a) and Mono$B$ (b). Each DNA double helix is represented as a cylinder. Dimensions were calculated using cylinder diameters of 2.4nm (a) and 2.6nm (b) and assuming 0.34nm per basepair.

The dimensions of Mono$A$ and Mono$B$ shown in figure 7.1 were estimated using an effective DNA helix diameter of $d_{\text{eff}} = 2.6$ nm and $d_{\text{eff}} = 2.4$ nm for square lattice and hexagonal lattice respectively, based on recent TEM and cryo-EM studies. [21, 41, 5] Their folding yield was analyzed using agarose gel electrophoresis. Figure 7.2 shows gel images of folded monomers, next to bare scaffold strands. In gel electrophoresis, DNA origamis with high folding yield and few side products are characterized by one sharp band, low folding yield and many side products yields one or several blurred bands. In spite of the geometrically similar design, gels of Mono$A$ and Mono$B$ yielded very different bands: Mono$A$ samples had two blurred bands, the faster of which traveled through the gel at a speed comparable to the bare scaffold strand (figure 7.2a). Mono$B$ samples only had only one sharp band, which traveled faster than its bare scaffold strand .

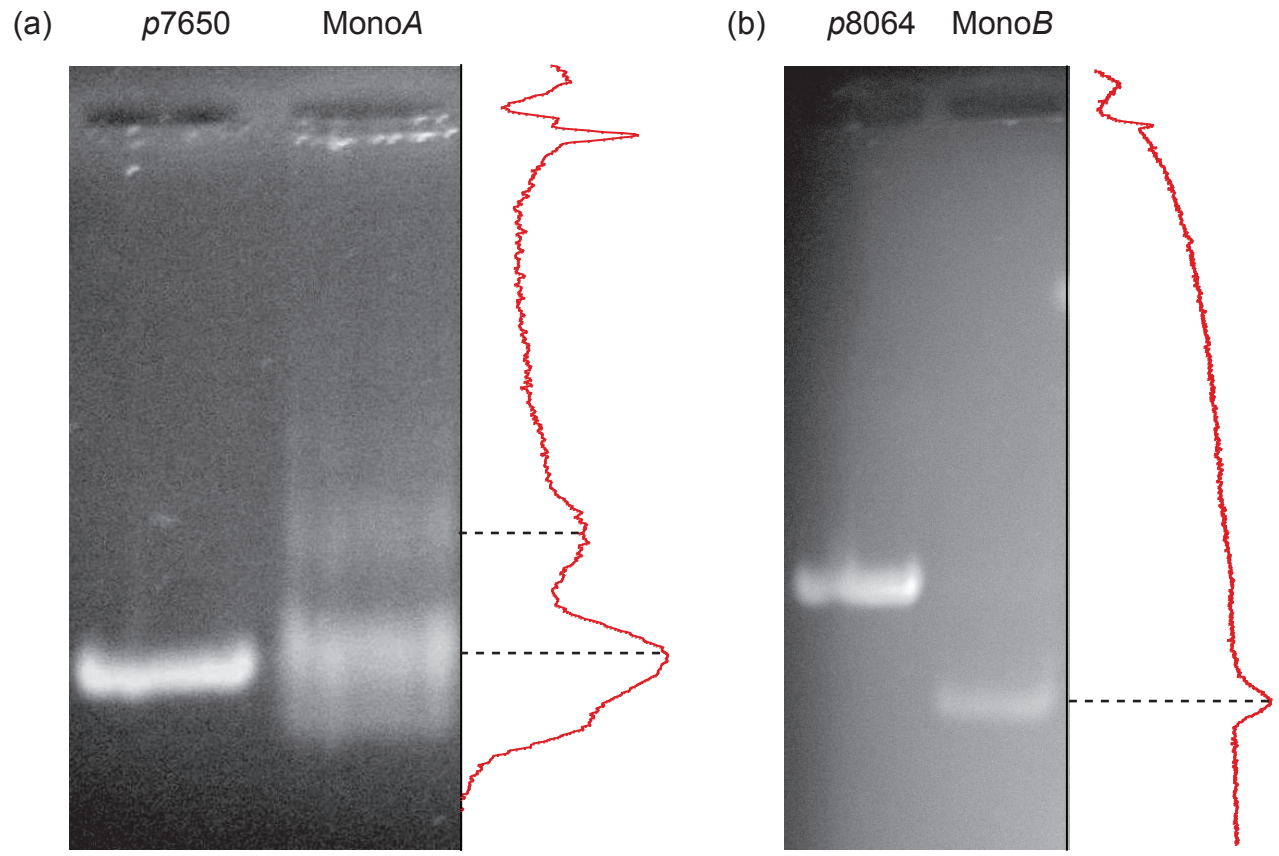

Figure 7.2: Agarose gel electrophoresis of bare scaffold strands and DNA origami monomers: Fluorescence images were obtained by staining the gels with ethidium bromide after electrophoresis. Intensity profiles of the monomer lanes are shown next to the gel images. (a) The Mono$A$ sample shows two blurred bands, the slow band may correspond to dimers. (b) Mono$B$ shows one sharp band.

The different speeds with respect to the bare scaffold strand may reflect that the fast moving Mono$B$ structures (designed in the square lattice) are more compact than the less densely packed Mono$A$ structures (designed in the hexagonal lattice). The second, slow band in the Mono$A$ sample may be caused by dimers (two scaffold strands, connected by staple strands). The width of the bands, which can easily be seen from intensity profiles along the lanes (plotted next to the images in figure 7.2) clearly suggests that Mono$B$ has a higher folding yield and fewer side products than Mono$A$.

The leading bands of both structures were cut out of the gel and imaged by TEM. The result is shown in figure 7.3. Both structures formed cuboid shapes as expected. The size of Mono$A$, measured from figure 7.3a is 33nm $\times$ 28nm, slightly smaller than expected from the design. Possible reasons may be that the structure shown in figure 7.3a was not folded completely or error due to limited contrast. The size of Mono$B$, obtained from 7.3b, c was 56nm$\times$28nm$\times$8nm. Length and depth are in good agreement with the geometrically

expected size. A possible reason for the discrepancy in width (2 nm per helix instead of the commonly observed 2.6 nm) may be that Mono$B$ has a curvature and thus the 2D projection, seen in TEM, is not equal to its full width.

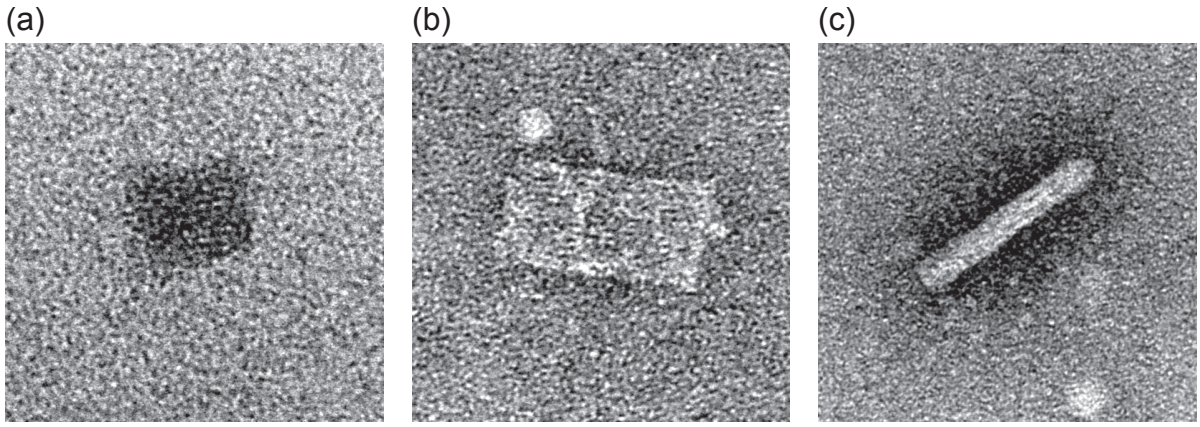

Figure 7.3: TEM images: (a) Mono$A$, top view (b) Mono$B$, top view (c) Mono$B$ side view. The size of Mono$A$ is $\approx$ 33nm $\times$ 28nm. The size of Mono$B$ is $\approx$ 56nm$\times$28nm$\times$8nm. Image size: 100nm $\times$ 100nm.

To avoid unspecific interaction between monomer structures *via* base stacking, their front and back ends were densely covered with 10 - 20 base long single-stranded DNA loops, formed by the scaffold strand. Each DNA loop had a specific sequence. The crystallization was mediated by a strand set called "connectors", that was added to purified monomer structures (figure 7.4a). Each connector strand had two motifs, each complementary to a section of a specific scaffold loop on opposite corners of the origami (*i.e.* binding sites in C1 and C3 or C2 and C4 in figure 7.4b). Figure 7.4c, d illustrates two scaffold loops of two distinct monomer units in close proximity and two connector strands before (c) and after (d) hybridization.

Connector strands have one short motif (4 bases for Mono$B$, 5 bases for Mono$A$), and one long motif of more than 10 bases. Hybridization of the short motif by itself is not stable at room temperature. Thus it is expected that the binding sites for long motifs get populated with connector strands first. Once a corner is populated with several connector strands, association of another monomer becomes possible *via* the cooperative hybridization of multiple short motifs.

The use of two motifs of equal length was intentionally avoided: connectors with two long motifs may occupy all monomer binding sites and hinder their association. We designed two sets of connector strands: C_{13}, binding between corners one and three, and C_{24}, binding between corners two and four (figure 7.4).

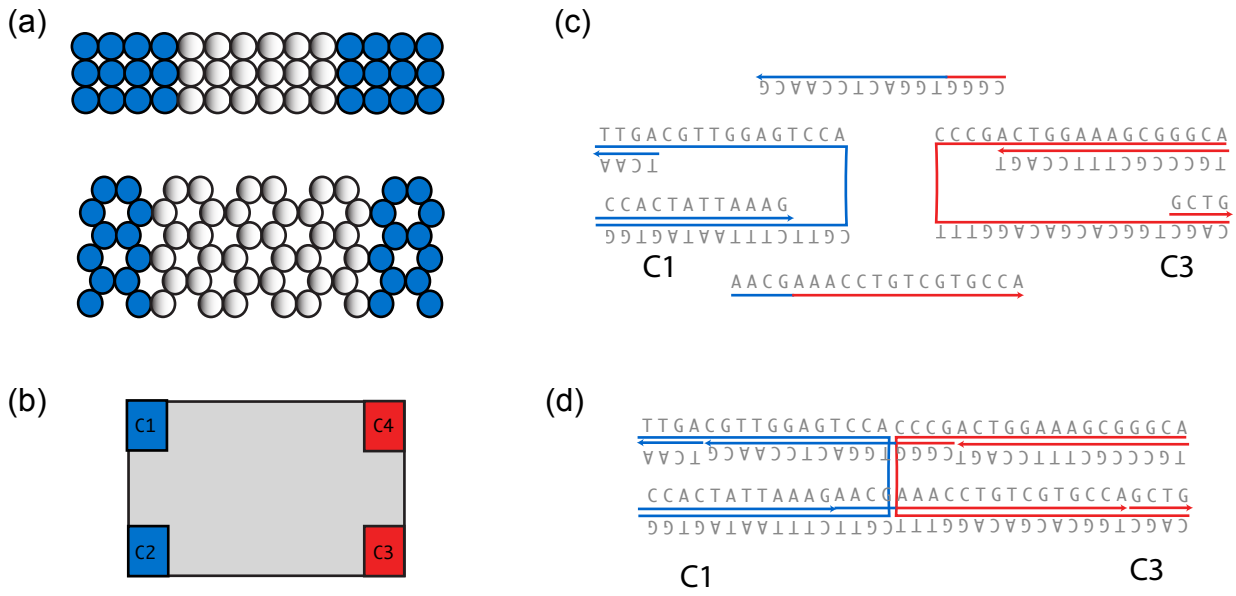

Figure 7.4: (a) Cross-sectional front views of Mono$A$ and Mono$B$. Binding sites for connector strands are marked in blue. (b) Top view, illustrating the four binding domains of connector strands at the corners of a monomer unit. (c) and (d): Sections of two monomer corners C1 and C3 before and after multimerization. Two connector strands, specific to the corner section, comprised of two motifs enable the C1-C3 hybridization

7.2 Crystallization Experiments

DNA origami crystallization experiments were done by mixing the (gel purified) monomer units with a certain set of connector strands at a 10-fold excess of each connector strand to its binding site. Samples were then exposed to thermal annealing over a certain temperature ramp. We considered that the purity of the monomer structure, the type of connector strands as well as temperature and time of the thermal annealing in this process may have an impact on the overall size and defect density in DNA origami crystals. Individual parameters were varied and the results are described in the following sections.

7.2.1 Crystallization with Different Monomer Structures

We first focused on determining which monomer unit yielded better crystallization results. Therefore 1 nM [1] of both monomer types were mixed with an excess of their respective connector strands (10 nM per strand) and thermally annealed from 45°C to room temperature over 60 hours. Figure 7.5 shows TEM images of 2D lattices, formed from Mono$A$.

[1] estimated concentration after folding with 10nM scaffold strand and subsequent agarose gel purification

The lattice size ranged between 5-100 monomers (N=6). A large fraction of monomers was damaged or incompletely folded and the lattice had only local ordering over a length scale of about one monomer unit. This could either be caused by the low folding yield and poor separation of Mono$A$ from mis-folded material by gel electrophoresis (figure 7.2) or by low thermal stability of Mono$A$.

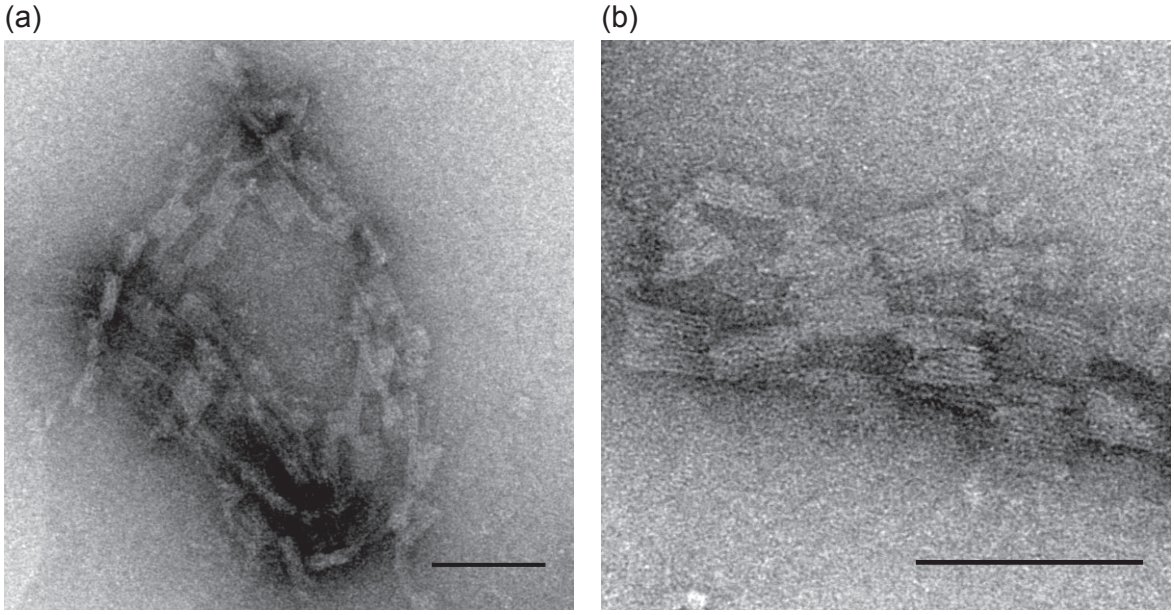

Figure 7.5: TEM of 2D lattices, assembled from Mono$A$ by thermal annealing with connector strands from 45°C to 20°C over 60h. A large fraction of monomer units are missing a significant fraction of DNA and deviate from the designed rectangular shape. Scale bars: 100nm

On the other hand, lattices self-assembled from Mono$B$ units ranged in size from 1 to over 1000 monomers (N=15) (figure 7.6). Regular lattice patterns were observable over distances of up to ten monomer units. The small fraction of damaged monomers shows that Mono$B$ was thermally stable under the lattice formation conditions.

The main lattice distortion, with respect to a flat 2D sheet was not defects of individual monomers, but rather large scale deformations such as lattice curvature (figure 7.6 b) or stacking of multiple lattices on top of each other. Figure 7.6 shows that the 2D lattices had the designed geometry on length scales well below one micrometer (a ,b). However this order was lost on the micrometer scale (c, d). Because of the higher lattice size and higher ordering, we used Mono$B$ for further experiments described in sections 7.2.3 and 7.2.2.

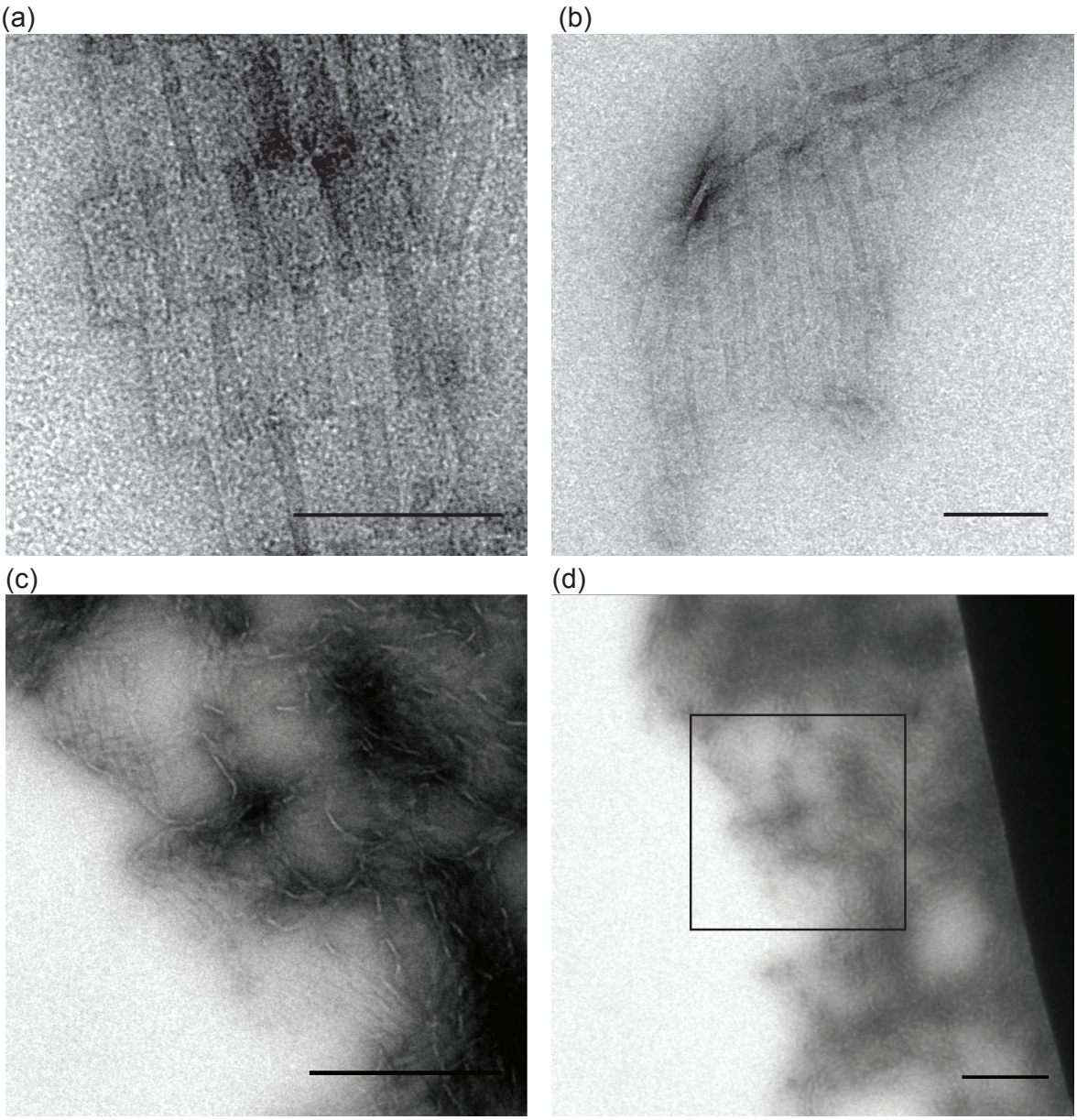

Figure 7.6: TEM of Mono$B$ 2D assemblies, thermally annealed with connector strands from 45°C to 20°C over 60h. Scale bars in (a)-(b): 100nm, (c)-(d): 500nm. (d) is a zoom in of the marked region in (c).

7.2.2 Crystallization with Different Connector Strands

Two parameters which may have an effect on the success of crystallization experiments are (i) the number of helices, linked together by connector strands and (ii) the hybridization energy of each of the two domains of the connector strands to their complementary sequence on the monomer unit. (i) determines the geometry of the target lattice. It is desirable to keep this quantity variable. Thus, we focused on determining the dependence of crystallization yield on (ii).

Here, crystallization yield is characterized by the lattice size and number of defects. Neither of those quantities is easily determined from 2D assemblies, because of their tendency to form multilayer structures described above. Thus we focused on 1D assemblies and measured the fraction of multimers without defects (branches or unspecific binding) and the size of defect free multimers.

We compared two sets of connector strands, designed to 1D crystallize Mono$B$ structures by hybridizing the ends of 18 DNA helices on corners C_1 and C_3 (figure 7.4). DNA sequences in the first set (M_{4B}) were partitioned as in previous experiments (one domain with 4 bases and one with >10 bases). The second set of connector sequences (M_{2B}) had a short domain of only 2 bases. To avoid a two base gap of single stranded DNA between M_{2B} connectors and Mono$B$ all staple strands adjacent to connector strands were elongated by two bases. Samples were thermally annealed from 45°C to 25°C over 80 hours. Typical TEM images are shown in figure 7.7.

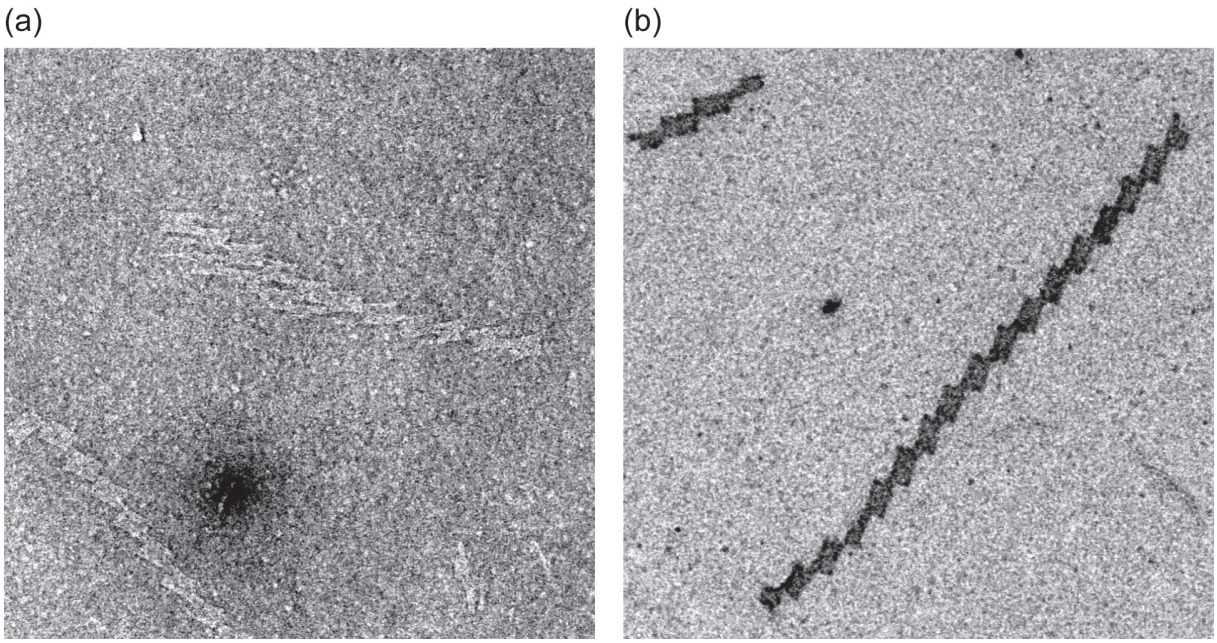

Figure 7.7: 1D assemblies of Mono$B$ using connector strands with (a) 2 bases / >10 bases domain partitioning (M_{2B}) and (b) 4 bases / >10 bases domain partitioning (M_{4B}). Image size: 1μm

Out of 19 M_{4B} multimers, 8 (42%) were defect free with an average size and standard deviation of N=14±6. Out of 8 M_{2B} multimers, 4 (50%) were defect free with N=7±3. The most common defect was unspecific binding and thus multimers with defects were typically larger in size than defect-free multimers. Accordingly, from the same data set, the number of monomer units within defect-free structure was only ≈22% and ≈29% for M_{4B} and M_{2B} respectively.

This rather small difference suggests that crystallization yield is not sensitive to connector strand design on the single base pair level. Besides unspecific binding, some 1D assemblies had incompletely folded Mono$B$ units at one or both ends of the chain (see figure 7.7), which indicates that improved monomer folding yield or purification may further increase the observed length of 1D assemblies.

7.2.3 Lattice Deposition on Different Substrates

As described in section 7.2.1, when imaged by TEM, the order of 2D lattices was not maintained over micrometer distances and the lattices often appeared curved or stacked on top of each other. We considered whether these distortions may be the result of shear forces, acting during deposition from solution onto the substrate (TEM grid) and flow during the subsequent drying and staining steps.

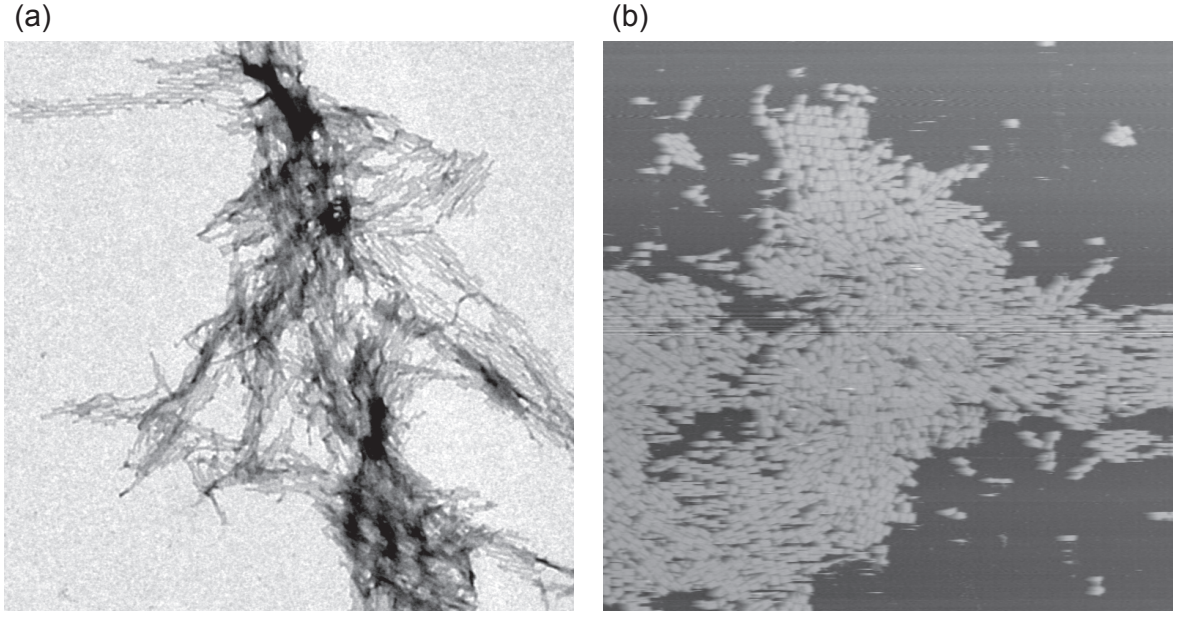

Figure 7.8: 2D Mono$B$ lattices assembled using the M_{2B} connector type. (a) TEM clearly shows domains with multiple layers. (b) AFM: the 2D lattice is completely laid out on the substrate. Image size: 3μm × 3μm.

To test this hypothesis, we used atomic force microscopy (AFM), which allows imaging under solution conditions on a mica substrate and thus does not require steps which expose

the samples to strong flow. Figure 7.8 shows a side by side comparison of Mono$B$, 2D crystallized in solution, using M_{2B} connectors and imaged using TEM (a) and AFM (b). In the AFM image, all Mono$B$ units are in one plane and are in contact with the mica substrate, no back-folding is observed.

Lattices in AFM images contained ordered domains. Their size was comparable to lattices imaged by TEM. On the micrometer scale the order was lost. Because of this loss of long-range order even in the absence of shear forces it is likely that the assemblies did already have deviations from the designed lattice geometry before coming in contact with the substrate. We propose that the underlying reason may be curvature or twist of the Mono$B$ structure due to stresses on DNA molecules, resulting from strand cross-overs placement: even though averaged over the full length of Mono$B$ each DNA duplex was at its equilibrium twist of 10.5 base pairs per turn local deviations from this value could not be avoided due the geometrical constraints of the square lattice cross-section geometry. Such deviations are known to introduce twist to DNA structures [17].

7.2.4 Crystallization on Supported Lipid Bilayer

To evaluate the potential of controlled association of DNA origami structures to guide the crystallization of membrane proteins, we studied the interaction of Mono$A$ structures with supported lipid bilayer (SLB). The method of substrate based crystallization relies on the interaction strength between the substrate and DNA: it must be strong enough to confine the monomer structures to 2D, but weak enough to allow rearrangement and diffusion within the substrate plane. The principle of substrate based crystallization of small DNA tiles has been demonstrated by Sun *et. al.* [101], by growing micrometer sized regular tile assemblies on mica.

It has been shown that the interaction strength between lipid bilayers and DNA molecules can be tuned by varying the fraction of cationic lipid molecules [74]. On supported lipid bilayers (SLB), DNA molecules on the length scale of 10^2 to 10^4 base pairs display two-dimensional diffusion [56, 55]. We asked if the interaction between DNA origami structures and SLB could be sufficiently tuned to enable surface mediated assembly of 2D lattices.

We therefore fluorescently labeled Mono$A$ structures by first elongating five stable strands ("handles") by 18 bases and adding the complementary DNA sequence, with a covalently bound Cy3 dye as illustrated in figure 7.9a. This modification allowed visualization and localization of Mono$A$ units by fluorescence microscopy in real time and under solution conditions, compatible with SLB (see methods in section 7.5.3).

Surprisingly, we found that Mono$A$ not only adhered to SLB with a cationic fraction (DOPC / DOTAP lipid compositions) but also to neutral SLB (100% DOPC) under buffer solution with divalent ions (1 × TAE, 12 mM Mg^{2+}). Mono$A$ structures, added to buffer solution on top of a fluid SLB appeared in the focal plane as resolution limited spots and immobilized within a few seconds. To weaken their adhesion and enable two-dimensional diffusion NaCl was added to a final concentration of 10 mM. An excess of connector strands was added.

Figure 7.10a shows a fluorescence image and diffusion traces of 10 fluorescent structures

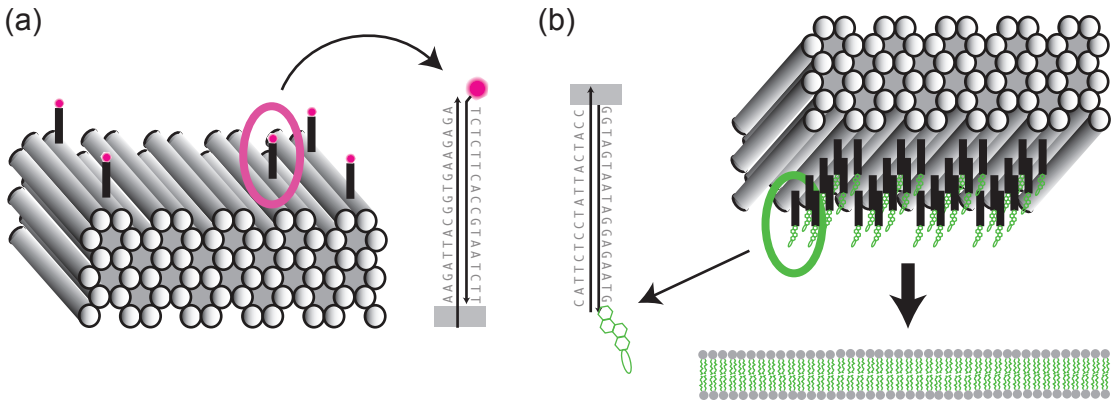

Figure 7.9: Illustration of "handle" sequences on Mono$A$. (a) top side: Cy3 labeled DNA sequences can bind to five complementary handles of 18 bases in length. Colored circles indicate Cy3 molecules (b) bottom side: Cholesterol modified DNA sequences can bind to 30 handles, evenly distributed on the structure.

over 10 minutes. Particle location was manually tracked as a function of time. The time delay, τ, between two images was 30s. Diffusion coefficients were obtained from each trace by determining the mean square displacement between two images:

$$\langle(\vec{r}(t+\tau) - \vec{r}(t))^2\rangle = 4D\tau \tag{7.1}$$

The measured diffusion coefficients ranged from $D = 5.9 \times 10^{-5}\mu m^2/s$ to $D = 4.4 \times 10^{-3}\mu m^2/s$. This large range may reflect that Mono$A$ units get stuck on immobile fractions within the SLB. Consistent with this idea, repeated addition of NaCl washed most of the structures off the surface but, within $\approx$ 1min structures from solution became confined on the SLB again. The number of immobile structures was lowest directly after deposition and increased with time.

For a 2D lattice to be larger than the resolution limit of light microscopy, its size must exceed about 100 Mono$A$ units. Because we found in section 7.1 that such lattice sizes were rare, even after 60 hour solution assemblies we investigated if the intensity of a resolution limited structure may serve as a measure for their size. Figure 7.10b shows a histogram of background corrected fluorescence intensity, I_F, of 231 structures after repeated washing off and re-confinement by addition of NaCl (see methods in section 7.5.3) normalized by the fluorescence intensity of the dimmest object in the sample, I_{min}. Under the assumption that I_{min} originated from a single monomer structure with five Cy3 molecules, the value of I_F directly corresponds to the number of monomers per resolution limited object. [2] The width of the intensity distribution ($\sigma > 5$) can not be explained by different labeling yield

[2]If instead one assumed that the intensity of the dimmest particle originated from a (rare) single labeled particle the intensity axis may instead be normalized by dividing the measured intensities by $5 \times I_{min}$

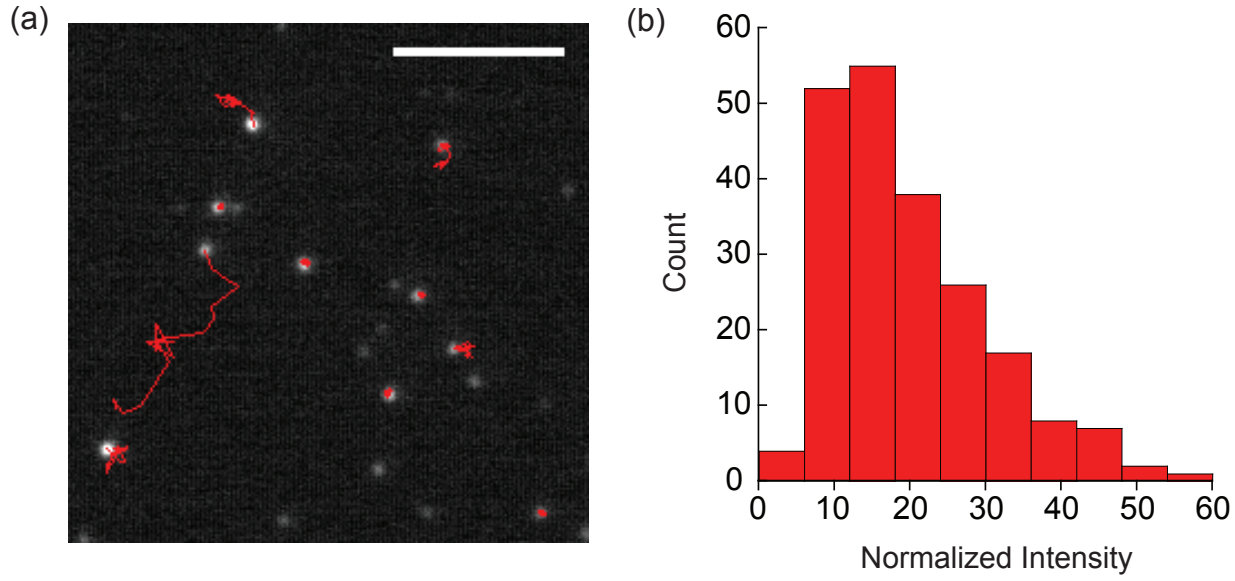

Figure 7.10: Fluorescnece microscopy of Mono$A$ with 2D connector strands on SLB. (a) Diffusion traces of ten fluorescent structures, recorded over ten minutes. Scale bar: 5 μm. Diffusion coefficients ranged from $D = 5.9 \times 10^{-5} \mu m^2/s$ to $D = 4.4 \times 10^{-3} \mu m^2/s$ (b) Intensity histogram of N=231 fluorescent structures, normalized by the intensity of the dimmest particle.

of Cy3-sequences to the Mono$A$ handles alone and suggests that multimers were present in the sample. Multimers may have formed directly on the SLB or during NaCl washing steps in solution.

In conclusion, fluorescence microscopy showed that DNA origami structures are mobile and diffuse on SLB in 2D under certain buffer conditions. The observed variation in intensity suggests that the presence of SLB does not hinder the crystallization process. As a next step for future work, we propose to better match the experimental conditions to those expected for DNA structures bound to proteins by decorating DNA origamis with cholesterol "anchors" as illustrated in figure 7.9b. The hydrophobic cholesterol molecule is known to intercalate into the hydrophobic inner layer of lipid membranes. Cholesterol anchors may thus resemble protein binding sites and contain DNA origami structures on SLB, even while their diffusion is increased by NaCl addition. They may also add an orientational preference to the adhesion of the DNA structures to SLB, which is important to allow crystallization.

The use of "tethered" SLBs which are known to contain a smaller fraction of immobile lipid molecules may enable a constant diffusion of DNA origamis without repeated addition of NaCl. Besides intensity as lattice size readout recently developed super-resolution techniques may yield a more detailed image of the assembly process. Finally it may be of great advantage to preform SLB based crystallization experiments with monomer units, with higher folding yield and stability, for instance Mono$B$, described in previous sections.

7.3 Metallization of DNA Origami Crystals

DNA origami crystals may serve as micrometer size bread boards, which can host complex arrangements of functional elements. With the ever increasing need for smaller electronics, one particularly interesting direction is the use of DNA nano structures to template the growth of electronic circuits. In recent years it has been shown, that periodic (tiled) 1D and 2D DNA lattices can serve as templates for the self-assembly of electrically conducting, metallic objects by deposition of cationic metal ions *via* the glutaraldehyde method [1, 49, 70, 71, 82, 114].

More complex DNA templates will be necessary to host more complex metallic objects or even electrical circuits on the nano-scale. DNA origami and in particular crystallized DNA origami lattices are therefore promising templates for metallization. Here, we demonstrate that DNA origami structures can be used to attract and template positively charged gold particles in desired conformations and that by further electroless deposition of metal ions from solution such structures can be converted into continuously metallized objects [84]. [3]

In contrast to previous work, where DNA nanostructures were metallized via a glutaraldehyde -based method, we used 1.4 nm gold clusters coated with positively charged amines, which bind to negatively charged DNA origami structures, as seeding sites for the gold cluster growth (see methods in section 7.5.4). Such metal-seeded objects were subsequently exposed to electroless deposition of gold ions, which yielded continuously metallized objects. This method is illustrated in figure 7.11 a.

We first applied this method to Mono$B$ structures. Figure 7.11 b shows representative TEM images before and after the metallization process. Metallized objects clearly maintained the rectangular shape of the Mono$B$ template and were slightly larger in size. When applied to 1D Mono$B$ assemblies (figure 7.11 c), prepared as described in section 7.2.2, the method yielded extended metallic objects, which clearly resembled the shape of the DNA template.

Schreiber *et. al.* additionally showed that this method can easily be applied to a wide range of shapes, including DNA nanotubes of different lengths and diameters, "Nanodonuts" and "DNA-kites" [84]. The size distribution of the smallest feature size of metallized DNA nanotubes - their width - was very narrow with approximately 50-60nm.

[3] Portions of section 7.3 is reprinted (adapted) with permission from: Schreiber, R., Kempter, S., Holler, S., Schller, V., Schiffels, D., Simmel, S. S., Nickels P. C. & Liedl, T. (2011). DNA Origami-Templated Growth of Arbitrarily Shaped Metal Nanoparticles. Small (Weinheim an der Bergstrasse, Germany), (c), 17951799. doi:10.1002/smll.201100465 D. Schiffels contributed the design and preparation of individual rectangular DNA origami structures, 1D crystalized DNA origami structures, TEM imaging of those samples (before metallization) and input to the text.

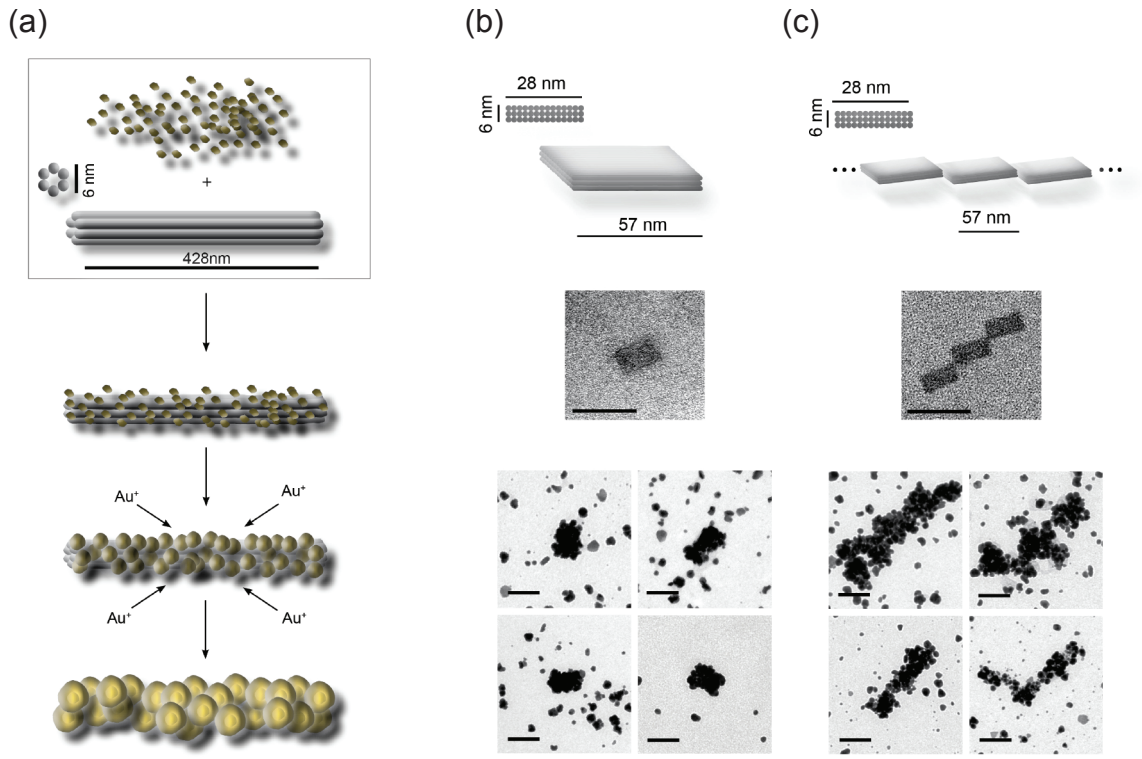

Figure 7.11: (a) Metallization strategy: Positively charged gold clusters cover the negatively charged DNA origami structure. Continuous metallization of such pre-seeded DNA origami structures is achieved by the electroless deposition of gold ions to the electrostatically bound Au clusters. Computer models, native DNA objects after negative staining with uranyl acetate and metallized objects are shown in (b) Mono$B$ and (c) 1D crystallized Mono$B$. Scale bars: 100 nm

7.4 Conclusion

We demonstrated that DNA origami structures can be crystallized into 1D chains and 2D lattices by using a set of "connector" oligonucleotides. We compared 2D crystals of two different rectangular monomer structures (Mono$A$ and Mono$B$) and found that monomers with higher folding yield formed larger crystals which were ordered over length scales of approximately ten monomer units.

The size and defect number of 1D assemblies of Mono$B$, crystallized using two different sets of connector strands with different motif partitioning were compared and yielded similar results. The length of defect free 1D chains was 4-22 monomer units and the fraction of monomer units within defect free chains was between 20% and 30%.

The appearance of 2D lattices depended on the substrate: on TEM grids, lattices were stacked on top of each other or folded back onto themselves while on mica each monomer was in contact with the substrate. However the length scale over which lattices were ordered was comparable on both substrates. On a third substrate, SLB, Mono$A$ structures displayed two-dimensional diffusion. The SLB-DNA origami adhesion could be reversed by the addition of monovalent salt to the solution. The intensity distribution of SLB-bound Mono$A$, incubated with "connector" strands suggested a size range between zero and 50 monomers 2D lattice. Finally we demonstrated that individual Mono$B$ structures as well as 1D crystals can be used as templates for metallization of gold structures of similar geometry.

Taken together this set of experiments shows that rectangular DNA origamis can be spatially arranged to form interesting materials. This programmed assembly of DNA origami crystals may become useful in guiding the crystallization of target molecules such as membrane proteins. In addition DNA crystals may be functionalized with optical elements or serve as templates for the construction of nano-electronic circuits.

7.5 Methods

7.5.1 Preparation of DNA Origami

DNA origami were folded over at least 24 hours in TE buffer with $MgCl_2$ concentrations ranging from 10mM to 20mM. Best results were obtained using 12mM $MgCl_2$ for Mono$A$ and 15mM $MgCl_2$ for Mono$B$. The concentrations of scaffold strand and each staple strand were 20nM and 100nM for Mono$A$ and 10nM and 100nM for Mono$B$. DNA origami were purified using 2% agarose gels electrophoresis. Gels were stained using ethidium bromide and the leading band cut out. Samples were extracted from gel using Freeze 'N Squeeze DNA gel extraction spin columns (No. 732-6166, Biorad).

7.5.2 DNA Origami Crystallization

Purified monomer structures were mixed with an excess of connector strands (1:10) and subjected to a programmed temperature ramp as specified in the text.

7.5.3 Preparation of Supported Lipid Bilayer

Supported Lipid Bilayer (SLB) was made on bare glass-bottomed tissue-culture dishes (WillCo-Dish, #1.5 coverslip, 22 mm diameter) by covering the glass surface with 2 mL of extruded vesicle solution.

Vesicle solution was prepared according to Weirich et al. [109] using DOPC lipid, purchased in chloroform (Avanti Polar Lipids). DOPC was transferred into a clean glass vial, dried under nitrogen, resuspended in PBS buffer (140 mM NaCl, 8.5 mM Na_2HPO_4, 1.5 mM NaH_2PO_4) and extruded through filters (Whatman, diameter 13mm, pore sizes: 0.2 μm, 0.1 μm, 0.02 μm) using a Lipex Thermobarrel Extruder (Northern Lipids, Vancouver, Canada). To remove excess vesicles and, at the same time, create solution conditions suitable for DNA nanostructures, 1 mL of TAE/Mg buffer (40 mM Tris Acetate, 1 mM EDTA and 12.5 mM Mg Acetate at pH 8.3) was added. This volume solution was removed and replaced with a fresh 1 mL at least 10 times.

Before a measurement, 1 μL of Mono*A* sample was added to the glass-bottomed dish containing SLB. 5 μL of connector strands (1.25 μM per strand) was added. As Mono*A* diffused into contact with the SLB, they became immobilized. To weaken their adhesion and enable two-dimensional diffusion, 2 μL of 1M NaCl solution (in TAE/Mg buffer) was added to the 2 mL in the dish. This washed some of the fluorescent structures off the surface but, within $\approx$1 min, structures from the solution became confined on the SLB again and diffused in 2D. The fraction of diffusing particles decreased over time. The addition of NaCl was repeated multiple times.

7.5.4 Metallization of DNA Origami

Two-Step Metallization with Seeding in Solution

400μL H_2O were added to 25μL DNA origami objects (2 nM in 5 mM Tris, 1 mM EDTA and 18 mM $MgCl_2$) and spun through an Amicon Ultra filter (0.5 mL, 100 K, Millipore, USA) at 16 000 rcf for 5 min in a Biofuge fresco centrifuge (Kendro, Thermo Fisher Scientific Inc., USA). Then we added 0.5μL of 300μM Nanogold solution and 400μL H_2O to the DNA origami solution, mixed it with a Vortex Genie 2 (Scientific Industries, Inc., USA) and spun the solution in the same Amicon Ultra filter again at 16 000 rcf for another 5 min. Subsequently, four times a volume of 400μL H_2O was added to the Amicon Ultra filter and spun each time at 16 000 rcf. To recover the sample, we placed the Amicon Ultra filter upside down in a new centrifuge tube and spun at 900 rcf for 3 min. The solution of seeded DNA objects was applied for two minutes on hydrophylic formvar-carbon grids. The grids were washed with H_2O and ready for the gold enhancement process.

Gold Enhancement

In the second step we enhanced Au nano-clusters with Gold Enhancement for EM (Nanoprobes, USA) following the instructions of the supplier. The developing time for optimal particle size was 30 s.

Chapter 8

Scaffolded Tile Assembly

The two main strategies for the design of DNA nano structures are "tiled" assemblies and "scaffolded" assemblies. Tiles can self-assemble into large, periodic lattices with various geometries by programmable interaction of their "sticky ends" [77, 61, 59, 50, 66, 45, 117, 112, 105, 59, 105]. Scaffolded DNA origami self-assemble into predefined 2D [76] or 3D [21, 17] shapes.

From the perspective of a nano-scale engineer both techniques have distinct advantages. Tile assembly can yield micrometer sized objects with low defect density. Cost and experimental effort are very low. Scaffolded assembly has higher cost and experimental effort but also offers a much larger set of accessible geometries and yields objects of defined size.

We investigated strategies to combine the two techniques. Specifically we designed DNA nanotubes, which incorporate a scaffold and "tiles", bridged by staple strands. The designed length and diameter of such tile-origami tubes ("TO") significantly exceeds that of DNA origami nanotubes. Because TO have a scaffold strand along the entire tube length, each tube segment can specifically be modified via staple strands.

8.1 Strand Design

In DNA origami, the scaffold strand is routed through the entire structure in a zig-zag fashion. This limits the size of the assembly to N base pairs, N being the number of bases of the scaffold strand. For a typical scaffold $N \approx 8$ kB (kilo bases), and thus a tube with n helices circumference can have a length of (8000 / n) $\times$ 0.34nm. Thus a six-helix tube has a maximum length of ≈450 nm). Here, we present two alternate tube designs, TO_A and TO_B, in which the circular scaffold strand is stretched to its maximum length as illustrated in figure 8.1. This yields a maximum tube length of 1350 nm. To test the designs we only used a subset of the staple strands, forming a $\approx$ 400 nm long tube, leaving the remaining scaffold strand unfolded. Both designs use HX-tiles [117] and thus tube circumference is modular with a minimum of 4 and 6 helices for TO_A and TO_B respectively. To prevent growth of the helices made up of tiles past the length of the scaffolded part we designed a set of special staple strands, called "endcaps", that specifically bind to the tube ends and

prevent further tile assembly.

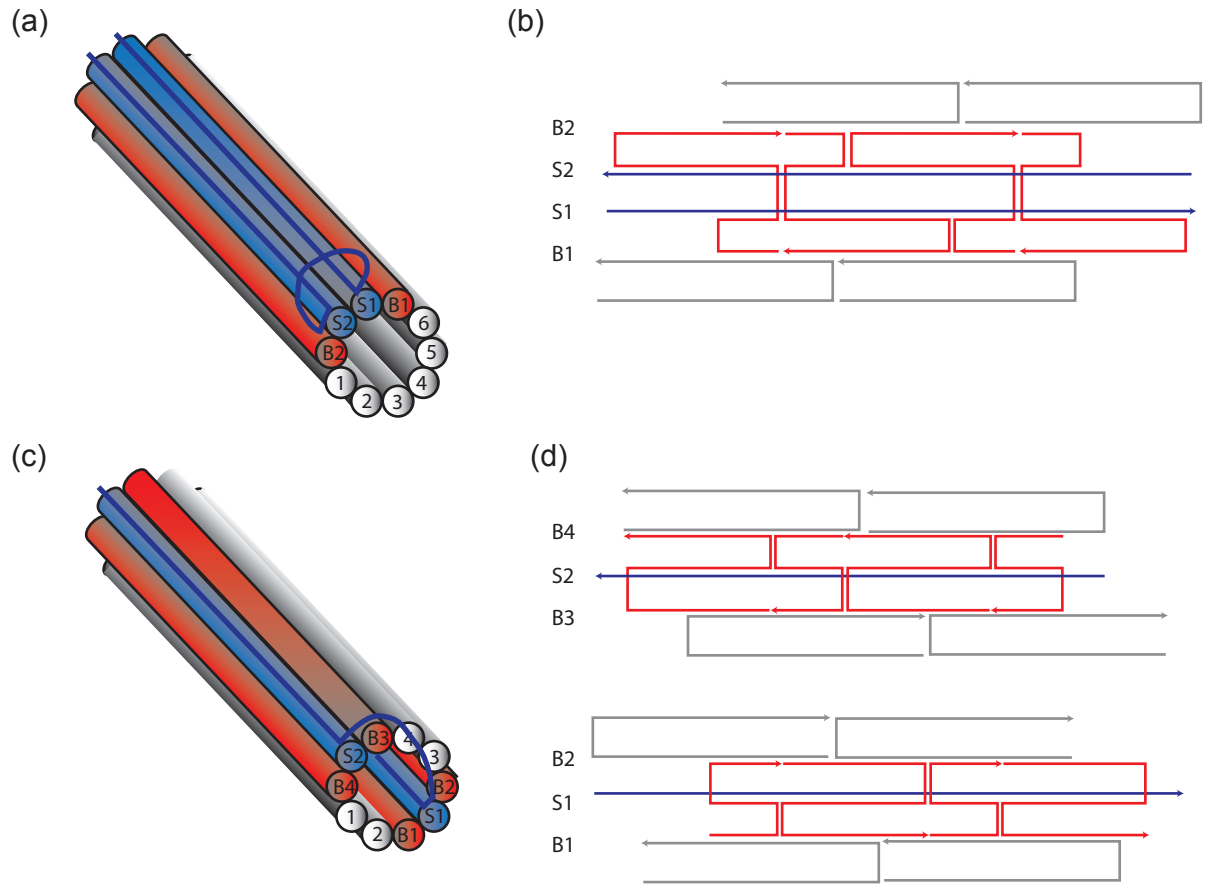

Figure 8.1: Illustration and strand design of TO_A (a), (b) and TO_B (c), (d). DNA helices comprised of the scaffold strand and staples, staples and tiles, and tiles only are shown as blue, red and grey cylinders respectively.

8.2 TO_A Characterization

TO_A with 7 helices circumference was folded in a one pot reaction (section 8.5) and imaged by TEM (figure 8.2 a). A large fraction of the tube-like structures formed closed rings. This is characteristic for purely tiled assemblies of HX-tubes with a missing strand. The mean and standard deviation of the length of non- circular tubes from figure 8.2 are 288 nm $\pm$ 297 nm and thus deviate from the designed length of approximately 400 nm.

To better understand the formation of TO_A and the heterogeneity of structures, seen in TEM, we folded different subsets of TO_A components separately and analyzed the products using agarose gel electrophoresis. We found that folding scaffold strand + staples (no tiles) as well as scaffold strand + staples + adjacent tiles resulted in sharp bands, characteristic

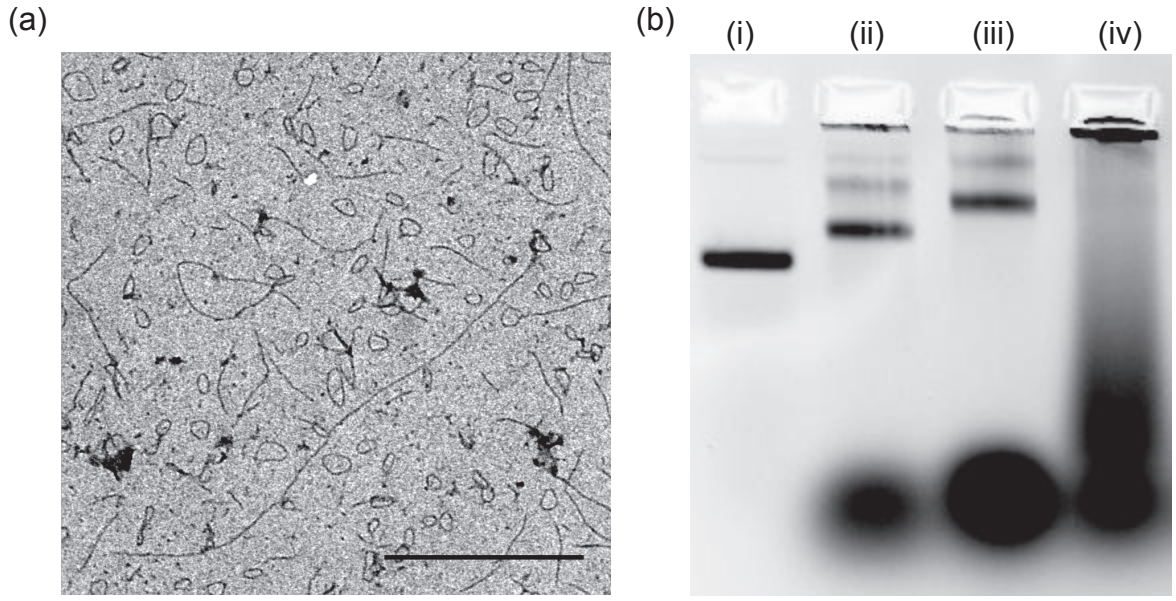

Figure 8.2: (a) TEM of unpurified TO_A, scale bar 500 nm. (b) 1.5% agarose gel: (i) bare scaffold strand (p8634), (ii) p8634 + staples, (iii) p8634 + staples + adjacent tiles, (iv) p8634 + staples + all tiles

for samples containing a single product only (figure 8.2 b). However when the full set of all DNA strands was used (lane (iv) in figure 8.2 b) the gel had no bands and indicated a continuous distribution of sample sizes, consistent with TEM images.

To explain why TO_A did not self-assemble as designed in the presence of all strands we considered two alternate folding paths, illustrated in figure 8.3. At high temperature, all DNA is single stranded. During thermal annealing, TO_A can only form correctly if scaffold strand and staple strand form a stable ribbon, before interacting with the tiles. This is because, the formation of a tile-ribbon can serve as a seed to align staple strands randomly and thus make their correct interaction with the scaffold strand impossible. Staple-scaffold and staple-tile interactions have comparable hybridization energies, however because of the much lower scaffold concentration it is likely that staple-tile hybridization starts at a higher temperature than staple-scaffold interaction.

Thus we propose that TO_A does not form, because its favored folding pathway leads to a local minimum in free energy. Consistent with this idea, foldings containing only tiles, directly adjacent to the staples, which can not form a stable ribbon by themselves, appeared as a sharp band in figure 8.2 b (lane iii).

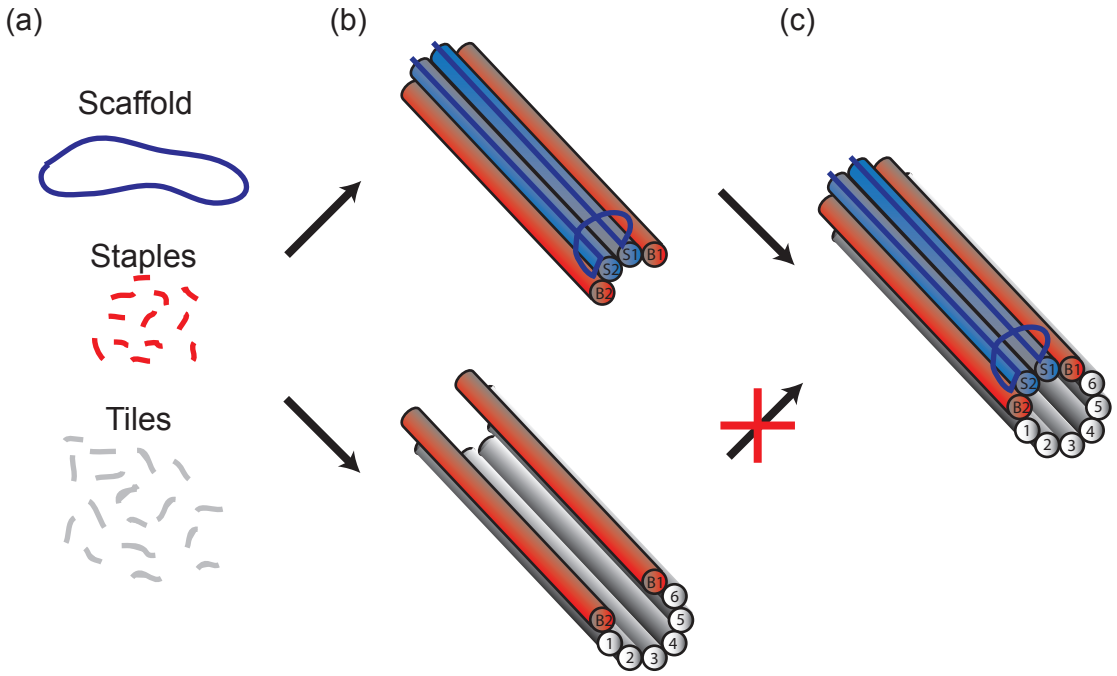

Figure 8.3: Folding path illustration of TO_A: (a) all DNA is un-hybridized at high temperature (b) top: scaffold-staple intermediate, bottom: staple-tile intermediate (c) fully folded TO_A.

8.3 TO_B Characterization

The TO_B design aimed on minimizing the chance of formation of purely tiled ribbons during assembly by dividing the tiled portion of the tube into two sections, on opposite sides of the tube circumference.

To further favor the folding pathway, leading to correctly formed tubes, TO_B was prepared in a two-step process. Scaffold and staple strands were folded first and stabilized by ligation. Therefore the 5' end of each staple strand was phosphorylated by kinase (see section 8.5). Scaffold, staples, and a set of "ligation" strands, which hybridized the ligation target sites of staple strands together were folded first and ligated. The ligation target sites are points were 3' and 5' end of two adjacent staple strands are in contact (helices B1, B2, B3, B4 in figure 8.1 d). In principle (if the ligation efficiency was perfect), this should ligate all staple strands into one continuous DNA strand stably bound to the scaffold strand.

In the second folding step, the sample was heated to 50°C, all tiles were added and the temperature was decreased to room temperature over two hours. The sample was analyzed using agarose gel electrophoresis (figure 8.4 a). Lane (iii), loaded with sample prior the second folding step showed a sharp band (similar to TO_A). Lane (iv), loaded with sample after completing the second folding step (containing all components of TO_B) did show a faint band, over imposed with a smear. Material, retrieved from the gel band and imaged

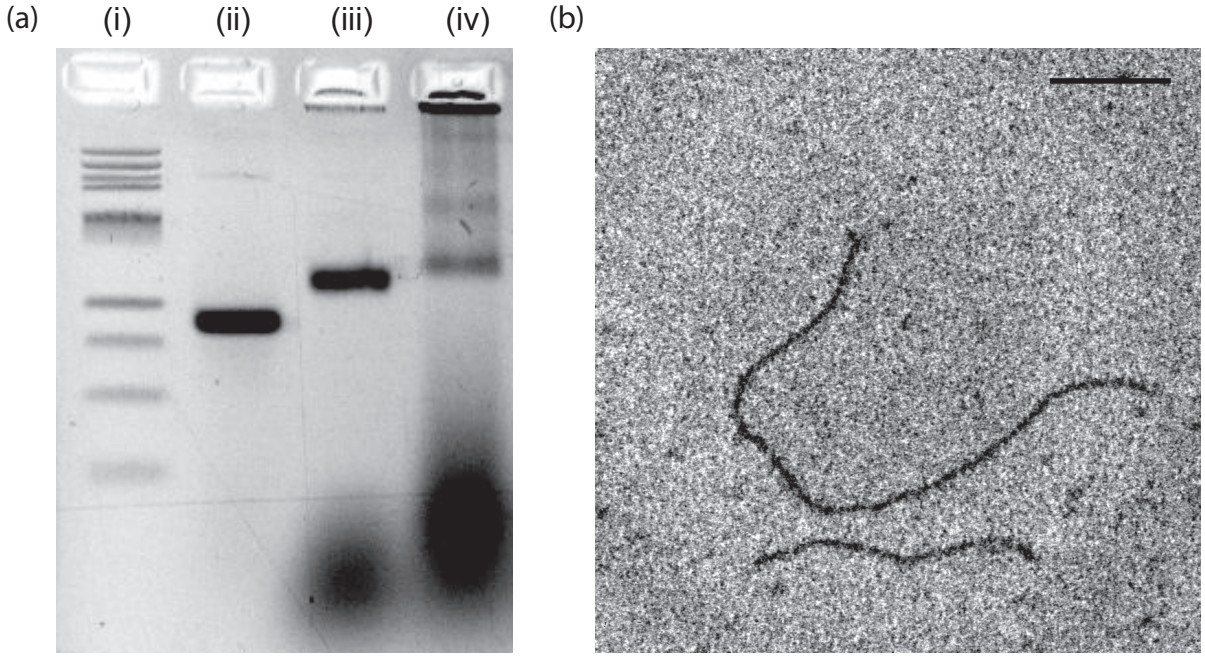

Figure 8.4: (a) 1.5% agarose gel: (i) 1kB DNA ladder, (ii) bare scaffold strand (p8634), (iii) p8634 + staples + ligation strands, after folding step 1 (iv) complete TO_B after two-step folding. (b) TEM of TO_B, from leading band of lane (iv). Scale Bar: 100 nm

by TEM consisted of non-circular DNA nanotubes only. The mean and standard deviation of 21 such tubes was 241 nm ± 114 nm respectively, close to the designed length of TO_B of ≈ 265 nm (figure 8.4 b).

8.4 Conclusion and Outlook

We designed two different DNA nanotubes, TO_A and TO_B, incorporating a scaffold and staple strands that provide sticky ends to align tiles. Gel and TEM analysis showed that TO_A did not properly fold when all components (scaffold, staples and tiles) were present. However, scaffold and staples alone formed well. We proposed that the underlying reason is that tiles can form stable ribbons by themselves, which make the formation of the target tube impossible.

The TO_B design aimed at stabilizing the scaffold - staple interaction and minimizing the stability of tile ribbons. Analysis by gel electrophoresis and TEM showed that TO_B formed DNA nanotubes at a higher yield with a length distribution on the same order as the designed length.

Future work should aim at improving the yield of the tile-origami target structure and facilitating the assembly process. One promising approach may be the use of DNA bricks [107, 42] to replace the scaffolded part because of their structural similarity to tile strands.

8.5 Methods

8.5.1 TO_A Preparation

$p8634$, staple strands and tiles were mixed at a ratio of 1:10:600 to final concentrations of 10, 100, 6000 nM in 1 × TE buffer with 12 mM MgAc. Samples were annealed from 90°C to 70°C with 4 minutes per degree and from 70°C to 20°C with 40 minutes per degree.

8.5.2 TO_B Preparation

Staple strands were incubated in kinase reaction buffer with kinase over night at 37 °C. In the first folding step $p8634$ at 10 nM, the 133 5' phosphorylated staple strands at 100 nM and 4 ligation strands at 6 μM were folded over 2 hours in 1× TE buffer with 12 mM MgAc. Ligase reaction buffer was added to 1× concentration. Ligase was added and the sample incubated at 8°C for two hours. The sample was heated to 50°C and tile strands added to a concentration of 6 μM. The sample was cooled to room temperature over 2 hours.

Chapter 9

DNA Nanotube Software Tools

The design of DNA nano-structures *i.e.* determination of a set of DNA oligonucleotides of specific sequence, that will self-assemble into the desired target structure is a complex geometric problem. Typically DNA duplexes are modeled as cylinders with two angular coordinates for the base positions of the two DNA strands, which are functions of the cylinder z-axis. Two parallel cylinders can be connected by strand cross-overs at z-values where the base positions of two strands are aligned. Once cylinders have been connected by cross-overs and the length of DNA strands has been restricted to the range of synthetically available DNA strands by backbone nick placement, one must assign DNA sequence to each strand under the constraint that the two strands of a DNA duplex must be complementary.

Recent software development applicable to the most commonly used types of DNA nano structures - DNA origami with honey-comb and square cross-sectional lattice - has greatly facilitated this process [23, 41, 21]. However, DNA nanotubes described in chapters 4 and 8 do not fall into this category and were designed using custom Matlab scripts, described in sections 9.1 to 9.3 of this chapter.

Besides for design purposes we used two maltab programs for the quantitative analysis of large microscopy data sets. In particular, the coordinates of DNA nanotube contours were obtained using an adapted version of a tracing program, written by Wiggins *et. al.* [111] (section 2.2). Persistence length and bootstrap error (section 2.2), as well as tube intensities in fluorescence polarization microscopy (section 5.3) were obtained using a custom made Matlab script, described in section 9.5.

9.1 Random Sequence

The random sequence tool can be used to generate X random DNA sequences with Y bases, where X and Y can be any integer. Random bases are generated using the Matlab function "rand". Sequences are generated in a text box from which they can be copied for use in other applications (figure 9.1).

In addition, this tool can be used to generate the complementary sequences to an input in the specified text box. Several sequences of different lengths can be entered at a time.

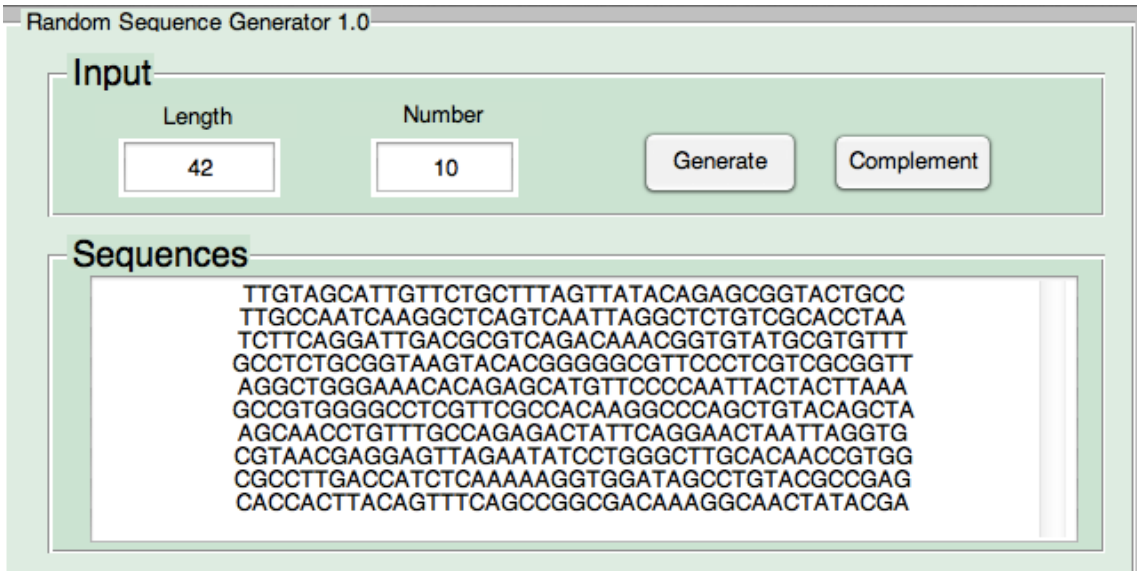

Figure 9.1: User interface (GUI) of the "Random Sequence" script.

All sequences are displayed from 5' to 3' end.

9.2 Cross-Over Planner

The cross-over planner is a simple tool to visualize how the positioning of DNA cross-overs affects the relative placement of DNA duplexes in a cross-sectional view. The graphical user interface (GUI) contains a display of the current cross-section, two panels, which can be used to add DNA duplexes to the current cross-section and a z-posittion slider (figure 9.2). Here the z-position is measured in base pairs along the DNA axis.

When started, the interface contains only one DNA duplex. Red and blue lines represent the angular position of DNA strands with 5' to 3' direction into the plane and out of the plane respectively. Moving the z-position slider or entering an integer value in the text box updates the angular strand positions, γ, according to:

$$\gamma = -\frac{720^\circ}{21} z + \gamma_0 \tag{9.1}$$

where $\gamma_0 = 165^\circ$ for the red strand and $\gamma_0 = 0^\circ$ for the blue strand.

A new DNA duplex can be added to the current DNA duplex by moving to the desired z-position and selecting the "Cross-Over" check box of red or blue strand.The new duplex is placed next to the current duplex, at the angular position of the selected strand. The angular orientation of the two strands of the new duplex is such that the cross-over strand of the old duplex aligns with the opposite direction strand of the new duplex. The new duplex now becomes the "current" duplex and the process can be repeated to sequentially build a DNA structure.

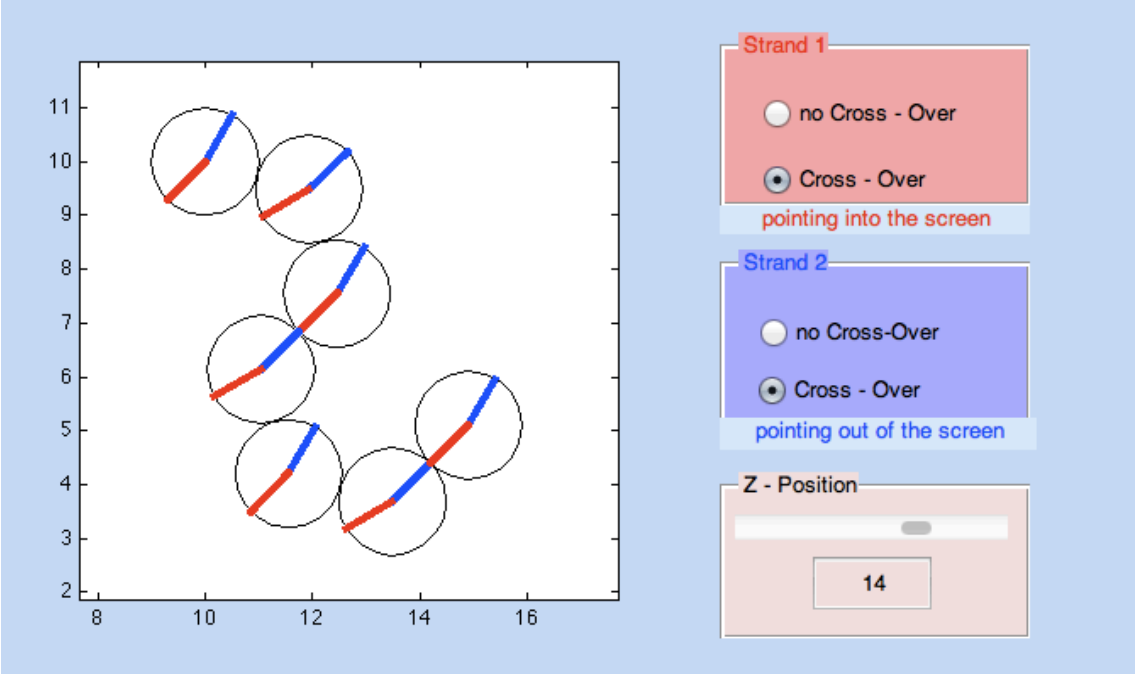

Figure 9.2: GUI of the Cross-Section Planner script.

9.3 Sequence Generator

This tool was used to generate the sequences for DNA nanotubes described in section 4.1.2. Figure 9.3 shows the strand design of 6HT-ST_2, overlaid with a raster, assigning a name to each motif of the assembly. Each grid position contains one sequence, going 5' to 3' from left to right, which we denote as Hx-My and its complementary sequence, Hx-M$y^\star$, going from right to left. The motif length alternates between 11 and 10 bases for odd and even motif numbers respectively. Each DNA strand is constructed from four motifs, *i. e.* U3-R3 consists of motifs H4-M6, H4-M7, H5-M7* and H5-M6*.

When "Sequence Generator" is started the user is prompted to enter the number of helices and "Rings", which refers to the number of distinct R-strands per row (4 in figure 9.3). The program then generates random sequences for each motif, Hx-My, calculates the complementary sequences Hx-M$y^\star$, adds the appropriate sets of four motifs together to obtain the full strand sequences and displays them in the sequence output window (figure 9.3). Four distinct sets of "T-Strands" are generated to make tubes with supertwist states ST_{-2}, ST_0, ST_{+2}, ST_{+4} for even nHT and ST_{-3}, ST_{-1}, ST_{+1}, ST_{+3} for odd nHT.

Each motif is displayed in a table within the GUI. Cells of the table can be edited and the modified sequences can be generated by choosing the "Generate Sequences" option from the menu. This option is useful to integrate specific sequences into a design. In chapter 4, this was used to give strands U1-R1 and U2-R2 identical sequences as U1 and U5 to be able to re-use expensive, dye labeled strands. Motif and strand sequences can be saved using the respective menu option.

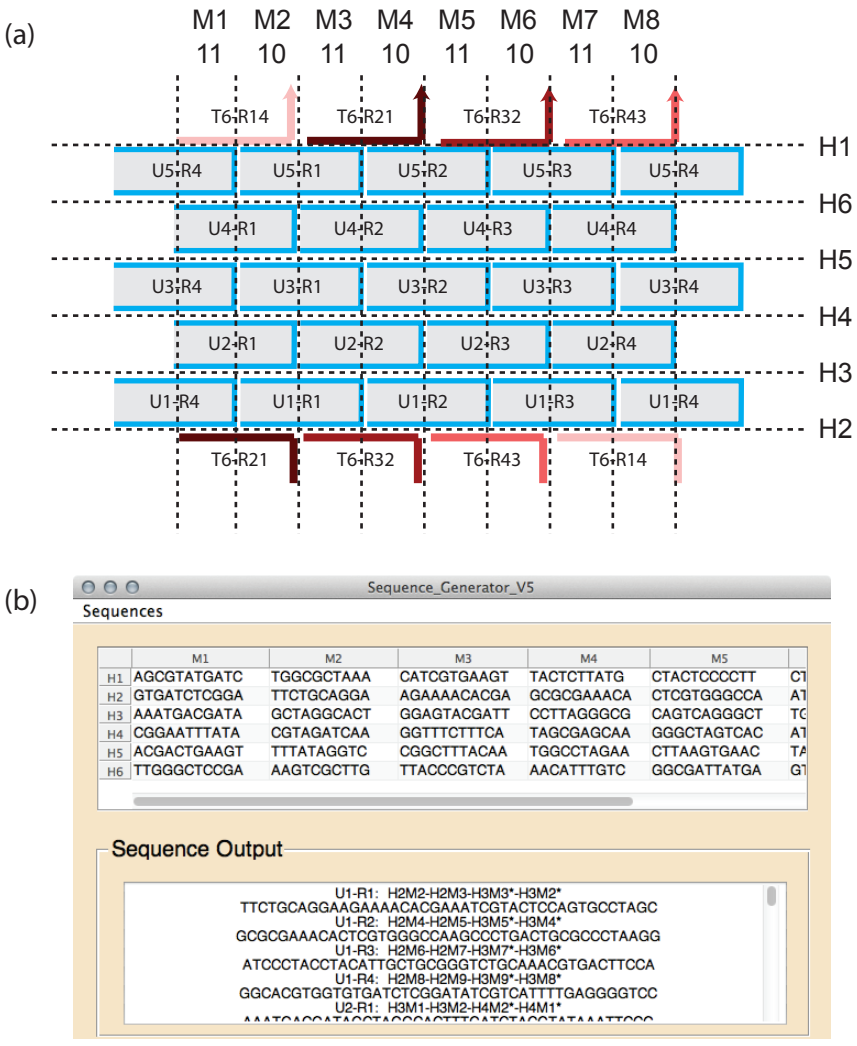

Figure 9.3: (a)Strand design of multi-tile 6HT-ST$_2$ overlaid with a raster, used to generate the strand sequences. (b) GUI of the "Sequence Generator" program. Cells of the top table contain individual motif sequences and can be edited. The output window contains sequence names and sequences, which can be copied for use in other applications.

9.4 Trace

An adapted version of the trace program, written by Paul Wiggins [111] was used to digitalize the contours of DNA nanotubes from fluorescence microscopy images. The program requires manual input of start and end point of a contour. When started, it automatically makes trace steps until it comes to within a specific distance of the end point. The direction of a step is determined by an iterative process, finding the maximum intensity of a line profile, normal to the current tangent.

Modifications to the original program were made to allow loading of image sequences and easily go back and forth between images of the sequence. This facilitates the tracing of data sets, containing only one contour per image.

9.5 Trace Analysis

The "Trace Analysis" program was used to determine persistence length and bootstrap errors from contour traces in chapter 2, 3.1.1 and anisotropy values from FPM data in chapter 5. It can be used to easily navigate large image data sets, visualize and edit contour traces and calculate various statistical properties of the data set. The program interface is shown in figure 9.4 and its functions are explained in the following. The program reads image and trace data in tif and txt format.

9.5.1 GUI Panels

Frame The "Previous" and "Next" buttons can be used to go back and forth between images of the current image sequence. Images are sorted alphabetically, the file name of the current image and its position within the sequence are displayed in two text boxes. Entering an integer number in the frame text box loads and displays the specified image. This panel is not editable and greyed out if the "Mode" is set to "PVP" in the menu.

Trace The buttons and text box can be used to navigate between trace .txt files. Selecting any of the buttons plots the new trace and zooms in on the image region, containing the trace. If in 'PVP Mode", both .txt and .tif file are updated.

Data Selection Panel Many data sets contain individual contour traces that need to be excluded from analysis because of defocusing or overlap of several contours. By setting the toggle button to "Exclude" before selecting the next trace button the current trace will be excluded in any subsequent analysis. The "Selection" check box allows to manually select a region of the current trace to be included. When loading an images sequence, all traces are excluded per default.

Prompter This text box displays results at the end of each analysis, selected in the menu.

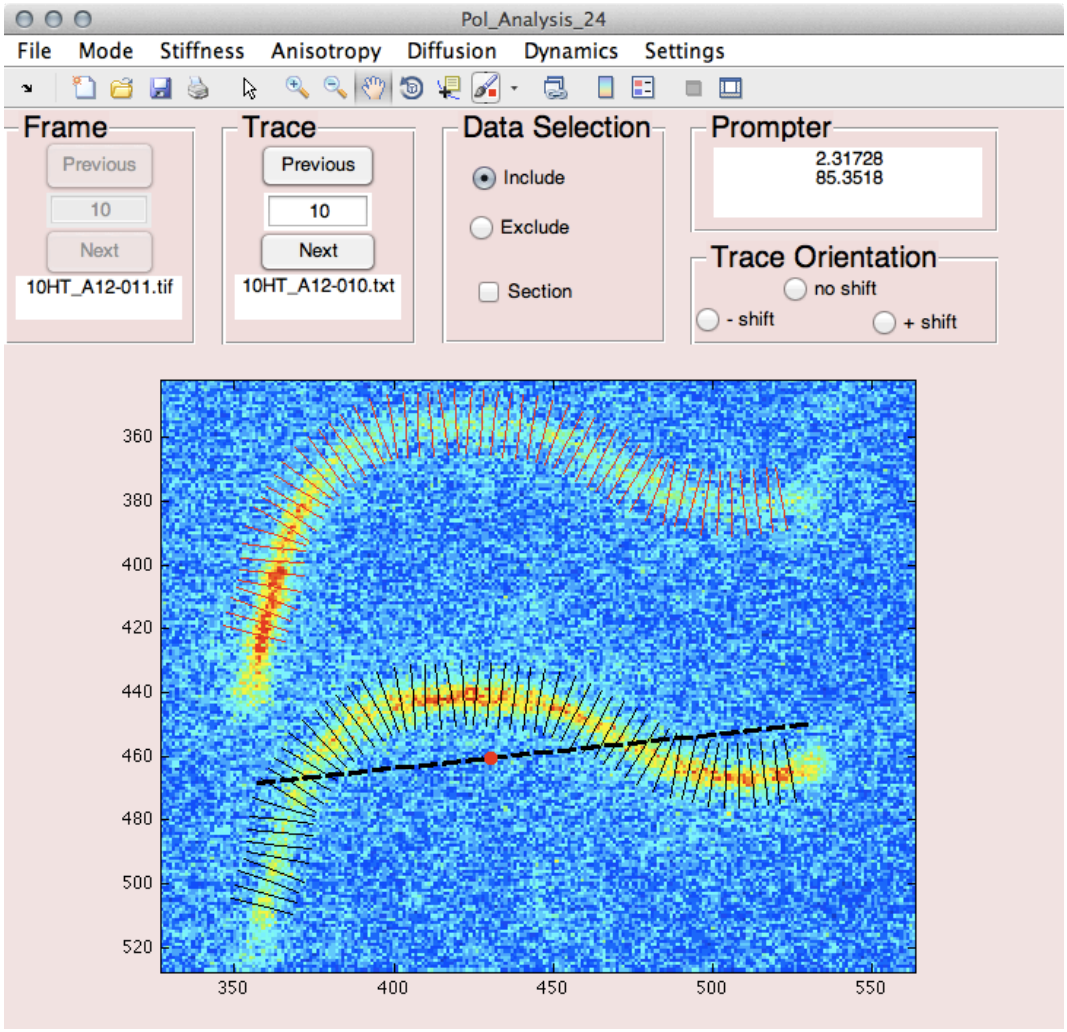

Figure 9.4: GUI of the "Trace Analysis" program.

Trace Orientation Since FPM images contain two contours of identical shape, it is convenient to only trace the contour of greater intensity and create the trace of the second contour by addition of an offset to the coordinates of the first trace. The trace orientation toggle buttons can be used to set the direction of the offset.

9.5.2 Menu Items

File "Open Data" opens an interface to select a folder. If the folder contains tif and txt files the first tif file is displayed and overlaid with the trace coordinates of the first txt file (all files are sorted alphabetically).

"Save Data" and "Load Data" saves / opens a .mat file. This option saves / opens all trace coordinates, settings, analysis results, data selections and trace orientations, but no image data.

Mode This menu can be used to switch between 1) "PVP" and "Glass" mode and 2) "Stiffness" and "Anisotropy" mode.

The "PVP" mode should be used for data sets, in which each image contains exactly one contour *i. e.* the number of .txt files equals the number of .tif files. In this setting the "Frame" panel is greyed out and the current image is automatically set to the same number as the current trace. This setting is useful for movies of a single tube.

The "Glass" mode can be used for data sets with several trace .txt files per image file. Trace and image number can independently be varied.

The stiffness mode is used for analyzing persistence length and is the default setting. The anisotropy mode should be used for analyzing FPM data.

Stiffness "Tangent Correlation" (TC) and "End-to-End Distance" (EE): The trace coordinates from txt files, selected for analysis are combined in two matrices, X and Y, containing one column per trace. Each trace is analyzed by running a loop, starting with point separation, Δx of 1 trace step and increasing by 1 until the point separation is equal to the contour length. In each iteration of the loop, the program computes and stores the inner product of all tangent pairs and end-to-end distance of all trace point pairs as illustrated figure 9.5 a. The average of all inner products / end-to-end distances of a given point separation Δx is computed over all traces and the result plotted in the GUI.

"1D Curve Fit" or "2D Curve Fit" can be used to fit:

$$f_{1D} = e^{-\Delta x/2P} \tag{9.2}$$

$$f_{2D} = e^{-(\Delta x - x_0)/2P} \tag{9.3}$$

to the TC data. The resulting fit parameters P and x_0 are displayed in the prompter panel.

"Bootstrap" can be used to estimate the error of the persistence length. This menu option starts a loop. In every iteration, a data set U_i is created from the original data set, U, by randomly drawing contours from the original set with replacement, until U_i has the same size as U. Persistence length P_i is obtained from the set U_i by the tangent correlation method and 1D or 2D curve fit as described above. The number of bootstrap iterations and curve fit type can be chosen in the settings menu. The mean of P_i and the standard deviation of P_i (the bootstrap error) are displayed in the prompter panel.

"Angle Histogram" prompts the user for input of a tangent separation Δx (in trace steps) and creates a histogram of tangent-tangent angles for the given Δx.

"Frame Correlation" computes the tangent correlation for each frame individually. For any given tangent separation distance, Δx, the tangent correlation is stored as a function of frame number (time). The autocorrelation function of this data is plotted

for all Δx. Correlations indicate, that the time between subsequent frames was not sufficient to randomize the tube contour.

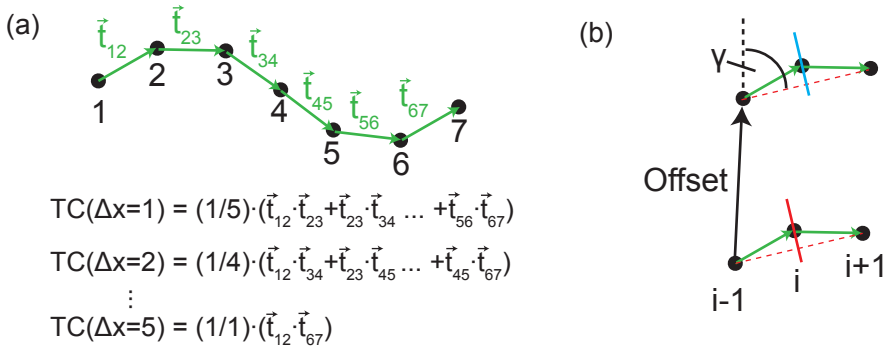

Figure 9.5: (a) Computation of tangent correlation from contour traces. The program runs two loops per contour: the outer loop increases tangent separation distance, the inner loop increases the tangent position on the contour. (b) Computation of trace segment anisotropy from FPM data: intensities I_x and I_y are obtained by computing maximum minus edge pixel value of a line profile, normal to the tube contour

Anisotropy Contains Analysis options for FPM data. The trace coordinate offset can be entered by keyboard or set by left mouse click in the image using the respective options under "Offset".

"Anisotropy": The anisotropy for each trace segment is calculated as illustrated in figure 9.5 b. The segment anisotropy is stored, along with the tube orientation, γ. After processing all trace segments, the anisotropy is binned in 5° intervals with respect to γ and plotted in the GUI.

"Curve Fit": Fits equation 5.23 to the anisotropy data.

Settings "Include All" and "Exclude All" can be used to include or exclude all traces in any of the analysis options. The default is set to "Exclude All". Individual traces can be added or deleted using the "Data Selection" Panel.

"Display Center of Mass": with this option checked, each trace is overlaid with a marker, showing the center of mass of the trace and the tube axis, obtained by fitting a straight line to the trace coordinates.

"View / Change Settings" opens three windows: The user is prompted to input the number of pixels per micrometer (default = 15.6), trace step length (default = 0.256 μm), number of trace points to be ignored at tube ends (default = 1), bootstrap settings and FPM settings. In particular angle γ bin size (default 5°), length of normals to the contour to obtain intensity line profiles (default 20 pixels) and the prism alignment, which can be used to specify which of the two contour images corresponds to I_x and which to I_y.

Appendix A

Tangent Correlation- and End-to-End Distance Data

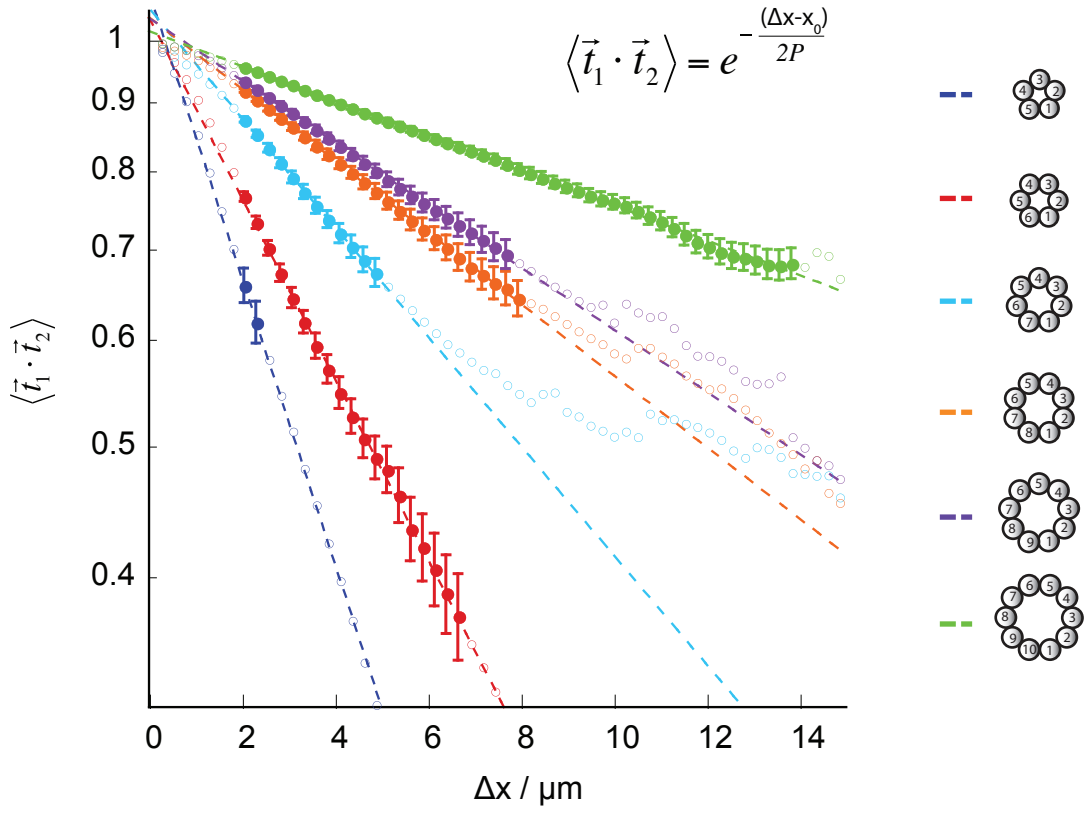

Figure A.1: Tangent correlation data of nHT with fits of equation 2.2. Data points plotted as hollow circles were excluded from the fit. The fit limits are chosen as $2\mu\text{m} < \Delta x < \Delta x_{max}$, where Δx_{max} is the point at which less than 500 tangent pairs can be obtained from the data set.

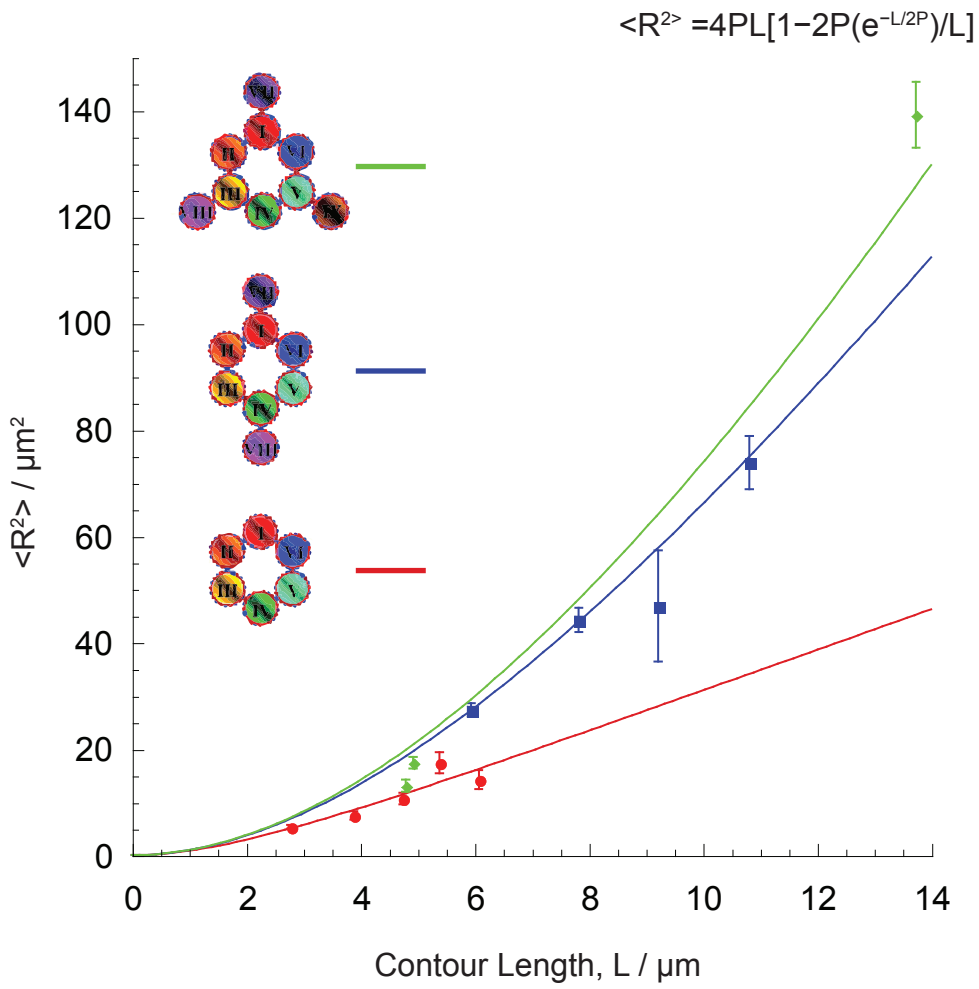

Figure A.2: End-to-End Distance Data of 6HB+X with fits of equation 3.1. Some data points for 6HB+3 are outside the plotted range of L. Best fits were obtained for $P = 1.0\mu$m, $P = 3.6\mu$m and $P = 5.0\mu$m for 6HB, 6HB+2 and 6HB+3 respectively.

Appendix B

Persistence Length of individual nHT

Table B.1: Persistence lengths of individual 5HT - 7HT and characteristics of the data sets from which they are derived. σ_P was obtained using 500 bootstrap iterations. $\Delta x_{\max}$ was the same for all tubes of the same n. For $\Delta x_{\max}$ we used the largest value at which each data set still contained more than U tangent pairs.

	P (μm)	σ_P (μm)	x_o (μm)	$\Delta x_{\max}$ (μm)	U (contours)	L (μm)
$5HT_A$	1.5	0.3	0.51	2.9	47	7.6
$5HT_B$	1.9	0.6	0.16	2.9	44	8.0
$5HT_C$	2.1	1.0	0.22	2.9	16	8.3
$5HT_D$	2.2	0.7	0.49	2.9	17	8.9
$5HT_E$	3.1	0.7	-0.11	2.9	43	7.9
$6HT_A$	1.6	0.3	1.02	4.4	22	14.6
$6HT_B$	1.8	0.4	0.88	4.4	19	8.5
$6HT_C$	2.3	1.0	0.67	4.4	23	10.5
$6HT_D$	2.4	0.7	0.79	4.4	24	11.5
$6HT_E$	2.5	1.0	0.54	4.4	15	10.2
$6HT_F$	2.6	0.6	0.61	4.4	95	6.0
$6HT_G$	2.8	0.8	0.40	4.4	48	8.7
$6HT_H$	3.1	0.5	0.48	4.4	12	31.1
$6HT_I$	3.5	0.8	0.06	4.4	49	10.8
$6HT_J$	3.6	0.9	0.09	4.4	95	5.9
$6HT_K$	4.3	0.6	0.14	4.4	59	14.3
$6HT_L$	4.7	1.1	0.01	4.4	24	13.6
$6HT_M$	-	-	-	-	18	7.5

Table B.2: Persistence lengths of individual 8HT - 10HT and characteristics of the data sets from which they are derived. σ_P was obtained using 500 bootstrap iterations. $\Delta x_{\max}$ was the same for all tubes of the same n. For $\Delta x_{\max}$ we used the largest value at which each data set still contained more than U tangent pairs.

	P (μm)	σ_P (μm)	x_o (μm)	$\Delta x_{\max}$ (μm)	U (contours)	L (μm)
$7HT_A$	4.4	2.0	0.80	6.9	38	9.5
$7HT_B$	4.6	1.1	0.79	6.9	50	11.2
$7HT_C$	4.8	1.6	0.49	6.9	45	9.1
$7HT_D$	5.4	2.1	0.53	6.9	17	14.8
$7HT_E$	6.3	1.5	0.12	6.9	30	16.8
$7HT_F$	7.7	1.9	0.42	6.9	16	23.6
$7HT_G$	8.7	2.3	-0.10	6.9	16	16.7
$8HT_A$	5.7	1.5	0.82	6.9	42	8.5
$8HT_B$	6.0	1.4	0.86	6.9	53	13.3
$8HT_C$	7.7	1.3	0.67	6.9	60	11.6
$8HT_D$	8.3	1.5	0.62	6.9	50	15.7
$8HT_E$	9.5	1.6	0.56	6.9	85	9.7
$8HT_F$	10.1	1.2	0.45	6.9	87	16.4
$9HT_A$	5.5	1.1	0.88	9.2	100	10.7
$9HT_B$	9.9	2.7	0.64	9.2	43	12.7
$9HT_C$	10.3	1.9	0.82	9.2	53	16.6
$9HT_D$	12.8	4.0	0.46	9.2	50	14.6
$9HT_E$	13.6	2.9	0.77	9.2	90	10.6
$10HT_A$	12.4	2.5	0.52	7.2	41	14.3
$10HT_B$	13.8	1.2	0.80	7.2	150	14.9
$10HT_C$	14.3	2.2	0.77	7.2	45	22.2
$10HT_D$	15.2	2.5	0.49	7.2	48	15.8
$10HT_E$	15.7	2.2	0.56	7.2	80	15.3
$10HT_F$	16.8	2.9	0.45	7.2	50	15.4
$10HT_G$	16.8	2.7	0.56	7.2	46	19.1
$10HT_H$	17.1	3.8	0.21	7.2	67	11.6
$10HT_I$	19.5	27.9	0.35	7.2	13	13.2
$10HT_J$	20.2	4.3	0.45	7.2	59	17.8
$10HT_K$	20.5	5.5	0.10	7.2	101	8.6
$10HT_L$	21.7	5.9	0.32	7.2	55	11.0
$10HT_M$	26.5	4.2	-0.07	7.2	89	12.8

Appendix C

DNA Sequences for DNA Nanotubes

Table C.1: **DNA sequences for DX-tubes**. All sequences were purchased from Integrated DNA Technologies (IDT) with HPLC purification.

Name	Sequence
Strand 1 (no Hairpin)	CTCAGTGGACAGCCGT-TCTGGAGCGTTGGACGAAACT
Strand 1 (with Hairpin)	CTCAGTGGACAGCCTACTTACCTCCCC - CCCCCAGGTAAGTATTGTTCTGGAGCGTTGGACGAAACT
Strand 2	GTCTGGTAGAGCACCACTGAGAGG TA
Strand 3	CCAGAACGGCTGTGGCTAAACAGTAACCGAAGCACCAACGCT
Strand 4	CAGACAGTTTCGTGGTCATCGTACCT
Strand 5	CGATGACCTGCTTCGGTTACTGTTTAGCCTGCTCTAC
free Hairpin	TACTTACCTCCCCCCCCCAGGTAAGTATT

Table C.2: **DNA sequences for nHT**. Sequences U2-Handle and 8T-thiol were purchased from Eurofins-MWG-Operon. All remaining DNA oligos were purchased from Integrated DNA Technologies. Unlabeled U- and T- strands were purchase both with and without HPLC purification, Cy3 labeled strands only with HPLC purification. Samples for fluorescence microscopy experiments were prepared from HPLC purified strands, samples for TEM experiments were prepared from unpurified strands (except for U1-HPLC).

Name	Sequence
U1	GGCGATTAGG ACGCTAAGCCA CCTTTAGATCC TGTATCTGGT
U2	GGATCTAAAGG ACCAGATACA CCACTCTTCC TGACATCTTGT
U3	GGAAGAGTGG ACAAGATGTCA CCGTGAGAACC TGCAATGCGT
U4	GGTTCTCACGG ACGCATTGCA CCGCACGACC TGTTCGACAGT
U5	GGTCGTGCGG ACTGTCGAACA CCAACGATGCC TGATAGAAGT
U6	GGCATCGTTGG ACTTCTATCA ATGCACCTCC AGCTTTGAATG
U7	GGAGGTGCAT CATTCAAAGCT AACGGTAACTA TGACTTGGGA
U8	TAGTTACCGTT TCCCAAGTCA AACACTAGAC ACATGCTCCTA
U9	GTCTAGTGTT TAGGAGCATGT CGAGACTACAC CCTTGCCACC
T5	GGTCGTGCGG ACTGTCGAACA CCTAATCGCC TGGCTTAGCGT
T6	GGCATCGTTGG ACTTCTATCA CCTAATCGCC TGGCTTAGCGT
T7	GGAGGTGCAT CATTCAAAGCT CCTAATCGCC TGGCTTAGCGT
T8	TAGTTACCGTT TCCCAAGTCA CCTAATCGCC TGGCTTAGCGT
T9	GTCTAGTGTT TAGGAGCATGT CCTAATCGCC TGGCTTAGCGT
T10	GTGTAGTCTCG GGTGGCAAGG CCTAATCGCC TGGCTTAGCGT

Table C.3: **Modified sequences for *n*HT** All sequences were purchased from Integrated DNA Technologies (IDT) with HPLC purification.

Name	Sequence
U1-Cy3	/5Cy3/TT GGCGATTAGG ACGCTAAGCCA - CCTTTAGATCC TGTATCTGGT
U1-Alexa	/5Alex647N/ TT GGCGATTAGG ACGCTAAGCCA - CCTTTAGATCC TGTATCTGGT
U1-FAM	/56-FAM/ TT GGCGATTAGG ACGCTAAGCCA - CCTTTAGATCC TGTATCTGGT
U4-Cy3	/5Cy3/TT GGTTCTCACGG ACGCATTGCA - CCGCACGACC TGTTCGACAGT
U5-Cy3	/5Cy3/TT GGTCGTGCGG ACTGTCGAACA - CCAACGATGCC TGATAGAAGT
U2+1	GGATCTAAAGG ACCAGATACA CCACTCTTCC TGACATCTTGT
U3+1	GGAAGAGTGG ACAAGATGTCA CCGTGAGAACC TGCAATGCGT
U5-1	GGTCGTGCGG ACTGTCGAACA CCAACGATGCC TGATAGAAGT
T6-1	GGCATCGTTGG ACTTCTATCA CCTAATCGCC TGGCTTAGCGT
U5-1-Chol	GGTCGTGCGG ACTGTCGAACA - CCAACGATGCC TGATAGAAGT /3CholTEG/
T6-1-Chol	GGCATCGTTGG ACTTCTATCA - CCTAATCGCC TGGCTTAGCGT /3CholTEG/
T9-NST	GTCTAGTGTT TAGGAGCATGT TGGCTTAGCGT CCTAATCGCC
U2-H	GGATCTAAAGG ACCAGATACA - CCACTCTTCC TGACATCTTGT - AAAAAAAA
U6-H	GGCATCGTTGGACTTCTATCA - ATGCACCTCCAGCTTTGAATG - TTTT - ATTTATACAACGGA
8T-thiol	thiol-TTTTTTTT
Rockstar	CACCGCTTTTGCCTTTTGGGGACGGATA-TTTT-TCCGTTGTATAAAT

Table C.4: **DNA sequences for 6HT$_2$ and 6HT-ST$_m$.** All sequences were purchased from Integrated DNA Technologies (IDT) with PAGE purification.

Name	Sequence
L1	GGCGATTAGGACGCTAAGCCA GGAAGAGTGGACAAGATGTCA - CCGTGAGAACCTGCAATGCGT CCTTTAGATCCTGTATCTGGT
L1-ST	ACAAGATGTCA GGCGATTAGG ACGCTAAGCCA GGAAGAGTGG TGTATCTGGT CCGTGAGAACC TGCAATGCGT CCTTTAGATCC
L1-NST	ACAAGATGTCA GGCGATTAGG ACGCTAAGCCA GGAAGAGTGG TGCAATGCGT CCTTTAGATCC TGTATCTGGT CCGTGAGAACC
L2-Cy3	/5Cy3/TT ACGCATTGCAGGTTCTCACGG - ACCAGATACAGGATCTAAAGG - AGTCCTGGAATCTGATTGCCT TCTCTTCACCGTAATCTTATC
L3	AGGCAATCAGATTCCAGGACT GATAAGATTACGGTGAAGAGA - TGTTCGACAGTCCGCACGACC AGCTTTGAATGATGCACCTCC
L3-ST	CGGTGAAGAGA AGGCAATCAG ATTCCAGGACT GATAAGATTA ATGCACCTCC TGTTCGACAGT CCGCACGACC AGCTTTGAATG
L3-NST	CGGTGAAGAGA AGGCAATCAG ATTCCAGGACT GATAAGATTA CCGCACGACC AGCTTTGAATG ATGCACCTCC TGTTCGACAGT
L4	GGTCGTGCGGACTGTCGAACA GGAGGTGCATCATTCAAAGCT - AACGGTAACTATGACTTGGGA CCAACGATGCCTGATAGAAGT
L5	TCCCAAGTCATAGTTACCGTT ACTTCTATCAGGCATCGTTGG - TGGACCAATGTGAATCGCTTA CGGAATGCTAGATACCATGCG
L5-ST	GGCATCGTTGG TCCCAAGTCA TAGTTACCGTT ACTTCTATCA GATACCATGCG TGGACCAATG TGAATCGCTTA CGGAATGCTA
L5-NST	GGCATCGTTGG TCCCAAGTCA TAGTTACCGTT ACTTCTATCA TGAATCGCTTA CGGAATGCTA GATACCATGCG TGGACCAATG
L6	TAAGCGATTCACATTGGTCCA CGCATGGTATCTAGCATTCCG - TGGCTTAGCGTCCTAATCGCC TGACATCTTGTCCACTCTTCC

Table C.5: **DNA sequences for 6HT-ST$_m$ and 7HT-ST$_m$.** All sequences were purchased from Integrated DNA Technologies (IDT) with standard desalting except for U1-R1-Cy3, which had HPLC purification

Name	Sequence
U1-R1	GGCGATTAGG ACGCTAAGCCA CCTTTAGATCC TGTATCTGGT
U1-R1-Cy3	/5Cy3/TT GGCGATTAGG ACGCTAAGCCA - CCTTTAGATCC TGTATCTGGT
U1-R2	GGTCGTGCGG ACTGTCGAACA CCAACGATGCC TGATAGAAGT
U1-R3	GCGTGGCAATTGCCATAAATTCATACATAACGGCGCCAGACG
U1-R4	TTTCAAGACCGGCACTTGTATGGCGTAGGGCGGGTTTAGCGG
U2-R1-6HT	GGATCTAAAGGACTTCTATCAAAGACGGGACGACTCCGGGAG
U2-R2-6HT	GGCATCGTTGGCGTCTGGCGCACGACTTCGATTTCGGATCCA
U2-R3-6HT	CGTTATGTATGCCGCTAAACCTTGCAAAAACTGAACTCGAAC
U2-R4-6HT	CGCCCTACGCCACCAGATACAAGGTCATGGCTTTGGGAGCTA
U2a-R1-7HT	AAATTTCGTAGCTGCTCTAACAAGACGGGACGACTCCGGGAG
U2a-R2-7HT	CACGTAATCCGTGCGCACTTCACGACTTCGATTTCGGATCCA
U2a-R3-7HT	GCAAACCAGGGTGAACTACTCTTGCAAAAACTGAACTCGAAC
U2a-R4-7HT	AGTTAATATTTTACTTACAACAGGTCATGGCTTTGGGAGCTA
U2b-R1-7HT	CGCCCTACGCCACCAGATACACTACGAAATTTGTTGTAAGTA
U2b-R2-7HT	GGATCTAAAGGACTTCTATCACGGATTACGTGGTTAGAGCAG
U2b-R3-7HT	GGCATCGTTGGCGTCTGGCGCCCCTGGTTTGCGAAGTGCGCA
U2b-R4-7HT	CGTTATGTATGCCGCTAAACCAAATATTAACTGAGTAGTTCA
U3-R1	GCCATGACCTCTCCCGGAGTCCGCTGCTGATCGGCTTAAGAT
U3-R2	GTCCCGTCTTTGGATCCGAAAGATATGTCCGTTCCGCCGCGA
U3-R3	TCGAAGTCGTGTTCGAGTTCAAATGTCTATGCGATGCAGCAG
U3-R4	GTTTTTGCAATAGCTCCCAAAATTTAATGTCGTTTACAGTAA
U4-R1	TCGCGGCGGAGATCAGCAGCGCTGCAGAAATAGGACCCCCAG
U4-R2	CTGCTGCATCACGGACATATCTTCCTGGCATGGCTGAATTCC
U4-R3	TTACTGTAAAGCATAGACATTACCTTACGTAACTTACAGCCA
U4-R4	ATCTTAAGCCCGACATTAAATTGACTGCCTATTTGAGTATTT

Table C.6: **DNA sequences for 6HT-ST$_m$ and 7HT-ST$_m$ (continued).** All sequences were purchased from Integrated DNA Technologies (IDT) with standard desalting.

Name	Sequence
U5-R1	TAGGCAGTCACTGGGGGTCCTCGAGGCGAAACGTGTTCACTC
U5-R2	ATTTCTGCAGGGAATTCAGCCTATTCACATAGGCGAAGGCTA
U5-R3	ATGCCAGGAATGGCTGTAAGTTGCATCATGGGGGTCCTCAAT
U5-R4	TACGTAAGGTAAATACTCAAACCTGAGTGATCCATGACCCTT
TR23	GTTTCGCCTCGTAGCCTTCGCATTGCCACGCTGTTCGACAGT
TR34	CTATGTGAATAATTGAGGACCGGTCTTGAAAAATTTATGGCA
TR41	CCCATGATGCAAAGGGTCATGCCTAATCGCCATACAAGTGCC
TR12	GATCACTCAGGGAGTGAACACCCGCACGACCTGGCTTAGCGT
TR11	GTTTCGCCTCGTAGCCTTCGCCCGCACGACCTGGCTTAGCGT
TR22	CTATGTGAATAATTGAGGACCATTGCCACGCTGTTCGACAGT
TR33	CCCATGATGCAAAGGGTCATGGGTCTTGAAAAATTTATGGCA
TR44	GATCACTCAGGGAGTGAACACCCTAATCGCCATACAAGTGCC
TR21	CTATGTGAATAATTGAGGACCCCGCACGACCTGGCTTAGCGT
TR32	CCCATGATGCAAAGGGTCATGATTGCCACGCTGTTCGACAGT
TR43	GATCACTCAGGGAGTGAACACGGTCTTGAAAAATTTATGGCA
TR14	GTTTCGCCTCGTAGCCTTCGCCCTAATCGCCATACAAGTGCC
TR13	GTTTCGCCTCGTAGCCTTCGCGGTCTTGAAAAATTTATGGCA
TR42	GATCACTCAGGGAGTGAACACATTGCCACGCTGTTCGACAGT
TR13	GTTTCGCCTCGTAGCCTTCGCGGTCTTGAAAAATTTATGGCA
TR24	GATCACTCAGGATTGAGGACCCCTAATCGCCATACAAGTGCC

Appendix D

Strand Design of 6HB

DNA strand sequences were designed using the program SEQUIN [90]. The DNA strands with fluorescein (FAM) were synthesized on an Applied Biosystems 394, removed from the support, and deprotected using routine phosphora- midite procedures. Other strands were purchased from Integrated DNA Technologies, Inc. (Coralville, IA). All strands have been purified by denaturing gel electrophoresis (PAGE); bands were cut out of 15-20% denaturing gels and eluted in a solution containing 500 mM ammonium acetate, 11 mM magnesium acetate, and 1 mM EDTA. All strands and buffers were finally filtered by 0.22 μm Ultrafree-MC centrifugal filter units (Millipore Corp.).

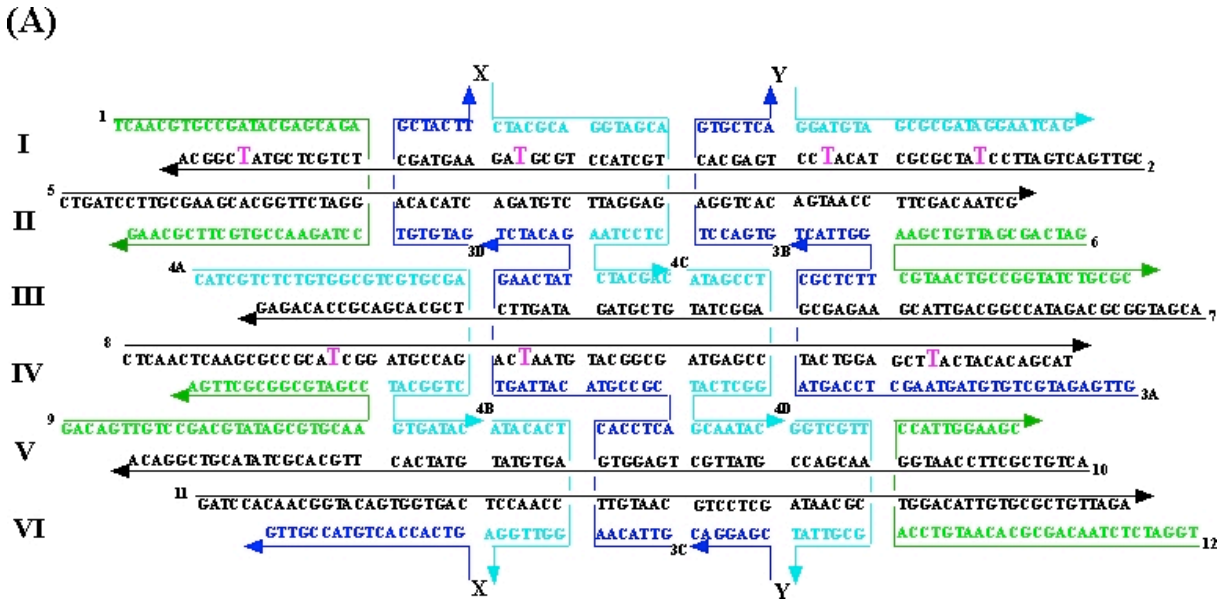

Figure D.1: Sequences and Strand Design of 6HB

DNA duplexes are indicated by Roman numerals. Oligonucleotide strands are indicated by different colors and strand numbering is shown. The arrows represent the polarity of

each strand: 5' → 3'. Both ends of each DNA duplex in the systems contain sticky ends. Sticky ends on the same DNA duplex are complementary to each other. Points X and Y are the places where the cyclic bundle closes. Fluorescein molecules are attached to 5-end of one oligonucleotide strand (indicated by red arrow in $6HB_P$+2) and to thymines, which are in purple and larger font size.

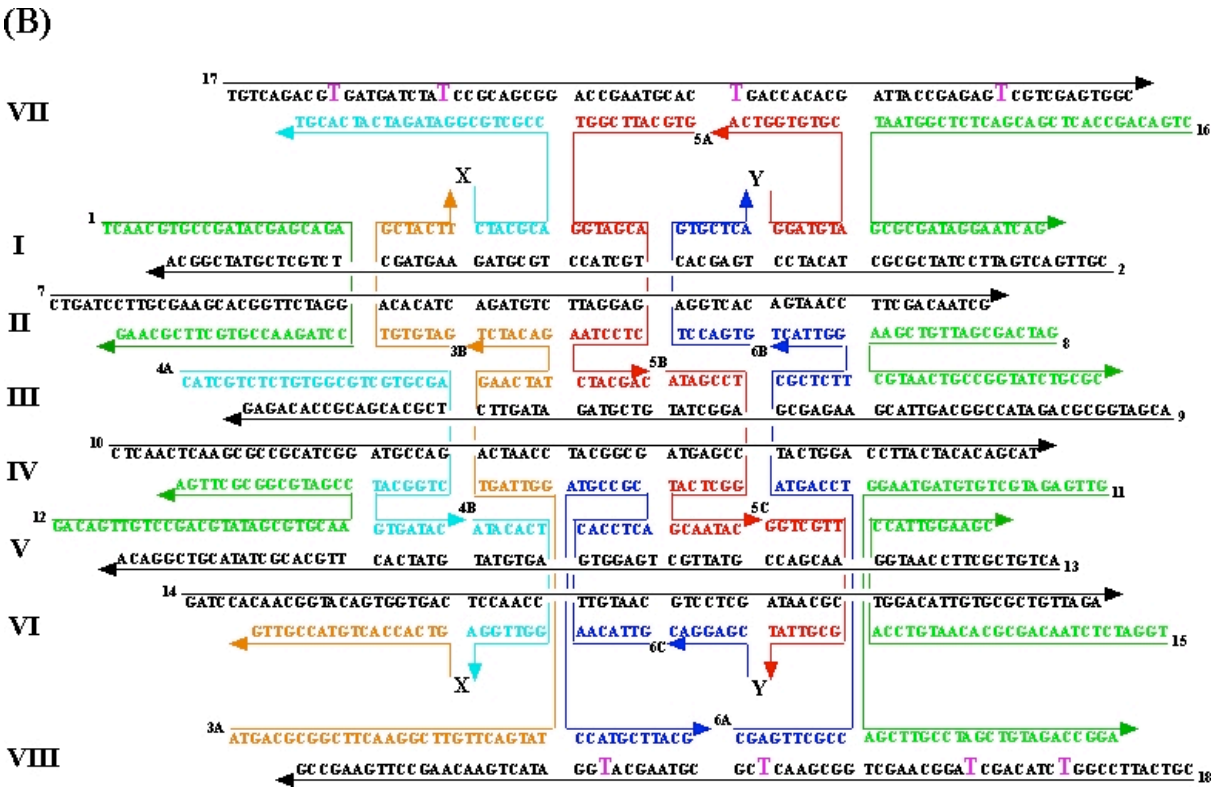

Figure D.2: Sequences and strand design of 6HB+2

Figure D.3: Sequences and strand design of 6HB+3

Figure D.4: Sequence and strand design of 6HB$_P$+2

Appendix E

Temperature Controlled UV-Absorbance Data of 6HT-ST$_m$

Folded tubes at a concentration of 100nM per strand (equivalent to 12.6μM concentration of base pairs) was placed in a cuvette (Starna Cells Inc., 100 μL, 10mm, Quartz Fluorometer Cell, catalog number: 16.100F-Q-10/Z8.5) and covered with 100μL of mineral oil to prevent evaporation. The sample was heated from 20°C to 95°C at a rate of 1°C per minute, left at 95°C for 5 minutes and cooled back to 20°C with -1°C per minute. The sample was illuminated using a high power Xenon light source (Mikropack, Order Number: HPX-2000) and absorbance was measured using a cooled array detector (Ocean Optics, QE65000).

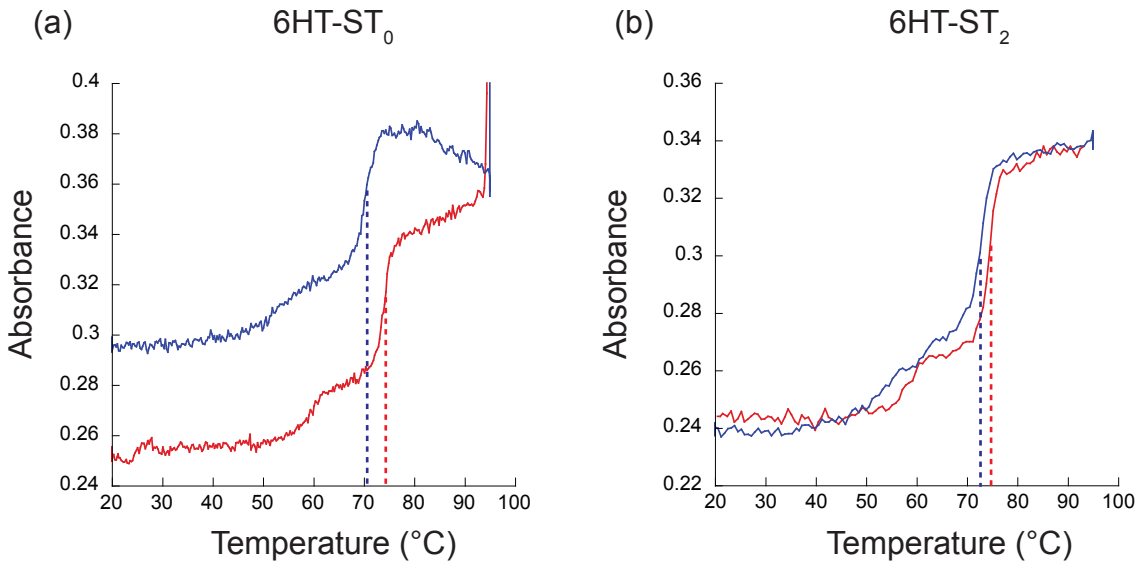

Figure E.1: UV absorbance at 260nm as function of temperature for 6HT-ST$_0$ (a) and 6HT-ST$_2$ (b). The increase in absorbance between 80°C and 95°C during melting and annealing in 6HT-ST$_0$ is most likely due to evaporation or air bubble formation.

Integration time and sampling rates were varied from sample to sample and are likely to be the cause for differences in the noise levels between the measurements.

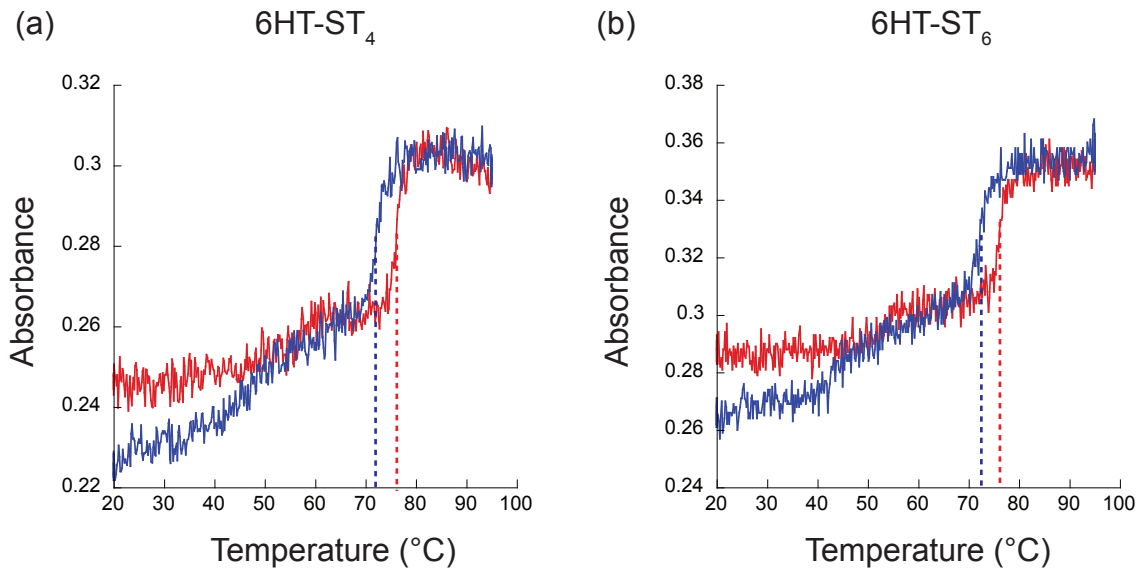

Figure E.2: UV absorbance at 260nm as function of temperature for 6HT-ST$_4$ (a) and 6HT-ST$_6$ (b).

Appendix F

Writhe of DNA Nanotubes with different Cy3 Attachment Positions

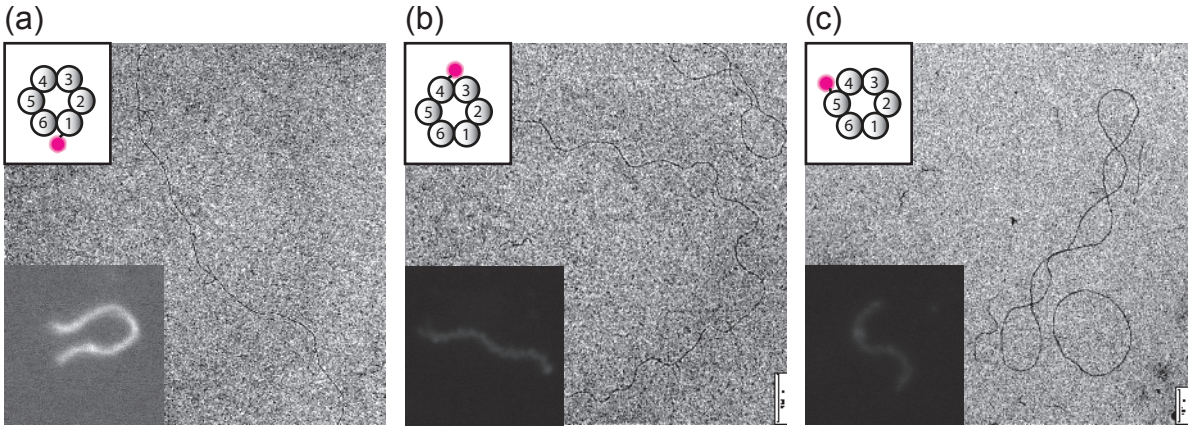

Figure F.1: TEM images (size 4.8μm x 4.8μm) and fluorescence images (size 10μm x 10μm) of 6HT, labeled with Cy3 on a single DNA oligonucleotide at positions indicated in inlets.

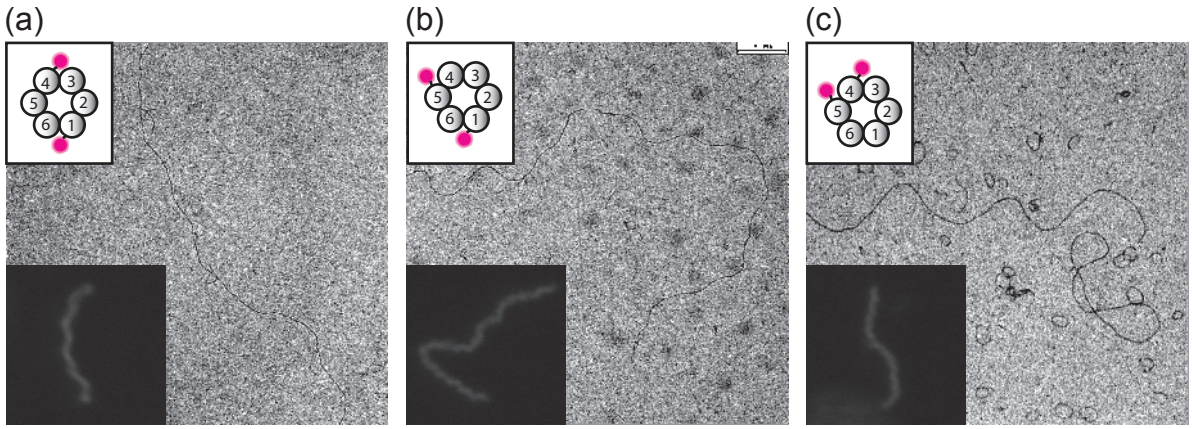

Figure F.2: TEM images (size 4.8μm x 4.8μm) and fluorescence images (size 10μm x 10μm) of 6HT, labeled with Cy3 on two different DNA oligonucleotide at positions indicated in inlets.

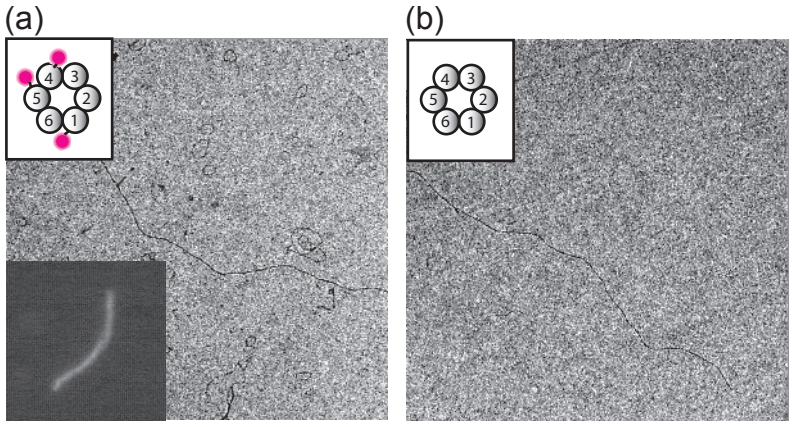

Figure F.3: TEM images (size 4.8μm x 4.8μm) and fluorescence images (size 10μm x 10μm) of 6HT, labeled with Cy3 on three different DNA oligonucleotides at positions indicated in inlets (a) and without Cy3 label (b).

Appendix G

FPM Data of nHT

Table G.1: Anisotropy measurements of nHT, labeled with Cy3 at strands denoted in subscript. Anisotropy was obtained using FPM and the angle between dipole and nanotube axis, α, was obtained by fitting equation 5.23 to the data. N specifies the number of tube segments from which the measurement of α was obtained.

Tube Type	α	Substrate	N
$9HT_{\{1\}}$	64.0	glass	
$9HT_{\{4\}}$	61.6	glass	
$9HT_{\{5\}}$	63.5	glass	
$9HT\text{-}NST_{\{1\}}$	-	glass	
$9HT\text{-}NST_{\{4\}}$	63.2	glass	
$9HT\text{-}NST_{\{5\}}$	62.3	glass	
$6HT_{\{145\}}$	57.3	glass	
$7HT_{\{145\}}$	59.4	glass	
$9HT_{\{145\}}$	59.7	glass	
$9HT_{\{145\}}$ A	62.1	PVP	
$9HT_{\{145\}}$ B	61.6	PVP	2689
$10HT_{\{145\}}$	61.4	glass	

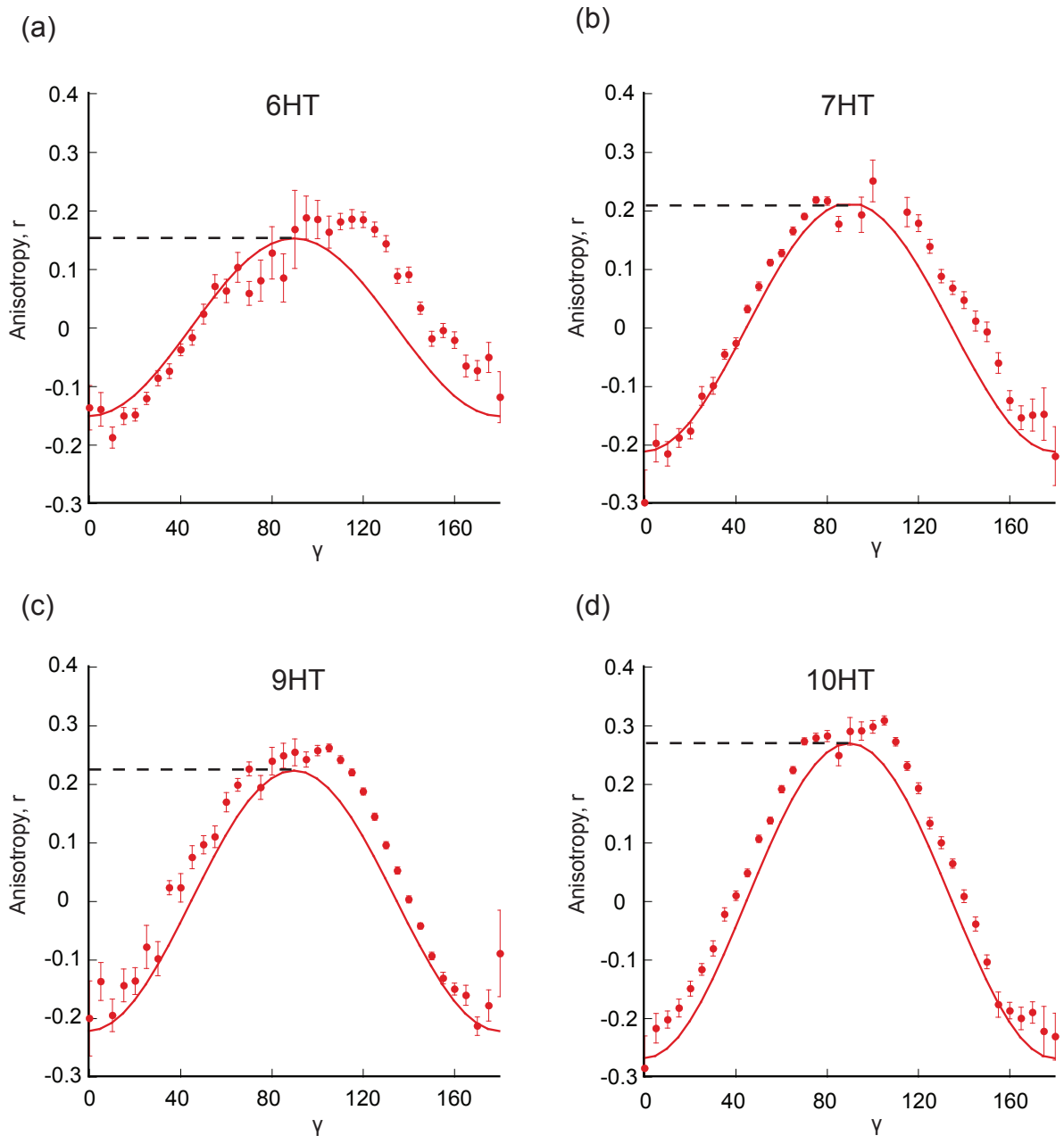

Figure G.1: Anisotropy as function of tube orientation, γ, for 6HT (a), 7HT (b), 9HT (c) and 10HT (d), labeled with Cy3 at strands "U1", "U4" and "U5". Solid lines are curve fits of equation 5.23.

Bibliography

[1] D. Aherne, A. Satti und D. Fitzmaurice, *Nanotechnology* **18** (2007), 125205.

[2] F.a. Aldaye, P.K. Lo, P. Karam, C.K. Mclaughlin, G. Cosa und H.F. Sleiman, *Nature nanotechnology* **4** (2009), 349.

[3] H. Arakawa, J.F. Neault und H.a. Tajmir-Riahi, *Biophysical journal* **81** (2001), 1580.

[4] D. Axelrod, *Biophysical journal* **26** (1979), 557.

[5] X.c. Bai, T.G. Martin, S.H.W. Scheres und H. Dietz, *PNAS* **109** (2012), 20012.

[6] C.G. Baumann, S.B. Smith, V.a. Bloomfield und C. Bustamante, *Proceedings of the National Academy of Sciences of the United States of America* **94** (1997), 6185.

[7] W. Becker: *Advanced Time-Correlated Single Photon Counting Techniques*. Springer, 2005.

[8] N.a.W. Bell, C.R. Engst, M. Ablay, G. Divitini, C. Ducati, T. Liedl und U.F. Keyser, *Nano letters* **12** (2012), 512.

[9] M.J. Berardi, W.M. Shih, S.C. Harrison und J.J. Chou, *Nature* **476** (2011), 109.

[10] L. Berti und G.A. Burley, *Nature nanotechnology* **3** (2008), 81.

[11] Z. Bryant, M.D. Stone, J. Gore, S.B. Smith, N.R. Cozzarelli und C. Bustamante, *Nature* **424** (2003), 338.

[12] C. Bustamante, Z. Bryant und S.B. Smith, *Nature* **421** (2003), 423.

[13] C. Bustamante, S.B. Smith, J. Liphardt und D. Smith, *Current opinion in structural biology* **10** (2000), 279.

[14] P. Charoenphol und H. Bermudez, *Acta Biomater* (2013).

[15] G.H. Clever und M. Shionoya, *Coordination Chemistry Reviews* **254** (2010), 2391.

[16] E. Czeizler und L. Kari, *Frontiers in computational neuroscience* **3** (2009), 20.

[17] H. Dietz, S.M. Douglas und W.M. Shih, *Science (New York, N.Y.)* **325** (2009), 725.

[18] M. Doi und S. Edwards: *Theory of polymer dynamics*. Clarendon Press, Oxford, UK, 1986 1986.

[19] S.M. Douglas, I. Bachelet und G.M. Church, *Science (New York, N.Y.)* **335** (2012), 831.

[20] S.M. Douglas, J.J. Chou und W.M. Shih, *Proceedings of the National Academy of Sciences of the United States of America* **104** (2007), 6644.

[21] S.M. Douglas, H. Dietz, T. Liedl, B. Högberg, F. Graf und W.M. Shih, *Nature* **459** (2009), 414.

[22] S.M. Douglas, A.H. Marblestone, S. Teerapittayanon, A. Vazquez, G.M. Church und W.M. Shih, *Nucleic Acids Research* **37** (2009), 5001.

[23] S.M. Douglas, A.H. Marblestone, S. Teerapittayanon, A. Vazquez, G.M. Church und W.M. Shih, *Nucleic acids research* **37** (2009), 5001.

[24] K. Du, S.H. Ko, G.M. Gallatin, H.P. Yoon, J.A. Liddle und A.J. Berglund, *Chemical communications (Cambridge, England)* **49** (2013), 907.

[25] A. Ekani-Nkodo, A. Kumar und D. Fygenson, *Physical Review Letters* **93** (2004), 1.

[26] M. Endo, Y. Katsuda, K. Hidaka und H. Sugiyama, *Journal of the American Chemical Society* **132** (2010), 1592.

[27] T.j. Fu und N.C. Seeman, *Biochemistry* **32** (1993), 3211.

[28] P. Furrer, J. Bednar, a.Z. Stasiak, V. Katritch, D. Michoud, a. Stasiak und J. Dubochet, *Journal of molecular biology* **266** (1997), 711.

[29] K. Günther, M. Mertig und R. Seidel, *Nucleic acids research* **38** (2010), 6526.

[30] E. Gwinn, P. O'Neill, a.J. Guerrero, D. Bouwmeester und D. Fygenson, *Advanced Materials* **20** (2008), 279.

[31] P.J. Hagerman, *Ann. Rev. Biophys. Biophys. Chem* **17** (1988), 265.

[32] D. Han, S. Pal, J. Nangreave, Z. Deng, Y. Liu und H. Yan, *Science (New York, N.Y.)* **332** (2011), 342.

[33] B. Huang, W. Wang, M. Bates und X. Zhuang, *Science (New York, N.Y.)* **319** (2008), 810.

[34] A. Iqbal, S. Arslan, B. Okumus, T.J. Wilson, G. Giraud, D.G. Norman, T. Ha und D.M.J. Lilley, *Proceedings of the National Academy of Sciences of the United States of America* **105** (2008), 11176.

[35] A. Iqbal, L. Wang, K.C. Thompson, D.M.J. Lilley und D.G. Norman, *Biochemistry* **47** (2008), 7857.

[36] R. Jungmann, M. Scheible, A. Kuzyk, G. Pardatscher, C.E. Castro und F.C. Simmel, *Nanotechnology* **22** (2011), 275301.

[37] R. Kamiya und S. Asakura, *J. Mol. Biol.* (1976), 167.

[38] M. Kampmann, C.E. Atkinson, A.L. Mattheyses und S.M. Simon, *Nature Publishing Group* **18** (2011), 643.

[39] M. Kampmann, C.E. Atkinson, A.L. Mattheyses und S.M. Simon, *Nature structural & molecular biology* **18** (2011), 643.

[40] D.J. Kauert, T. Kurth, T. Liedl und R. Seidel, *Nano letters* **11** (2011), 5558.

[41] Y. Ke, S.M. Douglas, M. Liu, J. Sharma, A. Cheng, A. Leung, Y. Liu, W.M. Shih und H. Yan, *Journal of the American Chemical Society* **131** (2009), 15903.

[42] Y. Ke, L.L. Ong, W.M. Shih und P. Yin, *Science* **338** (2012), 1177.

[43] J.W. Keum und H. Bermudez, *Chemical communications* (2009), 7036.

[44] S.H. Ko, K. Du und J.A. Liddle, *Angewandte Chemie (International ed. in English)* **52** (2013), 1193.

[45] A. Kuzuya, R. Wang, R. Sha und N.C. Seeman, *Nano letters* **7** (2007), 1757.

[46] A. Kuzyk, R. Schreiber, Z. Fan, G. Pardatscher, E.M. Roller, A. Högele, F.C. Simmel, A.O. Govorov und T. Liedl, *Nature* **483** (2012), 311.

[47] A. Larsson, C. Carlsson, M. Jonsson und B. Albinssont, *JACS* (1994), 8459.

[48] T. Liedl, B. Högberg, J. Tytell, D.E. Ingber und W.M. Shih, *Nature nanotechnology* **5** (2010), 520.

[49] D. Liu, S.H. Park, J.H. Reif und T.H. LaBean, *Proceedings of the National Academy of Sciences of the United States of America* **101** (2004), 717.

[50] H. Liu, Y. Chen, Y. He, A.E. Ribbe und C. Mao, *Angewandte Chemie (International ed. in English)* **45** (2006), 1942.

[51] W. Liu, H. Zhong, R. Wang und N.C. Seeman, *Angewandte Chemie (International ed. in English)* **50** (2011), 264.

[52] X. Liu, Y. Xu, T. Yu, C. Clifford, Y. Liu, H. Yan und Y. Chang, *Nano letters* **12** (2012), 4254.

[53] Y. Liu, T. Pérez, W. Li, J.D. Gunton und A. Green, *The Journal of chemical physics* **134** (2011), 065107.

[54] C. Lu, M. Reedy und H.P. Erickson, *Journal of bacteriology* **182** (2000), 164.

[55] B. Maier und J.O. Ra, *Macromolecules* **33** (2000), 7185.

[56] B. Maier und J.O. Rädler, *Physical Review Letters* **82** (1999), 1911.

[57] N.R. Markham und M. Zuker, *Nucleic acids research* **33** (2005), W577.

[58] J.F. Marko und E.D. Siggia, *Macromolecules* **27** (1994), 981.

[59] F. Mathieu, S. Liao, J. Kopatsch, T. Wang, C. Mao und N.C. Seeman, *Nano letters* **5** (2005), 661.

[60] H.T. Maune, S.P. Han, R.D. Barish, M. Bockrath, W.a.G. Iii, P.W.K. Rothemund und E. Winfree, *Nature nanotechnology* **5** (2010), 61.

[61] J.C. Mitchell, J.R. Harris, J. Malo, J. Bath und A.J. Turberfield, *Journal of the American Chemical Society* **126** (2004), 16342.

[62] G.M. Nam, N.K. Lee, H. Mohrbach, A. Johner und I.M. Kulić, *EPL (Europhysics Letters)* **100** (2012), 28001.

[63] P.R.O. Neill, E.G. Gwinn und D.K. Fygenson, *The Journal of Physical Chemistry C* **115** (2011), 24061.

[64] D.G. Norman, R.J. Grainger, D. Uhrín und D.M. Lilley, *Biochemistry* **39** (2000), 6317.

[65] S.S.R. Oemrawsingh, N. Markeševi, E.G. Gwinn, R. Eliel und D. Bouwmeester, *The Journal of Physical Chemistry C* **116** (2012), 25568.

[66] P. O'Neill, P.W.K. Rothemund, A. Kumar und D.K. Fygenson, *Nano letters* **6** (2006), 1379.

[67] P. O'Neill, P.W.K. Rothemund, A. Kumar und D.K. Fygenson, *Nano letters* **6** (2006), 1379.

[68] P.R. O'Neill, K. Young, D. Schiffels und D.K. Fygenson, *Nano letters* (2012).

[69] P.R. ONeill, L.R. Velazquez, D.G. Dunn, E.G. Gwinn und D.K. Fygenson, *The Journal of Physical Chemistry C* **113** (2009), 4229.

[70] S.H. Park, R. Barish, H. Li, J.H. Reif, G. Finkelstein, H. Yan und T.H. Labean, *Nano letters* **5** (2005), 693.

[71] F. Patolsky, Y. Weizmann, O. Lioubashevski und I. Willner, *Angewandte Chemie (International ed. in English)* **41** (2002), 2323.

[72] D. Patra, I. Gregor und J. Enderlein, *Journal of Physical Chemistry A* (2004), 6836.

[73] J.T. Petty, J. Zheng, N.V. Hud und R.M. Dickson, *Journal of the American Chemical Society* **126** (2004), 5207.

[74] J.O. Radler, *Science* **275** (1997), 810.

[75] A. Rajendran, M. Endo, Y. Katsuda, K. Hidaka und H. Sugiyama, *ACS Nano* **5** (2011), 665.

[76] P.W.K. Rothemund, *Nature* **440** (2006), 297.

[77] P.W.K. Rothemund, A. Ekani-Nkodo, N. Papadakis, A. Kumar, D.K. Fygenson und E. Winfree, *Journal of the American Chemical Society* **126** (2004), 16344.

[78] S. Rudorf und J.O. Rädler, *Journal of the American Chemical Society* **134** (2012), 11652.

[79] M.J. Rust, M. Bates und X. Zhuang, *October* **3** (2006), 793.

[80] P. Sa-Ardyen, A.V. Vologodskii und N.C. Seeman, *Biophysical journal* **84** (2003), 3829.

[81] M.E. Sanborn, B.K. Connolly, K. Gurunathan und M. Levitus, *The journal of physical chemistry. B* **111** (2007), 11064.

[82] A. Satti, D. Aherne und D. Fitzmaurice, *Chemistry of materials* **19** (2007), 1543.

[83] J.M. Schins, a. Agronskaia, B.G. de Grooth und J. Greve, *Cytometry* **37** (1999), 230.

[84] R. Schreiber, S. Kempter, S. Holler, V. Schüller, D. Schiffels, S.S. Simmel, P.C. Nickels und T. Liedl, *Small (Weinheim an der Bergstrasse, Germany)* (2011), 1795.

[85] V.J. Schüller, S. Heidegger, N. Sandholzer, P.C. Nickels, N.A. Suhartha, S. Endres, C. Bourquin und T. Liedl, *ACS nano* **5** (2011), 9696.

[86] D. Schultz, K. Gardner, S.S.R. Oemrawsingh, N. Markešević, K. Olsson, M. Debord, D. Bouwmeester und E. Gwinn, *Advanced materials (Deerfield Beach, Fla.)* **25** (2013), 2797.

[87] D. Schultz und E. Gwinn, *Chemical communications (Cambridge, England)* **47** (2011), 4715.

[88] D. Schultz und E.G. Gwinn, *Chemical communications (Cambridge, England)* **48** (2012), 5748.

[89] D.E. Schultz, S.M. Copp, N. Markesevic, K. Gardner, S.S.R. Oemrawsingh, D. Bouwmeester und E.G. Gwinn, *ACS nano (SUBMITTED)* (2013).

[90] N. Seeman, *Journal of Biomolecular Structure & Dynamics* **8** (1990), 573.

[91] N.C. Seeman, *Journal of Theoretical Biology* **99** (1982), 237 .

[92] N.C. Seeman, *Nature* **421** (2003), 427.

[93] N.C. Seeman, *Annual review of biochemistry* **79** (2010), 65.

[94] P. Selenyi, *Physical Review Letters* **56** (1939), 477.

[95] B. Sengupta, C.M. Ritchie, J.G. Buckman, K.R. Johnsen, P.M. Goodwin und J.T. Petty, *The Journal of Physical Chemistry C* (2008).

[96] J.P.J. Sobczak, T.G. Martin, T. Gerling und H. Dietz, *Science* **338** (2012), 1458.

[97] T.L. Sobey, S. Renner und F.C. Simmel, *Journal of physics. Condensed matter : an Institute of Physics journal* **21** (2009), 034112.

[98] K. Srinivasan, C. Pohl und N. Avdalovic, *Anal. Chem.* **69** (1997), 2798.

[99] I.H. Stein, V. Schüller, P. Böhm, P. Tinnefeld und T. Liedl, *Chemphyschem : a European journal of chemical physics and physical chemistry* **12** (2011), 689.

[100] C. Steinhauer, R. Jungmann, T.L. Sobey, F.C. Simmel und P. Tinnefeld, *Angewandte Chemie (International ed. in English)* **48** (2009), 8870.

[101] X. Sun, S.H. Ko, C. Zhang, A.E. Ribbe und C. Mao, *JACS* (2009), 13248.

[102] S.J. Tan, M.J. Campolongo, D. Luo und W. Cheng, *Nature nanotechnology* **6** (2011), 268.

[103] A.S. Walsh, H. Yin, C.M. Erben, M.J.A. Wood und A.J. Turberfield, *ACS nano* **5** (2011), 5427.

[104] R. Wang, W. Liu und N.C. Seeman, *Chemistry & biology* **16** (2009), 862.

[105] T. Wang, D. Schiffels, S. Martinez Cuesta, D. Kuchnir Fygenson und N.C. Seeman, *Journal of the American Chemical Society* **134** (2012), 1606.

[106] J.D. Watson und F.H.C. Crick, *Nature* **171** (1953), 737.

[107] B. Wei, M. Dai und P. Yin, *Nature* **485** (2012), 623.

[108] R. Wei, T.G. Martin, U. Rant und H. Dietz, *Angewandte Chemie (International ed. in English)* **51** (2012), 4864.

[109] K.L. Weirich, J.N. Israelachvili und D.K. Fygenson, *Biophysical journal* **98** (2010), 85.

[110] P.a. Wiggins, T. van der Heijden, F. Moreno-Herrero, A. Spakowitz, R. Phillips, J. Widom, C. Dekker und P.C. Nelson, *Nature nanotechnology* **1** (2006), 137.

[111] P.a. Wiggins, T. van der Heijden, F. Moreno-Herrero, A. Spakowitz, R. Phillips, J. Widom, C. Dekker und P.C. Nelson, *Nature nanotechnology* **1** (2006), 137.

[112] O.I. Wilner, R. Orbach, A. Henning, C. Teller, O. Yehezkeli, M. Mertig, D. Harries und I. Willner, *Nature Communications* **2** (2011), 540.

[113] H. Yamakawa und M. Fujii, *The Journal of chemical physics* **64** (1976), 5222.

[114] H. Yan, S.H. Park, G. Finkelstein, J.H. Reif und T.H. LaBean, *Science (New York, N.Y.)* **301** (2003), 1882.

[115] Y. Yang, Z. Zhao, F. Zhang, J. Nangreave, Y. Liu und H. Yan, *Nano letters* **13** (2013), 1862.

[116] P. Yin, H.M.T. Choi, C.R. Calvert und N.a. Pierce, *Nature* **451** (2008), 318.

[117] P. Yin, R.F. Hariadi, S. Sahu, H.M.T. Choi, S.H. Park, T.H. Labean und J.H. Reif, *Science (New York, N.Y.)* **321** (2008), 824.

[118] Y.x. Zhao, A. Shaw, X. Zeng, E. Benson, A.M. Nyström und B. Högberg, *ACS nano* **5** (2011), 5427.

[119] Y.X. Zhao, A. Shaw, X. Zeng, E. Benson, A.M. Nyström und B. Högberg, *ACS Nano* **6** (2012), 8684.

[120] J. Zheng, J.J. Birktoft, Y. Chen, T. Wang, R. Sha, P.E. Constantinou, S.L. Ginell, C. Mao und N.C. Seeman, *Nature* **461** (2009), 74.

Acknowledgment

I would like to thank both of my Ph.D advisors: Deborah and Tim for their great support over the past years. I appreciate all the efforts you took for setting up meetings with nine hour time shifts, traveling across the atlantic and investing time in proposals for travel grants.

Thank you to Joachim Rädler, whose class got me interested in biophysics and who encouraged me and enabled an initial collaboration with UCSB.

Thank you to Elisabeth Gwinn and Paul W. K. Rothemund for letting my use their labs, helpful discussions about my research and invitations to delicious burgers (HBC) and sandwiches in Goleta and Pasadena.

Thank you to Cornelia and Wilfried Weber for valuable advice on how to plan a career in science at various stages of graduate school.

Thank you to all of my colleagues in Munich and Santa Barbara: Kim Weirich, Patrick O'Neill and Stacy Shiffler-Copp, Phillip Nickels, David Smith, Robert Schreiber, Tobias Preiss, Verena Schüller, Stephanie Simmel, Tao Zhang, Alex Maier, Samet Kocabey and Susi Kempter and everyone else from the Rdler, Liedl and Fygenson labs for vivid scientific discussions, countless table soccer matches, lots of fun around the lab and good times at conferences and winter schools.

Thank you to Dani who was always there for me and put up with our complicated travel schedule and long distance constraints.

Finally, I would like to thank my parents as well as my grandmother, who have encouraged and supported me all the way through graduate school.

Publications

1. Schiffels, D., Liedl, T., & Fygenson, D. K. (2013). Nanoscale Structure and Microscale Stiffness of DNA Nanotubes. ACS Nano, 7(8), 67006710. doi:10.1021/nn401362p

2. ONeill, P. R., Young, K., Schiffels, D., & Fygenson, D. K. (2012). Few-Atom Fluorescent Silver Clusters Assemble at Programmed Sites on DNA Nanotubes. Nano letters, 12(11), 54645469. doi:10.1021/nl3017797

3. Wang, T., Schiffels, D., Martinez Cuesta, S., Fygenson, D. K., & Seeman, N. C. (2012). Design and Characterization of 1D Nanotubes and 2D Periodic Arrays Self-Assembled from DNA Multi-Helix Bundles. Journal of the American Chemical Society, 134(3), 16061616. doi:10.1021/ja207976q

4. Schreiber, R., Kempter, S., Holler, S., Schller, V., Schiffels, D., Simmel, S. S., Nickels, P. C., & Liedl, T. (2011). DNA Origami-Templated Growth of Arbitrarily Shaped Metal Nanoparticles. Small (Weinheim an der Bergstrasse, Germany), 7(13), 17951799. doi:10.1002/smll.201100465